Film height in soft elastohydrodynamic lubrication with application to roll-to-plate nanoimprinting

Snieder, J.

DOI
10.4233/uuid:e117b8a4-dbe7-4a31-adeb-299b625e2ae1

Publication date
2026

Document Version
Final published version

Citation (APA)
Snieder, J. (2026). *Film height in soft elastohydrodynamic lubrication: with application to roll-to-plate nanoimprinting*. [Dissertation (TU Delft), Delft University of Technology].
https://doi.org/10.4233/uuid:e117b8a4-dbe7-4a31-adeb-299b625e2ae1

Important note
To cite this publication, please use the final published version (if applicable).
Please check the document version above.

Film height in soft elastohydrodynamic lubrication

with application to roll-to-plate nanoimprinting

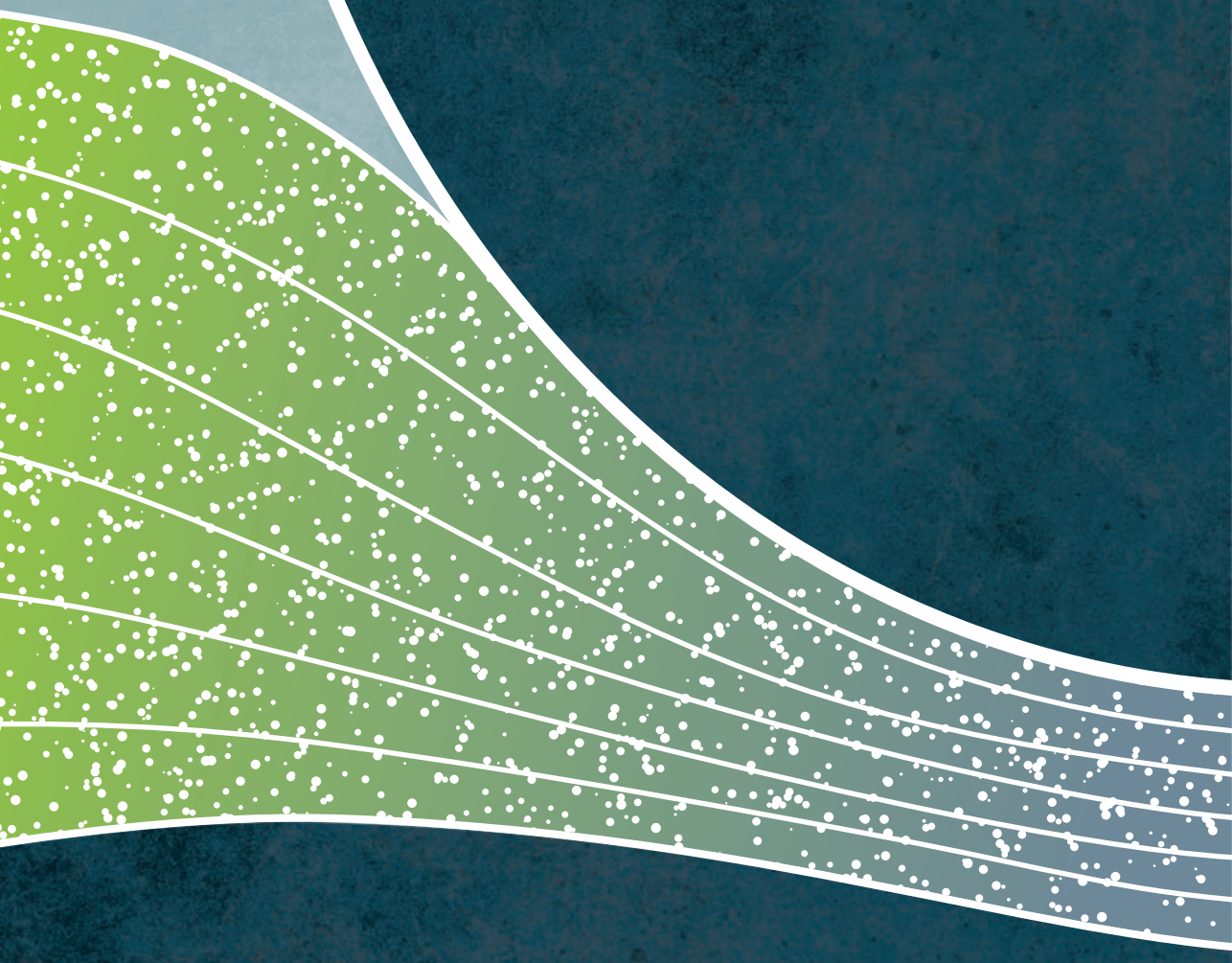

Jelle Snieder

Film Height in Soft Elastohydrodynamic Lubrication

with application to roll-to-plate nanoimprinting

Film Height in Soft Elastohydrodynamic Lubrication

with application to roll-to-plate nanoimprinting

Dissertation

for the purpose of obtaining the degree of doctor
at Delft University of Technology
by the authority of the Rector Magnificus Prof. dr. ir. H. Bijl,
chair of the Board for Doctorates
to be defended publicly on
Tuesday 20 January 2026 at 12:30 o'clock

by

Jelle SNIEDER

Master of Science in Mechanical Engineering,
Delft University of Technology, The Netherlands
born in Amsterdam, The Netherlands

This dissertation has been approved by the promotors.

Composition of the doctoral committee:

Rector Magnificus,	chairperson
Dr. ir. R. A. J. van Ostayen,	Delft University of Technology, promotor
Prof. dr. ir. J. L. Herder,	Delft University of Technology, promotor
Independent members:	
Prof. Dr.-Ing. G. Poll,	Leibniz University Hannover
Prof. dr. ir. M. B. de Rooij,	University of Twente
Prof. C. A. Dransfeld,	Delft University of Technology
Prof. dr. R. Pecnik,	Delft University of Technology
Dr. N. Bhattacharya,	Delft University of Technology

This research was funded by the Topsector Energy Subsidy of the Dutch Ministry of Economic Affairs with project number TEHE119003.

Keywords: soft elastohydrodynamic lubrication, inverse hydrodynamic lubrication, roll-to-plate nanoimprinting, ratiometric fluorescence imaging, film height prediction, measurement, and steering

Cover design: Alexandra Touw

Printed by: Ridderprint

ISBN 978-94-6537-089-7

An electronic version of this dissertation is available at
`http://repository.tudelft.nl`

Contents

Summary

Roll-to-plate nanoimprinting is a manufacturing method to replicate micro- and nanotextures with high resolution on large-area substrates. The applied textures vary in shape and size and are used to enhance the optical or mechanical properties of a substrate, such as anti-reflection or light-trapping surface layers for displays and solar panels or drag reduction surface layers for aviation and shipping.

The working principle of roll-to-plate nanoimprinting is based on a molding process, in which a flexible stamp, containing the textures to be replicated and wrapped around a soft-layered roller, is pressed into a liquid resin. After UV-curing the resin film, the flexible stamp is delaminated from the substrate. The final imprint consists of the preferred texture on top of a residual layer, which should ideally be thin and uniform over the entire surface for optimal performance of the product. Both thickness and uniformity are governed by the liquid film height before curing. To ensure that the imprinted pattern is accurately replicated and matches the features of the flexible stamp, it is essential to control the magnitude and uniformity of the film height during the imprint process. However, this is challenging due to variations in the substrate surface topography and a general trend towards imprinting larger substrates for improved production capacity. The motivation behind this work is to improve the imprint quality by addressing these challenges in roll-to-plate nanoimprinting to achieve uniform film heights on large-area, non-flat substrates.

The roll-to-plate nanoimprint process can be considered as a form of fluid film lubrication. It qualifies as soft elastohydrodynamic lubrication (EHL), due to the combination of low pressures and large elastic deformation. This dissertation focuses on the film height in soft EHL, with application to roll-to-plate nanoimprinting. The objective is to develop theory and methods to predict, measure, and steer the film height. The research is structured in three parts, which correspond to the threefold approach taken in this study: film height prediction, film height measurement, and film height steering.

In the first part, the physics of the roll-to-plate nanoimprint process are captured in numerical models to describe the elastohydrodynamic lubrication. The model development including experimental validation is carried out in several steps, in which the model complexity is increased to better describe the underlying physics of the roll-to-plate nanoimprint process. These models contribute to a better understanding of the elastohydrodynamic lubrication of soft-layered rollers and tensioned webs (i.e. flexible stamps) in roll-to-plate nanoimprinting. The addition of the tensioned web and its contact mechanics with the imprint roller to traditional soft EHL theory provides valuable insights on the influence of web tension and bending stiffness on the film height and pressure distributions in the lubricated roller contact. Moreover, the addition of substrate waviness and its negative effect on the film height uniformity clearly underscores the need for a film height steering concept.

The second part, about film height measurement, presents a novel analytical model and the experimental validation of the ratiometric fluorescence film height measurement

method. In general, a film height measurement in fluid film lubrication is challenging, because the fluid film is trapped between two surfaces. Ratiometric fluorescence imaging, which uses two fluorophores dissolved in the fluid, is an efficient optical measurement method to map the film height over large areas at once. In this work, the fluorophores Fluorescein and Eosin Y are used for this purpose. The original model, developed by Hidrovo and Hart [1], is extended with the emission and reabsorption of both fluorophores and the surface reflection of the background. The more accurate model description of the measurement method makes the analytical model an efficient design tool to tune or optimize the measurement response for a desired film height range. Moreover, the experimental fluorescence spectra provide an intuitive understanding of the working principle behind the measurement method.

In the third part, a novel concept is presented to steer the film height in soft EHL. The feasibility of this concept, which is inspired by inverse hydrodynamic lubrication theory, was demonstrated in a one-dimensional, numerical, EHL model of a deformable tilting pad slider bearing on a wavy substrate surface. The film height distribution can be steered by applying a distributed zero-stiffness load to the deformable slider surface, hereby approaching the corresponding pressure distribution of the initially prescribed, desired film height distribution. Next, the film height steering concept is experimentally validated in a novel experimental setup, in which a fluid film is formed between the deformable slider and a rotating disk with a flat substrate surface. Ratiometric fluorescence imaging is used for mapping the film height. The results effectively demonstrate the feasibility and efficacy of this innovative concept to steer the film height in soft EHL.

This dissertation contributes to various aspects of the film height in soft EHL, with application to roll-to-plate nanoimprinting. The developed theory and methods on film height prediction, measurement, and steering form a solid basis for future research and facilitate practical implementation to realize a uniform film height in soft EHL processes, such as liquid film coating, roller-based UV-cure nanoimprinting, or lithographic printing.

Samenvatting

Roll-to-plate nanoimprinten is een fabricagemethode waarmee micro- en nanostructuren met hoge resolutie op grote oppervlakken worden gekopieerd. De aangebrachte structuren variëren in vorm en grootte en worden toegepast om de optische of mechanische eigenschappen van een substraat te verbeteren. Voorbeelden hiervan zijn anti-reflecterende of lichtvangende lagen voor beeldschermen en zonnepanelen, of weerstandsverlagende lagen voor de lucht- en scheepvaart.

Het werkingsprincipe van roll-to-plate nanoimprinten is gebaseerd op een stempelproces, waarin een flexibele stempel met de gewenste structuren rondom een rol met een elastische laag is gespannen. De flexibele stempel wordt met een rollende beweging in een vloeibare hars gedrukt. Na het uitharden van de harslaag met UV-licht kan de flexibele stempel van het substraat worden afgerold. De uiteindelijke imprint bestaat uit de gewenste structuur bovenop een residulaag, die bij voorkeur dun en uniform is over het gehele oppervlak, voor een optimale werking van het product. Zowel de dikte als de uniformiteit van de residulaag worden bepaald door de filmdikte vóór uitharding. Om te garanderen dat de gekopieerde structuur nauwkeurig overeenkomt met de kenmerken van de stempel, is het daarom belangrijk om de hoogte en gelijkmatigheid van de filmdikte tijdens het imprintproces goed te controleren. Dit is echter uitdagend vanwege hoogtevariaties en oneffenheden van het substraat, en een algemene trend richting het imprinten van grotere substraten voor een hogere productiecapaciteit. De motivatie voor dit onderzoek is het verbeteren van de imprintkwaliteit door een gelijkmatige filmdikte te realiseren op grote, niet-vlakke substraten.

Het roll-to-plate nanoimprintproces kan worden beschouwd als een vorm van filmsmering. Het valt onder de categorie van zachte elastohydrodynamische smering vanwege de lage druk en grote elastische vervorming. Dit proefschrift richt zich op de filmdikte in zachte elastohydrodynamische smering, met de specifieke toepassing van roll-to-plate nanoimprinten. Het doel is om theorieën en methoden te ontwikkelen om de filmdikte te kunnen voorspellen, meten en controleren. Het onderzoek is opgebouwd uit drie delen, die overeenkomen met deze doelstelling: het voorspellen, meten en sturen van de filmdikte.

In het eerste deel zijn numerieke modellen ontwikkeld en experimenteel gevalideerd om de elastohydrodynamische smering van het roll-to-plate nanoimprintproces te beschrijven. De ontwikkeling van deze modellen is opgebouwd in meerdere stappen, waarbij de complexiteit stapsgewijs is verhoogd om de onderliggende fysica beter te beschrijven. De traditionele theorie van elastohydrodynamische smering is daarom uitgebreid met fysica om het gedrag van het voorgespannen folie en de contactmechanica met de elastische laag van de imprintrol te beschrijven. Daarnaast zijn in een volgende iteratie van het model ook de hoogtevariaties en oneffenheden van het substraat meegenomen door een golvend substraatoppervlak te modelleren. Deze uitbreidingen leveren waardevolle inzichten op in hoe de voorspanning en de buigstijfheid van het folie de filmdikte en filmdruk in het

gesmeerde rolcontact beïnvloeden. De modellen kunnen direct worden gebruikt om de filmdikte te voorspellen. Bovendien laten de resultaten zien dat een golving van het substraatvlak een negatieve invloed heeft op de uniformiteit van de filmdikte. Dit benadrukt de noodzaak voor het ontwikkelen van een concept om de filmdikte te controleren.

Het tweede deel, over het meten van de filmdikte, introduceert een nieuw analytisch model en de experimentele validatie van een meetmethode om de filmdikte te bepalen met behulp van een ratiometrische fluorescentiemeting. Het meten van de filmdikte in een smeerfilm is vaak lastig, omdat de smeerfilm zich tussen twee (bewegende) oppervlakken bevindt. Een ratiometrische fluorescentiemeting, die gebruikmaakt van twee fluoroforen, opgelost in de vloeistof, is een efficiënte optische meetmethode om de filmdikte over een groot oppervlak te bepalen. In dit onderzoek worden de fluoroforen fluoresceïne en eosine Y gebruikt. Het oorspronkelijke model van Hidrovo en Hart [1] is uitgebreid met de emissie en reabsorptie van beide fluoroforen en de effecten van achtergrondreflectie. Met deze verbeterde modelbeschrijving is het model een handig hulpmiddel om de meetmethode af te stemmen en te optimaliseren voor een gewenst meetbereik van de filmdikte. De experimentele fluorescentiespectra bieden daarnaast ook nuttige inzichten in het werkingsprincipe van de meetmethode.

In het derde deel wordt een nieuw concept gepresenteerd om de filmdikte in zachte elastohydrodynamische smering te controleren. Dit concept is geïnspireerd op inverse hydrodynamische smering. De werking en haalbaarheid van het concept zijn aangetoond met een eendimensionaal, numeriek model van de elastohydrodynamische smering van een flexibele, kantelbare glijlager (kantelblokje) op een golvend substraatoppervlak. De filmdikteverdeling kan worden gecontroleerd door een verdeelde nulstijfheidsbelasting aan te brengen op het flexibele oppervlak van het glijlager. De grootte van de aangebrachte belastingen is zo gekozen dat de drukverdeling wordt benaderd die hoort bij de gewenste filmdikteverdeling. De uiteindelijke filmdikteverdeling is onafhankelijk van de golving van het substraatoppervlak, dankzij de nulstijfheidsbelasting. Vervolgens is dit concept experimenteel gevalideerd in een innovatieve opstelling, waarin een dunne vloeistoffilm wordt gevormd tussen het vervormbare glijlager en een roterende vlakke schijf. De filmdikteverdeling is bepaald met een ratiometrische fluorescentiemeting en de resultaten laten zien dat het mogelijk is om met dit nieuwe concept de filmdikte in zachte elastohydrodynamische smering te controleren.

Samengevat levert dit proefschrift bijdragen aan verschillende aspecten van de filmdikte in zachte elastohydrodynamische smering, met de specifieke toepassing van roll-to-plate nanoimprinten. De ontwikkelde theorieën en methoden voor het voorspellen, meten en controleren van de filmdikte vormen een sterke basis voor toekomstig onderzoek en praktische toepassingen om een gelijkmatige filmdikte te realiseren op niet-vlakke substraten. Dit is niet alleen toepasbaar in roll-to-plate nanoimprinten, maar kan ook worden gebruikt in andere processen, zoals vloeistoffilmcoating of lithografisch printen.

1

Introduction

1.1 Motivation

1.1.1 Micro- and nanotextures

Texturing of surfaces can be used to modify or improve the physical properties of the underlying surface, such as its wettability or hydrophobicity, lubricity, optical reflection, transparency, and many more [2–5]. The development of these textures is inspired and driven by the many examples found in plants and animals in nature [6–8]. Some examples of natural textures and their remarkable properties are shown in Figures 1.1a–1.1f. They are a result of millions of years of evolutionary processes to help them survive or adapt to their environment in ingenious ways [9]. Mimicking these natural designs can help the development of innovative materials, coatings, and technologies.

The natural textures in Figures 1.1a–1.1f will be described in more detail. Most insects have so-called compound eyes, which are formed by small, closely packed lens-shaped textures. Figure 1.1a shows the eyes of the robber fly, which contain thousands of microlenses. They enable vision by directing the light toward photoreceptors. Moth eyes even contain small nanopillars to increase the anti-reflection [10], see Figure 1.1b. This helps them to see at night and to avoid being seen by predators by preventing light from reflecting off their eyes. Anti-reflection textures can also increase the the transparency of the underlying surface. The glasswing butterfly wings in Figure 1.1c are covered with small conical-shaped nanopillars to achieve almost perfect transparency. Other optical effects are found in nature as well. The blue color of the Morpho butterfly in Figure 1.1d is not created by pigment but by the refraction of light, which is influenced by complex microtextures [11, 12]. Natural textures can also change the way a surface interacts with water. Figure 1.1e shows a famous example of a water-repellent texture on the Lotus leaf, which shows extreme hydrophobicity. The 'Lotus effect' gives the plant self-cleaning properties, as water droplets easily fall off the leaves while picking up dirt particles on the way. A last example of a natural texture can be seen in Figure 1.1f, which shows the relatively large tooth-shaped textures on shark skin. These denticles reduce the drag in the seawater and increase the shark's hydrodynamic efficiency [13, 14].

1

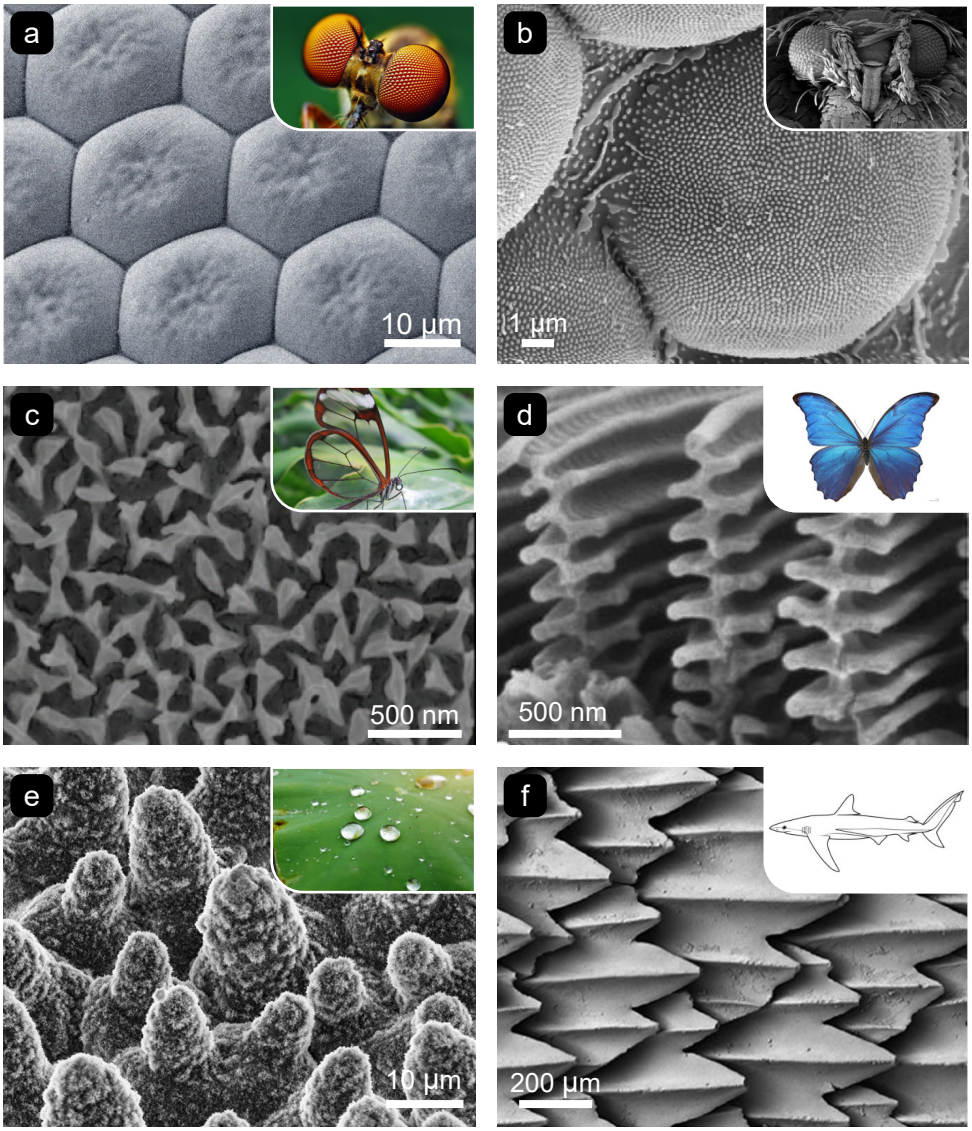

Figure 1.1: Examples of micro- and nanotextures found in nature. All pictures are adapted under the terms of the CC-BY license. (a) Lens-shaped textures on the eyes of the robber fly [9, 15]. (b) Nanopillars on moth eyes [16]. (c) Conical-shaped nanopillars give the glasswing butterfly transparent wings [17, 18]. (d) The complex microtextures on the Morpho butterfly wings give them their blue color [19, 20]. (e) Hydrophobic microtextures on a Lotus leaf [21, 22]. (f) Tooth-shaped textures on the flank of the Copper Shark [13, 23].

Engineered textures are often inspired by textures found in nature. For example, in the field of photovoltaics, light-management surface layers can be used on top of solar panels. These textures, such as the pyramid shaped textures in Figure 1.2a, enhance the anti-reflection and light-trapping properties of the underlying surface to increase the overall solar panel efficiency [24–26]. Other applications are found in anti-reflection or anti-glare surface layers in the display industry to reduce energy consumption and increase visibility [27, 28]. Figure 1.2b clearly shows how a 'moth-eye' anti-reflection texture, which is only applied in the middle of the square glass plate, decreases the surface reflection. Optical gratings for waveguides, as shown in Figure 1.2c, are used to couple in or out light for augmented reality devices [29–31]. The application of hydrophobic textures in Figure 1.2d can be beneficial to increase the self-cleaning or anti-fouling properties [32, 33]. Lastly, anti-drag textures are used to minimize friction in aviation and shipping [34, 35].

To enable the use of these textures in the various applications, they must be produced in a cost-effective way. An attractive production method is nanoimprint lithography (NIL), which is an emerging manufacturing technology to replicate the engineered micro- and nanotextures with high resolution on rigid or flexible substrates [36, 37].

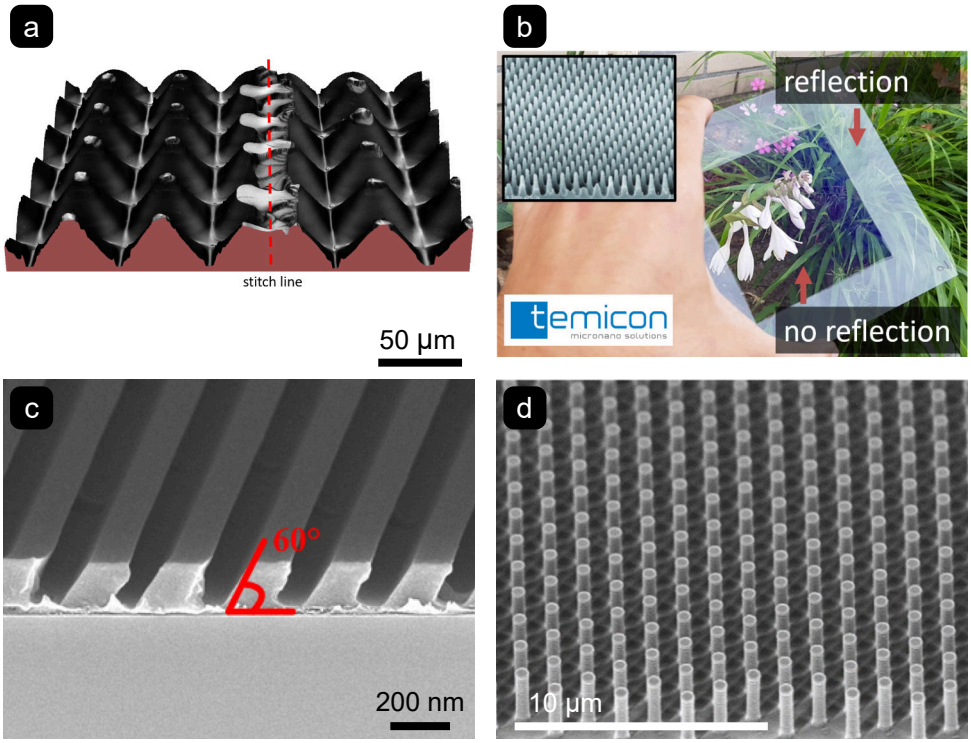

Figure 1.2: Examples of engineered textures. (a) Pyramid shaped textures with anti-reflection and light-trapping properties [26]. (b) The textured surface decreases the reflection of the glass surface [38]. (c) Slanted grating for coupling in light. Adapted under the terms of the CC-BY license (supplementary materials) [39]. (d) A nanopillar surface with anti-fouling properties. Adapted under the terms of the CC-BY license [33].

1

1.1.2 Nanoimprint lithography

The working principle behind nanoimprint lithography, which is also referred to as nanoimprinting, is based on a molding process, in which a textured stamp is pressed into a liquid resist material, see Figure 1.3. The resist material is mechanically deformed to conform to the surface topography of the stamp. After solidification of the resist material, the stamp is delaminated, and a negative of the textured pattern is left on the substrate, on top of a residual layer. The residual layer represents a thin layer of material, which is left behind during the imprinting step. In an optional, subsequent etching step, the residual layer can be removed or the imprinted texture is transferred into the substrate material by utilizing the imprinted pattern as an etching mask [37, 40].

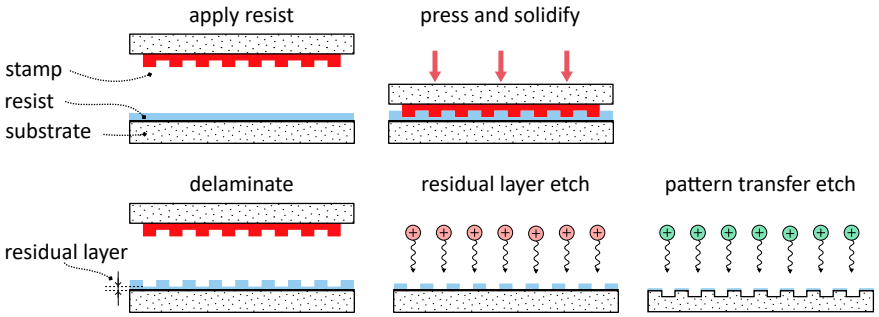

Figure 1.3: Schematic of the nanoimprint process. Adapted under the terms of the CC-BY license [41].

A distinction can be made between thermal nanoimprint lithography (T-NIL) and ultraviolet nanoimprint lithography (UV-NIL). T-NIL employs thermoplastic polymers as resist material. The polymer is heated above the glass transition temperature to become a highly viscous liquid. The stamp is then pressed into the polymer, which fills the patterns. This process involves high temperatures and high imprint pressure [36]. UV-NIL employs relatively low viscosity photopolymerizable resist material, which is typically referred to as a resin [42]. The liquid resin can quickly fill the stamp features and is cured by exposure to UV light through the UV-transparent stamp. The UV-NIL process is associated with low imprint pressures and can be performed at room temperature.

Besides the difference in solidification of the resist material, different contact types can be distinguished. The three main contact types are shown in Figure 1.4. Plate-to-plate (P2P) nanoimprinting is typically performed with wafer sized substrates and rigid stamps and is known for its high accuracy in positioning of the textures. In roll-to-plate (R2P) and roll-to-roll (R2R) nanoimprinting the imprint pressure is applied with a roller, which results in a line contact between the stamp and the substrate. Roller-based nanoimprinting enables an increased fabrication throughput and the possibility to pattern large-area substrates at once [41, 43, 44]. The imprint systems can be equipped with one or multiple rollers for imprinting and support of the substrate.

Figure 1.5 shows a schematic diagram of a variant of a UV-cure roll-to-plate nanoimprint system. It uses several rollers to guide a flexible stamp, ensuring a large contact zone between the stamp and substrate. The flexible stamp is tensioned around the rollers, which have a relatively soft, elastomeric layer to promote conformal contact with the substrate

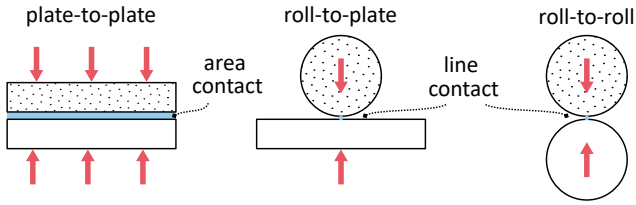

Figure 1.4: The three main contact types. Adapted under the terms of the CC-BY license [41].

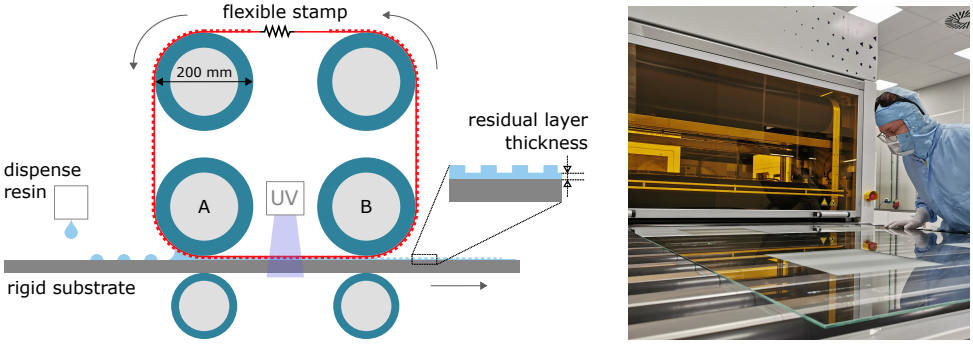

Figure 1.5: Schematic and picture of a roll-to-plate imprint system. Adapted under the terms of the CC-BY license [45].

during imprinting. The imprint roller (A) presses the flexible stamp into the UV-curable resin droplets, which have been dispensed on the substrate. The resin droplets merge and spread into a thin film. After UV-curing the liquid film, the flexible stamp is delaminated from the substrate by the delamination roller (B). Due to this setup of the imprint system, the location of imprinting (A), solidification by UV curing (between A and B), and delamination (B) is different, which offers the possibility to control and tune each of these processes individually.

The imprint fidelity, which is essentially a measure of the texture quality, describes the degree to which a texture is accurately transferred from the stamp to the substrate surface. The pattern must be replicated with high precision and minimal defects to achieve a high imprint fidelity, which is essential for maximum performance of the texture. A closer look at the final imprint in Figure 1.5 reveals the presence of the desired texture on top of a residual layer. In some applications, the residual layer is intentionally left behind to provide support for the imprinted textures. It is ideally thin and uniform over the entire surface to prevent poor (optical) performance of the product [46]. If a subsequent etching step is performed to remove the residual layer, a thin and uniform residual layer is also essential for an efficient and high-quality etch [37, 47, 48].

It is important to realize that the liquid film height governs the solidified residual layer thickness and its uniformity after curing. The film height is established in the imprint process in between the roller and substrate. To guarantee that the imprinted pattern is accurately replicated and matches the features of the stamp, it is crucial to control the film height and its uniformity.

1

1.1.3 Challenges

Controlling the film height and its uniformity during the imprint process is challenging because of possible variations in the substrate surface topography. Substrate non-flatness can either be intended or unintended. Intended substrate non-flatness can be found when replicating textures on objects with defined non-flatness or curvature, such as light bulbs, lamp shades, or lenses. These can be imprinted with functional textures to enhance their optical properties. Conformal imprints have been fabricated in stationary, air pressure-based imprint tools using flexible stamps and low viscous UV-curable resins [49, 50].

Unintended non-flatness can appear in the form of large-scale substrate waviness or the presence of particles or other small-scale contaminants on top of the substrate. For the latter, robust imprint methods have been developed for plate-to-plate imprint configurations to handle these undesired small-scale variations of the substrate surface [51–53]. The use of soft stamps allows for substrate conformal imprinting. Additionally, production facilities strive to minimize the presence of contaminants during the imprint process. On the other hand, the presence of (unintended) large-scale substrate waviness makes it extremely challenging to achieve a thin and uniform film height over the entire surface in roller-based imprinting. The substrates in roll-to-plate nanoimprinting are usually assumed to be rigid and flat. In reality, they always show a certain amount of waviness. For example, large-area, heat-treated or tempered glass substrates used for solar panel production can show significant substrate waviness. Here, the local non-flatness of rectangular substrates must not exceed 1.6 mm over any 300 mm span, as specified by the ASTM standard specification [54]. Another example is given by the maximum allowable overall bow or warp for laminated glass, which can reach values in the order of 10 mm over a 1.5 m length span [55]. The impact of local and global waviness of the initial, undeformed substrate geometry is visualized in Figure 1.6. In both scenarios, the imprint roller is not able to apply a uniform pressure on the substrate surface. The substrate waviness will modify the roller contact zone, which results in pressure and film height fluctuations. Any bending of the roller, which is not shown in the figure, can further increase these pressure fluctuations.

Moreover, a general trend towards imprinting larger substrates can be identified, for improved production capacity. Scaling the substrates results in larger imprint rollers and larger flexible stamps. With larger imprint rollers, it becomes harder to accurately control the (local) imprint pressure, especially in combination with non-flat substrates. Current roller-based imprint systems cannot achieve imprints with thin and uniform film heights on these large-area, wavy substrates. There is a need for theory and concepts to ensure a uniform film height to further improve the roll-to-plate nanoimprint technology.

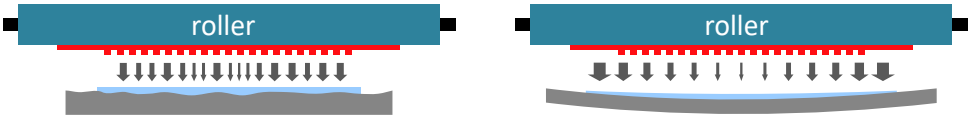

Figure 1.6: Cross-sections of the imprint roller and a wavy substrate surface on the local (left) and global (right) scale. The substrate waviness of the initial, undeformed substrate geometry results in pressure fluctuations, as indicated with the arrow thickness, and corresponding film height fluctuations.

1.2 Vision: fluid film lubrication

In this study, we will consider the roll-to-plate imprint process as a form of fluid film lubrication and approach the challenges from the fluid film point of view. A schematic diagram of the imprint roller and the involved physics in the imprint process is shown in Figure 1.7. The imprint textures are neglected and the prestressed, flexible stamp is treated as a tensioned web: a thin, flexible sheet under tension. The two moving surfaces in the lubricated contact, the tensioned web around the roller and the substrate surface, are separated by a thin fluid film. The fluid film is formed due to hydrodynamic action, as a result of the fluid supply and the in-plane motion of the surfaces. It can be shown that this is described by hydrodynamic lubrication theory [56]. The hydrodynamic pressure build-up in the fluid film results in elastic deformation of the moving surfaces. The ratio of elastic deformation relative to the film height can be used to classify the type of hydrodynamic fluid film lubrication. Different modes and their corresponding problem definitions can be identified, as presented by Blok [57]:

1. Hydrodynamic lubrication (HL).

   When the elastic deformation of the moving surfaces is negligibly small, relative to the film height, the moving surfaces can be assumed to be rigid. This form of lubrication is considered as the classic problem definition. The hydrodynamic pressure distribution can be directly determined for the given film height geometry, as the moving surface profiles are known.

2. Elastohydrodynamic lubrication (EHL).

   When the elastic deformation has the same order of magnitude as the film height, it may no longer be neglected. Elastohydrodynamic lubrication (EHL) is "a mode of fluid film lubrication in which hydrodynamic action is significantly enhanced by surface elastic deformation" [58]. The elastic deformation is a result of the hydrodynamic pressure distribution in the fluid film. As this deformation is relatively large compared to the film height, it will affect the hydrodynamic pressure distribution, in return. The result is a strong coupling between the hydrodynamic and elastic forces, which is described by elastohydrodynamic lubrication theory.

3. Inverse hydrodynamic lubrication (IHL).

   In some situations, the elastic deformation of at least one of the moving surfaces is significantly larger than the film height. The pressure distribution will be more or less constant, irrelevant of the fluid film height, which is negligibly small compared to the elastic deformation. This is typically the case in strongly elastically deformed contacts, such as rubber seals [57]. For these problems, the problem definition can be inverted, compared to the classic problem definition in hydrodynamic lubrication. The film height geometry is now determined for the applied pressure distribution, which is known beforehand. It can be measured or simulated, and sometimes it may be approximated with the dry contact pressure distribution [59].

The roll-to-plate imprint process in Figure 1.7 is an example of elastohydrodynamic lubrication. It qualifies as soft EHL, due to the combination of low pressures and large elastic deformation of the tensioned web and elastomeric layer [59]. The film height is

1

governed by the interaction of hydrodynamic forces of the fluid film and elastic forces of the moving surfaces. Achieving a uniform fluid film height is challenging, as variations in the surface topography influence the interaction between the hydrodynamic and elastic forces.

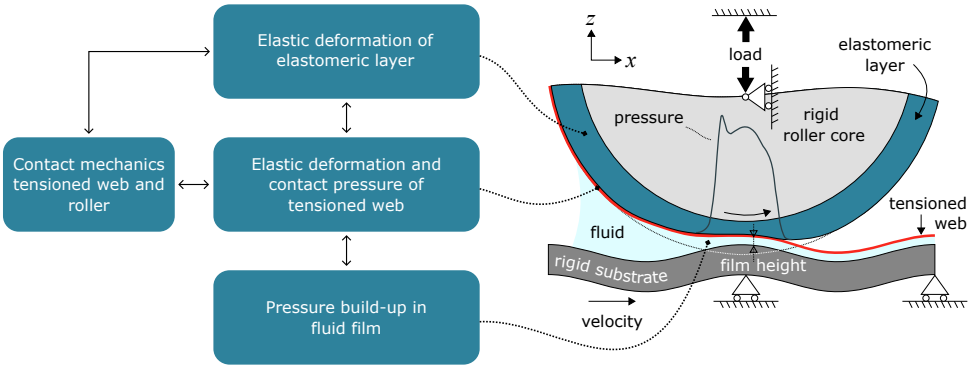

Figure 1.7: Schematic diagram of the imprint roller with tensioned web (i.e., flexible stamp) and the corresponding physics in the imprint process. Reproduced and adapted with permission from [60].

1.3 Aim & approach

This dissertation aims to develop theory and methods to predict, measure, and steer the film height in soft elastohydrodynamic lubrication. These will be specifically focused on the application of roll-to-plate nanoimprinting, as depicted in Figure 1.5 and Figure 1.7. To achieve this goal, a threefold approach is taken:

1. **Film height prediction.**

   With access to simulation tools to predict the film height accurately, it is possible to investigate the process parameter sensitivities and to demonstrate the influence of substrate non-flatness on the film height. Numerical models are developed and experimentally validated to be able to accurately predict the film height. Textures are neglected in this part and subsequent parts. We only consider smooth surfaces.

2. **Film height measurement.**

   A measurement method is required to measure the fluid film height in a lubricated contact. Ratiometric fluorescence imaging is used for this purpose. A fundamental understanding is desired to effectively use the measurement method. The original analytical model, as developed by Hidrovo and Hart [1], is modified and extended for a more accurate model description of the measurement method. This method can also be used to experimentally validate the film height steering concept.

3. **Film height steering.**

   The principle of inverse hydrodynamic lubrication (IHL) theory is employed to realize the desired film height geometry by applying the corresponding pressure profile.

1.4 Outline

This dissertation is divided in three parts, which correspond to different aspects of the film height in soft elastohydrodynamic lubrication. The dissertation is based on multiple papers, which are included as-is, with only minor changes in layout. Any additions to the original content are clearly indicated in the footnotes. Due to the paper-based set-up, the mathematical notation might slightly differ and some repetition is inevitable.

Part 1: Film height prediction.

Part I starts with Chapter 2, which presents the first development of a numerical EHL model to predict the film height, and hereby the residual layer thickness, in roll-to-plate nanoimprinting. It also includes an experimental validation. The model is extended with the bending stiffness and contact mechanics of the tensioned web in Chapter 3 to better describe the elastohydrodynamics of the roll-to-plate imprint process. The numerical results are experimentally validated. This chapter also contains a technical note on film height survey diagrams for EHL and soft-layered EHL. Chapter 4 describes a case study where substrate non-flatness is added to the numerical model to show its influence on the film height.

Part 2: Film height measurement.

Part II contains Chapter 5, which presents a novel analytical and experimental study of the ratiometric fluorescence film height measurement method. It provides an intuitive understanding of the working principle of the measurement method.

Part 3: Film height steering.

In part III, Chapter 6 presents the development of a concept to control the film height in an elastohydrodynamic lubrication process by applying the corresponding pressure distribution. This concept, which is inspired by inverse lubrication theory, is theoretically studied in a one-dimensional numerical model of a deformable tilting pad slider bearing. The concept is experimentally validated in Chapter 7. This chapter describes the extension of the one-dimensional numerical model and the development of an experimental set-up to steer and measure the film height. The film height measurement is performed with ratiometric fluorescence imaging.

This dissertation is concluded with Chapter 8 and Chapter 9, which provide a discussion and conclusion on the results in this dissertation, respectively. Limitations and recommendations of this research in relation to roll-to-plate nanoimprinting are included.

I

Film height prediction

2

Film height prediction in roll-to-plate nanoimprinting

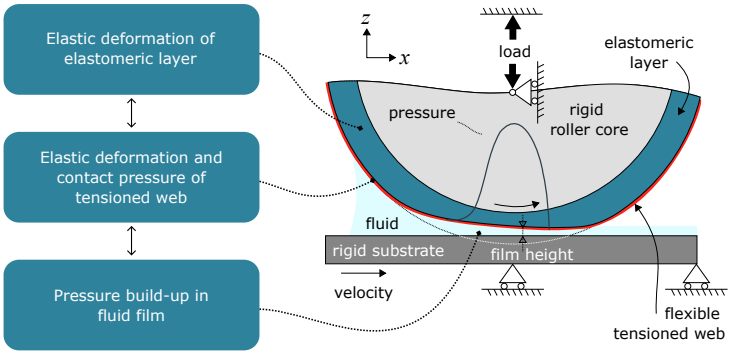

This chapter presents the development of a numerical EHL model to predict the film height as a function of the process parameters. It combines different physics to describe the pressure build-up in the liquid resin film and the elastic deformation of the elastomeric roller material and the flexible stamp, which is treated as a tensioned web. The residual layer thickness after curing is governed by the liquid film height, which is established in the imprint process between the roller and the substrate. The chapter contains a detailed description of the model setup, the governing equations, and the experimental method to validate the numerical results. The numerical and experimental results are presented for a variation of the process parameters.

This chapter was published as:
Snieder, J., Dielen, M., & van Ostayen, R. A. J. (2022). *Simulating the residual layer thickness in roll-to-plate nanoimprinting with tensioned webs.* Micromachines, 13(3), 461.

Note: for consistency within this dissertation, the term layer height from the original publication was changed to film height, where applicable.

2

Simulating the residual layer thickness in roll-to-plate nanoimprinting with tensioned webs

Abstract *Roll-to-plate nanoimprinting with flexible stamps is a fabrication method to pattern large-area substrates with micro- and nanotextures. The imprint consists of the preferred texture on top of a residual layer, of which the thickness and uniformity is critical for many applications. In this work, a numerical model is developed to predict the residual layer thickness (RLT) as a function of the imprint parameters. The model is based on elastohydrodynamic lubrication (EHL) theory, which combines lubrication theory for the pressure build-up in the resin film, with linear elasticity theory for the elastic deformation of the roller material. The model is extended with inextensible cylindrical shell theory to capture the effect of the flexible stamp, which is treated as a tensioned web. The results show that an increase in the tension of the web increases the effective stiffness of the roller, resulting in a reduction in the RLT. The numerical results are validated with layer height measurements from flat layer imprints. It is shown that the simulated minimum film height corresponds very well with the experimental results for a wide range of resin viscosities, imprint velocities, and imprint loads.*

2.1 Introduction

Nanoimprint lithography (NIL) is a high-resolution, high-throughput fabrication technology to replicate micro- and nanopatterns on rigid and flexible substrates. The concept of NIL is essentially based on a moulding process, in which a liquid resist is deformed to conform to the surface topography of a stamp [37]. The stamp surface is equipped with the inverse polarity of the preferred texture. After solidification of the resist material, the stamp is removed and a negative of the pattern is replicated onto the substrate. A distinction can be made between thermal NIL with a thermoplastic polymer resist material [36], and ultraviolet (UV) cure NIL, which employs UV-curable resin [42]. Moreover, depending on the contact method, the NIL process can be divided into plate-to-plate, roll-to-plate, and roll-to-roll nanoimprinting. To further increase the throughput and imprint area of the NIL process, a shift towards large-area NIL can be identified [44]. Practical applications of large-area NIL can be found in the fabrication of optical surface layers for displays or augmented reality [29], anti-reflection surfaces for solar panels [61], antifouling surfaces [33], and many more [44]. In particular, roller-based NIL is an attractive method, as it offers the advantage of a reduced contact area during the imprint process, which results in lower imprint forces, and reduced issues regarding bubble trapping [41]. The first thermal NIL roller-based imprint system was introduced by Tan [62], and Ahn has

developed the first UV-cure roll-to-roll imprint system [63]. Various roller-based imprint systems are available, and can be classified based on the configuration of stamp, roller, and substrate [46, 64].

A roll-to-plate imprint system can be equipped with one or multiple rollers. Figure 2.1 shows a schematic of a UV-cure roll-to-plate imprint system. It uses multiple rollers, for imprinting and for guiding a textured flexible stamp. The UV-curable resin is dispensed on the substrate. The middle-left imprint roller presses the flexible stamp into the liquid resin, which is then UV-cured through the transparent stamp. The middle-right roller delaminates the flexible stamp from the hardened resin. When taking a closer look at the imprinted substrate, it can be seen that the imprint consists of the preferred texture on top of a residual layer. For many applications, the residual layer thickness (RLT) must be thin and uniform, in order to prevent poor optical or mechanical performance of the product, or to facilitate efficient and high-quality etching as a subsequent process step to transfer the pattern into the substrate material [65]. Simulation of the imprint process can assist in predicting the imprint quality to further optimize the imprint process. The imprint quality is mainly governed by the replication fidelity of the preferred textures and the RLT and its uniformity over the imprint area. In the literature, research on the simulation of the replication fidelity can be found for different aspects of the imprint process: the texture filling and potential bubble trapping [66–69], the UV curing step [70, 71], and the potential fracture of textures during delamination [68], to name a few. This work specifically focuses on the prediction of the RLT.

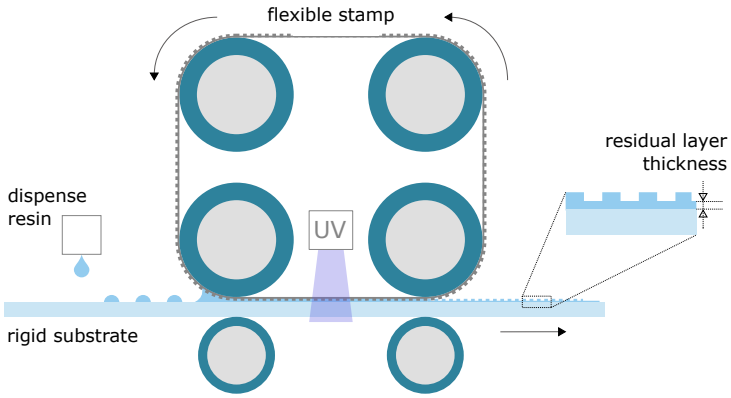

Figure 2.1: Schematic of a roll-to-plate imprint system. Picture is adapted from [38].

Previous work on the simulation of the RLT and its uniformity is given for plate-to-plate imprint systems [72–75]. For roller-based imprint systems, analytical expressions for the RLT [43] and droplet merging under the imprint roller [70] are presented. The elastic deformation of the roller material is not taken into account. It is included by Taylor [76], who developed a contact mechanics-based model to simulate the RLT. The rollers in roller-based imprint systems are typically equipped with a relatively soft, elastomeric layer, which elastically deforms during the imprint process, due to the hydrodynamic pressure build-up in the resin film. The elastic deformation is relatively large compared to the

film height, and affects the hydrodynamic pressure profile in the resin film, in return. The result is a strong coupling between the hydrodynamic and elastic effects, which is described by elastohydrodynamic lubrication (EHL) theory. The working principle behind roller-based imprint systems is analogous to roller-based coating and printing processes [77–80]. These studies also use EHL theory for the prediction of the coating or printing layer height. When the thickness of the elastomeric layer is relatively small, it influences the elastic deformation and its finite thickness needs to be taken into account [78, 81–83]. Cochrane also employs EHL theory to predict the RLT in a roll-to-roll set-up to imprint deformable substrates [84]. Lubrication theory is combined with the inextensible cylindrical shell theory to couple the pressure build-up in the thin film of resin with the motion and elastic forces of the deformable substrate.

In this work, a numerical EHL model is developed to predict the RLT in roll-to-plate imprint systems. The EHL model couples lubrication theory for the pressure build-up in the thin film of resin with linear elasticity theory for the elastic deformation in the elastomeric layer of the imprint roller with finite thickness. The model is extended with inextensible cylindrical shell theory to include the effect of the flexible stamp, which is treated as a tensioned web. The study focuses on the RLT, and the influence of textures on the flexible stamp is not taken into account. Unique contributions of this work are the implementation of EHL theory in roll-to-plate nanoimprinting, including the experimental validation of the numerical results. Moreover, the effects of the tensioned web in a roll-to-plate imprint set-up on the RLT have not been studied before, to the authors' knowledge. The numerical model can directly be used to determine the required amount of resin in an imprint, for a given set of imprint parameters. Furthermore, the numerical model can be used to study the RLT as a function of the resin viscosity, imprint velocity, and imprint load. The material properties of the elastomeric layer (elastic modulus and Poisson ratio) and the system geometry (roller radius and elastomeric layer thickness) can be adjusted as well, in order to study the influence on the RLT.

2.2 Methods

In this section, the applied methods are described in detail. First, the development of the numerical model for the lubricated roller contact with a tensioned web is discussed. Next, the experimental method to validate the model is described.

2.2.1 Model development

The numerical model is based on the full-system finite element approach for EHL problems [85]. The modeled system geometry is shown in Figure 2.2a. The imprint roller with an elastomeric layer is pressed onto the substrate. They are separated by a tensioned web, which applies a contact pressure onto the elastomeric layer, and a thin film of resin. The roller contact is treated as an infinite line contact. Furthermore, it is assumed that the substrate and roller core are rigid, and all elastic deformation occurs in the relatively compliant, elastomeric layer, which is wrapped around the imprint roller core. If the contact width is small relative to the roller radius, a simplified equivalent geometry can be used, as shown in Figure 2.2b [86]. A rigid roller of radius R is pressed onto the flat, elastomeric layer of thickness t, which is essentially unwrapped from the roller core. With this im-

plementation, the tensioned web follows the roller shape, instead of losing contact with the roller and moving away with the substrate. The kinematics of the tensioned web and its contact mechanics with the roller are not taken into account. Both the roller and substrate move with a unidirectional surface velocity u_1 and u_2, in the positive x-direction. This is in fact the imprint velocity of the imprint process. The contact area is subject to an effective imprint load per unit length $\overline{W}$. It is assumed that a surplus of resin is available in front of the roller, which makes the contact fully flooded.

Three film heights are identified in the formed thin film of resin: the central film height h_C at the roller center, the minimum film height h_M close to the outlet of the roller contact, and the final film height h_F between the tensioned web and substrate. The final film height h_F is the film height of interest, but due to the absence of the web kinematics, this film height cannot be determined directly. However, it will be shown in Section 2.2.1 that the final film height h_F should be equal to the central film height h_C.

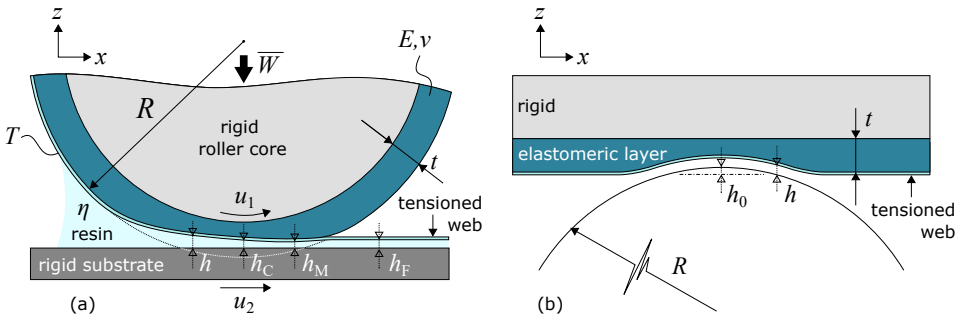

Figure 2.2: (**a**) Schematic of the imprint roller with tensioned web. The elastic deformation of the elastomeric layer is highly exaggerated for illustrative purposes. (**b**) Equivalent geometry of the imprint roller with tensioned web.

The numerical model is governed by four main equations: the Reynolds equation for the resin flow, the linear elasticity equations for the elastic deformation, the inextensible cylindrical shell equations for the web tension physics, and a load balance equation. For the sake of numerical robustness and faster convergence, the relevant variables are scaled. The scaling parameters and dimensionless equations are presented in the supplementary materials[1]. For readability, the dimensional equations are presented in the following subsections. The equations are applied on the computational domain in Figure 2.3, which represents the elastomeric layer. It has a dimensional width of $20 \times a_H$, and a dimensional height which is equal to the elastomeric layer thickness. The parameters a_H and p_H, which are already introduced for later use, correspond to the Hertz dry contact half-width and peak pressure, respectively. They are based on the mechanical properties of the elastomeric layer:

$$a_H = \sqrt{\frac{8\overline{W}R}{\pi E'}}, \qquad p_H = \frac{2\overline{W}}{\pi a_H}. \tag{2.1}$$

[1]The supplementary materials can be found in the open-access online publication [45].

As it is assumed that all elastic deformation occurs in the elastomeric layer, the effective elastic modulus reduces to:

$$\frac{2}{E'} = \frac{1-\nu^2}{E}. \tag{2.2}$$

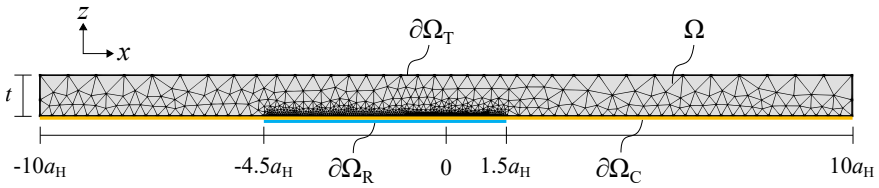

Figure 2.3: Computational domain and mesh.

Elastic deformation

The elastic deformation is determined by applying the classical linear elasticity equations on the elastic layer domain Ω in Figure 2.3, with appropriate boundary conditions. The linear elasticity equations are given by [85]:

$$\begin{aligned} x\text{-direction: } & \frac{\partial}{\partial x}\left[(\lambda+2\mu)\frac{\partial u}{\partial x}+\lambda\frac{\partial w}{\partial z}\right]+\frac{\partial}{\partial z}\left[\mu\left(\frac{\partial u}{\partial z}+\frac{\partial w}{\partial x}\right)\right]=0, \\ z\text{-direction: } & \frac{\partial}{\partial x}\left[\mu\left(\frac{\partial u}{\partial z}+\frac{\partial w}{\partial x}\right)\right]+\frac{\partial}{\partial z}\left[\lambda\frac{\partial u}{\partial x}+(\lambda+2\mu)\frac{\partial w}{\partial z}\right]=0, \end{aligned} \tag{2.3}$$

where λ and μ correspond to the Lamé parameters:

$$\lambda = \frac{\nu E}{(1-2\nu)(1+\nu)}, \qquad \mu = \frac{E}{2(1+\nu)}. \tag{2.4}$$

The upper boundary $\partial\Omega_T$ in Figure 2.3 is fixed. The contact domain $\partial\Omega_c$ is loaded with the contact pressure p_C, which follows from the tensioned web physics. This results in the following boundary conditions:

$$\begin{cases} u = w = 0 & \text{on } \partial\Omega_T, \\ \sigma_n = p_C & \text{on } \Omega_C, \\ \sigma_n = \sigma_t = 0 & \text{elsewhere.} \end{cases} \tag{2.5}$$

The parameters σ_n and σ_t are the normal and tangential components of the stress tensor, respectively.

Hydrodynamic lubrication

As the film height of the thin film of resin is small compared to the roller contact width, the resin flow can be described by thin film theory, which assumes a constant pressure across the film height. The steady-state, incompressible Reynolds equation in one dimension is given by [56]:

$$\frac{\partial}{\partial x}\left(-\frac{h^3}{12\eta}\frac{\partial p}{\partial x}+\frac{h(u_1+u_2)}{2}\right)=0, \tag{2.6}$$

where η is the dynamic viscosity of the resin, and u_1 and u_2 are the top and bottom surface velocities, respectively. Equation (2.6) assumes Newtonian fluid behavior and isothermal conditions. The first part in the Reynolds equation is the Poiseuille term, which describes the volume flow rate due to pressure gradients within the thin film. The second term is the Couette term and describes the volume flow rate due to the surface velocities. The hydrodynamic film pressure p is determined for a given film height profile h:

$$h(x) = h_0 + \frac{x^2}{2R} + w(x), \tag{2.7}$$

where h_0 is the unknown gap between the roller and substrate at $x = 0$. A negative gap indicates roller engagement, as shown in Figure 2.2b. The second term is an approximation to describe the circular roller shape, and the last term represents the elastic deformation, which follows from Equation (2.3). The Reynolds equation is applied on domain $\partial\Omega_R$ in Figure 2.3. It is defined by $-4.5a_H \leq x \leq 1.5a_H$, which is sufficiently wide to capture the pressure build-up in the thin film of resin [85]. Zero pressure boundary conditions are applied on the edges of the domain. In the outlet region of the roller contact, negative pressures will follow from the Reynolds equation, due to the diverging surfaces. These negative pressures are physically not tolerated and the fluid will cavitate. The location of the cavitation boundary is unknown beforehand. When it is assumed that the cavitation pressure is equal to ambient pressure, the following cavitation condition must be satisfied:

$$p \geq 0 \quad \text{on} \quad \partial\Omega_R, \quad \text{and} \quad p = \frac{\partial p}{\partial x} = 0 \quad \text{on the cavitation boundary.} \tag{2.8}$$

To satisfy the cavitation condition, different methods are available and implemented in the literature. Habchi [87] uses a penalty method to force any negative pressures towards zero. Other methods are based on the observation that two regions can be identified: the full film region in which p is unknown (but larger than 0) and the liquid volume fraction f is known (namely 1), and the cavitated region where p is known (namely 0) and the liquid volume fraction f is unknown (but smaller than 1). This reasoning can be captured in a complementarity condition when introducing the cavity fraction $\theta = 1 - f$:

$$\begin{aligned} p \geq 0 \quad &\text{and} \quad \theta = 0, \\ p = 0 \quad &\text{and} \quad \theta \geq 0, \end{aligned} \tag{2.9}$$

Alakhramsing [88] suggests a variable transformation to combine both p and f into one variable. In this work, the complementarity condition is satisfied by adding a modified constraint function to the model, known as the Fischer–Burmeister function [89]:

$$p + \theta - \sqrt{p^2 + \theta^2} = 0. \tag{2.10}$$

The Reynolds equation in Equation (2.6) is essentially a mass flow balance, and conservation of mass must be satisfied on the entire domain. Similar conditions are present at the roller center (at $x = 0$) and outlet (at the cavitation boundary). The pressure gradient $\partial p/\partial x$ is equal to zero and the surface velocities u_1 and u_2 are the same. Conservation of mass then yields that the film height at the cavitation boundary should be equal to the central film height h_C at the roller center. As the film height is assumed to be constant downstream of the roller outlet, the final film height h_F should be equal to the central film height h_C.

Web tension

The tensioned web is relatively thin, and therefore cylindrical shell equations can be used to describe the web tension physics [84, 90]. It is assumed that the bending stiffness of the web and tangential traction acting on the web are negligible. The normal stress balance reduces to:

$$\kappa T + p_n = 0. \tag{2.11}$$

This equation states that the normal stress or pressure p_n is a function of the web curvature κ and the applied web tension T. The tensioned web follows the roller shape and its potential elastic deformation, which are described by the last two terms in Equation (2.7), respectively. The curvature can be approximated by the second spatial derivative:

$$\kappa = -\frac{\partial^2 z_{\text{roller}}}{\partial x^2} = -\frac{\partial^2}{\partial x^2}\left(\frac{x^2}{2R} + w\right) = -\left(\frac{1}{R} + \frac{\partial^2 w}{\partial x^2}\right). \tag{2.12}$$

The normal stress is equal to the tensioned web contact pressure p_C minus the hydrodynamic film pressure p. The resulting normal stress balance is equal to:

$$p_C = p + T\left(\frac{1}{R} + \frac{\partial^2 w}{\partial x^2}\right). \tag{2.13}$$

Equation (2.13) explains that the web contact pressure, which acts on the elastomeric layer, is the sum of the hydrodynamic film pressure and the pressure as induced by the web tension itself. This last term scales with the curvature of the roller and the local curvature due to the elastic deformation of the elastomeric layer. Equation (2.13) is applied on the contact domain $\partial\Omega_C$ in Figure 2.3. Zero pressure boundary conditions for the web tension pressure are applied on the edges of the domain.

Load Balance

The load equilibrium is derived by balancing the pressure force from the hydrodynamic film pressure build-up with the effective roller load per unit length:

$$\int_{\Omega_R} p\mathrm{d}x = \overline{W}. \tag{2.14}$$

This equation is satisfied by regulating the gap h_0 in Equation (2.7), which is one of the unknowns in the system of equations.

Numerical implementation

The linear elasticity equations in Equation (2.3), the Reynolds equation in Equation (2.6), the Fischer–Burmeister function in Equation (2.10), the tensioned web equation in Equation (2.13), and the load balance equation in Equation (2.14) completely define the EHL model with a tensioned web. The unknowns of these equations are the elastic deformation components u and w, the hydrodynamic film pressure p, the cavity fraction θ, the tensioned web contact pressure p_C, and the constant film height gap h_0. The equations are implemented in the commercial finite element method (FEM) software COMSOL Multiphysics® [91]. The Reynolds equation in Equation (2.6) and web tension equation in

Equation (2.13) are discretized using second-order (quadratic) Lagrangian finite elements. The linear elasticity equations in Equation (2.3) are discretized using third-order (cubic) Lagrangian finite elements, to allow for a smooth second-order derivative of the curvature in Equation (2.13). The load balance equation is a simple ordinary integral equation, which is associated with the unknown constant film height gap h_0. It is directly added to the system of equations as formed by Equations (2.3), (2.6), and (2.13), together with the Fischer–Burmeister constraint function.

The Reynolds equation, which is an example of a typical convection–diffusion equation, is convection-dominated in the cavitated region, where the film pressure is equal to zero. Convection-dominated partial differential equations are known to be unstable using FEM [85]. Therefore, the formulation is stabilized with a mesh-dependent artificial diffusion term. Moreover, to speed up the solution time, a small mesh-dependent diffusion term is added to the Fischer–Burmeister equation.

The use of FEM allows for non-structured, non-regular meshing of the computational domain; see Figure 2.3. A relatively course triangular mesh is used in the solid domain. The mesh is refined at the lower boundaries $\partial\Omega_C$ and $\partial\Omega_R$. The mesh is set fine in the inlet and outlet regions ($-4.5a_\mathrm{H} \le x \le -a_\mathrm{H}$ and $a_\mathrm{H} \le x \le 1.5a_\mathrm{H}$), finer in the central (Hertz) roller contact zone ($-a_\mathrm{H} \le x \le 0.5a_\mathrm{H}$), and finest in the outlet of the central contact zone ($0.5a_\mathrm{H} \le x \le a_\mathrm{H}$), where the pressure and elastic deformation gradients are most important. Mesh convergence studies have been performed to guarantee a mesh-independent solution. The solution procedure starts with selecting an appropriate initial guess for the unknown p, p_C, u, w, and h_0. The Hertz dry contact pressure is taken as an initial guess for the Reynolds pressure and tensioned web contact pressure. It is defined by:

$$p_{\mathrm{R,initial}} = p_{\mathrm{C,initial}} = \begin{cases} p_\mathrm{H}\sqrt{\left(1-\frac{x^2}{a_\mathrm{H}^2}\right)} & \text{for } -a_\mathrm{H} \le x \le a_\mathrm{H}, \\ 0 & \text{elsewhere.} \end{cases} \tag{2.15}$$

The elastic deformation resulting from the Hertz dry contact pressure is taken as an initial guess for the elastic deformation components u and w. The initial guess for the constant film height gap h_0 is simply taken as a small, positive number (e.g., 10 µm). The set of equations is iteratively solved in a fully coupled manner using a damped Newton–Raphson approach until convergence is reached.

2.2.2 Experimental

The numerical EHL model is validated with experimental results. Multiple flat layer imprints have been made on a Morphotonics Portis NIL1100 roll-to-plate nanoimprint set-up [38]; see Figure 2.4. A schematic of the working principle is shown in Figure 2.1. Each imprint is performed on a flat 150 mm × 150 mm glass substrate of 0.5 mm thickness, which is placed on a thick 5 mm glass carrier plate. To improve the adhesion between the resin and the glass substrates, the substrates are cleaned with isopropyl alcohol and pretreated with atmospheric pressure oxygen plasma and a primer containing an adhesion promoter. The flat layer imprints are fabricated using a flexible polymer stamp without textures. The stamp is pre-tensioned around the test rollers, which are equipped with a 7.5 mm thick elastomeric layer with an elastic modulus of 3.2 MPa and a Poisson ratio of 0.47. The linear elastic material behavior is confirmed by experimental compression tests.

The experimental validation procedure consists of multiple measurement series, in which the resin viscosity, imprint velocity, and imprint load are varied. Five different in-house-developed acrylate-based resins are used [38]. The viscosities and volumetric shrinkage levels upon UV curing are listed in Table 2.1. The viscosity is determined at 25 °C.

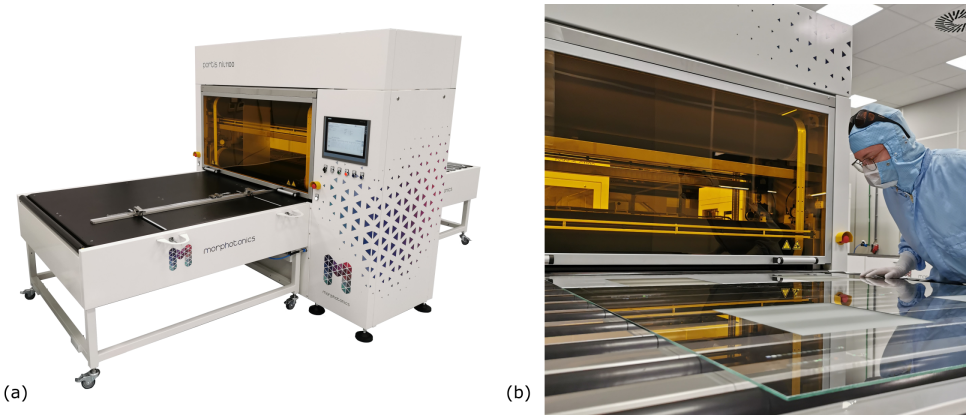

Figure 2.4: (**a**) Morphotonics Portis NIL1100 roll-to-plate nanoimprint equipment [38]. (**b**) Detailed view of the rollers inside the Morphotonics Portis NIL1100 nanoimprint tool.

Table 2.1: Properties of the imprint resins. The viscosities are measured at 25 °C.

Resin	Viscosity (mPa s)	Volumetric shrinkage (%)
A	6.3	12.5
B	38	8.1
C	134	7.2
D	181	8.8
E	349	7.8

The imprint layer height of each imprint is determined using a Keyence VK-X1100 laser confocal microscope, by optically measuring the step height of a small scratch made in the cured imprint layer. This is done on multiple locations of the imprint surface, to determine the layer height average and variation. To be able to compare the modeled film heights with the measured, cured layer heights, the latter are converted to the liquid, pre-cured film height using the shrinkage values in Table 2.1. Finally, the material properties of the elastomeric layer and resin are considered to be the most sensitive to variations in environmental temperature or material composition. A variation of ±10% in both the elastic modulus of the elastomeric layer and the resin viscosity is included in the model, to provide insight into their impact on the film height. The amount of variation is based on measurements of the elastic modulus of the elastomeric layer and the resin viscosity, given the possible variations in the material composition of the elastomeric layer and the temperature dependency of the viscosity.

2.3 Results

This section presents the numerical and experimental results. The numerical results give an indication of the pressure and film height profiles within the roller contact, including the influence of web tension. Next, the numerical results are validated with experimental results for a wide range of imprint parameters.

2.3.1 Model

The numerical model has been run with varying web tension values and a specific set of imprint parameters: a resin viscosity of 30 mPa s, an imprint velocity of 3 mm s^{-1}, and an imprint load of 2000 N m^{-1}. The resulting pressure profiles for the hydrodynamic film pressure and tensioned web contact pressure are shown in Figure 2.5a. It also shows the Hertz dry contact pressure, for reference. The Hertz pressure and contact half-width are equal to 1.53×10^5 Pa and 8.3 mm, respectively. Starting from the inlet of the roller contact, the hydrodynamic film pressure smoothly increases up to the peak pressure in the center ($x = 0$), after which it decreases to ambient pressure again. The finite thickness of the elastomeric layer results in smaller contact widths and larger peak pressures in the resin film, compared to the Hertz solution. A similar phenomenon can be identified when web tension is included in the model. The tensioned web restricts the elastic deformation of the elastomeric layer material, thereby increasing the effective stiffness of the roller contact. For zero web tension, the tensioned web contact pressure is equal to the hydrodynamic film pressure, as also indicated by Equation (2.13). Increasing values of the web tension result in smaller contact widths and increased peak pressures in the thin film of resin. Outside the roller contact zone, the tensioned web contact pressure approaches a constant value of T/R. This can be explained by an absence of hydrodynamic film pressure, while the second-order derivative of the elastic deformation in Equation (2.13) approaches zero.

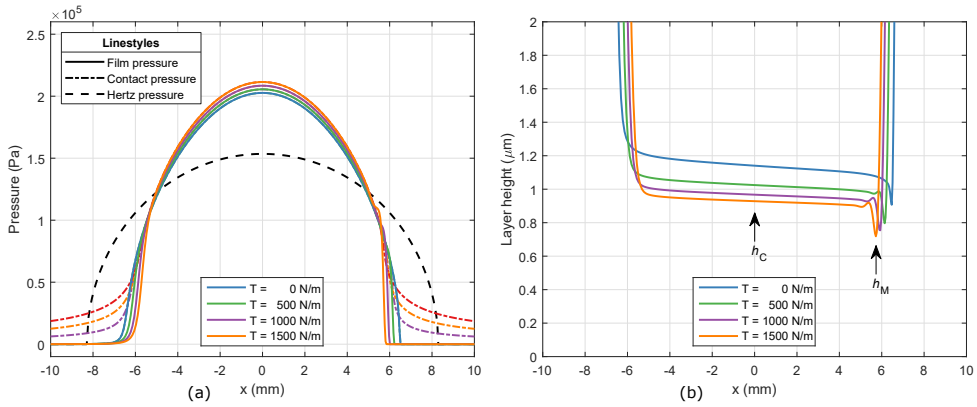

Figure 2.5: (**a**) The hydrodynamic film pressure (p) and tensioned web contact pressure (p_C) along the x-coordinate for varying web tension values. The Hertz dry contact pressure profile from Equation (2.15) is shown for reference. (**b**) The film height (h) along the x-coordinate for varying web tension values.

The corresponding film height profiles are shown in Figure 2.5b. Due to the diverging surface of the roller, the film height rapidly decreases until the roller contact zone. Within

the contact zone, the film height follows a nearly uniform, slowly decreasing profile. The central film height h_C in the center and the minimum film height h_M near the outlet are clearly visible. This does not hold for the final film height h_F. With the implemented model approach, the tensioned web follows the roller shape, which quickly increases after the location of the minimum film height. For zero web tension, the central and minimum film heights are equal to 1.14 µm and 0.91 µm, respectively. The influence of web tension is in line with the effect on the pressure profiles. The film height decreases for increasing web tension, due to the increased effective stiffness of the roller contact.

2.3.2 Experimental validation

Figures 2.6–2.8 visualize the simulated and measured film heights for different imprint loads and for a variation in imprint velocity, resin viscosity, and imprint load, respectively. The modeled variation of ±10% in both the elastic modulus of the elastomeric layer and the resin viscosity is shown as well. The variation is modeled around the results including web tension. The results in each graph will be discussed separately.

Figure 2.6 visualizes the film heights for varying velocity and three different imprint loads. In both model and measurement, the viscosity is kept constant at 38 mPa s. The film height increases with increasing velocity and decreasing load. Furthermore, the film height slightly decreases when the web tension of 370 $\mathrm{N\,m^{-1}}$ is taken into account. This behavior is also shown in Figure 2.5b. When taking a closer look at the film height for a 1000 $\mathrm{N\,m^{-1}}$ imprint load, it can be seen that there is good agreement between the measured film heights and the minimum film height from the numerical model with web tension. Contrary to the hypothesis, the minimum film height seems to be the best predictor of the RLT, instead of the central film height. For clarity, the central film heights for the other imprint loads, which show similar behavior, are not shown. The film heights for a varying resin viscosity and two different imprint loads are shown in Figure 2.7. The imprint velocity is kept constant at 6.7 $\mathrm{mm\,s^{-1}}$. The results are comparable to the results for a varying imprint velocity in Figure 2.6. The film height increases with increasing resin viscosity and decreasing imprint load. Again, good agreement is found between the measured film heights and the minimum film height from the numerical model. The film height for a varying imprint load is shown in Figure 2.8. The experimental data in this graph are in fact deduced from the measurements in Figures 2.6 and 2.7. The resin viscosity and imprint velocity are kept constant at 38 mPa s and 6.7 $\mathrm{mm\,s^{-1}}$, respectively. The film height decreases with increasing imprint load, as expected. Again, good agreement is found between the measured film heights and the minimum film height from the numerical model.

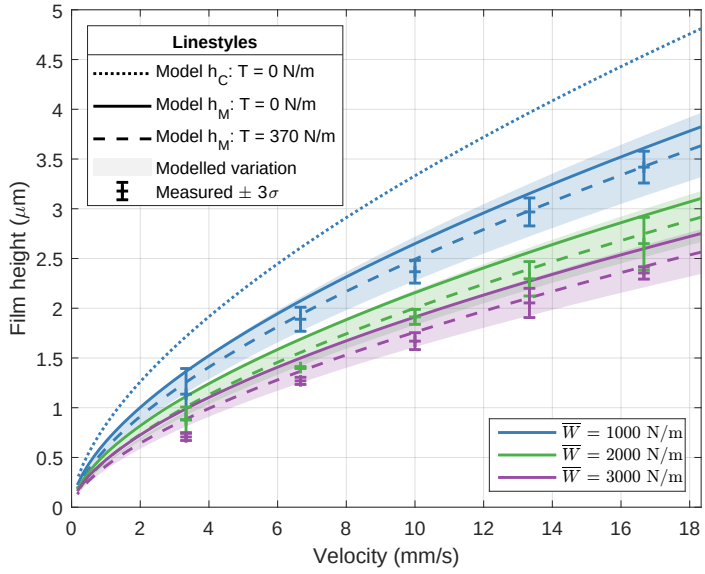

Figure 2.6: Numerical and experimental results for the film height for varying imprint loads and imprint velocities. The modeled results include a ±10% variation in both elastic modulus of the elastomeric layer and resin viscosity. The simulations and imprints are performed with Resin B from Table 2.1 (viscosity of 38 mPa s).

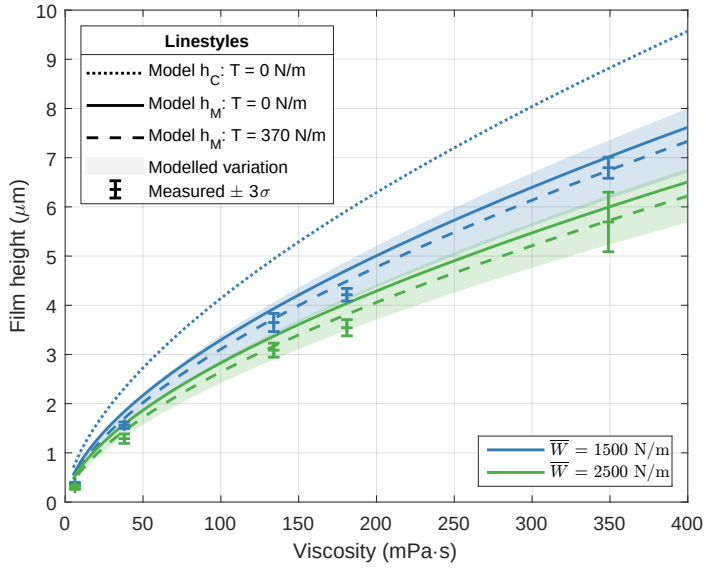

Figure 2.7: Numerical and experimental results for the film height for varying imprint loads and resin viscosities. The modeled results include a ±10% variation in both elastic modulus of the elastomeric layer and resin viscosity. The simulations and imprints are performed with a constant imprint velocity of 6.7 mm s^{-1}. The imprints are performed with the resins as listed in Table 2.1.

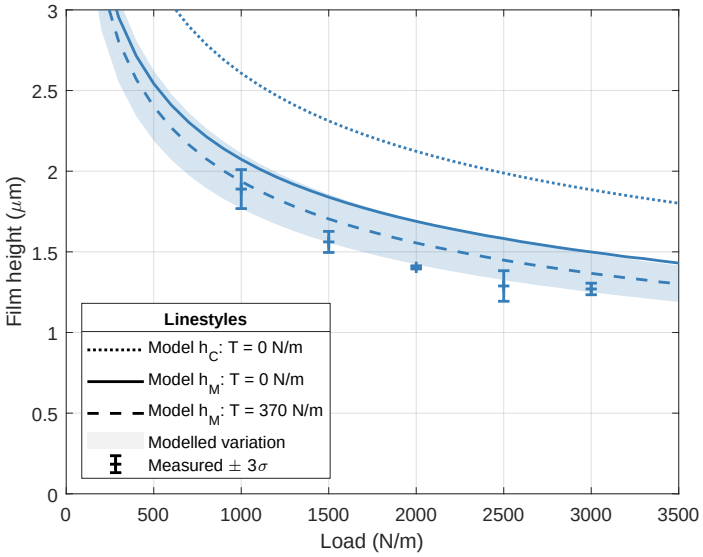

Figure 2.8: Numerical and experimental results for the film height for a varying imprint load. The modeled results include a ±10% variation in both elastic modulus of the elastomeric layer and resin viscosity. The simulations and imprints are performed with Resin B from Table 2.1 (viscosity of 38 mPa s) and a constant imprint velocity of 6.7 mm s^{-1}.

2.4 Discussion

The numerical results for the minimum film height and the experimental results agree very well. This contradicts the hypothesis that the final layer thickness corresponds to the central film height. The validity of the numerical model and the corresponding results will be discussed.

The EHL model consists of different physics, each with its own assumptions. The assumptions in material properties and behavior are considered to be the most critical. The relevant materials in the imprint process are the elastomeric layer and the imprint resin. The numerical results in Figures 2.6–2.8 include a modeled variation of ±10% in both the elastic modulus of the elastomeric layer and the viscosity of the resin. The results clearly indicate that any changes in the material properties have a direct impact on the film height of the imprint. The elastic deformation in the elastomeric layer is described by linear elasticity theory, which assumes small deformations and a linear relation between stress and strain. Although the elastic deformation is large compared to the film height, it is still small compared to the elastomeric layer thickness. For the maximum load case of 3000 N m^{-1}, the maximum elastic deformation is equal to 0.26 mm. This corresponds to a linear strain of 0.034, which is considered to be small. The resin is the other relevant material in the imprint process. It is assumed to be isoviscous. In practice, the resin viscosity can depend on pressure, shear rate, and temperature. The EHL contact is part of the soft EHL regime, which is characterized by relatively low contact pressures [59, 92], as can also be seen in the typical film pressure profiles in Figure 2.5a. This confirms the assumption that any piezoviscous effects can be neglected. The Newtonian fluid behavior, which assumes a

shear-rate-independent viscosity, is confirmed by viscosity measurements for a varying shear rate. Moreover, because the roller and substrate move with a similar velocity, the shear rate in the thin film of resin will be relatively low. Lastly, the process is assumed to be isothermal. It is known that the resin viscosity depends on temperature, similar as with other fluids and lubricants [56]. However, because the location of curing is relatively far way from the imprint roller (see Figure 2.1), any heating due to the UV source or the exothermal curing process can be neglected. This is confirmed by monitoring the imprint roller temperature during the experiments.

An important difference between the numerical model and the experimental set-up is the contact mechanics and kinematics of the tensioned web. The numerical model assumes that the tensioned web follows the imprint roller, as shown in Figures 2.2b and 2.5b. In reality, the tensioned web and roller lose contact in the outlet region, as the tensioned web moves away with the substrate in the imprint direction and the contact pressure diminishes. Furthermore, the bending stiffness of the tensioned web is not yet taken into account. The tensioned web is a relatively flexible stamp. The bending stiffness will be low, but might not be negligible. The hypothesis is that the bending stiffness slightly increases the effective stiffness of the roller contact, which results in a small reduction in the RLT. It is believed that both aspects must be included to better describe the roll-to-plate imprint process with tensioned, flexible stamps.

2.5 Conclusions

In this work, a numerical model is developed to predict the imprint layer thickness in UV-cure roll-to-plate nanoimprinting. The numerical model combines multiple physics in an elastohydrodynamic lubrication model to describe the fluid flow of the thin film of resin, the elastic deformation of the elastomeric layer, the mechanics of the tensioned web, and the coupling between them. We have shown that the simulated minimum film height in the roller contact corresponds very well to the experimental layer thickness values for a wide range of resin viscosities, imprint velocities, and imprint loads. The model finds direct practical use for determining the required amount of resin in a specific imprint, for a given set of machine and process parameters. Furthermore, it can be employed to study the impact of the various parameters in the imprint process on the RLT and its uniformity over the imprint area. Future work will address the contact mechanics of the tensioned web and the roller, the bending stiffness and kinematics of the tensioned web, and the influence of different textures on the resin flow and the RLT. These extensions of the numerical model will help in an even better understanding of the roller-based nanoimprint process to further improve the prediction of the RLT in UV-cure roll-to-plate nanoimprinting.

3

EHL of roll-to-plate nanoimprinting on flat substrates

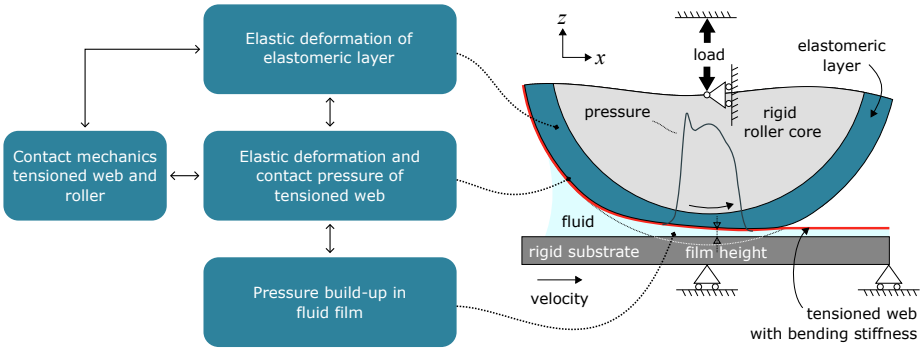

In the previous chapter, the first development of a numerical EHL model to analyze the roll-to-plate nanoimprint process was presented. This chapter presents an improved and extended version of the EHL model to describe the underlying physics accurately. The model considers the bending stiffness of the tensioned web and the contact mechanics between the tensioned web and the roller. The latter offers the advantage that the cavitation algorithm can be eliminated because the fluid film is trapped between the tensioned web and the substrate. A set of five non-dimensional numbers is proposed to characterize the EHL model. The numerical results are compared with benchmarks from literature and the simulated film heights are experimentally validated for a variation of the imprint parameters.

This chapter was published as:
Snieder, J., Dielen, M., & van Ostayen, R. A. J. (2023). *Elastohydrodynamic lubrication of soft-layered rollers and tensioned webs in roll-to-plate nanoimprinting.* Proceedings of the Institution of Mechanical Engineers, Part J: Journal of Engineering Tribology, 237(10), 1871–1884.

Elastohydrodynamic lubrication of soft-layered rollers and tensioned webs in roll-to-plate nanoimprinting

3

Abstract *This work presents the development of a numerical model for the elastohydrodynamic lubrication of roll-to-plate nanoimprinting with flexible stamps. Roll-to-plate nanoimprinting is a manufacturing method to replicate micro- and nanotextures on large-area substrates with ultraviolet-curable resins. The roller is equipped with a relatively soft elastomeric layer, which elastically deforms during the imprint process. The elastic deformation is described by linear elasticity theory. It is coupled to the pressure build-up in the liquid resin film, which is described by lubrication theory. The flexible stamp, which is treated as a tensioned web, is pre-tensioned around the roller. The elastic deformation of the tensioned web is described by the large-deflection bending of thin plates equations, considering its non-negligible bending stiffness. A Fischer–Burmeister complementarity condition captures the contact mechanics between the tensioned web and the roller. The governing equations combine in a coupled elastohydrodynamic lubrication model, which is fully described by a set of non-dimensional numbers. These are used in a parameter study to investigate the effect on the pressure and film height distributions. It is shown that the bending stiffness of the tensioned web results in an additional hydrodynamic pressure peak and corresponding minimum in the film height, near the inlet of the roller contact. An increase of the bending stiffness corresponds to a decrease in film height. The numerical results are compared with benchmarks from literature and experimentally validated with layer height measurements from flat layer imprints. Good agreement is found between the numerical and experimental results.*

3.1 Introduction

Nanoimprint Lithography (NIL) is an emerging manufacturing technology to replicate micro- and nanotextures with high resolution on rigid and flexible substrates [36, 37]. The working principle is based on a moulding process, in which a stamp is pressed into a liquid resist material. The resist material is mechanically deformed to conform to the surface topography of the stamp. Ultraviolet (UV) NIL employs photo-polymerizable resins, which can quickly fill the stamp features, in combination with UV-transparent stamps [42]. After solidification of the resin by UV-light, the stamp is delaminated and a negative of the textured pattern is left on the substrate. Roller-based nanoimprinting enables an increased fabrication throughput and the possibility to pattern large-area substrates at once [41, 43, 44]. The stamps may be re-used many times, which makes roller-based NIL

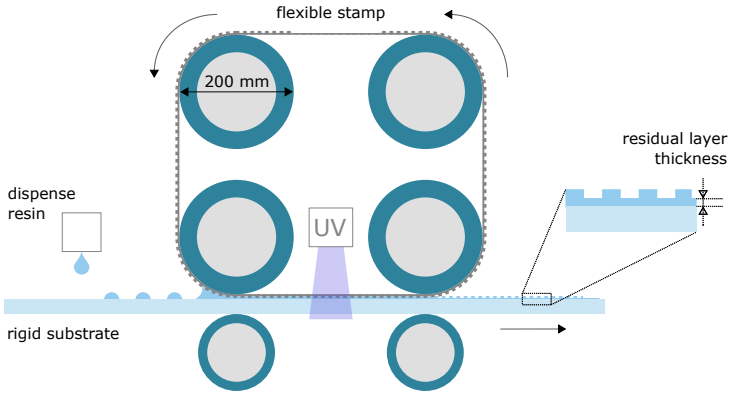

Figure 3.1: Reproduced with permission from [45]. Roll-to-plate nanoimprint system.

an interesting and versatile technology for cost-effective volume manufacturing [93]. The patterning method can be used to fabricate functional layers or to enhance the optical or mechanical properties of a substrate. Applications can be found in for example anti-reflection or light-trapping surface layers for displays and solar panels [26, 27], optical waveguides for augmented reality [29], drag reduction surface layers for aviation and shipping [34, 35], antifouling surfaces [32, 33], and many more.

A roller-based imprint system can be equipped with one or multiple rollers. Various configurations of the stamp, roller(s) and substrate are available and can be used to classify the different systems [46, 64]. Figure 3.1 shows a schematic of a UV-cure roll-to-plate nanoimprint system, which is considered in this study. It makes use of a number of rollers to guide a flexible stamp. The rollers are equipped with a relatively soft, elastomeric layer to ensure conformal contact with the substrate. The imprint roller (middle left) presses the flexible stamp into the UV-curable resin droplets, which have been dispensed on the substrate. The resin droplets merge and spread into a thin layer. After UV-curing of the resin layer, the flexible stamp is delaminated from the substrate by the delamination roller (middle right). The final imprint consists of the preferred texture on top of a residual layer. The residual layer is ideally thin and uniform over the entire surface, in order to prevent poor optical performance of the product [46]. Moreover, the imprinted texture can optionally be transferred into the substrate material in a subsequent etching process step by utilizing the imprinted pattern as an etching mask. A thin and uniform residual layer is essential for an efficient and high quality etch [37, 47, 48].

Simulation of the imprint process will allow for the improved prediction of the residual layer thickness to further improve the imprint quality. The residual layer thickness is governed by the interaction of the hydrodynamic forces in the resin and the elastic forces of the flexible stamp and the elastomeric layer around the imprint roller. The hydrodynamic pressure-build up in the liquid resin film results in elastic deformation of both the flexible stamp and the elastomeric layer. The pre-tensioned, flexible stamp exerts an additional contact pressure on part of the elastomeric layer, after which it loses contact with the roller downstream of the roller contact. The elastic deformation is relatively large compared to the film height and will affect the hydrodynamic pressure build-up, in return.

This coupling is described by elastohydrodynamic lubrication (EHL) theory, which can be used to predict the residual layer thickness. Soft-layered EHL deals with the lubrication of relatively soft, elastomeric layers. The finite thickness of the elastomeric layer increases the effective stiffness of the roller contact, which influences the pressure build-up and film height in the roller contact [78, 82, 83, 94].

In literature, analytical and numerical models are presented to simulate the residual layer thickness in roller-based imprint systems [43, 70, 76]. Moreover, when excluding the textures, roller-based imprinting shows a resemblance with forward roll coating and printing [77, 78, 80, 95, 96]. These are well-known industrial methods to apply thin liquid coatings on flexible, foil-like substrates using rubber covered rollers. EHL theory is used to determine the process dependencies on the coating or printing layer height. In all of these simulations, the influence of the elastic deformation of the flexible stamp or foil and the interaction with the rollers are not taken into account. In previous work, the development of an EHL model to predict the residual layer thickness in roll-to-plate nanoimprint systems with pre-tensioned, flexible stamps is presented [45]. It has been shown that an increase in tension of the flexible stamp, which is assumed to be perfectly flexible, results in a reduction of the residual layer thickness. The contact mechanics between the flexible stamp and the roller are a unique aspect of the roll-to-plate nanoimprint process. Moreover, the bending stiffness of the flexible stamp is not negligible and differs based on the geometry and material properties. Both contact mechanics and bending stiffness must be included in the EHL model to further improve the prediction of the residual layer thickness.

The current work presents the development of a numerical EHL model to accurately describe the physics of the roll-to-plate nanoimprint process with flexible stamps, which are treated as tensioned webs with a non-negligible bending stiffness. The study focuses on the flat layer thickness and the influence of textures is not taken into account. The numerical model is described in detail and the numerical results are experimentally validated with layer height measurements of flat layer imprints. Unique contributions of this work are the implementation of the elastic deformation and contact mechanics of tensioned webs in an EHL system, and the application of this theory in a roll-to-plate nanoimprint process. The model can be used to study the influence of the process parameters, machine parameters, and material properties on the pressure and film height distributions. Moreover, it can be used to directly assess the film thickness for a given set of process parameters. This information is useful to determine the required amount of resin for a specific imprint or to tune the process parameters for a preferred film thickness.

3.2 Methods

This section describes the set-up of the numerical EHL model, including the governing equations and the numerical implementation. Thereafter, the experimental validation method is discussed.

3.2.1 Model description

The numerical model is based on the full-system finite element approach for EHL problems [85]. The modelled system geometry of the imprint roller contact, which is treated as a line contact, is shown in Figure 3.2a. The imprint roller with radius R is pressed onto

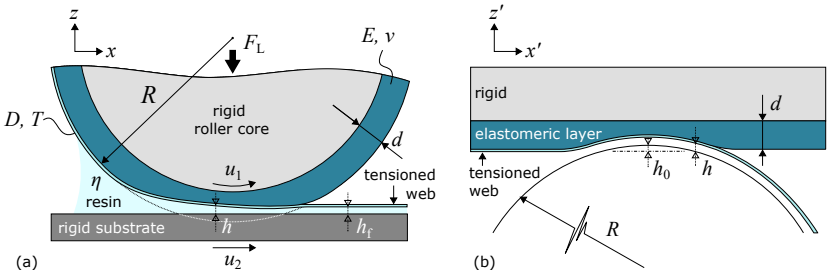

Figure 3.2: Adapted with permission from [45]. (**a**) Schematic of the imprint roller with tensioned web. The elastic deformation of the elastomeric layer is highly exaggerated for illustrative purposes. (**b**) Equivalent geometry of the imprint roller with tensioned web.

the rigid substrate. The roller is equipped with an elastomeric layer of thickness d. A tensioned web (i.e., flexible stamp) is partly wrapped around the imprint roller and applies a contact pressure onto the elastomeric layer. Downstream of the roller contact, the tensioned web looses contact with the roller and moves along with the substrate. The tensioned web and substrate are separated by a thin film of resin with film height h. The final film height is indicated by h_f. The lubricated roller contact is assumed to be fully-flooded and is subject to an effective load F_L in vertical z-direction. The load is a combination of the externally applied roller load and web tension. The substrate and tensioned web are assumed to be smooth and are moving with a unidirectional, constant surface speed of u_1 and u_2, respectively. It is assumed that all elastic deformation occurs in the relatively compliant, elastomeric layer. As the contact width is relatively small compared to the roller radius, a simplified equivalent geometry can be used, as shown in Figure 3.2b. A rigid roller with radius R is pressed onto the flat, elastomeric layer, which is unwrapped from the roller core. A new coordinate system is introduced: x' is the coordinate tangential to the roller surface and z' is the coordinate normal to the roller surface, pointing towards the rigid roller.

The model is governed by five main equations: linear elasticity equations, Reynolds equation, large-deflection bending of thin plates equations, the Fischer–Burmeister constraint function, and a load balance equation. The equations are solved together to determine the elastic deformation components u and w of the elastomeric layer, the hydrodynamic pressure p, the contact pressure p_c, the tensioned web curvature κ, and the elastic deformation of the tensioned web w_w. To ensure numerical robustness and faster convergence, the model variables are scaled. Before the governing equations are presented, the definition of the dimensionless scaling is discussed. The following dimensionless variables are used in the description of the equations:

$$
\begin{aligned}
&P = \frac{p}{p_h}, \quad P_c = \frac{p_c}{p_h} \\
&U = \frac{uR}{a_h^2}, \quad W = \frac{wR}{a_h^2}, \quad W_w = \frac{w_w R}{a_h^2}, \quad G = \frac{gR}{a_h^2}, \quad H = \frac{hR}{a_h^2}, \\
&K = R\kappa, \quad X' = \frac{x'}{a_h}, \quad Z' = \frac{z'}{d}
\end{aligned}
\tag{3.1}
$$

with the dimensionless hydrodynamic film pressure P, tensioned web contact pressure P_c, elastic deformation components U and W, web deformation W_w, gap G, film height H, tensioned web curvature K, and spatial coordinates X' and Z'. The parameters a_h and p_h correspond to the Hertz dry contact half-width and peak pressure, respectively. They are based on the mechanical properties of the elastomeric layer:

$$\begin{aligned} a_h &= \sqrt{\frac{8F_L R}{\pi E'}}, \\ p_h &= \frac{2F_L}{\pi a_h}, \end{aligned} \tag{3.2}$$

where E' is the effective elastic modulus. As it is assumed that all elastic deformation occurs in the elastomeric layer, it is given by:

$$\frac{2}{E'} = \frac{1-\nu^2}{E}, \tag{3.3}$$

where ν is the Poisson's ratio. The equations are applied on the computational domain in Figure 3.3, which represents the unwrapped elastomeric layer. The dimensionless scaling results in a fixed computational domain with a dimensionless length of 20 and unit dimensionless height, due to the above definition of X' and Z'. The coordinate $X' = 0$ represents the roller centre.

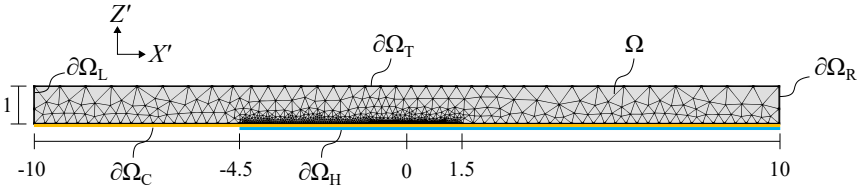

Figure 3.3: Adapted with permission from [45]. Dimensionless computational domain and mesh. The contact domain Ω_C (yellow) extends over the entire domain length ($-10 \leq X' \leq 10$), while the hydrodynamic domain Ω_H (blue) extends over part of the domain length ($-4.5 \leq X' \leq 10$).

The dimensionless linear elasticity equations are applied on the elastomeric layer domain Ω in Figure 3.3. For a derivation of these scaled equations, the reader is referred to [97]. They are given by:

$$\begin{aligned} &\frac{\partial}{\partial X'}\left[\left(\lambda+2\mu\right)\frac{d}{a_h}\frac{\partial U}{\partial X'}+\lambda\frac{\partial W}{\partial Z'}\right] \\ &+\frac{\partial}{\partial Z'}\left[\mu\left(\frac{a_h}{d}\frac{\partial U}{\partial Z'}+\frac{\partial W}{\partial X'}\right)\right]=0, \\ &\frac{\partial}{\partial X'}\left[\mu\left(\frac{\partial U}{\partial Z'}+\frac{d}{a_h}\frac{\partial W}{\partial X'}\right)\right] \\ &+\frac{\partial}{\partial Z'}\left[\lambda\frac{\partial U}{\partial X'}+\left(\lambda+2\mu\right)\frac{a_h}{d}\frac{\partial W}{\partial Z'}\right]=0, \end{aligned} \tag{3.4}$$

where λ and μ correspond to the Lamé parameters:

$$\begin{aligned} \lambda &= \frac{\nu E_{\mathrm{eq}}}{(1-2\nu)(1+\nu)}, \\ \mu &= \frac{E_{\mathrm{eq}}}{2(1+\nu)}. \end{aligned} \tag{3.5}$$

The parameter E_{eq} corresponds to the equivalent elastic modulus of the elastomeric layer, which is defined by:

$$E_{\mathrm{eq}} = E\frac{a_{\mathrm{h}}}{Rp_{\mathrm{h}}}. \tag{3.6}$$

The elastic modulus is multiplied by $a_{\mathrm{h}}/\left(Rp_{\mathrm{h}}\right)$ to directly use the dimensionless tensioned web contact pressure P_{c} as a pressure load on domain boundary $\partial\Omega_{\mathrm{C}}$ [98]. The boundary conditions are specified as follows:

$$\begin{cases} U = W = 0 & \text{on } \partial\Omega_{\mathrm{T}}, \\ U = 0 & \text{on } \partial\Omega_{\mathrm{L}} \text{ and } \partial\Omega_{\mathrm{R}}, \\ \sigma_n = \sigma \cdot \vec{n} = \sigma_{zz} = & \\ \quad \lambda\dfrac{\partial U}{\partial X} + \left(\lambda + 2\mu\right)\dfrac{a_{\mathrm{h}}}{d}\dfrac{\partial W}{\partial Z} = P_{\mathrm{c}} & \text{on } \Omega_{\mathrm{C}}, \\ \sigma_n = \sigma_t = 0 & \text{elsewhere.} \end{cases} \tag{3.7}$$

The parameters σ_n and σ_t are the normal and tangential components of the stress tensor, respectively.

The resin flow is described by lubrication theory, which assumes a constant pressure across the film thickness. The dimensionless, steady-state, incompressible Reynolds equation in one dimension is given by [56]:

$$\frac{\partial}{\partial X'}\left(-\frac{a_{\mathrm{h}}^3 p_{\mathrm{h}}}{12R^2\eta u_\Sigma}H^3\frac{\partial P}{\partial X'} + \frac{H}{2}\right) = 0, \tag{3.8}$$

where η is the dynamic viscosity of the resin, and u_Σ is the sum of the top and bottom surface velocity u_1 and u_2, respectively. The Reynolds equation assumes Newtonian fluid behaviour and isothermal conditions. The validity of these assumptions is confirmed by viscosity measurements and monitoring of the roller temperature. Equation (3.8) is applied on domain $\partial\Omega_{\mathrm{H}}$ in Figure 3.3. It is defined by $-4.5 \le X' \le 10$, which is sufficiently wide to capture the pressure build-up in the thin film of resin [85]. Zero pressure boundary conditions are applied on the edges of the domain. The hydrodynamic film pressure P is determined for a given film height distribution H:

$$\begin{aligned} H(X') &= H_0 + H_{\mathrm{w}} + W_{\mathrm{w}}(X'), \\ H_{\mathrm{w}} &= \begin{cases} \dfrac{X'^2}{2} & \text{for } X' \le 0, \\ 0 & \text{for } X' > 0. \end{cases} \end{aligned} \tag{3.9}$$

where H_0 is the unknown rigid body displacement. A negative value indicates roller engagement, as shown in Figure 3.2b. The second term H_{w} describes the initial web shape,

which partly follows the roller surface. The last term $W_w(X')$ represents the web deformation, which will follow from Equation (3.11). It is assumed that the resin can sustain small negative pressures without cavitating. Downstream of the roller contact zone, the resin is trapped between the tensioned web and the substrate. Due to the absence of a diverging roller surface, which is typically present in conventional EHL problems [99], the presence of negative pressures will be minimum.

The tensioned web is a relatively thin plate with a non-negligible bending stiffness, and therefore the Föppl–von Kármán equations can be applied to describe the deformation of the web under tension and pressure [100, 101]. These equations are based on the extended theory for small deflections of thin plates, by taking into account the in-plane membrane stresses, and they describe the large-deflection bending of thin plates. In the case of an infinite line contact and by assuming a constant web tension, the dimensionless stress balance in normal direction is given by:

$$\left(-\frac{D}{{a_h}^2 p_h R}\right)\frac{\partial^2 K}{\partial X'^2}+\left(\frac{T}{p_h R}\right)K+P_n=0. \tag{3.10}$$

where D is the bending stiffness of the web and T is the web tension. The normal stress P_n is equal to the difference of the hydrodynamic film pressure and the tensioned web contact pressure; $P_n = P - P_c$. The web curvature K is approximated by the second spatial derivative of the web shape, which is described by the last two terms in Equation (3.9):

$$\begin{aligned} K &= \frac{\partial^2}{\partial X'^2}\left(H_w + W_w(X')\right) \\ &= \begin{cases} 1+\frac{\partial^2 W_w}{\partial X'^2} & \text{for } X' \le 0, \\ \frac{\partial^2 W_w}{\partial X'^2} & \text{for } X' > 0. \end{cases} \end{aligned} \tag{3.11}$$

The bending stiffness of the tensioned web is a function of the elastic modulus E_w, web thickness t and Poisson's ratio ν_w of the tensioned web:

$$D=\frac{E_w t^3}{12\left(1-\nu_w^2\right)} \tag{3.12}$$

Equation (3.10) and Equation (3.11) are applied on domain $\partial\Omega_C$ in Equation 3.3.

The contact mechanics between the roller and tensioned web are described by two variables; the contact pressure P_c and the gap between the roller and the tensioned web G. The contact pressure P_c can be traced back to Equation (3.10). The dimensionless gap is defined by:

$$\begin{aligned} G &= G_0 + W - W_w, \\ G_0 &= \begin{cases} 0 & \text{for } X' \le 0, \\ \frac{X'^2}{2} & \text{for } X' > 0. \end{cases} \end{aligned} \tag{3.13}$$

in which G_0 is the initial gap between the roller and the tensioned web, and W and W_w are the elastomeric layer and web deformation, respectively. The initial gap is equal to zero

at the locations where the tensioned web and roller are initially in contact, and increases with the approximated roller shape from the location where the tensioned web and roller lose contact at $X' = 0$. In general, two different regions can be identified: a contact region in which the contact pressure is unknown (but larger than 0) and the gap is known (namely 0), and a region without contact where the contact pressure is known (namely 0) and the gap is unknown. This reasoning can be captured in a complementarity condition:

$$\begin{aligned} P_c \geq 0 \quad &\text{and} \quad G = 0, \\ P_c = 0 \quad &\text{and} \quad G \geq 0. \end{aligned} \tag{3.14}$$

The complementarity condition of the contact problem is satisfied by adding a modified constraint function to domain Ω_C in the model, known as the Fischer–Burmeister function [89]:

$$P_c + G - \sqrt{P_c^2 + G^2} = 0. \tag{3.15}$$

This function is often used in (elasto)hydrodynamic lubrication models as a mass-conserving cavitation algorithm [45, 102], with the film pressure and the mass fraction as dependent variables. In the present study, the Fischer–Burmeister function will reveal the occurrence of contact between the tensioned web and the roller.

The load equilibrium is derived by balancing the pressure force from the hydrodynamic film pressure build-up with the effective roller load per unit length:

$$\int_{\Omega_H} P \mathrm{d}X' = \frac{\pi}{2}. \tag{3.16}$$

The right side of this equation relates to the Hertz scaling from Equation (3.2). The equation is satisfied by regulating the gap H_0 in Equation (3.9), which is one of the unknowns in the system of equations.

3.2.2 Numerical implementation

The elastohydrodynamic model is composed of the linear elasticity equations in Equation (3.4), the Reynolds equation in Equation (3.8), the large-deflection bending of plates equations in Equation (3.10) and Equation (3.11), the Fischer–Burmeister function in Equation (3.15), and the load balance equation in Equation (3.16). The equations are implemented in the finite element method (FEM) software package COMSOL Multiphysics® [91]. A second-order (quadratic) discretization is employed for the Reynolds equation, the large-deflection bending of plates equations and the Fischer–Burmeister constraint function. The linear elasticity equations are discretized with third-order (cubic) elements, to ensure a smooth second-order derivative of the web curvature in Equation (3.11). The use of FEM allows for unstructured meshing of the computational domain in Figure 3.3. The domain Ω is built with a coarse triangular mesh, while the mesh is refined at the lower boundary $\partial\Omega_C$, on which the mesh size varies. A relatively coarse mesh is used on the outer parts ($-10 \leq X' \leq -4.5$ and $1.5 \leq X' \leq 10$), while the mesh size is fine in the outer regions of the roller contact ($-4.5 \leq X' \leq -1$ and $1 \leq X' \leq 10$), finer in the central region of the roller contact ($-1 \leq X' \leq 0.5$), and finest in the last region of the roller contact ($0.5 \leq X' \leq 1$). These settings have been confirmed by mesh convergence studies.

The starting point of the numerical procedure is the selection of a set of appropriate initial values for the variables as listed in Equation (3.1). The initial hydrodynamic pressure distribution is equal to the Hertz dry contact pressure:

$$P = \begin{cases} \sqrt{(1 - X'^2)} & \text{for } -1 \leq X' \leq 1, \\ 0 & \text{elsewhere.} \end{cases} \tag{3.17}$$

The initial guess for the elastic deformation components U and W is equal to the elastic deformation corresponding to the Hertz dry contact pressure. The initial contact pressure is equal to the sum of the Hertz dry contact pressure and the contact pressure from the tensioned web on the locations where the web and roller are initially in contact:

$$P_c = \begin{cases} \frac{T}{p_h R} + \sqrt{(1 - X'^2)} & \text{for } X' \leq 0, \\ 0 & \text{for } X' > 0. \end{cases} \tag{3.18}$$

The gap between the roller and tensioned web G is initialized with the initial gap G_0. The initial curvature of the tensioned web is equal to the dimensionless roller curvature of 1 for $X' \leq 0$ and equal to zero for $X' > 0$. The initial elastic deformation of the tensioned web W_w is set to zero. The Fischer–Burmeister complementarity function will directly ensure that the tensioned web follows the roller shape wherever the initial gap is equal to zero. Lastly, the initial constant gap H_0 is set to a small positive number (e.g. ~0.01). Starting from the initial values, the system of equations is iteratively solved to find the hydrodynamic pressure P, contact pressure P_c, film height H, elastic deformation components U and W, tensioned web curvature K, and tensioned web deformation W_w. This is done in a fully-coupled manner until convergence is reached. The final film height H_f is determined by evaluating the film height at the end of the hydrodynamic domain $\partial\Omega_H$ at $X' = 10$.

3.2.3 Experimental

The numerical model is validated with multiple flat layer imprints, which have been produced on the Morphotonics Portis NIL1100 roll-to-plate nanoimprint tool in Figure 3.4. The imprints are fabricated using flexible, transparent stamps, which do not contain any textures. The stamps are given an anti-adhesive treatment to ensure a smooth delamination from the UV-cured resin layer. They are pre-tensioned around test rollers, which are equipped with a 7.5 mm thick elastomeric layer. It has an effective elastic modulus of 3.2 MPa and a Poisson ratio of 0.47. Elastomers are known for their viscoelastic material behaviour. The viscoelasticity can be quantified by the dimensionless Deborah number, which represents the ratio between the material relaxation time and the process time. The linear elastic behaviour of the elastomeric layer is confirmed by compression tests. The combination of a relatively high relaxation time (~14 s) and a relatively low process time (~0.35 s to 3.1 s) results in a relatively high Deborah number (~4.5 to 40). This justifies the use of a linear elastic material model with an effective elastic modulus [103]. Each imprint is performed on a 0.5 mm thick glass substrate with dimensions of 150 mm x 150 mm. The substrates are placed on a stiff carrier plate during the imprint process. To improve the adhesion between the resin and the glass substrates, the latter are cleaned with isopropyl alcohol and pretreated with an atmospheric pressure oxygen plasma and a primer containing an adhesion promoter. The average thickness of each imprinted layer is determined

by optically measuring the step height of multiple small scratches fabricated in the cured imprint layer. These measurements are performed on a Keyence VK-X1100 laser confocal microscope.

The experimental validation consists of three different measurement datasets. In each dataset, different imprint parameters are varied. The first two datasets originate from previous work [45]. The experimental results are reused in this study. These imprints are performed for a variation of imprint velocity and imprint load and various in-house-developed resins are used. The viscosities and volumetric shrinkage ratios of these acrylate-based resins are shown in Table 3.1. Additionally, a third measurement dataset is generated. The imprints in this dataset are performed with multiple tensioned webs and a variation of imprint velocity. Each web has a different bending stiffness, as shown in Table 3.2. Finally, the measured layer heights are converted to the liquid, pre-cured film heights using the volumetric shrinkage values in Table 3.1, before comparing them to the simulated film heights.

Figure 3.4: Morphotonics Portis NIL1100 roll-to-plate nanoimprint equipment [38].

Table 3.1: Properties of the imprint resins. The viscosities are measured at 25 °C.

Resin	Viscosity (mPa s)	Volumetric shrinkage (%)
A	6.3	12.5
B	38	8.1
C	89	9.0
D	134	7.2
E	181	8.8
F	349	7.8

Table 3.2: Calculated bending stiffness of the tensioned webs.

Tensioned web	Bending stiffness (N m)
A	0.0057
B	0.0223
C	0.0823

3

3.3 Results

This section presents the numerical and experimental results. First, the numerical model will be benchmarked to numerical results from literature. Next, a parameter study will be performed to show the impact of the various parameters in the numerical model. Lastly, the numerical model is validated by experimental results. The results are presented for a minimal set of independent, non-dimensional numbers, which fully describe the EHL problem. These are the non-dimensional modified load number $\overline{M}$, elastomeric layer thickness number $\overline{d}$, bending stiffness number $\overline{D}$, web tension number $\overline{T}$, and Poisson's ratio ν:

$$\begin{aligned} \overline{M} &= \overline{W}\left(2\overline{U}\right)^{-\frac{1}{2}}, \\ \overline{d} &= \frac{d}{a_\mathrm{h}}, \\ \overline{D} &= \frac{D}{{a_\mathrm{h}}^2 p_\mathrm{h} R}, \\ \overline{T} &= \frac{T}{p_\mathrm{h} R}, \\ \nu. \end{aligned} \tag{3.19}$$

The modified load number $\overline{M}$ is composed of the non-dimensional load number $\overline{W}$ and speed number $\overline{U}$, which are given by [59, 104]:

$$\begin{aligned} \overline{W} &= \frac{F_\mathrm{L}}{E' R}, \\ \overline{U} &= \frac{\eta u_\Sigma}{2E' R}. \end{aligned} \tag{3.20}$$

The non-dimensional numbers $\overline{d}$, $\overline{D}$, and $\overline{T}$ can be traced back to Equation (3.4) and Equation (3.10), respectively. In contrast to infinite plane EHL problems, the elastic modulus E and Poisson's ratio ν cannot be fully combined in a reduced number E' for soft-layered contacts [78]. Therefore, the Poisson's ν is part of the non-dimensional numbers. It represents the effect of the compressibility of the elastomeric layer.

3.3.1 Benchmark validation

The numerical EHL model is benchmarked to results from literature for soft-layered EHL problems without a tensioned web. For this benchmark validation, the influence of the

tensioned web in the present work is minimized by setting the bending stiffness number $\overline{D}$ to zero and the web tension number $\overline{T}$ to a very low value of 1×10^{-6}. The comparison between the present work and the results from Dowson and Jin and Xue are shown in Figure 3.5 and Figure 3.6, respectively [78, 94]. The graphs show the hydrodynamic film pressure P and film height H for a specific set of the non-dimensional numbers $\overline{M}$, $\overline{d}$, and ν. The Hertz dry contact pressure and roller height profile are included for reference. The hydrodynamic film pressure smoothly increases up to a maximum at approximately the centre of the roller contact, after which it decreases. The film height quickly decreases due to the converging roller surface. A more uniform, slowly decreasing film height is shown within the roller contact zone while the minimum film height can be found near the outlet of the roller contact. In contrast to results from literature, in the present work the film height does not diverge downstream the outlet of the roller contact. The tensioned web looses contact with the roller and the film height reaches a constant value. It is interesting to note that this behaviour in the outlet region shows a resemblance with a starved EHL contact, where only part of the gap between the two surfaces in the cavitated zone is filled. A fractional film content is introduced, which represents the film height as a fraction of the diverging roller surface [105]. The film height in the current problem follows the same trend and remains constant. Despite the differences in modelling approaches, good agreement with results from literature is found for the results obtained within the current work. This confirms the basis of the present EHL model.

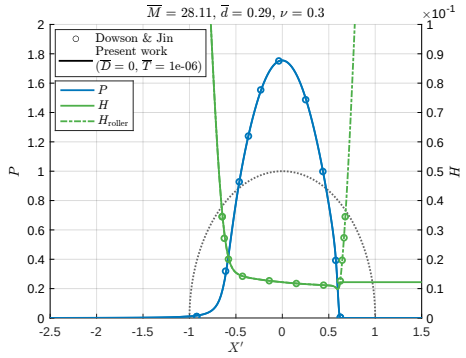

Figure 3.5: Comparison of the present work with results Dowson & Jin [94]. The Hertz dry contact pressure is included for reference (black dotted line).

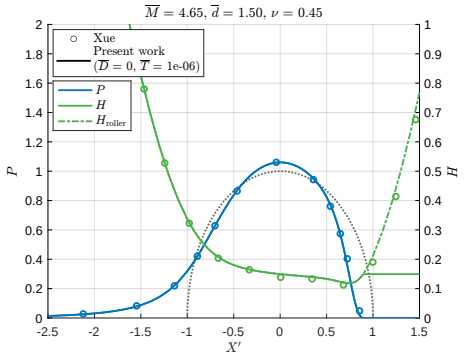

Figure 3.6: Comparison of the present work with results Xue [78]. The Hertz dry contact pressure is included for reference (black dotted line).

3.3.2 Parameter study

The starting point of the parameter study is the set of input parameters in Table 3.3, which are typical for a roll-to-plate nanoimprint system. The parameters result in a set of non-dimensional numbers $\overline{M}$, $\overline{d}$, $\overline{D}$, $\overline{T}$ and ν.

Before the parameter study is presented, the influence of the web tension and bending stiffness of the tensioned web will be illustrated. Figure 3.7 shows the pressure distributions for varying values of $\overline{D}$ and $\overline{T}$. The corresponding film height distributions are shown in Figure 3.8. For a bending stiffness number of zero and a small web tension number, the

Table 3.3: Input parameters used for the parameter study.

Parameter	Value	Unit
F_L	2000	$N m^{-1}$
η	100	mPa s
R	100	mm
E	3	MPa
u_Σ	21.2	$mm s^{-1}$
d	9.9	mm
D	0.01	N m
T	464.3	$N m^{-1}$
a_h	8.23	mm
p_h	0.16	MPa

Parameter	Value	Unit
$\overline{M}$	50	-
$\overline{d}$	1.2	-
$\overline{D}$	0.01	-
$\overline{T}$	0.03	-
ν	0.45	-

pressure and film height distributions are qualitatively similar to the benchmark results in Figure 3.5 and 3.6. The hydrodynamic pressure profile differs from the Hertz dry contact pressure due to the finite thickness of the elastomeric layer. Moreover, the hydrodynamic pressure and contact pressure are overlapping, due to the lack of web tension and bending stiffness. The film height shows a slowly decreasing profile in the contact zone, with the minimum film height near the outlet. The tensioned web looses contact with the roller once the contact pressure is equal to zero.

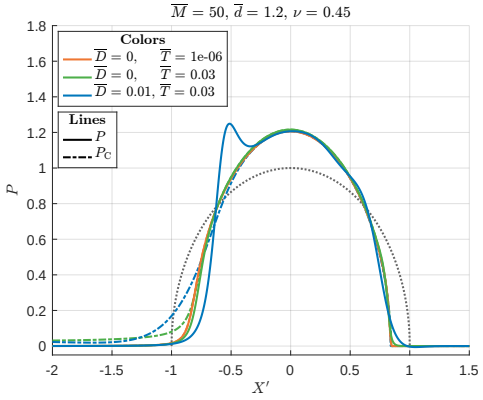

Figure 3.7: Hydrodynamic and contact pressure distributions for a varying web tension and bending stiffness number. The Hertz dry contact pressure is included for reference (black dotted line).

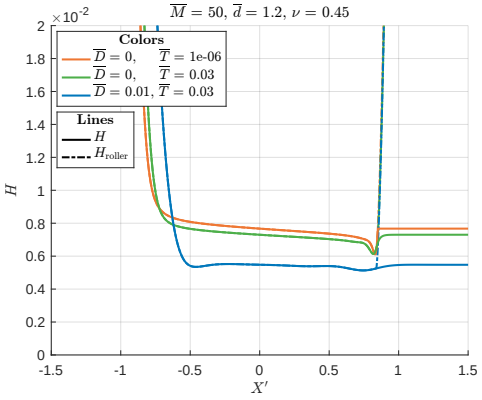

Figure 3.8: Film height distribution for a varying web tension and bending stiffness number.

An increase in the web tension number results in a small change in the pressure and film height distribution. In this case, the tensioned web is still considered to be perfectly flexible. It exerts an additional pressure onto the elastomeric layer material, which results in a slightly reduced contact width and film height. The hydrodynamic pressure and contact pressure are no longer overlapping. A uniform contact pressure equal to $\overline{T}$ is found

in front of the roller contact, where the hydrodynamic pressure is negligibly small and the web curvature is constant.

The results become different once the bending stiffness is included. The tensioned web with bending stiffness hinders the elastic deformation of the elastomeric layer and increases the effective stiffness of the roller contact. This results in a reduced contact width and film height distribution in Figure 3.8 and variations in the pressure distributions in Figure 3.7. The difference between the hydrodynamic pressure and contact pressure is enlarged as well. The impact of web tension and bending stiffness is most severe near the inlet and outlet of the roller contact, where the highest web curvature and the highest web curvature gradients are found. These are relatively small in the centre, where the roller surface is flattened. Just before the inlet of the contact, around the location of maximum curvature at $X' = -1$, the contact pressure is increased compared to the situation without bending stiffness. The combination of the bending stiffness and the increased contact pressure results in deformation of the tensioned web in other locations. Far from the inlet, around $X' = -1.5$, the contact pressure is reduced due to this deformation. The tensioned web and roller are still in contact as the contact pressure is larger than zero. It can also be observed that the contact pressure approaches the value of $\overline{T}$ further upstream. Deformation of the tensioned web also occurs more downstream, around $X' = -0.5$. The tensioned web deforms towards the substrate surface, hereby decreasing the film height. The inlet film constriction, which is clearly visible at the inlet in Figure 3.8, corresponds to an additional hydrodynamic pressure peak left of the central pressure peak. This second peak is found at the location of the maximum value of the second order derivative of the web curvature. Due to the increase in hydrodynamic pressure, which is applied onto the tensioned web from below, the resulting contact pressure does not vary too much at this location. The argument that the additional hydrodynamic pressure peak and corresponding inlet film constriction are caused by the bending stiffness of the tensioned web is supported by the fact that a similar trend is observed in viscoelastic hydrodynamic lubrication (VEHL) [103]. Here, the hydrodynamic pressure peak and inlet film constriction are a result of the larger rigidity of the material entering the contact. At the outlet of the contact a different phenomenon can be observed. The tensioned web with bending stiffness is not able to follow the sharp curvatures of the elastomeric layer and effectively flattens the minimum film height. A slightly negative hydrodynamic pressure can be observed around $X' = 1$, due to the deformation of the tensioned web with bending stiffness, which does not directly obtain a stationary film height downstream of the roller contact. The final roller height profile appears to be remarkably symmetric, with a minimum film height near the inlet and outlet and a relatively uniform and constant film height in between.

The non-dimensional numbers are used to sweep through the solution space in an effective manner. Initial numerical experiments have shown that a variation of the non-dimensional numbers $\overline{T}$ and ν has a minor impact on the pressure and film height distribution. The results for a variation in these numbers can be found in the supplementary materials[1]. The non-dimensional numbers $\overline{M}$, $\overline{d}$, and $\overline{D}$ are varied by changing the sum of the velocities u_Σ, the elastomeric layer thickness d, and the bending stiffness D, respectively. Each non-dimensional number is increased and decreased with respect to its

[1]The supplementary materials can be found in the open-access online publication [106].

reference value in Table 3.3, while the other non-dimensional numbers are kept constant. The results are shown in Figure 3.9. Note that the reference solution is equal to the solution for $\overline{D} = 0.01$ and $\overline{T} = 0.03$ in Figure 3.7 and Figure 3.8.

Figure 3.9a and Figure 3.9b show the pressure and film height distributions for a variation of the non-dimensional modified load number $\overline{M}$. A decrease of $\overline{M}$ results in a reduction of the web curvature near the inlet and outlet and a less pronounced influence of the tensioned web with bending stiffness. The contact pressure does show an increase near the inlet of the roller contact, which is a result of the increased hydrodynamic pressure. This is a typical result for lightly loaded EHL contacts [82]. The corresponding film height distribution is increased and a minimum film height near the outlet is still present. The situation is opposite for an increase of $\overline{M}$, which corresponds to a highly loaded EHL contact. The increased web curvature near the inlet results in a sharp hydrodynamic pressure peak and a corresponding inlet film constriction. The film height distribution is decreased and flattened compared to the reference solution.

The influence of a variation of the non-dimensional elastomeric layer thickness number $\overline{d}$ corresponds to soft-layered EHL results from literature [78, 82, 94]. The pressure and film height distributions are presented in Figure 3.9c and Figure 3.9d, respectively. An increase of $\overline{d}$ results in a larger contact width, a decreased hydrodynamic pressure, and an increased film height distribution. On the contrary, a decrease of $\overline{d}$ corresponds to a reduced contact width, an increased hydrodynamic pressure, and a decreased film height distribution. It is interesting to note that for $\overline{d} = 0.6$, the contact pressure near the inlet is equal to zero for a short distance. The gap between the roller and tensioned web is larger than zero at this location, which means that they are not in contact. This can be explained by the elastic deformation of the tensioned web, which is not able to exactly follow the roller shape. The roller height profiles in Figure 3.9d all show an approximately symmetric shape.

The results for a variation in the non-dimensional bending stiffness number $\overline{D}$ are shown in Figure 3.9e and Figure 3.9f. When the bending stiffness number is decreased to 0.001, the hydrodynamic pressure distribution and the contact pressure distribution approach the solution for $\overline{D} = 0$ and $\overline{T} = 0.03$ in Figure 3.7. The influence of the low bending stiffness number on the pressure and film height distributions is minor. An increase of $\overline{D}$ gives a large change in the pressure and film height distributions. The high bending stiffness of the tensioned web results in a strong increase of both the contact pressure near the inlet and the hydrodynamic pressure peak, which is also shifted towards the roller centre. The corresponding film height distribution is decreased and the contact width is reduced.

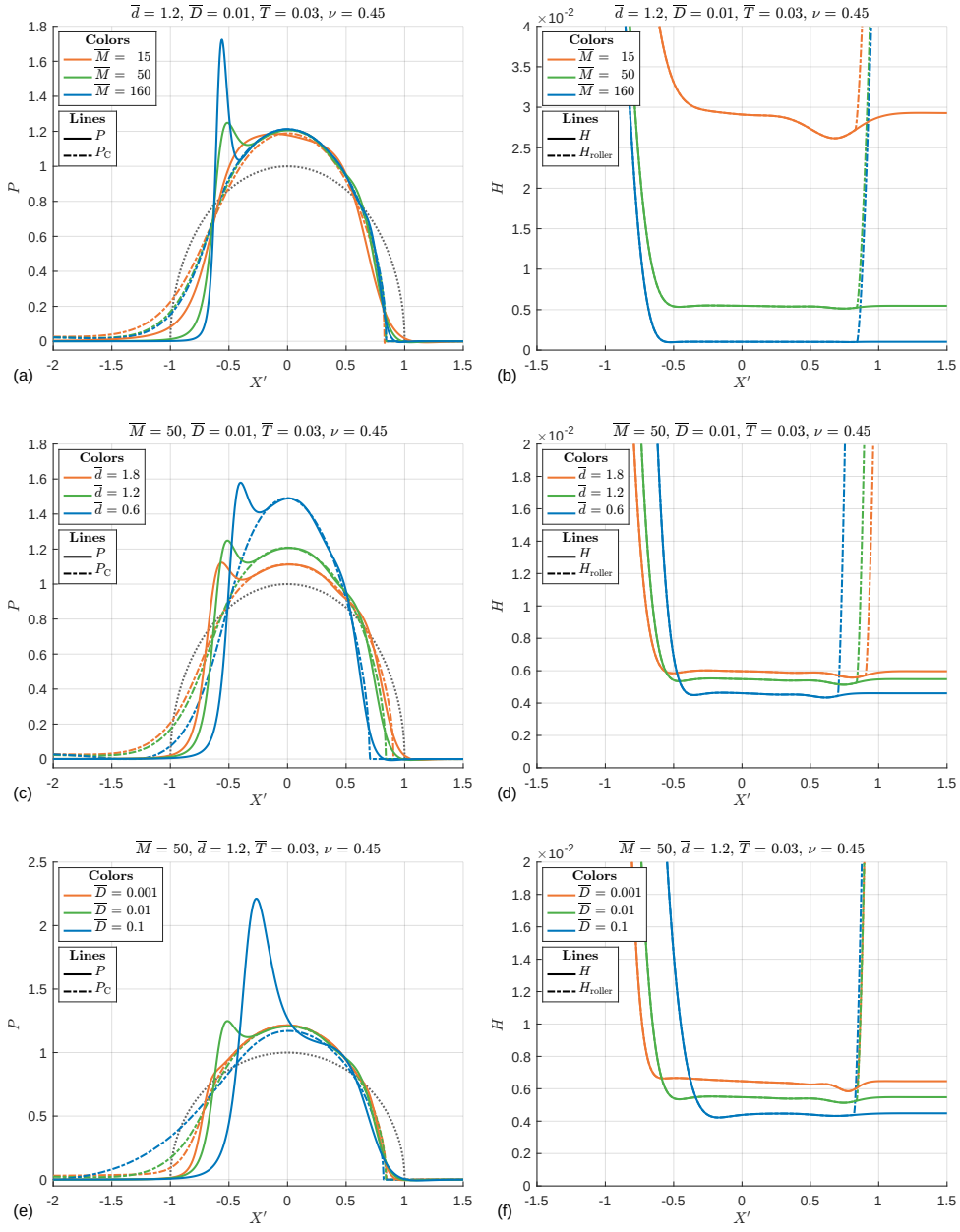

Figure 3.9: These figures show the hydrodynamic and contact pressure distributions (left column) and corresponding film height distribution (right column) for a variation of the non-dimensional modified load number $\overline{M}$ (top row), elastomeric layer thickness number $\overline{d}$ (middle row) and bending stiffness number $\overline{D}$ (bottom row). The Hertz dry contact pressure is included for reference (black dotted line).

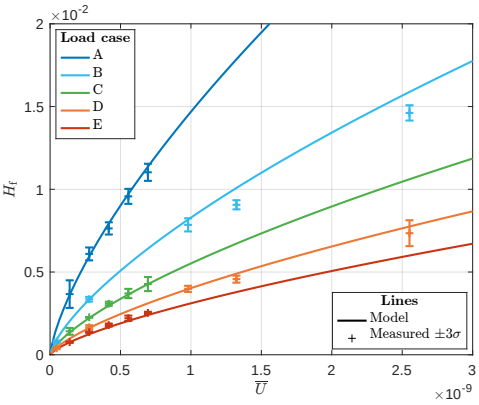

Figure 3.10: Numerical and experimental film heights for a variation of the load case and non-dimensional speed number $\overline{U}$. A specification of the load cases and the corresponding non-dimensional numbers can be found in Table 3.4.

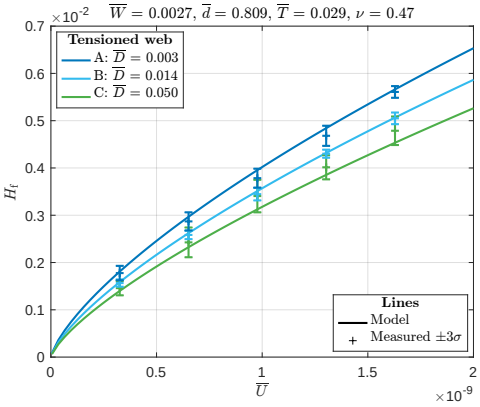

Figure 3.11: Numerical and experimental film heights for a variation of the non-dimensional bending stiffness number $\overline{D}$ and speed number $\overline{U}$.

3.3.3 Experimental validation

The numerical EHL model is validated with experimental results. To clearly distinguish the film heights for various imprint parameters, the results are shown for a variation of the non-dimensional speed number $\overline{U}$, as described in Equation (3.20). Note that the measured layer heights are converted to the liquid, pre-cured film height using the volumetric shrinkage values in Equation 3.1.

Figure 3.10 shows the numerical and experimental results for a variation of the load case and the non-dimensional speed number $\overline{U}$. Each load case represents a different imprint load and results in a variation of the non-dimensional numbers $\overline{W}$, $\overline{d}$, $\overline{D}$, and $\overline{T}$, which are listed in Table 3.4. All results are generated with tensioned web A from Table 3.2 and a web tension of $370\,\mathrm{N\,m^{-1}}$. The film heights for each load case are determined for a variation of the imprint velocity or resin viscosity. The film heights for load case A, C, and E arise from flat layer imprints, which are fabricated with Resin B from Table 3.1 (viscosity of 38 mPa s) and a varying imprint velocity. The experimental results for load case B and D correspond to a constant imprint velocity of $6.7\,\mathrm{mm\,s^{-1}}$ and a variation of the resin viscosity, as listed in Table 3.1. All resins are used except for Resin C. The film heights increase for an increasing speed number $\overline{U}$ and a decreasing load F_L. Good agreement is found between the results from the numerical model and the experiment.

The numerical and experimental results for a variation of the non-dimensional bending stiffness number $\overline{D}$ and non-dimensional speed number $\overline{U}$ are shown in Figure 3.11. The bending stiffness numbers correspond to the different tensioned webs in Table 3.2. A web tension of $555\,\mathrm{N\,m^{-1}}$ and an imprint load of $2500\,\mathrm{N\,m^{-1}}$ are used in both model and experiment. The film heights for each bending stiffness number are determined for a constant viscosity and a variation of the imprint velocity. The imprints are fabricated with Resin C from Table 3.1 (viscosity of 89 mPa s). The simulated and measured film heights increase for an increasing speed number $\overline{U}$, similar to the results in Figure 3.10. It can

Table 3.4: Specification of the load cases in Figure 3.10 and the corresponding non-dimensional numbers.

Load case	F_L ($N m^{-1}$)	$\overline{W}$	$\overline{d}$	$\overline{D}$	$\overline{T}$	ν
A	1000	0.0011	1.2786	0.0138	0.0307	0.47
B	1500	0.0016	1.0439	0.0075	0.0251	0.47
C	2000	0.0022	0.9041	0.0049	0.0217	0.47
D	2500	0.0027	0.8086	0.0035	0.0194	0.47
E	3000	0.0033	0.7382	0.0027	0.0177	0.47

also be noticed that the film height decreases for an increasing bending stiffness number D. The simulated and measured film heights agree well.

3.4 Discussion and conclusions

In this work, a numerical EHL model is developed to describe the elastohydrodynamic lubrication in roll-to-plate nanoimprinting. The model is a multiphysics simulation with a set of coupled equations to describe the elastic deformation of the elastomeric layer, the pressure build-up in the thin film of resin, the elastic deformation of the tensioned web, and the contact mechanics between the tensioned web and the roller. The numerical results with zero bending stiffness and negligible web tension agree well with benchmark results for soft-layered EHL problems from literature, which confirms the validity of the basis of the current model approach.

The EHL problem is described by the set of non-dimensional numbers $\overline{M}$, $\overline{d}$, $\overline{D}$, $\overline{T}$ and ν. These are used in a parameter study to investigate the influence of the various process parameters. The results show that web tension has a minor effect on the pressure distribution and film height distribution. On the other hand, the bending stiffness of the tensioned web does have a significant impact. It results in an additional hydrodynamic pressure peak and corresponding inlet film constriction left of the roller centre. Moreover, it effectively flattens the film height distribution, which also decreases in magnitude. The impact of the tensioned web with bending stiffness becomes more severe when the web curvature or bending stiffness is increased. It results in an increase of the additional hydrodynamic pressure peak and a further reduction of the film height distribution. The effect of the tensioned web with bending stiffness does not significantly change when the elastomeric layer thickness is varied. A decrease of the elastomeric layer thickness will result in an increased pressure distribution and decreased film height distribution. The numerical model is validated by experimental results for a wide range of the non-dimensional numbers. Good agreement is found between the numerical results and experimental results.

The present results contribute to a better understanding of the elastohydrodynamic lubrication of soft-layered rollers and tensioned webs in roll-to-plate nanoimprinting. The developed model can be used in the optimisation of a roll-to-plate imprint system for achieving a thin and uniform film height. Moreover, it can directly be used to determine the film height as a function of the process parameters, machine parameters, and material properties. This information can help in optimising the required amount of dispensed

resin for a specific imprint or in tuning the process parameters for realising a desired film height. The simulated film heights can be converted to the cured flat layer thickness by taking into account the volumetric shrinkage ratio of the UV-curable resin. The present study is focused on the application of roll-to-plate nanoimprinting, but the model may be useful for the analysis of any EHL process which involves tensioned webs or foils, such as forward roll coating of flexible substrates or printing of paper.

3.5 EHL survey diagrams

This chapter presented a detailed description of the numerical model to simulate the elastohydrodynamic lubrication of soft-layered rollers with tensioned webs. This model can be used to simulate the film height and pressure profiles in the lubricated roller contact and to predict the final film height in roll-to-plate nanoimprinting.

Generally, in EHL studies, one is mostly interested in the minimum or Couette film height in the lubricated contact. The minimum film height height can be compared to the critical film height to ensure proper lubrication. Besides numerical EHL models, which can become very complex, survey diagrams or rules of thumb can be applied to quickly assess the film height of interest. The survey diagrams are based on analytical curve fits and non-dimensional similarity groups.

In this technical note, which is an addition to the original publication, a brief overview of existing survey diagrams for EHL and soft-layered EHL is presented. The latter is also compared to results from the developed soft-layered EHL model in this chapter. Moreover, the experimental results from this chapter are presented in a similar format. It is shown that experimental curve fits can be determined, based on the non-dimensional similarity groups, to quickly predict the film height in roll-to-plate nanoimprinting.

3.5.1 The Delft diagram: a survey diagram for EHL

The analytical curve fits to predict the minimum or Couette film height in an EHL contact are based on non-dimensional similarity groups. The idea behind these similarity groups is to efficiently combine the relevant EHL parameters in non-dimensional parameter groups to minimize the number of parameters that describe the problem. Various non-dimensional similarity groups have been derived in the past by Dowson and Higginson [107, 108], Blok and Moes [59, 109], and Johnson [110], among others. A comprehensive overview of these non-dimensional similarity groups is presented by Marian [104]. Here, we limit ourselves to the similarity groups as derived by Blok and Moes, as they provide the minimum number of non-dimensional parameter groups. The derivation of these similarity groups is well explained by Van Leeuwen [109]. The similarity groups for

Section 3.5 on "EHL survey diagrams" is an addition to the original publication and was partly presented as: Snieder, J., & van Ostayen, R. A. J. (2021, May 27-28). *Simulating the layer thickness in roll-to-plate nanoimprint lithography* [conference presentation]. 7th International Conference on Polymer Replication on Nanoscale (virtual), Windisch, Switzerland.

an infinite EHL line contact read as follows [59]:

$$\begin{aligned} M &= \frac{F_L}{E'R}\left(\frac{E'R}{\eta u_\Sigma}\right)^{\frac{1}{2}}, \quad H_M = \frac{h_M}{R}\left(\frac{E'R}{\eta u_\Sigma}\right)^{\frac{1}{2}}, \\ L &= \alpha E'\left(\frac{\eta u_\Sigma}{E'R}\right)^{\frac{1}{4}}, \quad H_C = \frac{h_C}{R}\left(\frac{E'R}{\eta u_\Sigma}\right)^{\frac{1}{2}}, \end{aligned} \tag{3.21}$$

with the load per unit length F_L, viscosity at nominal pressure η, pressure viscosity coefficient α, minimum film height h_M and Couette film height h_C. Moreover, the effective radius R, effective surface velocity u_Σ and effective elastic modulus E' are defines as:

$$\frac{1}{R} = \frac{1}{R_1} + \frac{1}{R_2}, \quad u_\Sigma = u_1 + u_2, \quad \frac{2}{E'} = \frac{1-\nu_1^2}{E_1} + \frac{1-\nu_2^2}{E_2}, \tag{3.22}$$

where E_1, E_2, ν_1, ν_2, R_1, and R_2 represent the elastic moduli, Poisson ratios and radii of the two surfaces of the EHL line contact, respectively. The non-dimensional number M, which is identical to the definition as presented in Equation 3.19, is named after the Swiss researcher Meldahl [109]. The viscosity variable L is a measure of the pressure dependent viscosity changes in the EHL contact and is probably referring to 'lubricant' [109]. The non-dimensional film heights H_M and H_C are a function of the non-dimensional numbers M and L:

$$\begin{aligned} H_M &= f_M(M,L) \\ H_C &= f_C(M,L) \end{aligned} \tag{3.23}$$

The final survey diagram, which is generally adopted as the Delft diagram, is composed of an analytical curve fit to numerical solutions. The complete solution is a based on asymptotic solutions of the different regimes within EHL: rigid-isoviscous, rigid-piezoviscous, elastic-isoviscous, and elastic-piezoviscous. For a full definition of the curve fit, the reader is referred to this publication from Moes [59].

The original Delft diagram for the minimum film height is shown in Figure 3.12. With regard to this dissertation, the isoviscous solution ($L = 0$), which is indicated by the dashed blue line, is of most interest. This solution starts at the rigid-isoviscous asymptote at low values of M, for which the amount of elastic deformation of the bounding surfaces is negligible. The solution approaches the elastic-isoviscous asymptote for increasing values of M. This asymptote corresponds to significant elastic deformation of the bounding surfaces. The film heights in soft-layered EHL line contacts will be smaller than predicted by the Delft diagram, due to the finite thickness of the elastomeric layer. The relevant solution domain is indicated by the light blue area, which will be discussed in the next section.

3.5.2 Survey diagram for soft-layered EHL

An analytical curve fit has also been developed for soft-layered EHL contacts by Moes [59]. Here, it is assumed that both surfaces of the soft-layered EHL contact are equipped with an incompressible, elastomeric layer of layer thickness b, which is bonded to a rigid substrate. The effective surface velocity u_Σ and effective radius R follow the same definition as in Equation 3.22, but the definition of the effective elastic modulus E is slightly different to

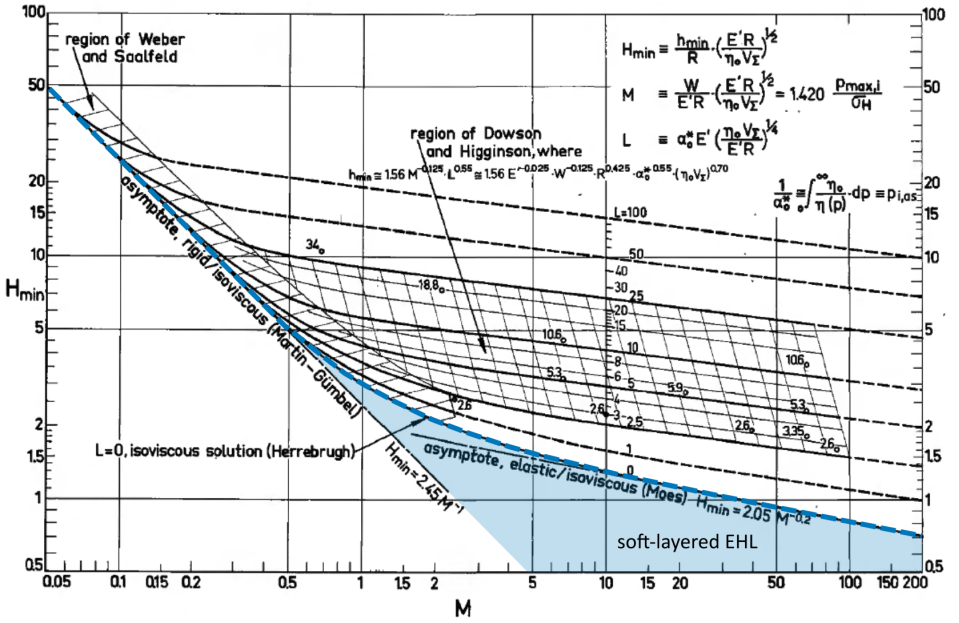

Figure 3.12: The Delft diagram: a survey diagram for the non-dimensional minimum film height in an EHL line contact.

the previous section:

$$b = b_1 = b_2, \quad \nu = \nu_1 = \nu_2, \quad \frac{1}{E} = \frac{1}{E_1} + \frac{1}{E_2}, \tag{3.24}$$

The similarity groups for an infinite soft-layered EHL line contact read as follows [59]:

$$\begin{aligned} M &= \frac{F_\mathrm{L}}{ER}\left(\frac{ER}{\eta u_\Sigma}\right)^{\frac{1}{2}}, \quad H_\mathrm{M} = \frac{h_\mathrm{M}}{R}\left(\frac{ER}{\eta u_\Sigma}\right)^{\frac{1}{2}}, \\ B &= \frac{b}{R}\left(\frac{ER}{\eta u_\Sigma}\right)^{\frac{1}{4}}, \quad H_\mathrm{C} = \frac{h_\mathrm{C}}{R}\left(\frac{ER}{\eta u_\Sigma}\right)^{\frac{1}{2}}, \end{aligned} \tag{3.25}$$

The non-dimensional number M is similar to Equation 3.21, except for the different definitions for the effective elastic modulus E and E'. The non-dimensional number B is a measure of the influence of the elastomeric layer thickness. Similar to the survey diagram for EHL contacts, the non-dimensional film heights H_M and H_C are a function of the non-dimensional numbers M and B:

$$\begin{aligned} H_\mathrm{M} &= f_\mathrm{M}(M, B) \\ H_\mathrm{C} &= f_\mathrm{C}(M, B) \end{aligned} \tag{3.26}$$

The complete solution of the analytical curve fit for soft-layered EHL contacts is given by:

$$H = \left(\left(H_{\mathrm{B}}^{-4/3} + H_{\mathrm{E}}^{-4/3} \right)^{-7/4} + H_{\mathrm{R}}^{7/3} \right)^{3/7}. \tag{3.27}$$

It is based on the three asymptotic solutions H_{R}, H_{E}, and H_{B}, which are defined by:

$$\begin{aligned} H_{\mathrm{R}} &= C_{\mathrm{R}} \cdot M^{-1}, & C_{\mathrm{R}} &= 3, \\ H_{\mathrm{E}} &= C_{\mathrm{E}} \cdot M^{-1/5}, & C_{\mathrm{E}} &= 1.77047, \\ H_{\mathrm{B}} &= C_{\mathrm{B}} \cdot M^{-3/10} \cdot B^{3/5}, & C_{\mathrm{B}} &= 1.46275. \end{aligned} \tag{3.28}$$

The constants C_{R}, C_{E}, and C_{B} can be determined by hand calculation and vary for H_{M} and H_{C}. The coefficients presented above apply for the Couette film height H_{C}. For the derivation of these constants, the reader is referred to Moes [59].

The powers in Equation 3.27 provide the smooth transitions between the asymptotic solutions. The asymptotic solution H_{R}, which applies for $M \longrightarrow 0$ and $B \longrightarrow 0$, corresponds to the rigid-isoviscous asymptote in Figure 3.12. The asymptotic solution H_{E}, which applies to $M \longrightarrow \infty$ and $B \longrightarrow \infty$ corresponds to the elastic-isoviscous asymptote in Figure 3.12. It must be noted that a transformation is required because of the different definitions for the effective elastic moduli E and E'. Overall, an accuracy of 10% can be expected, according to Moes [59].

The numerical model as developed in this chapter is also used to compute the final film height for a variation of the non-dimensional numbers M and B. The input parameters as listed in Table 3.3 define the starting point of the numerical model. A few modifications are required to mimic the problem definition of the analytical curve fits for soft-layered solids. First, the bending stiffness of the tensioned web is equal to zero ($D = 0$) and the web tension is set to a very low value (i.e., $T = 1\,\mathrm{N\,m^{-1}}$). Next, the Poisson ratio is equal to 0.49, to approach an incompressible material, and the elastic modulus of the elastomeric layer is halved to follow the problem definition in Equation 3.24. The non-dimensional number M is varied by changing the load per unit length F_{L}, while the non-dimensional number B is varied by changing the elastomeric layer thickness d. The results are scaled using the scaling in Equation 3.25.

The results of the analytical curve fit for the Couette film height H_{C} in soft-layered EHL and the results of the final film height H_{F} from the numerical model are shown in Figure 3.13. The solutions are found in between the rigid-isoviscous and elastic-isoviscous asymptotic solutions. This area corresponds to the light blue area in Figure 3.12. Given the very different nature of the derivation of the analytical curve fits and the underlying assumptions, the results of the numerical model and the analytical curve fits agree reasonably well.

Next, the experimental film heights from this chapter are scaled using the non-dimensional scaling in Equation 3.25. The results are shown in Figure 3.14. The non-dimensional film heights can also be found in between the rigid-isoviscous and elastic-isoviscous solutions, as expected. Three different measurement sets can be identified. These are based on the tensioned web, which has been used in the experiment, as listed in Table 3.2.

For each measurement set, an experimental curve is determined. These curve fits are defined as follows:

$$H = c_1 M^{c_2}, \tag{3.29}$$

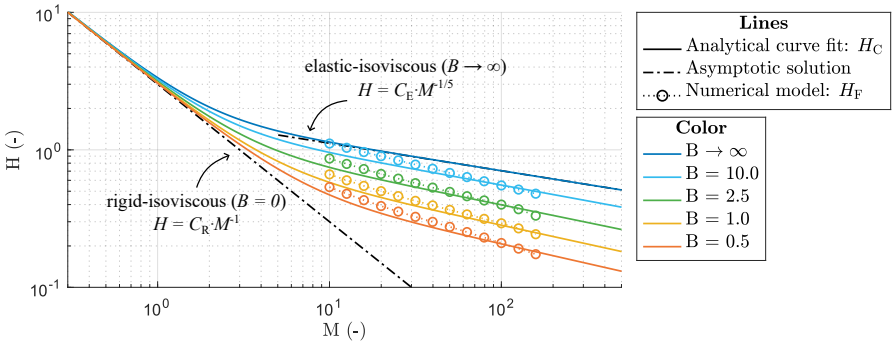

Figure 3.13: Survey diagram for soft-layered EHL contacts. The diagram shows the analytical curve fit and the results from the numerical model.

in which c_1 and c_2 are constants to be fitted. The values lie in between those for the rigid-isoviscous and elastic-isoviscous asymptotic solutions in Equation 3.28: c_1 between C_R and C_E, and c_2 between -1 and -1/5. When writing out this equation in the dimensional form, using the scaling as presented in Equation 3.25, the following expression is obtained:

$$h = c_1 \left(\eta u_\Sigma R\right)^{\frac{1-c_2}{2}} \left(\overline{F_L}\right)^{c_2} \left(E'\right)^{\frac{-c_2-1}{2}}. \tag{3.30}$$

These experimental curve fits, which are based on the non-dimensional similarity groups, can be used to quickly predict the film height in roll-to-plate nanoimprinting, as a function of the process parameters (velocity, viscosity, load).

Overall, the numerical and experimental results comply well with the analytical curve fits for soft-layered EHL contacts. The experimental results in the soft-layered EHL survey diagram strongly suggest the introduction of a new non-dimensional similarity group which represents the influence of the bending stiffness and web tension of the tensioned webs. This new similarity group can be used to define new analytical curve fits to quickly asses the film height in (soft-layered) EHL contacts with tensioned webs.

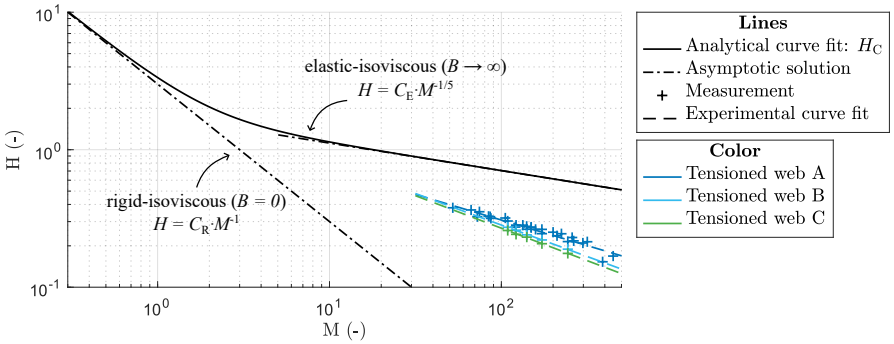

Figure 3.14: Survey diagram for soft-layered EHL contacts. The diagram shows the scaled experimental film heights for different tensioned webs and the corresponding experimental curve fits.

4

EHL of roll-to-plate nanoimprinting on wavy substrates

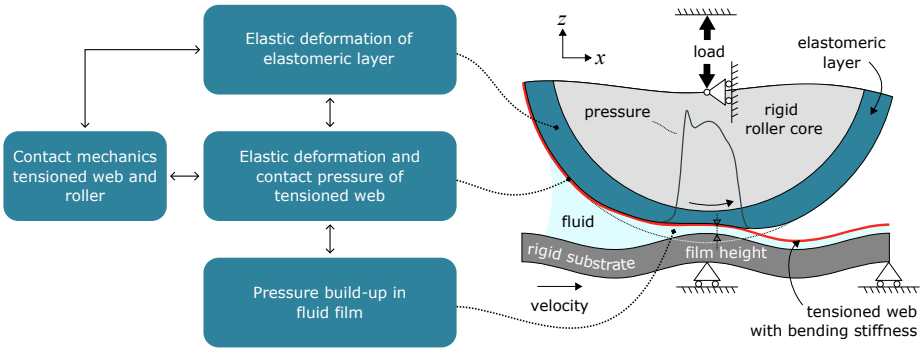

The previous chapter presented the development of an improved and extended version of the EHL model of Chapter 2. In this model, the rigid substrate in the EHL model was assumed to be completely flat. In reality, the substrates show a certain non-flatness. This chapter presents a case study in which the EHL model is used to study the influence of substrate waviness on the film height.

This chapter was published as:
Snieder, J., & van Ostayen, R. A. J. (2023). *Elastohydrodynamics of roll-to-plate nanoimprinting on non-flat substrates.* Papers and Presentations from the COMSOL Conference 2023. Comsol Conference 2023, Munich.

Elastohydrodynamics of roll-to-plate nanoimprinting on non-flat substrates

Abstract *Roll-to-plate nanoimprinting is a replication technology to texture large-area substrates with UV-curable resins. A small and uniform film thickness is essential for many applications. Substrate non-flatness or waviness can cause undesired film thickness variations. The film thickness is a result of the hydrodynamic forces in the resin and the elastic forces of the flexible stamp and the elastomeric layer around the imprint roller. They combine into an elastohydrodynamic lubrication (EHL) system. This work presents an EHL model to study the film height on non-flat substrates. The numerical model is an extension of previous work. The substrate non-flatness is approximated with a cosine wave with a certain amplitude and wavelength. The results indicate that waviness of the substrate can have a significant impact on the film height. The variation of the film height will be most severe for large amplitude and a small wavelength substrate waviness.*

4.1 Introduction

Roll-to-plate nanoimprinting is a manufacturing method to replicate micro- and nanotextures on large-area substrates with UV-curable resins [37]. The nanoimprinted textures can enhance the functionality of the substrate in several ways by altering its optical or mechanical properties, such as anti-reflection or light-trapping surface layers for solar panels and displays [26, 27], hydrophobic/oleophobic layers for self-cleaning or anti-fouling surfaces [33], and many more [44]. Figure 4.1 illustrates the Morphotonics roll-to-plate imprint process, which is considered in this study. It employs multiple rollers to both imprint and guide a textured, flexible stamp. A relatively soft, elastomeric layer surrounds the roller core to ensure conformal contact with the substrate. The imprint roller, positioned at the middle left, presses the flexible stamp into the UV-curable resin droplets. The droplets merge into a thin layer, which is solidified by UV-light. Upon delamination of the stamp, a negative of the textured pattern remains on the substrate. The final imprint consists of the desired texture on top of a residual layer, which ideally exhibits a small and uniform thickness across the entire substrate area. Typical film heights have a micrometer order of magnitude, but this can even be smaller.

Numerical simulation of the imprint process can assist in improving the predictability and uniformity of the film height. The film height is governed by the interaction of the hydrodynamic forces in the resin and the elastic forces of the flexible stamp and the elastomeric layer around the imprint roller. The physics and couplings are described by elastohydrodynamic lubrication (EHL) theory. In previous work, we developed an EHL model to study the film height as a function of the imprint process parameters [106]. The numerical model was experimentally validated and good agreement has been found be-

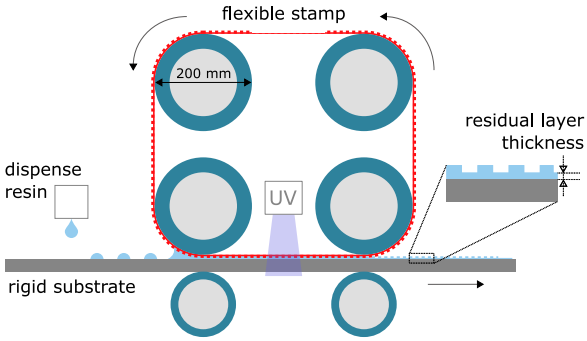

Figure 4.1: Schematic of the Morphotonics roll-to-plate imprint process. Reproduced and modified with permission from [106].

tween the results from simulation and experiment. However, the numerical model is only valid for flat substrates. In reality, the substrates are never perfectly flat. Substrate waviness will modify the roller contact zone, and hereby the pressure and film height profiles. Especially heat-treated or tempered glass substrates, which are used for solar panel production, can show significant substrate waviness. The local warp of rectangular substrates must not exceed 1.6 mm over any 300 mm span [54].

This work presents a numerical model to describe the physics of the roll-to-plate imprint process. The model is based on the previously developed EHL model and extended with substrate waviness. A detailed description of the implementation in COMSOL Multiphysics® is given [91]. The extended model can be used to study the impact of varying substrate waviness on the final film height.

4.2 Methods

This section presents the model description with the governing equations and numerical implementation in COMSOL Multiphysics® to solve the EHL problem. The model is an extension of previous work [106], which is based on the model set-up presented by Habchi [85]. For sake of completeness, the modelling approach is summarized here as well, including modifications to take into account the substrate waviness.

4.2.1 Model description

A cross-section of the imprint roller can be seen on the top right of Figure 4.2. Typical parameter values are listed in Table 4.1. The roller with radius R is pressed onto the rigid, wavy substrate with an effective load F_L per unit length in z-direction. The waviness of the substrate is defined by a cosine function with amplitude a_s, wavelength λ_s, and phase shift phi_s. The flexible stamp, which is treated as a tensioned web with distributed web tension force T and distributed bending stiffness D, is assumed to be smooth and any textures are neglected in this study. It is partly wrapped around the roller and applies a contact pressure p_c onto the elastomeric layer with thickness d. Downstream the roller contact, the tensioned web loses contact with the roller and the gap g is formed. The roller/web and substrate are moving with an equal surface velocity of u_1 and u_2, respectively. They

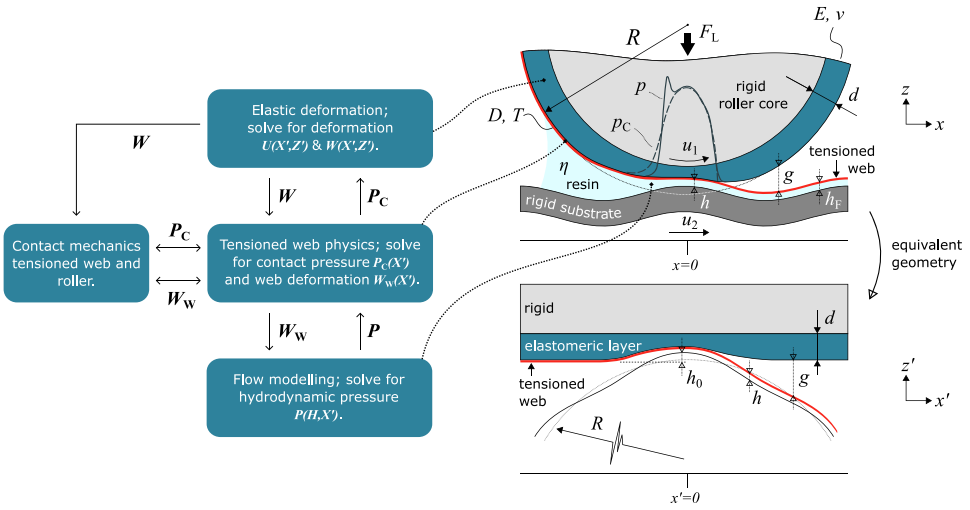

Figure 4.2: Left: physics of the EHL model and couplings between them. Top right: schematic of the imprint roller including parameters. Bottom right: equivalent geometry of the imprint roller. Reproduced and modified with permission from [106].

are separated by a thin film of resin with viscosity η and film height h. The film height of interest is the final layer height h_f. The hydrodynamic pressure build-up p is applied onto the tensioned web surface. Because the contact width is relatively small compared to the roller radius, a simplified equivalent geometry can be used, as shown on the bottom right in Figure 4.2. The elastomeric layer is unwrapped from the roller core and a rigid roller with a wavy surface around the nominal radius R is pressed into its surface. The equivalent geometry is described in a new coordinate system; the coordinates tangential and normal to the roller surface are represented by x' and z', respectively.

Table 4.1: Input parameters used for numerical model.

Parameter	Value	Unit
F_L	2000	$\mathrm{N\,m^{-1}}$
η	100	mPa s
R	100	mm
E	3	MPa
ν	0.45	-
u_1 & u_2	10.6	$\mathrm{mm\,s^{-1}}$
d	9.9	mm
D	0.01	N m
T	464.3	$\mathrm{N\,m^{-1}}$

The model is governed by five main equations, which are solved simultaneously; the linear elasticity equations, Reynolds equation, large-deflection bending of thin plates equa-

tion, the Fischer–Burmeister constraint function used to determine the contact between roller and stamp, and a load balance equation. They are shown on the left in Figure 4.2, including the couplings between them. A quasi-static solution procedure is employed, which is valid even for a varying substrate curvature, given the slow nature of the nanoimprint process. The model is written in dimensionless form. The following dimensionless variables are used in the description of the equations:

$$\begin{aligned} P &= \frac{p}{p_\mathrm{h}}, & P_\mathrm{c} &= \frac{p_\mathrm{c}}{p_\mathrm{h}}, & W_\mathrm{w} &= \frac{w_\mathrm{w} R}{a_\mathrm{h}^2}, \\ U &= \frac{uR}{a_\mathrm{h}^2}, & W &= \frac{wR}{a_\mathrm{h}^2}, & A_\mathrm{s} &= \frac{a_\mathrm{s} R}{a_\mathrm{h}^2}, \\ G &= \frac{gR}{a_\mathrm{h}^2}, & H &= \frac{hR}{a_\mathrm{h}^2}, & \Lambda_\mathrm{s} &= \frac{\lambda_\mathrm{s}}{a_\mathrm{h}}, \\ X' &= \frac{x'}{a_\mathrm{h}}, & Z' &= \frac{z'}{d}, & \Phi_\mathrm{s} &= \frac{\phi_\mathrm{s}}{a_\mathrm{h}}, \\ K &= R\kappa, \end{aligned} \tag{4.1}$$

with the dimensionless hydrodynamic pressure P, contact pressure P_C, elastic deformation of the tensioned web W_w, elastic deformation components U and W of the elastomeric layer, substrate waviness amplitude A_s, gap G, film height H, substrate waviness wavelength Λ_s, spatial coordinates X' and Z', substrate waviness phase shift Φ_s, and tensioned web curvature K. The Hertz dry contact half-width a_h and peak pressure p_h for a line contact are used for scaling. These are based on the mechanical properties of the elastomeric layer:

$$\begin{aligned} a_\mathrm{h} &= \sqrt{\frac{8 F_\mathrm{L} R}{\pi E'}}, \\ p_\mathrm{h} &= \frac{2 F_\mathrm{L}}{\pi a_\mathrm{h}}, \end{aligned} \tag{4.2}$$

It is assumed all deformation occurs in the relatively soft elastomeric layer, so the effective elastic modulus E' is given by:

$$\frac{2}{E'} = \frac{1-\nu^2}{E}, \tag{4.3}$$

with Poisson ratio ν and elastic modulus E. The equations are applied on the computational domain in Figure 4.3. It has a dimensionless length of 20 and dimensionless height of 1. The roller center is located at $X' = 0$.

The elastic deformation of the elastomeric layer is determined via the dimensionless linear elasticity equations, which are given by:

$$\begin{aligned} \frac{\partial}{\partial X'}\left[\left(\lambda+2\mu\right)\frac{d}{a_\mathrm{h}}\frac{\partial U}{\partial X'} + \lambda\frac{\partial W}{\partial Z'}\right] + \frac{\partial}{\partial Z'}\left[\mu\left(\frac{a_\mathrm{h}}{d}\frac{\partial U}{\partial Z'} + \frac{\partial W}{\partial X'}\right)\right] &= 0, \\ \frac{\partial}{\partial X'}\left[\mu\left(\frac{\partial U}{\partial Z'} + \frac{d}{a_\mathrm{h}}\frac{\partial W}{\partial X'}\right)\right] + \frac{\partial}{\partial Z'}\left[\lambda\frac{\partial U}{\partial X'} + \left(\lambda+2\mu\right)\frac{a_\mathrm{h}}{d}\frac{\partial W}{\partial Z'}\right] &= 0, \end{aligned} \tag{4.4}$$

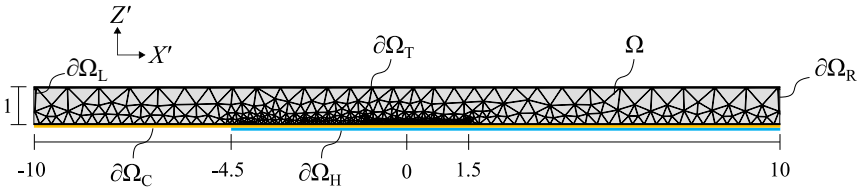

Figure 4.3: Dimensionless computational domain and mesh. Reproduced and modified with permission from [106].

The parameters λ and μ represent the Lamé parameters, which are defined by:

$$\begin{aligned} \lambda &= \frac{\nu E_{\mathrm{eq}}}{(1-2\nu)(1+\nu)}, \\ \mu &= \frac{E_{\mathrm{eq}}}{2(1+\nu)}, \end{aligned} \tag{4.5}$$

with the equivalent elastic modulus of the elastomeric layer [98]:

$$E_{\mathrm{eq}} = E\frac{a_{\mathrm{h}}}{Rp_{\mathrm{h}}}. \tag{4.6}$$

The equations are applied on domain Ω in Figure 4.3 and the contact pressure P_{c} is applied on domain boundary $\partial\Omega_{\mathrm{C}}$, using these boundary conditions:

$$\begin{cases} U = W = 0 & \text{on } \partial\Omega_{\mathrm{T}}, \\ U = 0 & \text{on } \partial\Omega_{\mathrm{L}} \text{ and } \partial\Omega_{\mathrm{R}}, \\ \sigma_n = P_{\mathrm{c}} & \text{on } \Omega_{\mathrm{C}}, \\ \sigma_n = \sigma_t = 0 & \text{elsewhere.} \end{cases} \tag{4.7}$$

The parameters σ_n and σ_t are the normal and tangential stress tensor components, respectively.

The resin flow between the tensioned web and the substrate is described by lubrication theory. The pressure build-up in the thin film of resin is determined with the dimensionless, incompressible, steady-state Reynolds equation in 1D [56]:

$$\frac{\partial}{\partial X'}\left(-\frac{a_{\mathrm{h}}^3 p_{\mathrm{h}}}{12R^2\eta(u_1+u_2)}H^3\frac{\partial P}{\partial X'}+\frac{H}{2}\right)=0. \tag{4.8}$$

The Reynolds equation is applied on domain boundary $\partial\Omega_{\mathrm{H}}$. The following boundary conditions are applied:

$$\begin{cases} P = 0 & \text{at } X' = -4.5, \\ \dfrac{\partial P}{\partial X'} = \dfrac{H}{2} & \text{at } X' = 10. \end{cases} \tag{4.9}$$

In contrast to previous work [106], the Neumann boundary condition at the right domain boundary describes a continuation of the resin flow via the convection term in the

Reynolds equation. The dimensionless film height is described by the difference between the surfaces of the tensioned web and substrate, which now shows a non-flatness:

$$\begin{aligned} H &= H_0 + H_\mathrm{w} + W_\mathrm{w} - H_\mathrm{sub}, \\ H_\mathrm{w} &= \begin{cases} \frac{X'^2}{2} & \text{for } X' \le 0, \\ 0 & \text{for } X' > 0, \end{cases} \\ H_\mathrm{sub} &= A_\mathrm{s} \cos\left(\frac{2\pi}{\Lambda_\mathrm{s}} (X' - \Phi_\mathrm{s})\right). \end{aligned} \tag{4.10}$$

The constant H_0 represents the offset or roller engagement, as indicated in Figure 4.2. It will be determined with the load balance equation.

The tensioned web is characterized by its initial shape H_w and its elastic deformation W_w, which follows from Equation (4.12). The web partly follows the roller surface, which is approximated with a parabolic function. The waviness of the substrate surface is described by a cosine function. By varying the phase shift Φ_s, the motion of the substrate can be simulated in a quasi-static manner. Moreover, it is assumed that the resin can handle small negative pressures and cavitation is not included [106]. The film height between the roller surface and substrate is also defined:

$$H_\mathrm{roller} = H_0 + \frac{X'^2}{2} + W - H_\mathrm{sub} \tag{4.11}$$

The elastic deformation of the tensioned web is determined with the Föppl–von Kármán equations, which describe the large-deflection bending of thin plates under tension and pressure [100]:

$$\left(-\frac{D}{{a_\mathrm{h}}^2 p_\mathrm{h} R}\right) \frac{\partial^2 K}{\partial X'^2} + \left(\frac{T}{p_\mathrm{h} R}\right) K + P_\mathrm{n} = 0. \tag{4.12}$$

The normal pressure P_n is defined by the difference between the hydrodynamic pressure and the contact pressure, which are both acting on the web: $P_\mathrm{n} = P - P_\mathrm{c}$. The web curvature K is approximated by the second spatial derivative of the web shape:

$$\begin{aligned} K &= \frac{\partial^2}{\partial X'^2} \left(H_\mathrm{w} + W_\mathrm{w}\right) \\ &= \begin{cases} 1 + \frac{\partial^2 W_\mathrm{w}}{\partial X'^2} & \text{for } X' \le 0, \\ \frac{\partial^2 W_\mathrm{w}}{\partial X'^2} & \text{for } X' > 0. \end{cases} \end{aligned} \tag{4.13}$$

The bending stiffness of the tensioned web is defined by its thickness t, elastic modulus E_w, and Poisson's ratio ν_w:

$$D = \frac{E_\mathrm{w} t^3}{12\left(1 - \nu_\mathrm{w}^2\right)} \tag{4.14}$$

Equation (4.12) and Equation (4.13) are applied on domain boundary $\partial\Omega_C$. Due to the presence of substrate waviness, the boundary conditions at the right side of the domain at $X' = 10$ will be defined explicitly. It is assumed that the tensioned web will adopt the substrate direction and curvature on this location.

$$\begin{aligned}\left.\frac{\partial W_w}{\partial X'}\right|_{X'=10} &= \left.\frac{\partial H_{sub}}{\partial X'}\right|_{X'=10} = -A_s\left(\frac{2\pi}{\Lambda_s}\right)\sin\left(\frac{2\pi}{\Lambda_s}(X'-\Phi_s)\right)\Bigg|_{X'=10},\\ \left.\frac{\partial K}{\partial X'}\right|_{X'=10} &= \left.\frac{\partial^3 H_{sub}}{\partial X'^3}\right|_{X'=10} = A_s\left(\frac{2\pi}{\Lambda_s}\right)^3\sin\left(\frac{2\pi}{\Lambda_s}(X'-\Phi_s)\right)\Bigg|_{X'=10}.\end{aligned} \tag{4.15}$$

The contact mechanics between the tensioned web and the roller surface are described by the contact pressure P_c and the gap G, which can be combined in a complementarity condition. A contact pressure will be present when the gap is zero. And vice versa, if the contact pressure is zero, the gap will be larger than zero:

$$\begin{aligned}P_c \geq 0 \quad &\text{and} \quad G = 0,\\ P_c = 0 \quad &\text{and} \quad G \geq 0.\end{aligned} \tag{4.16}$$

The gap is defined by:

$$\begin{aligned}G &= G_0 + W - W_w,\\ G_0 &= \begin{cases}0 & \text{for } X' \leq 0,\\ \frac{X'^2}{2} & \text{for } X' > 0.\end{cases}\end{aligned} \tag{4.17}$$

The term G_0 is the initial gap between the web and roller. It increases with the approximated roller shape for $X' > 0$. The complementarity condition is solved by a Fischer–Burmeister constraint function, which is applied on domain boundary $\partial\Omega_C$ [89]:

$$P_c + G - \sqrt{P_c^2 + G^2} = 0. \tag{4.18}$$

The hydrodynamic pressure build-up must be in equilibrium with the applied effective load. The dimensionless load balance equation is given by:

$$\int_{\Omega_H} P\,\mathrm{d}X' = \frac{\pi}{2}. \tag{4.19}$$

This equation is satisfied by adjusting the offset H_0 in the definition of the film height.

4.2.2 Implementation in COMSOL Multiphysics®

The equations combine into an EHL model, which is implemented in COMSOL Multiphysics®. They are applied on different parts of the computational domain in Figure 4.3, as specified in the previous section. The computational domain also shows the mesh, of which the size varies over the lower domain boundary, see Table 4.2. A *free triangular mesh* is employed in domain Ω. The mesh is refined near the center, where the largest pressure and film height gradients will be present. In contrast to previous work, the boundary with

Table 4.2: Mesh settings.

Domain/boundary	Location	Mesh size
Ω	entire domain	coarser
$\partial\Omega_C$	$-10 < X' < -4.5$	max. 0.3
$\partial\Omega_C$	$1.5 < X' < 10$	max. 0.3
$\partial\Omega_C$	$-4.5 < X' < -1$	max. 0.1
$\partial\Omega_C$	$-1 < X' < 0.5$	max. 0.02
$\partial\Omega_C$	$0.5 < X' < 1.5$	max. 0.01

the finest mesh is extended because the location of the pressure and film height profiles will slightly vary, due to the substrate waviness.

The linear elasticity equations in Equation (4.4) are implemented via the *Weak Form PDE interface* with the elastic deformation components U and W as dependent variables [111]. The boundary conditions are added via two *Dirichlet Boundary Conditions* and the contact pressure is implemented via a *Boundary Flux/Source term*. The equations are discretized with third-order (cubic) elements. The initial solution for the elastic deformation is determined by applying the dimensionless Hertz pressure distribution on the contact domain boundary:

$$P_{\text{initial}} = \begin{cases} \sqrt{(1-X'^2)} & \text{for } -1 \le X' \le 1, \\ 0 & \text{elsewhere.} \end{cases} \tag{4.20}$$

The Reynolds equation in Equation (4.8) is implemented via the *General Form Boundary PDE interface*. The dependent variable is the hydrodynamic pressure P. The left boundary condition at $X' = -4.5$ is implemented via a *Dirichlet Boundary Condition* while the right boundary condition at $X' = 10$ is implemented via a *Flux/Source node*. Second-order (quadratic) elements are used for discretization. The hydrodynamic pressure is initialized with the dimensionless Hertz pressure distribution. The load balance is added via a *Global Equation*, which solves for the film height offset H_0. The initial value is set to a small positive number, to ensure a feasible starting point for the solver.

The large-deflection bending of thin plates equations in Equation (4.12) and (4.13) and the Fischer–Burmeister constraint function in Equation (4.18) are implemented together via another *General Form Boundary PDE interface*, with dependent variables W_w, K, and P_c. Because of the nested fourth order spatial derivative in Equation (4.12), the implementation is achieved via two second order PDEs. The boundary conditions for the large-deflection bending of thin plates equations are implemented via a *Flux/Source* term. The equations are discretized with third-order (cubic) elements, and the curvature K is initialized with the dimensionless roller curvature:

$$K = \begin{cases} 1 & \text{for } X' \le 0, \\ 0 & \text{for } X' > 0. \end{cases} \tag{4.21}$$

The set of equations are solved in a fully-coupled manner in Comsol Multiphysics® using two stationary study steps. The first study step is only involved with the calcula-

tion of the elastic deformation of the elastomeric layer, which follows from applying the dimensionless Hertz pressure distribution on the contact domain boundary. The result is used as initial solution in the secondary study step. The model is then iteratively solved until convergence. The final film height H_f is evaluated at the end of the domain boundary $\partial\Omega_H$ at $X' = 10$.

4.3 Results and discussion

The numerical model is solved for the input parameters in Table 4.1 and a variation of the substrate waviness parameters. These are benchmarked at a dimensionless amplitude A_s of 1 and a dimensionless wavelength Λ_s of 15, which correspond to a dimensional value of 0.68 mm and 123 mm, respectively. The phase shift Φ_s is varied as a fraction of the wavelength, hereby effectively moving the wavy substrate underneath the roller and web. Figure 4.4 shows the simulated height profiles of the roller, tensioned web and substrate on (non-)flat substrates for a variation of the phase shift. The phase shift of $\Phi_s = 0$ and $\Phi_s = \Lambda_s/2$ correspond to a peak or valley at the roller center, respectively. The actual film heights H, which are defined as the distance between the tensioned web and substrate surface, are too small to distinguish. The figure clearly shows that the tensioned web follows the roller surface up to the outlet, after which it moves along with the substrate surface and the roller surface diverges. Both roller and web deform conform to the substrate surface, which results in a modified contact zone. The presence of a peak at the roller center results in a reduced contact zone, while the presence of a valley at the roller center results in an increased contact zone, compared to the flat substrate case.

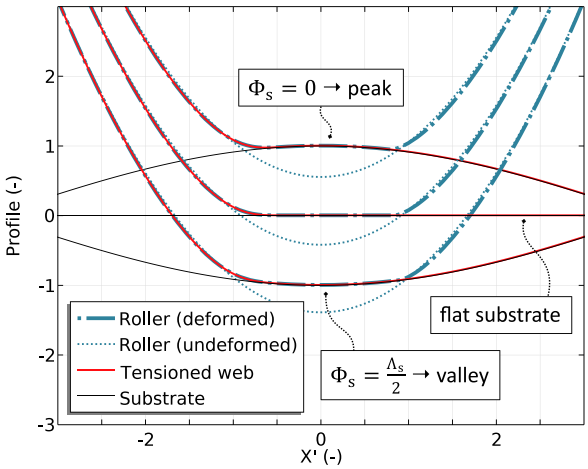

Figure 4.4: Height profiles of the roller, tensioned web and substrate on (non-)flat substrates for a variation of the phase shift ($\Phi_s = 0 \longrightarrow$ peak and $\Phi_s = \Lambda_s/2 \longrightarrow$ valley).

The actual film heights and corresponding pressure profiles are shown in Figure 4.5 to Figure 4.7. For a detailed explanation about the EHL behavior of the roll-to-plate imprint process with tensioned webs, the reader is referred to our previous publication [106]. The profiles on a flat substrate can be seen in Figure 4.5. The Hertz pressure and roller

height profile are shown for reference. In front of the contact zone, the tensioned web exerts a contact pressure on the roller surface. The hydrodynamic pressure is negligible in this region. Towards the roller center, both contact pressure and hydrodynamic pressure increase. The hydrodynamic pressure peak just before the roller center can be explained by the bending stiffness of the tensioned web, which causes the web to deform towards the substrate surface, hereby forming a constriction for the resin flow. After the roller center, the pressures decrease to ambient pressure. The corresponding film height profile decreases due to the converging roller surface, and stays more or less constant in the contact zone. The tensioned web follows the roller surface until the outlet, after which they lose contact. A uniform film height can be found, which represents the final film height H_f.

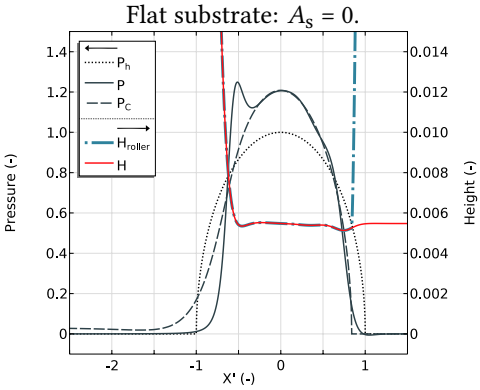

Figure 4.5: Pressure and film height profiles on a flat substrate surface.

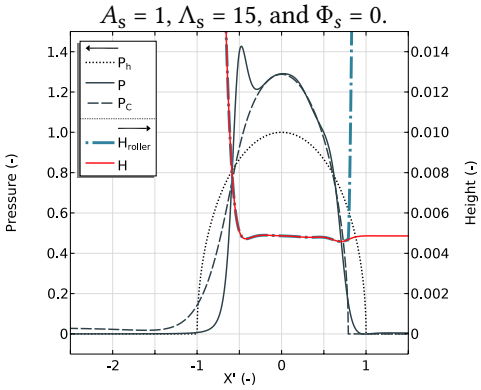

Figure 4.6: Pressure and film height profile on a non-flat substrate surface. A peak is located at the roller center.

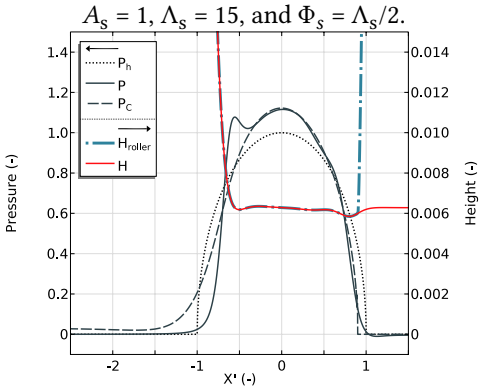

Figure 4.7: Pressure and film height profile on a non-flat substrate surface. A valley is located at the roller center.

Figure 4.6 shows the pressure and film height profiles on a non-flat substrate surface for a phase shift Φ_s equal to zero. The decreased contact area results in an increase of the pressure profiles and a decrease of the corresponding film height profiles, compared to the flat substrate scenario. Therefore, the final film height is smaller. The opposite is true for a phase shift Φ_s equal to $\Lambda_s/2$, which is shown in Figure 4.7. The contact area is increased, and as a result, the pressure profiles are decreased and the film height profiles are increased. The final film height is now larger compared to the value on a flat substrate.

The last study in Figure 4.8 presents the final film height for a variation of the substrate waviness amplitude, wavelength and phase shift. Dimensional values are presented, to give the reader a sense of the order of magnitude. The nominal film height on a flat substrate is equal to 3.71 µm. The top graph shows that the film height changes for a variation of the phase shift, which increases from zero to a full wavelength. A repetitive pattern can be recognized, which corresponds the results in Figure 4.6 and Figure 4.7. The final film height is smaller than nominal when the peak is located near the roller center, and larger than nominal when the valley is located near the roller center. The deviation increases for increasing substrate waviness amplitude. The figure at the bottom of Figure 4.8 shows the final film height for a variation of the wavelength. Again, the final film height is either smaller or larger compared to the nominal value, depending on the presence of a peak or valley at the location of the roller center. The deviation from the nominal value is largest for small wavelengths and large amplitude. The difference diminishes for increasing wavelength, when the contact width becomes negligibly small compared to the wavelength of the substrate waviness.

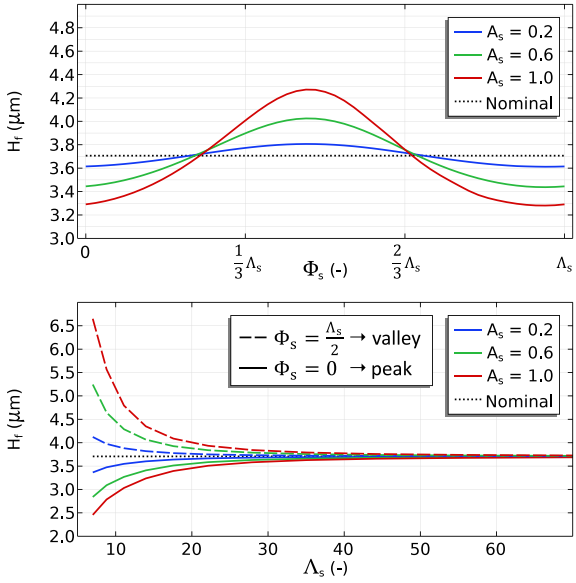

Figure 4.8: Top: final film height for a variation of substrate waviness amplitude and phase shift. Bottom: final film height for a variation of substrate waviness amplitude, phase shift ($\Phi_s = 0$ and $\Phi_s = \Lambda_s/2$), and wavelength.

4.4 Conclusion

A numerical EHL model, which is an extension of previous work, is developed to study the film height on non-flat substrates. The model combines several physics to describe the elastic deformation and contact mechanics of the elastomeric layer and tensioned web around the roller and the fluid flow of the thin film of resin between the tensioned web and the substrate. The results show that the substrate waviness can have a significant impact on the final film height. The deviation from the nominal case, which is defined as the film height on a flat substrate, is most severe for large amplitude and small wavelength substrate waviness. The numerical model can be used to study the influence of the process parameters on the final film height in the presence of substrate waviness. These insights can be used to design new imprint systems, to make them more robust to substrate waviness and to further improve the imprint quality.

II

Film height measurement

5

Analysis of ratiometric fluorescence imaging to measure the film height

There is a need for an efficient method to map the film height in elastohydrodynamic lubrication and fluid film lubrication in general. Ratiometric fluorescence imaging is an attractive measurement method because it offers the possibility to map the film height over large areas at once in a contactless manner. This chapter presents a novel analytical and experimental study of this measurement method. It is written with an audience of (mechanical) engineers in mind, and anyone else who is interested in utilizing the phenomenon of fluorescence for film height mapping. The goal is to provide an intuitive understanding of the working principle behind ratiometric fluorescence imaging, to assist and encourage the application of the measurement method for mapping the film height in fluid film lubrication.

This chapter is intended for publication in a tribology journal as:
Snieder, J., & van Ostayen, R. A. J. *Extended analytical model and experimental validation of the ratiometric fluorescence film height measurement method.* To be submitted.

Extended analytical model and experimental validation of the ratiometric fluorescence film height measurement method

Abstract *Ratiometric fluorescence imaging is an optical measurement method to map the fluid film height over large areas at once. The measurement method is based on the emission and reabsorption of two fluorophores, which are dissolved in the fluid. This paper presents a novel analytical model and experimental study of the measurement method for the fluorophores Fluorescein and Eosin Y. These fluorophores share a large spectral overlap between the emission spectrum of Fluorescein and the absorption spectrum of Eosin Y, which results in strong emission reabsorption. The original analytical model, as developed by Hidrovo and Hart [1], is extended with the emission and reabsorption of both fluorophores and the surface reflection of the background. The analytical and experimental results are in good agreement for a wide range of film heights, fluorophore concentrations and two different surface reflections. The results demonstrate that the surface reflectivity of the background has a significant influence on the measurement response. Moreover, the experimentally determined fluorescence spectra provide an intuitive understanding of the working principle behind the measurement method. The extended analytical model is an efficient design tool to tune or optimize the measurement response for the film height range of interest. It can be used to study any combination of fluorophores with the fluorophore spectral properties as input.*

5.1 Introduction

In fluid film lubrication, a thin fluid film is separated by two bounding surfaces [56]. Depending on the operating conditions and the material properties (load, velocity, viscosity, surface geometry, texturing, roughness, et cetera), the film height in the lubricated contact can range from a few nanometers up to a few hundreds of micrometers. Knowledge about the film height is essential for understanding and optimizing the lubrication mechanisms. Over the years, several methods have been developed to measure the film height in the lubricated contact. A distinction can be made based on the physics behind them:

- Electrical: resistive methods, capacitive methods.
- Electromagnetic radiation based / optical: optical interferometry, Raman spectroscopy, X-ray transmittance, ellipsometry, spectral reflectance [112], fluorescence.
- Acoustical: ultrasonic reflectance [113, 114].
- Mechanical: direct displacement.

This list of measurements methods is by no means complete. The reader is referred to the extensive literature reviews from Visscher [115], Spikes [116, 117], and Albahrani [118] for a detailed overview and description of the various measurement methods, which are applied to measure the film height of fluid films in sealing applications and elastohydrodynamic lubrication in general.

Most of these film height measurement methods are essentially a point-wise measurement. They are performed on a small measurement area, hereby only giving information of the local film height. Scanning of the contact zone is required to measure the film height over a line or over the full area. In that sense, fluorescence film height mapping, which is categorized as an optical measurement technique, is an attractive measurement method. It offers the possibility to measure the film height over a significantly larger area at once [1, 119, 120]. The working principle behind fluorescence and its use in film height mapping will be explained in detail in the next section.

5.1.1 Basics of fluorescence

Fluorescence is the process in which a fluorophore or fluorescent dye absorbs a photon at a specific wavelength (e.g. purple) and emits this photon at a longer, lower-energy wavelength (e.g. blue) [121, 122]. A well-known example is Quinine, which is found in tonic water. Its fluorescence was first reported by Sir John Frederick William Herschel in 1845 [123]. Figure 5.1 shows a glass of gin–tonic which is exposed to sunlight. The Quinine fluorophore is excited by the ultraviolet light from the sun. After absorption, the photons are emitted at a wavelength of about 450 nm, and a faint blue glow can be observed near the surface. Here, the presence of alcohol actually helps to reduce the dielectric constant to make the fluorescence more apparent [121]. The fluorescence becomes even better visible when the excitation light intensity is increased, as shown in Figure 5.2. Here, the fluorophore molecules in the tonic water are excited by a high-power, ultraviolet light source, which results in the ”beautiful celestial blue color” [123].

Figure 5.1: A glass of gin-tonic shows a faint blue color due to the fluorescence of Quinine [124].

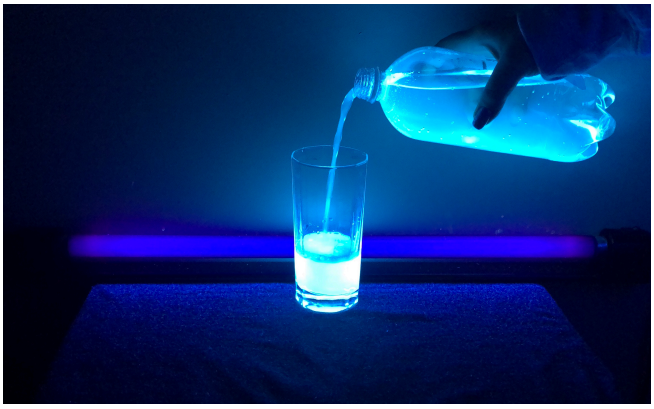

Figure 5.2: The fluorescence of Quinine in tonic water is increased by excitation with a high-power UV light source (vaguely visible by the purple bar in the background). Reproduced under the terms of the CC-BY license [125].

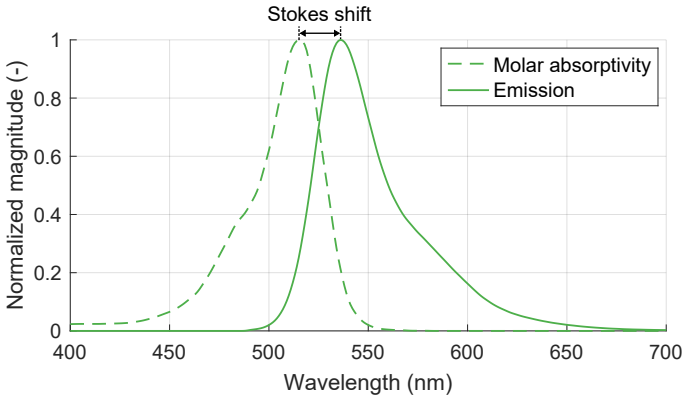

Figure 5.3: Normalized absorption and emission spectra of Eosin Y.

For a detailed explanation of the fluorescence process of absorption and emission of light, the reader is referred to the excellent explanation by Haugland [126] or Lakowicz [121]. In short, the fluorescence process is a three stage process: excitation, excited–state, and emission. After absorption of a photon, a fluorophore gets to a higher electronic energy level. In the excited–state, the energy level is decreased by internal conversions where energy is dissipated in a radiation-less manner. In the last step, the fluorophore returns to its initial energy level by emitting a photon. Due to the energy dissipation in the excited–state, the energy of the emitted photon is lower and therefore of a longer wavelength than the excitation photon. Typical fluorescence lifetimes, which are defined by the time difference between absorption and emission, are in the order of 10 ns. The efficiency of the fluorescence process is described by the quantum yield or efficiency, which is the ratio between the number of absorbed photons and the emitted photons.

The wavelength dependency of the fluorescence process is best described by the absorption and emission spectra. An example can be seen in Figure 5.3, which shows the normalized spectra of the fluorophore Eosin Y. The absorption spectrum describes the amount of photon absorption for each wavelength. In this case, the highest absorption occurs at a wavelength of 515 nm. After absorption, the photon is emitted at a longer wavelength. The probability of a photon emission at a specific wavelength is described by the emission spectrum. Here, the peak emission wavelength of Eosin Y is 537 nm. The emission wavelength is independent of the excitation wavelength. It only depends on the chemical structure of the fluorophore and its environment (solvent, temperature, et cetera). For many fluorophores, the emission spectrum is a mirror image of the absorption spectrum [121]. This is also the case for Eosin Y. The emission is spectrally red-shifted (towards higher wavelengths) relative to the absorption spectrum. The spectral red-shift is indicated by the Stokes shift [121, 127], which is defined as the wavelength difference between the maxima of the absorption and emission spectra. If the absorption and emission spectra of one or more fluorophores have a significant spectral overlap, the photons can get absorbed and emitted multiple times. This is referred to as fluorescence cascade.

Due to the distinction between the absorption and emission spectra, fluorescence is very suitable for optical investigations in fluorescence spectroscopy [121, 122]. The dif-

ference in wavelength between absorption and emission allows for separation of the (reflected) excitation light and the fluorescence light emitted by the fluorophores by using appropriate spectral filters. It is primarily used in biochemistry and medical technology to identify and locate specific substances. However, the fluorescence phenomenon can also be used as a quantitative tool in film height mapping.

5.1.2 Fluorescence for film height imaging

The fluorescence phenomenon can be utilized to measure the fluid film height. The fluorescence can originate from the fluid itself, but often one or more fluorescent dyes are dissolved in the fluid to increase the fluorescence intensity. A measurement setup typically contains a light source to excite the fluorophores and one or more cameras to image the area of interest. The measurement area depends on the optical design and the selection of optical components (zoom objectives, camera, et cetera). Spectral filters are used to measure the fluorescence emission at the wavelengths of interest and to block the excitation light. The result is a pixel-wise map of the film height.

In the most simple form, a natural or dissolved fluorophore is excited by a monochromatic light source (laser or LED). The emitted light intensity is proportional to the excitation light intensity, the spectral properties of the fluorophore, and the fluorophore concentration. As the emitted light intensity scales with the number of fluorophore molecules, it can be related to the film height. This method has been used to measure the film height of free surface liquid films using the natural fluorescence of the mineral oil [128]. In later studies, the method has been employed with fluorescent dyes to measure the film height in various applications: free surface liquid films [129], sealing applications [119], elastohydrodynamic contact [130, 131], open-channel flow and droplets [132], and many more. Calibration is always required to relate the fluorescence intensity to a film height. This is typically done by imaging a fluid film with a known film height distribution. Care must be taken to mimic the actual operating conditions as these can influence the measurement response. Especially the surface reflectivity can have a significant impact on the fluorescence intensity, as discussed by Poll [119] and Wittek [133].

The emitted fluorescence intensity is directly proportional to the excitation light intensity, which can fluctuate in time and space. Especially in the case of larger measurement areas, the light intensity is not uniform over the entire area. To eliminate this dependency, a ratiometric approach was suggested by Husen [134]. By measuring both the fluorescence intensity and the reflected excitation light intensity, using appropriate spectral filters, the ratio between the two signals can be determined. By taking the ratio, the influence of the excitation light intensity and its potential spatial and temporal variation is removed. The method requires a fluid film with negligible absorption to ensure that the excitation light intensity, which reflects from the background and is measured by the camera, has approximately the same intensity when entering the fluid film. Moreover, a diffuse-reflecting background (Lambertian) is required such that the intensity of the reflected excitation light is independent of the viewing angle.

An even more elegant ratiometric approach was proposed by Hidrovo and Hart [1] and is also used in this work. This method was originally presented as emission reabsorption laser-induced fluorescence (ERLIF) and was used to measure the fluid film height between two stationary quartz plates. Ratiometric fluorescence imaging employs two fluorescent

dyes, which are dissolved in the fluid. The method relies on the spectral overlap between the two fluorophores. Photons emitted by the first fluorophore can be reabsorbed by the other fluorophore before they leave the fluid film, and emitted at longer wavelengths. As a result, the emission of the first fluorophore in the spectral overlap region is lowered and the overall fluorescence emission shows a red-shift. The probability of reabsorption depends on the fluid film height. Thicker films result in longer photon travel paths and a higher probability of reabsorption. The amount of reabsorption and corresponding red-shift is measured by capturing the overall fluorescence emission at two small wavelength bands, using spectral filters. These are typically chosen around the peak emission wavelengths for the highest measurement sensitivity [120, 135]. The ratio between the two fluorescence emission intensities is a dimensionless measure of the film height. By taking the ratio, measurement errors due to optical distortions and variations in excitation light are minimized. Calibration is still required to find the relation between the ratio and the film height [1, 120, 135].

5.1.3 Approach in this work

In this work, the emission reabsorption ratiometric fluorescence imaging method with two fluorophores is theoretically and experimentally studied. This method will often be referred to as ratiometric fluorescence imaging. The fluorophores Fluorescein and Eosin Y are selected for the theoretical and experimental analyses. These fluorophores share a large spectral overlap between the emission spectrum of Fluorescein and the absorption spectrum of Eosin Y. Moreover, both fluorophores have been extensively studied for various applications and have well-documented fluorophore properties [136–138]. This makes them reliable for experimental design and reproducibility.

Hidrovo and Hart [1] presented an analytical model of the ratiometric fluorescence measurement method. The model was used to characterize and analyze the measurement method, but was not experimentally validated. Moreover, surface reflectivity of the background was neglected. In this work, the analytical model is adapted and extended to include the emission and reabsorption of both fluorophores and the influence of surface reflectivity of the background. The analytical model requires the fluorophores spectral properties as input. For the most accurate results and comparison with the experimental film height measurements, the fluorophore spectral properties are determined experimentally. Section 5.2 describes the experimental methods to determine these properties and the corresponding results.

This work also contains an experimental analysis of the ratiometric fluorescence imaging method. The experimental results ares used to demonstrate the working principle of the film height measurement method by presenting the overall fluorescence spectra of the fluid films for varying film heights and fluorophore concentrations. The measurement results are also used to experimentally validate the analytical model.

5.2 Fluorophore spectral properties

The excitation and emission spectra are measured in an Agilent Cary Eclipse spectrofluorometer. Fluorescein sodium salt[1] and Eosin Y disodium salt[2], are separately dissolved in deionized water at a concentration of 0.5 µmol L^{-1}. The pH-value is increased to about 10 with sodium hydroxide (NaOH). An alkaline environment gives the highest quantum yields and ensures excitation and emission spectra with well-defined peaks [137, 139]. The measurements are performed with an excitation and emission slit size of 5 nm. The emission spectra of Fluorescein and Eosin Y are determined for an excitation wavelength of 470 nm and 480 nm, respectively. The excitation spectra of Fluorescein and Eosin Y are determined for an emission wavelength of 555 nm and 590 nm, respectively. Before the spectra are measured, the system is zeroed using a blank solution of the solvent. The measured spectra are directly corrected for the inherent equipment sensitivity via the correction spectra, which are provided by the manufacturer. Each spectrum is measured 10 times and the average spectra are smoothed with a Gaussian filter with a window size of 5 data points. The resulting normalized excitation and emission spectra are shown in Figure 5.4. The peak excitation and emission wavelength of Fluorescein are 491 nm and 514 nm, respectively. Moreover, the peak excitation and emission wavelength of Eosin Y are 515 nm and 537 nm, respectively.

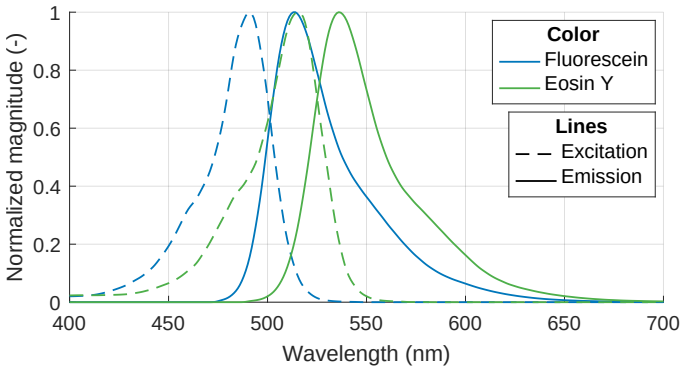

Figure 5.4: Normalized excitation and emission spectrum of Fluorescein and Eosin Y.

The absorption coefficients of the fluorophores are determined with a spectrophotometer (VWR UV-6300PC). Each fluorophore is dissolved at various concentrations in the same solvent as described above (deionized water with NaOH, pH of 10). Standard sized cuvettes with an optical path length of 10 mm are used. The absorption coefficients are determined with the Beer–Lambert law, which describes the attenuation of the intensity of radiation when passing through a homogeneous medium with which it interacts [140, 141]. Here, care must be taken what definition of the Beer–Lambert law is used. Chemists tend to use the decimal logarithm (or common algorithm), which is also typically applied when determining the absorption coefficient of a substance. In contrast, the natural logarithm is usually applied in physics [121]. In this work, the Beer–Lambert law is defined with

[1]Sigma–Aldrich, CAS number 518-47-8.
[2]Sigma–Aldrich, CAS number 17372-87-1.

the natural logarithm, which will also be the basis of the analytical model. As such, the molar absorption coefficients as a function of the wavelength must be determined with that same definition, which is:

$$-\ln \frac{I_{\text{out}}(\lambda)}{I_0(\lambda)} = \varepsilon(\lambda) C d. \tag{5.1}$$

with molar absorption coefficient ε, fluorophore concentration C, and path length d. By measuring the intensities I_{out} and I_0 for different fluorophore concentrations and a known path length, the absorption coefficient can be determined.

The ratios of the measured light intensities at the peak excitation wavelength of each fluorophore are shown in Figure 5.5. The transmitted intensity I_{out} decreases for increasing fluorophore concentrations. The molar absorption coefficients at the peak excitation wavelengths $\lambda_{\text{ex}}^{\text{max}}$ are determined by fitting Equation 5.1 to the measurement results. They are listed in Table 5.1. For the sake of completeness, the molar absorption coefficients as determined with the decimal logarithm are shown as well. These are in line with values from literature [136, 138, 142]. The difference in the molar absorption coefficient is a factor ln(10), due to the difference in the logarithm base. The fluorophore quantum efficiencies ϕ_{max} at the peak emission wavelengths $\lambda_{\text{em}}^{\text{max}}$ are adapted from literature and shown in Table 5.1 as well [137].

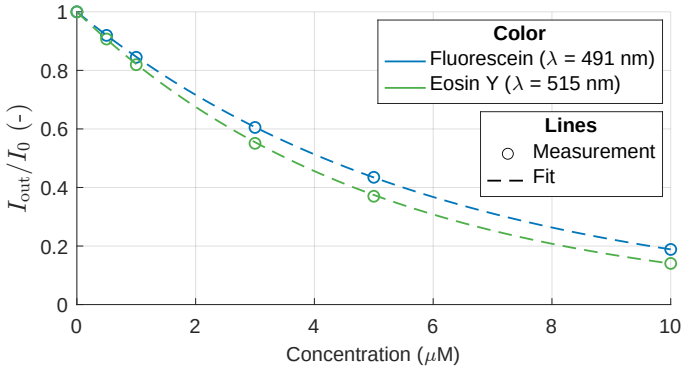

Figure 5.5: Ratio of the transmitted light intensity I_{out} relative to the incident light intensity I_0 for varying fluorophore concentrations at the peak excitation wavelength of each fluorophore for a path length of 10 mm.

Table 5.1: Spectral properties of Fluorescein and Eosin Y. For clarity, the values in the shaded cells are used in the analytical model.

Fluorophore	$\lambda_{\text{ex}}^{\text{max}}$ (nm)	ε ($\text{L mol}^{-1}\,\text{m}^{-1}$) (natural log.)	ε ($\text{L mol}^{-1}\,\text{m}^{-1}$) (decimal log.)	$\lambda_{\text{em}}^{\text{max}}$ (nm)	ϕ_{max} (-) [137]
1: Fluorescein	491	1.67×10^7	7.24×10^6	514	0.92
2: Eosin Y	515	1.96×10^7	8.53×10^6	537	0.20

The normalized spectra in Figure 5.4 are used to determine the absorption and effective emission spectra. The final absorption spectra are found by multiplying the normalized

excitation spectrum of each fluorophore with the corresponding molar absorption coefficient in Table 5.1. Moreover, the effective emission spectra are found by multiplying the normalized emission spectrum of each fluorophore with the corresponding peak quantum efficiency in Table 5.1. The resulting spectra, which are direct input to the analytical model, are presented in Section 5.3.1.

5.3 Methods

This section presents the analytical model to describe the fluorescence of a fluid film with two fluorophores. It is based on the derivation as presented by Hidrovo and Hart [1]. First, the original model description is adapted and extended to incorporate reabsorption and emission of both fluorophores. Next, surface reflection of the background is included. This section ends with a description of the experimental validation method.

Table 5.2: Overview of the model parameters.

Symbol	Description	Unit
C	total fluorophore concentration	$\mathrm{mol\,L^{-1}}$
C_i	fluorophore concentration of fluorophore i	$\mathrm{mol\,L^{-1}}$
i	fluorophore index (1 or 2)	-
$I_0(\lambda)$	initial excitation light intensity	$\mathrm{W\,sr^{-1}}$
$I_\mathrm{E}(\lambda, x)$	excitation light intensity	$\mathrm{W\,sr^{-1}}$
$I_\mathrm{ER}(\lambda, x)$	reflected excitation light intensity	$\mathrm{W\,sr^{-1}}$
$I_\mathrm{F}(\lambda, x)$	fluorescence intensity	$\mathrm{W\,sr^{-1}}$
$I'_\mathrm{F}(\lambda, x)$	fluorescence intensity with reabsorption	$\mathrm{W\,sr^{-1}}$
$I''_\mathrm{F}(\lambda, x)$	fluorescence intensity with reabsorption and background surface reflectivity	$\mathrm{W\,sr^{-1}}$
$I_\mathrm{FR}(\lambda, x)$	reflected fluorescence intensity	$\mathrm{W\,sr^{-1}}$
$I'_\mathrm{FR}(\lambda, x)$	reflected fluorescence intensity with reabsorption	$\mathrm{W\,sr^{-1}}$
j	bandpass filter index (A or B)	-
R	ratio	-
x	coordinate	m
$\varepsilon(\lambda)$	total absorption coefficient	$\mathrm{L\,mol^{-1}\,m^{-1}}$
$\varepsilon_i(\lambda)$	absorption coefficient of fluorophore i	$\mathrm{L\,mol^{-1}\,m^{-1}}$
$\phi_i(\lambda)$	quantum efficiency of fluorophore i	-
λ	wavelength	nm
λ_A	central wavelength bandpass filter A	nm
λ_B	central wavelength bandpass filter B	nm
λ_E	excitation wavelength	nm
ρ	surface reflectivity	-

5.3.1 Analytical model

A schematic of the model can be seen in Figure 5.6. The various model parameters are also listed in Table 5.2, for reference. The schematic shows a thin fluid film on a background. The film height h is very small relative to the spatial dimensions and any change in film height is assumed to be gradual. Therefore, we can only consider a single point of the fluid film, for which the emission and (re-)absorption of light is analyzed along the film height.

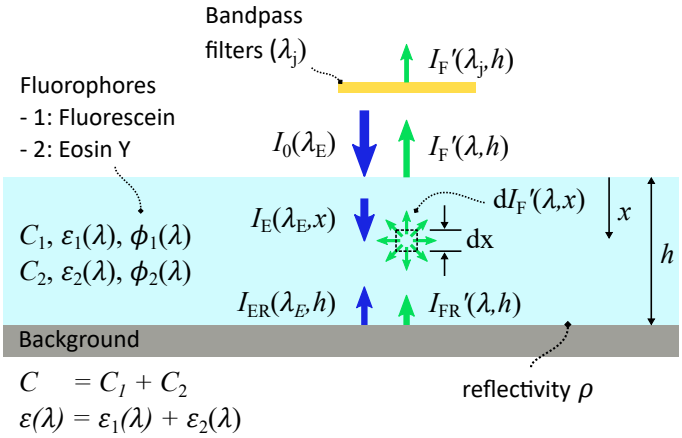

Figure 5.6: Schematic of the analytical model setup. Two fluorophores are dissolved in a fluid film with film height h on a background with surface reflectivity ρ. The fluid film is excited with the initial excitation light intensity $I_0(\lambda_E)$. Consider a small differential fluid element with length dx. It is excited with the local excitation light intensity $I_E(\lambda_E, x)$, which results in the differential fluorescence intensity $dI_F'(\lambda, x)$. The total fluorescence intensity $I_F'(\lambda, h)$, which leaves the fluid film, is measured through spectral bandpass filters. When surface reflectivity is taken into account, the excitation light and fluorescence can reflect on the background. The reflected excitation light intensity is indicated by $I_{ER}(\lambda_E, h)$, and the reflected fluorescence intensity is indicated by $I_{FR}'(\lambda, h)$.

The fluid film is illuminated with the direct, monochromatic light intensity I_0 of excitation wavelength λ_E. The incident angle is orthogonal to the fluid film. Fluorescein (fluorophore 1) and Eosin Y (fluorophore 2) are dissolved in the fluid at a concentration of C_1 and C_2, respectively. The total fluorophore concentration is given by C. The spectral properties of the fluorophores are described by the wavelength dependent absorption coefficients $\varepsilon_1(\lambda)$ and $\varepsilon_2(\lambda)$, and the wavelength dependent effective quantum efficiencies $\phi_1(\lambda)$ and $\phi_2(\lambda)$. Moreover, the total absorption coefficient is given by $\varepsilon(\lambda)$. The excitation light will be partly absorbed and re-emitted by the fluorophores when passing through the fluid film. The direct, omnidirectional fluorescence emission from the fluid element is indicated by $dI_F'(\lambda, x)$. The emitted fluorescence intensity $I_F'(\lambda, h)$ that leaves the fluid film is measured through narrow spectral bandpass filters with center wavelengths λ_j. The parameter j is the filter index (A or B).

The absorption and effective emission spectra of Fluorescein and Eosin Y are shown in Figure 5.7. The spectra have been determined in Section 5.2 and clearly show that absorption and emission occur over a wide range of wavelengths. However, the use of the narrow spectral bandpass filter and the monochromatic excitation light source allows for a very useful simplification in the analytical model setup. Only the fluorophore spectral properties (absorption and effective emission) at these specific wavelengths are considered. The

spectral properties at the excitation wavelength and bandpass filter wavelengths are indicated in the figure. The modeled excitation wavelength λ_E is equal to 448 nm. Moreover, two spectral bandpass filters are used: filter A (λ_A = 520 nm) and filter B (λ_B = 540 nm). The wavelengths are selected to match the experimental settings.

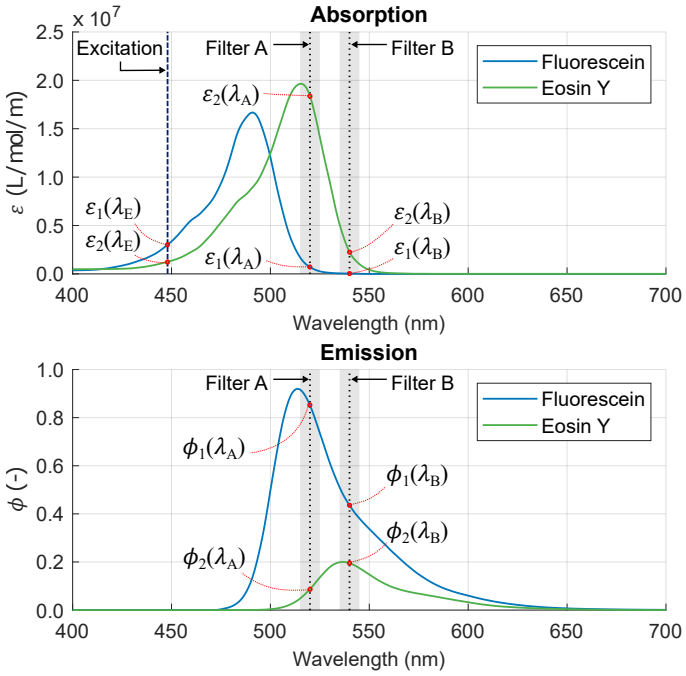

Figure 5.7: Measured absorption and emission spectra of Fluorescein and Eosin Y. The excitation wavelength of the light source and the bandpass filters are shown as well.

If the emission spectrum of one of the fluorophores overlaps with the absorption spectrum of the other fluorophore or with its own absorption spectrum, reabsorption of the fluorescence emission occurs. The photons emitted by the fluorophore can be reabsorbed before they leave the fluid film. The reabsorption effect is twofold:

1. The fluorescence emission in the spectral overlap region is lowered as the emitted photons get reabsorbed.

2. The absorbed photons are re-emitted, hereby increasing the fluorescence emission at higher wavelengths.

Typically, the intensity of the external excitation light source is significantly higher than the fluorescence intensity from the fluorophores. Therefore, it is assumed that only the first effect mentioned above is relevant and the second effect can be neglected: the reduction in fluorescence emission is taken into account, while the increase in fluorescence emission due to reabsorption is neglected [1]. The model includes just a single event of reabsorption: a possible fluorescence cascade is neglected.

If surface reflection of the background is taken into account, the background reflects the left-over excitation light intensity $I_{\mathrm{ER}}(\lambda_{\mathrm{E}}, x)$ and the downwards directed fluorescence intensity $I'_{\mathrm{FR}}(\lambda, h)$ back into the fluid film, as indicated in Figure 5.6. It is assumed only specular reflection is present. The amount of reflection is described by the surface reflectivity ρ, which takes a value between 0 and 1.

Model description - no reflection

In this model description, it is assumed that the background has zero reflection ($\rho = 0$) and behaves as a perfect blackbody [143]. Consider a small differential fluid element within the fluid film with length dx. The local excitation light intensity is described by the Beer–Lambert law [140, 141]. As surface reflection is neglected, only the direct excitation light intensity is considered, and the local excitation light intensity is given by:

$$I_{\mathrm{E}}(\lambda_{\mathrm{E}}, x) = I_0(\lambda_{\mathrm{E}})\, e^{-\varepsilon(\lambda_{\mathrm{E}})Cx}, \tag{5.2}$$

The differential fluorescence intensity from the fluid element for fluorophore i at a certain emission wavelength λ is defined as [1]:

$$\mathrm{d}I_{\mathrm{F},i}(\lambda, x) = I_{\mathrm{E}}(\lambda_{\mathrm{E}}, x)\, \varepsilon_i(\lambda_{\mathrm{E}})\, C_i \phi_i(\lambda)\, \mathrm{d}x\, \mathrm{d}\lambda, \tag{5.3}$$

with fluorophore concentration C_i, absorption coefficient ε_i, and quantum efficiency $\phi_i(\lambda)$. The parameter i is the fluorophore index, which is equal to 1 (Fluorescein) or 2 (Eosin Y). This equation describes how the local excitation light intensity is absorbed at the excitation wavelength λ_{E} and re-emitted over a range of wavelengths. The quantum efficiency describes the emission strength at a given wavelength.

The differential fluorescence intensity can be reabsorbed before the photons leave the fluid film. In contrast to Hidrovo and Hart [1], where the reabsorption of only one fluorophore is included, here we consider the reabsorption of both fluorophores. The resulting differential fluorescence intensity, including absorption by both fluorophores as described by the Beer–Lambert law, is given by:

$$\mathrm{d}I'_{\mathrm{F},i}(\lambda, x) = \mathrm{d}I_{\mathrm{F},i}(\lambda, x)\, e^{-[\varepsilon_1(\lambda)C_1 + \varepsilon_2(\lambda)C_2]x}. \tag{5.4}$$

As the fluorescence intensity is measured through narrow bandpass filters, the differential fluorescence intensity can only be computed for the specific wavelength of the bandpass filter. The total fluorescence intensity at the bandpass filter wavelength λ_{j} is found by integrating over the fluid film height:

$$
\begin{aligned}
I'_{\mathrm{F},i}\left(\lambda_\mathrm{j},h\right) &= \int_0^h \mathrm{d}I'_{\mathrm{F},i}\left(\lambda_\mathrm{j},x\right) \\
&= \int_0^h \mathrm{d}I_{\mathrm{F},i}\left(\lambda_\mathrm{j},x\right) e^{-\left[\varepsilon_1\left(\lambda_\mathrm{j}\right)C_1+\varepsilon_2\left(\lambda_\mathrm{j}\right)C_2\right]x} \\
&= \int_0^h I_\mathrm{E}\left(\lambda_\mathrm{E},x\right)\varepsilon_i\left(\lambda_\mathrm{E}\right)C_i\phi_i\left(\lambda_\mathrm{j}\right) e^{-\left[\varepsilon_1\left(\lambda_\mathrm{j}\right)C_1+\varepsilon_2\left(\lambda_\mathrm{j}\right)C_2\right]x}\,\mathrm{d}x \\
&= \int_0^h I_0\left(\lambda_\mathrm{E}\right) e^{-\varepsilon\left(\lambda_\mathrm{E}\right)Cx}\varepsilon_i\left(\lambda_\mathrm{E}\right)C_i\phi_i\left(\lambda_\mathrm{j}\right) e^{-\left[\varepsilon_1\left(\lambda_\mathrm{j}\right)C_1+\varepsilon_2\left(\lambda_\mathrm{j}\right)C_2\right]x}\,\mathrm{d}x \\
&= I_0\left(\lambda_\mathrm{E}\right)\varepsilon_i\left(\lambda_\mathrm{E}\right)C_i\phi_i\left(\lambda_\mathrm{j}\right)\left[\frac{1-e^{-\left[\varepsilon\left(\lambda_\mathrm{E}\right)C+\varepsilon_1\left(\lambda_\mathrm{j}\right)C_1+\varepsilon_2\left(\lambda_\mathrm{j}\right)C_2\right]h}}{\varepsilon\left(\lambda_\mathrm{E}\right)C+\varepsilon_1\left(\lambda_\mathrm{j}\right)C_1+\varepsilon_2\left(\lambda_\mathrm{j}\right)C_2}\right]
\end{aligned}
\tag{5.5}
$$

To summarize, Equation (5.5) describes the total fluorescence intensity from a dissolved fluorophore in a fluid film with film height h. The fluid film is excited with wavelength λ_E and the fluorescence intensity is measured through a narrow bandpass filter with central wavelength λ_j.

The ratiometric fluorescence measurement method uses two spectral bandpass filters: filter A and filter B. The total fluorescence intensity which is measured through filter A is defined as the sum of the fluorescence intensities from both fluorophores at the filter wavelength λ_A:

$$
I'_\mathrm{F}\left(\lambda_\mathrm{A},h\right) = I'_{\mathrm{F},1}\left(\lambda_\mathrm{A},h\right) + I'_{\mathrm{F},2}\left(\lambda_\mathrm{A},h\right) \tag{5.6}
$$

$$
\begin{aligned}
&= I_0\left(\left[\varepsilon_1\left(\lambda_\mathrm{E}\right)C_1\phi_1\left(\lambda_\mathrm{A}\right)+\varepsilon_2\left(\lambda_\mathrm{E}\right)C_2\phi_2\left(\lambda_\mathrm{A}\right)\right]\times\right. \\
&\qquad\left.\left[\frac{1-e^{-\left[\varepsilon\left(\lambda_\mathrm{E}\right)C+\varepsilon_1\left(\lambda_\mathrm{A}\right)C_1+\varepsilon_2\left(\lambda_\mathrm{A}\right)C_2\right]h}}{\varepsilon\left(\lambda_\mathrm{E}\right)C+\varepsilon_1\left(\lambda_\mathrm{A}\right)C_1+\varepsilon_2\left(\lambda_\mathrm{A}\right)C_2}\right]\right)
\end{aligned}
\tag{5.7}
$$

If the film height is equal to zero, the fluorescence intensity will be zero as well. The fluorescence intensity for infinitely thick films has a constant value, which is a function of the fluorophore concentrations and spectral properties:

$$
\lim_{h\to\infty} I'_\mathrm{F}\left(\lambda_\mathrm{A},h\right) = I_0\frac{\varepsilon_1\left(\lambda_\mathrm{E}\right)C_1\phi_1\left(\lambda_\mathrm{A}\right)+\varepsilon_2\left(\lambda_\mathrm{E}\right)C_2\phi_2\left(\lambda_\mathrm{A}\right)}{\varepsilon\left(\lambda_\mathrm{E}\right)C+\varepsilon_1\left(\lambda_\mathrm{A}\right)C_1+\varepsilon_2\left(\lambda_\mathrm{A}\right)C_2} \tag{5.8}
$$

Similarly, the total fluorescence intensity which is measured through filter B is given by the sum of the fluorescence intensities from both fluorophores at the filter wavelength λ_B:

$$
I'_\mathrm{F}\left(\lambda_\mathrm{B},h\right) = I'_{\mathrm{F},1}\left(\lambda_\mathrm{B},h\right) + I'_{\mathrm{F},2}\left(\lambda_\mathrm{B},h\right) \tag{5.9}
$$

$$
\begin{aligned}
&= I_0\left(\left[\varepsilon_1\left(\lambda_\mathrm{E}\right)C_1\phi_1\left(\lambda_\mathrm{B}\right)+\varepsilon_2\left(\lambda_\mathrm{E}\right)C_2\phi_2\left(\lambda_\mathrm{B}\right)\right]\times\right. \\
&\qquad\left.\left[\frac{1-e^{-\left[\varepsilon\left(\lambda_\mathrm{E}\right)C+\varepsilon_1\left(\lambda_\mathrm{B}\right)C_1+\varepsilon_2\left(\lambda_\mathrm{B}\right)C_2\right]h}}{\varepsilon\left(\lambda_\mathrm{E}\right)C+\varepsilon_1\left(\lambda_\mathrm{B}\right)C_1+\varepsilon_2\left(\lambda_\mathrm{B}\right)C_2}\right]\right)
\end{aligned}
\tag{5.10}
$$

The fluorescence intensity for infinitely thick fluid film is given by:

$$\lim_{h\to\infty} I'_{\mathrm{F}}(\lambda_{\mathrm{B}},h) = I_0 \frac{\varepsilon_1(\lambda_{\mathrm{E}})C_1\phi_1(\lambda_{\mathrm{B}}) + \varepsilon_2(\lambda_{\mathrm{E}})C_2\phi_2(\lambda_{\mathrm{B}})}{\varepsilon(\lambda_{\mathrm{E}})C + \varepsilon_1(\lambda_{\mathrm{B}})C_1 + \varepsilon_2(\lambda_{\mathrm{B}})C_2} \tag{5.11}$$

The last step is to determine the ratio of the fluorescence intensities, as measured through each filter:

$$R(h) = \frac{I'_{\mathrm{F}}(\lambda_{\mathrm{B}},h)}{I'_{\mathrm{F}}(\lambda_{\mathrm{A}},h)} \tag{5.12}$$

When taking a closer look at Equation (5.7) and Equation (5.10), it can be observed that the light intensity I_0 appears in both equations and thus cancels out in the expression for the ratio in Equation (5.12). Two limits for the ratio $R(h)$ can be identified. The ratio limit for very thin fluid films is equal to:

$$\lim_{h\to 0} R(h) = \frac{\varepsilon_1(\lambda_{\mathrm{E}})C_1\phi_1(\lambda_{\mathrm{B}}) + \varepsilon_2(\lambda_{\mathrm{E}})C_2\phi_2(\lambda_{\mathrm{B}})}{\varepsilon_1(\lambda_{\mathrm{E}})C_1\phi_1(\lambda_{\mathrm{A}}) + \varepsilon_2(\lambda_{\mathrm{E}})C_2\phi_2(\lambda_{\mathrm{A}})} \tag{5.13}$$

It is a function of the concentration and spectral properties of both fluorophores. The ratio limit for infinitely thick fluid films is equal to the ratio limit for very thin fluid films multiplied by a factor:

$$\lim_{h\to\infty} R(h) = \lim_{h\to 0} R(h) \cdot \frac{\varepsilon(\lambda_{\mathrm{E}})C + \varepsilon_1(\lambda_{\mathrm{A}})C_1 + \varepsilon_2(\lambda_{\mathrm{A}})C_2}{\varepsilon(\lambda_{\mathrm{E}})C + \varepsilon_1(\lambda_{\mathrm{B}})C_1 + \varepsilon_2(\lambda_{\mathrm{B}})C_2} \tag{5.14}$$

Model description - reflection

The model description for the situation of a reflecting background is very similar to the model description for a non-reflecting background in the previous section. The result of including surface reflection is twofold:

1. The definition of the local excitation light intensity is changed. It is now a combination of the direct excitation light intensity and the excitation light intensity which reflects back into the fluid film from the background.

2. The same applies for the fluorescence intensity. The fluorescence emission which leaves the fluid film is a combination of the direct fluorescence emission and its reflected part.

First, the definition of the local excitation light intensity and its impact on the fluorescence intensity is presented. The reflected excitation light intensity at a distance of $x = h$ is defined by the product of the surface reflectivity ρ and the transmitted part of the direct excitation light intensity at the path distance $x = h$, which is given by Equation (5.2):

$$\begin{aligned} I_{\mathrm{ER}}(\lambda_{\mathrm{E}},h,\rho) &= \rho I_{\mathrm{E}}(\lambda_{\mathrm{E}},h) \\ &= \rho I_0(\lambda_{\mathrm{E}})\, e^{-\varepsilon(\lambda_{\mathrm{E}})Ch}. \end{aligned} \tag{5.15}$$

Using the Beer–Lambert law for attenuation of light intensity, the local excitation light intensity is then given by:

$$\begin{aligned} I_{\mathrm{E}}\left(\lambda_{\mathrm{E}}, x, \rho\right) &= I_{\mathrm{E}}\left(\lambda_{\mathrm{E}}, x\right) + I_{\mathrm{ER}}\left(\lambda_{\mathrm{E}}, h, \rho\right) e^{-\varepsilon(\lambda_{\mathrm{E}})C(h-x)} \\ &= I_0\left(\lambda_{\mathrm{E}}\right) e^{-\varepsilon(\lambda_{\mathrm{E}})Cx} + I_{\mathrm{ER}}\left(\lambda_{\mathrm{E}}, h, \rho\right) e^{-\varepsilon(\lambda_{\mathrm{E}})C(h-x)} \\ &= I_0\left(\lambda_{\mathrm{E}}\right)\left(\underbrace{e^{-\varepsilon(\lambda_{\mathrm{E}})Cx}}_{\text{direct excitation}} + \underbrace{\rho e^{-\varepsilon(\lambda_{\mathrm{E}})C(2h-x)}}_{\text{reflected excitation}} \right) \end{aligned} \tag{5.16}$$

The contributions of the direct excitation and the reflected excitation are indicated in the equation. From here, the model description follows the same steps as presented in Equation (5.3) to Equation (5.5) for the situation without reflection, using the updated definition of the local excitation light as presented in Equation (5.16). The direct fluorescence intensity at the filter wavelength λ_{j} for fluorophore i, including reabsorption by both fluorophores, is found by integrating over the fluid film height:

$$\begin{aligned} I'_{\mathrm{F},i}\left(\lambda_{\mathrm{j}}, h, \rho\right) &= \int_0^h \mathrm{d}I'_{\mathrm{F},i}\left(\lambda_{\mathrm{j}}, x, \rho\right) \\ &= I_0\left(\lambda_{\mathrm{E}}\right)\varepsilon_i\left(\lambda_{\mathrm{E}}\right) C_i \phi_i\left(\lambda_{\mathrm{j}}\right) \left[\underbrace{\frac{1 - e^{-\left[\varepsilon(\lambda_{\mathrm{E}})C + \varepsilon_1\left(\lambda_{\mathrm{j}}\right)C_1 + \varepsilon_2\left(\lambda_{\mathrm{j}}\right)C_2\right]h}}{\varepsilon\left(\lambda_{\mathrm{E}}\right)C + \varepsilon_1\left(\lambda_{\mathrm{j}}\right)C_1 + \varepsilon_2\left(\lambda_{\mathrm{j}}\right)C_2}}_{\text{direct excitation}} + \right. \\ &\quad \left. \underbrace{\rho \cdot \frac{e^{-\left[\varepsilon(\lambda_{\mathrm{E}})C + \varepsilon_1\left(\lambda_{\mathrm{j}}\right)C_1 + \varepsilon_2\left(\lambda_{\mathrm{j}}\right)C_2\right]h} - e^{-[2\varepsilon(\lambda_{\mathrm{E}})C]h}}{\varepsilon\left(\lambda_{\mathrm{E}}\right)C - \varepsilon_1\left(\lambda_{\mathrm{j}}\right)C_1 - \varepsilon_2\left(\lambda_{\mathrm{j}}\right)C_2}}_{\text{reflected excitation}} \right] \end{aligned} \tag{5.17}$$

Again, the contributions of the direct excitation and the reflected excitation are indicated in the equation. When the surface reflection is omitted ($\rho = 0$), the contribution from the surface reflection disappears and Equation (5.17) reduces to the expression in Equation (5.17).

The fluorescence intensity, which leaves the fluid film, is also changed due to the surface reflection. The total fluorescence intensity at the filter wavelength λ_{j} for fluorophore i is equal to the sum of the direct fluorescence intensity, which is given by Equation (5.17), and the contribution of the reflected fluorescence intensity. The fluorescence emission is omnidirectional. Therefore, the fluorescence intensity which reaches the background is identical to the direct fluorescence intensity that leaves the fluid film at the top, as described by Equation (5.17). The reflected fluorescence intensity is equal to the product of the surface reflectivity and the direct fluorescence intensity. The reflected fluorescence intensity will be partly attenuated when passing through the fluid film, as described by

the Beer–Lambert law. The total fluorescence intensity is then given by:

$$
\begin{aligned}
I''_{\mathrm{F},i}\left(\lambda_\mathrm{j},h,\rho\right) &= I'_{\mathrm{F},i}\left(\lambda_\mathrm{j},h,\rho\right) + I'_{\mathrm{FR},i}\left(\lambda_\mathrm{j},h,\rho\right) e^{-\left[\varepsilon_1\left(\lambda_\mathrm{j}\right)C_1+\varepsilon_2\left(\lambda_\mathrm{j}\right)C_2\right]h} \\
&= I'_{\mathrm{F},i}\left(\lambda_\mathrm{j},h,\rho\right) + \rho I'_{\mathrm{F},i}\left(\lambda_\mathrm{j},h,\rho\right) e^{-\left[\varepsilon_1\left(\lambda_\mathrm{j}\right)C_1+\varepsilon_2\left(\lambda_\mathrm{j}\right)C_2\right]h} \\
&= I'_{\mathrm{F},i}\left(\lambda_\mathrm{j},h,\rho\right)\left(1+\rho e^{-\left[\varepsilon_1\left(\lambda_\mathrm{j}\right)C_1+\varepsilon_2\left(\lambda_\mathrm{j}\right)C_2\right]h}\right) \\
&= I_0\left(\lambda_\mathrm{E}\right)\varepsilon_i\left(\lambda_\mathrm{E}\right)C_i\phi_i\left(\lambda_\mathrm{j}\right)\Bigg(\underbrace{1}_{\text{direct fluorescence}} + \underbrace{\rho e^{-\left[\varepsilon_1\left(\lambda_\mathrm{j}\right)C_1+\varepsilon_2\left(\lambda_\mathrm{j}\right)C_2\right]h}}_{\text{reflected fluorescence}}\Bigg)\times \\
&\quad \Bigg[\underbrace{\frac{1-e^{-\left[\varepsilon\left(\lambda_\mathrm{E}\right)C+\varepsilon_1\left(\lambda_\mathrm{j}\right)C_1+\varepsilon_2\left(\lambda_\mathrm{j}\right)C_2\right]h}}{\varepsilon\left(\lambda_\mathrm{E}\right)C+\varepsilon_1\left(\lambda_\mathrm{j}\right)C_1+\varepsilon_2\left(\lambda_\mathrm{j}\right)C_2}}_{\text{direct excitation}} + \\
&\quad \underbrace{\rho\cdot\frac{e^{-\left[\varepsilon\left(\lambda_\mathrm{E}\right)C+\varepsilon_1\left(\lambda_\mathrm{j}\right)C_1+\varepsilon_2\left(\lambda_\mathrm{j}\right)C_2\right]h}-e^{-\left[2\varepsilon\left(\lambda_\mathrm{E}\right)C\right]h}}{\varepsilon\left(\lambda_\mathrm{E}\right)C-\varepsilon_1\left(\lambda_\mathrm{j}\right)C_1-\varepsilon_2\left(\lambda_\mathrm{j}\right)C_2}}_{\text{reflected excitation}}\Bigg]
\end{aligned}
\tag{5.18}
$$

The contributions of the direct fluorescence, reflected fluorescence, direct excitation, and reflected excitation are all indicated in the equation.

The ratio is determined in a similar way as described for the situation without reflection, but now with the fluorescence intensity as presented in Equation (5.18):

$$
R(h,\rho) = \frac{I''_\mathrm{F}\left(\lambda_\mathrm{B},h,\rho\right)}{I''_\mathrm{F}\left(\lambda_\mathrm{A},h,\rho\right)} = \frac{I''_{\mathrm{F},1}\left(\lambda_\mathrm{B},h,\rho\right)+I''_{\mathrm{F},2}\left(\lambda_\mathrm{B},h,\rho\right)}{I''_{\mathrm{F},1}\left(\lambda_\mathrm{A},h,\rho\right)+I''_{\mathrm{F},2}\left(\lambda_\mathrm{A},h,\rho\right)} \tag{5.19}
$$

Interestingly, the fluorescence intensity limits for infinitely thick fluid films, as presented in Equation (5.8) and Equation (5.11), remain the same. The same applies for the ratio limits for infinitely thin and infinitely thick fluid films in Equation (5.13) and Equation (5.14), respectively. The limits are not affected by the introduction of the surface reflection.

5.3.2 Experimental

A schematic of the experimental setup is shown in Figure 5.8. Thin fluid films are created using prefabricated channel slides[3], which can be bonded to any background surface with the self-adhesive underside. In these experiments, the slides are bonded to standard-sized aluminum micro-slides (75 mm × 25 mm) with two different background surface reflectivities. The low reflection background is matt black anodized aluminum, which has a surface reflectivity of about 6% in the visible spectrum [144]. The high-reflection background is made from highly reflective aluminum with a surface reflectivity of about 92% [143] in the visible spectrum. The channel slides are firmly pressed together in a mechanical press. The channel heights, including the 50 µm bonding layer, are equal to 150 µm, 250 µm, 450 µm, 650 µm, and 850 µm. The tolerance on the channel heights is equal to 5%, according to the supplier.

[3]Channel slides: Ibidi® sticky-Slide I Luer.

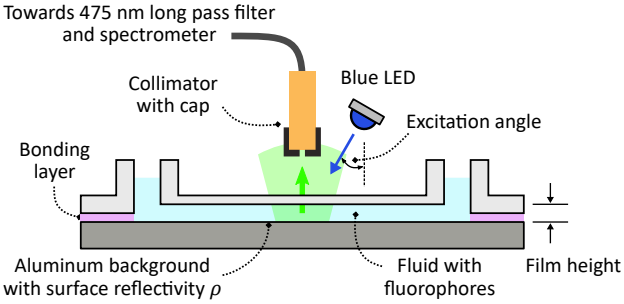

Figure 5.8: Schematic of the experimental setup to measure the fluorescence spectrum of a fluid film. The dimensions are not to scale.

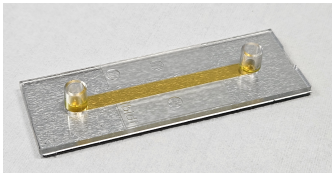

Figure 5.9: Channel slide with high reflection background. The channel is filled with the fluorophore solution.

The channels are filled with similar liquid solutions (deionized water, pH of 10) as described in Section 5.2. The fluorophores Fluorescein and Eosin Y are dissolved at different concentrations: 0.1 mmol L^{-1}, 0.2 mmol L^{-1}, and 0.3 mmol L^{-1} for each fluorophore. Figure 5.9 shows an example of a channel slide on the high reflection background. The channel is already filled with the fluorophore solution.

Figure 5.8 also shows the components which are used to generate and measure the net fluorescence emission from the two fluorophores. They are excited with a single royal blue LED light[4], which is equipped with a clip-on lens[5]. Due to spatial limitations, the excitation light is not orthogonal to the fluid film. The excitation angle is about 30°. The fluorescence spectra are measured with a spectrometer[6]. A 4 mm aperture collimator captures the fluorescence emission, which is guided towards the spectrometer via a fiber-optic cable. A cap on the collimator reduces the measurement spot area to a diameter of approximately 1 mm. A second collimating lens is used to guide the light bundle through a 475 nm long pass emission filter[7] to prevent the excitation light from reaching the spectrometer. An overview of all spectra is shown in Figure 5.10. The measured LED light excitation spectrum is centered around 448 nm with a 20 nm FWHM bandwidth. The spectrum of the long pass filter, as provided by the manufacturer, shows that the emission of both fluorophores is passed, while most of the excitation light is blocked. Some excitation light in the 475–500 nm range will still bleed through and is removed in post-processing of the measurement data.

The spectrometer and LED light are software controlled via an external controller board. The LED light current is set to 30 mA and only activated during a spectrum measurement. The sampling time is equal to 800 ms for the measurements with the low reflection background and equal to 400 ms for the measurements with the high reflection background. Each measurement is repeated ten times.

[4]LED light source: New Energy Cree Starboard XPE, 450-465 nm.
[5]Clip-on lens: LEDil FP11085 LISA2-RS-CLIP16-XP.
[6]Spectrometer: Avantes StarLine AvaSpec-ULS2048CL-EVO, UV/VIS/NIR 200-1100 nm grating, 100 µm slit size.
[7]Long pass filter: Edmund Optics TECHSPEC® 475 nm 12.5 mm Dia., High Performance.

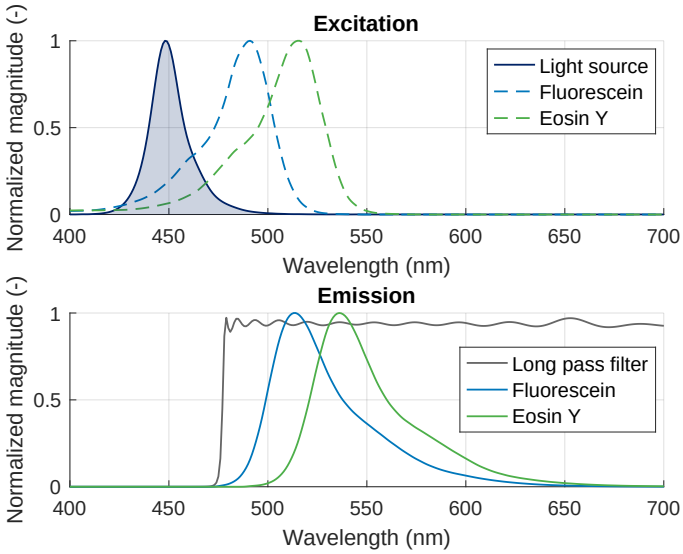

Figure 5.10: Measured and normalized excitation and emission spectra of Fluorescein and Eosin Y. The LED light excitation spectrum and long pass filter spectrum are shown as well.

The measured spectra are used to determine the ratio of the fluorescence emission at two specific wavelengths, similar to what is done in the analytical model. The wavelengths are chosen around around the peak emission wavelengths of the two fluorophores: 520 nm and 540 nm:

$$\text{ratio} = \frac{\text{fluorescence emission at } 540\,\text{nm}}{\text{fluorescence emission at } 520\,\text{nm}} \tag{5.20}$$

The measured ratios are compared to the ratios as determined with the analytical model.

5.4 Results

This section presents the analytical and experimental results.

5.4.1 Analytical model

The analytical model is used to study the ratiometric fluorescence film height measurement method. The results for varying fluorophore concentrations and surface reflectivities are plotted in Figure 5.11. The excitation light intensity I_0 is set to unity and the fluorophore concentration is equal for both fluorophores ($C_1 = C_2$). The fluorescence intensities through filter A and filter B are shown on the left, while the corresponding ratios of the fluorescence intensities are shown on the right. The figures also show the limit values of the fluorescence intensity and ratio for infinitely thin and infinitely thick fluid films.

Figure 5.11a and Figure 5.11b (top row) show the results of the analytical model without surface reflection, which was presented in Section 5.3.1. The fluorescence intensities through both filters in Figure 5.11a increase with increasing film height. Both fluorescence

intensities converge to their limit for infinitely thick fluid films. They approach the limit faster when the concentration of the fluorophores is increased. Although the effective fluorescence emissions at the wavelength of filter A are larger than the effective fluorescence emissions at the wavelength of filter B (see Figure 5.7), the fluorescence intensities of filter B are higher than the fluorescence intensities of filter A. This can be explained by the reabsorption effect, which results in a significant decrease of the fluorescence intensities of filter A. The corresponding fluorescence intensity ratios can be seen in Figure 5.11b. For each value of the fluorophore concentration, the ratio starts at the ratio limit for infinitely thin fluid films. From there, the ratios increase towards the upper ratio limit for infinitely thick fluid films. The approach towards the upper limit is more aggressive for higher fluorophore concentrations. For low fluorophore concentrations, the ratio increase with film height is almost linear in this film height range.

The results become very different when surface reflection is taken into account. Figure 5.11c and Figure 5.11d (middle row) show the results of the analytical model with surface reflection, as presented in Section 5.3.1. The surface reflectivity is set to unity $(\rho = 1)$ for maximum surface reflection. The fluorescence intensities through both filters in Figure 5.11c have increased compared to the fluorescence intensities in Figure 5.11a. It can also be observed that the fluorescence intensities show an overshoot and then slowly converge to the original fluorescence intensity limits, which are equal to the limits in Figure 5.11a. The fluorescence intensity overshoot peaks are found at lower film heights for an increasing value of the fluorophore concentration. This behavior can be explained by the balancing act between reflection and absorption. The reflection at the background surface will increase the overall fluorescence intensity. However, if the fluid film height increases, the fluorescence intensity decreases due to general absorption and reabsorption. For each fluorophore concentration, there is an optimal film height for which the fluorescence intensity is maximum.

The corresponding ratios in Figure 5.11d also show a significant overshoot, after which they converge to the upper ratio limit for infinitely thick fluid films. This is not visible in the plotted film height range. The location of the ratio maximum depends on the fluorophore concentration. It shifts towards lower film heights for an increasing fluorophore concentration. For each intended film height measurement range, there is an optimal fluorophore concentration for which the range in fluorescence intensity ratio is maximum. The presence of the ratio maximum also means that ratio values larger than the upper ratio limit correspond to more than one film height. For example, the ratio value of 2 for a fluorophore concentration of $0.6\,\mathrm{mmol\,L^{-1}}$ corresponds to a film height of about 217 µm and 787 µm, respectively. This duality is not preferred if the ratio is used to determine the film height, as it does not have a unique solution. Care must be taken to analyze in what film height range the measurement method can be used safely.

The effect of surface reflectivity is further analyzed in Figure 5.11e and Figure 5.11f (bottom row), which show the results of the analytical model for varying surface reflectivities and a fixed fluorophore concentration of $0.3\,\mathrm{mmol\,L^{-1}}$. The behavior is similar to what can be observed in the other figures. The fluorescence intensities in Figure 5.11e increase with increasing film height and surface reflectivity and converge to their limits for infinitely thick fluid films. The corresponding ratios are shown in Figure 5.11f. The ratio appears to linearly increase with the surface reflectivity.

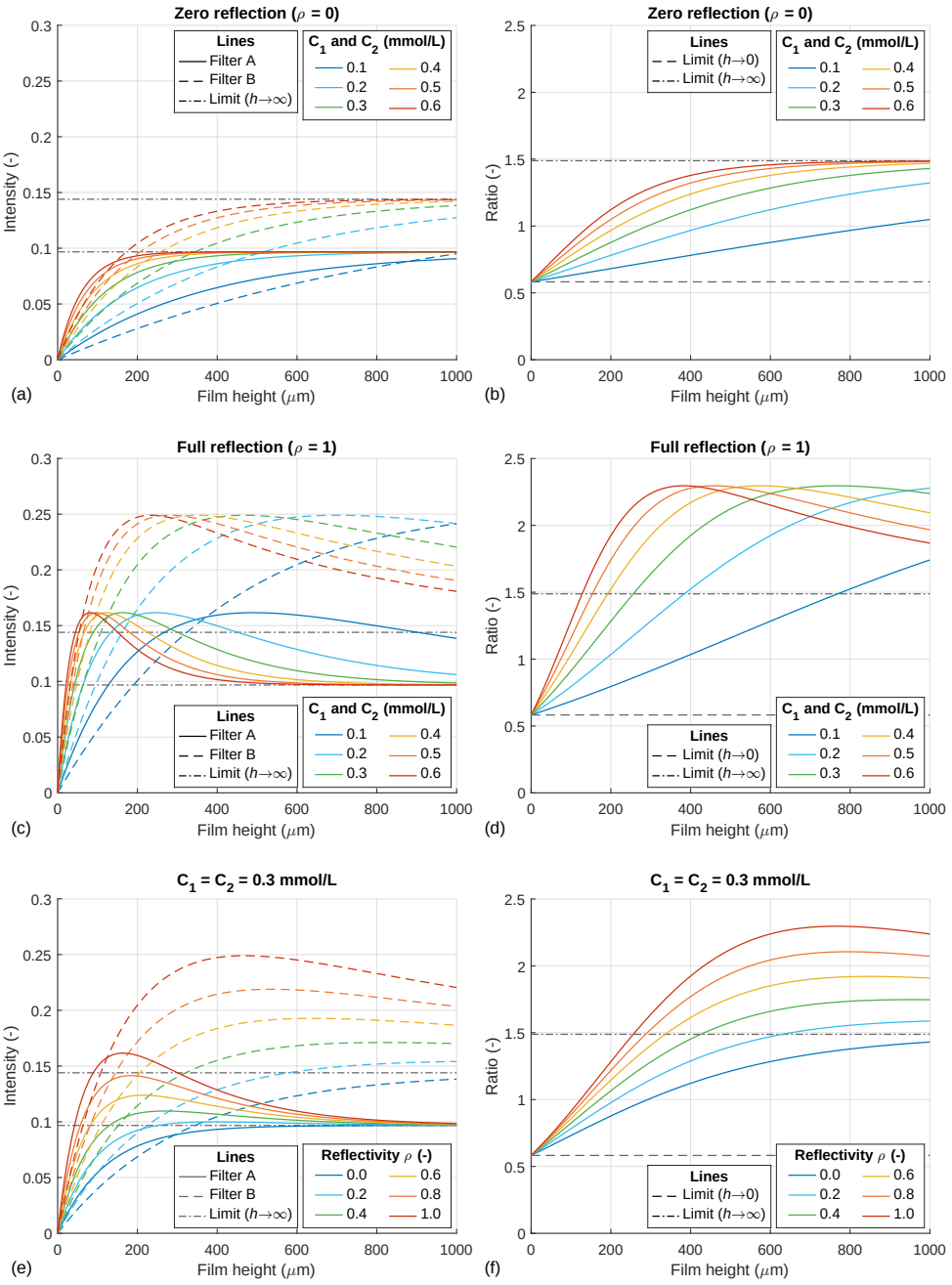

Figure 5.11: Results of the analytical model for varying fluorophore concentrations and surface reflectivities. The fluorescence intensities are shown on the left and the fluorescence intensity ratios are shown on the right. Top row (a and b): zero surface reflectivity. Middle row (c and d): full surface reflectivity. Bottom row (e and f): varying surface reflectivity and fixed fluorophore concentration.

5.4.2 Measured spectra

Figure 5.12 shows the measured spectra for varying film heights and fluorophore concentrations on the two different background surfaces. The plots show the spectra averages and the corresponding standard deviation around the mean values. The measured spectra on the low reflection background can be seen on the left, while the spectra on the high reflection background can be seen on the right. The concentrations for each fluorophore are $0.1\,\mathrm{mmol\,L^{-1}}$ (top row), $0.2\,\mathrm{mmol\,L^{-1}}$ (middle row), and $0.3\,\mathrm{mmol\,L^{-1}}$ (bottom row). The filter wavelengths are indicated for reference.

First, the results of the low reflection background are discussed. The spectra for a concentration of $0.1\,\mathrm{mmol\,L^{-1}}$ for each fluorophore are shown in Figure 5.12a. For thin films, the rate of reabsorption and the corresponding decrease of the Fluorescein emission is low, as the emitted Fluorescein photons quickly leave the fluid film. Therefore, the measured spectra of these thin fluid films are very close to the Fluorescein emission spectrum, as shown in Figure 5.10. The Fluorescein spectrum is dominant over the Eosin Y spectrum, because of the higher absorption at the excitation wavelength and the overall higher effective emission efficiencies, see Figure 5.7. When the film height increases, the shape of the normalized spectrum changes and slowly shifts towards the Eosin Y spectrum. For the largest film height of 850 µm, the overall spectrum peak is found near the peak of the Eosin Y spectrum around 535 nm. Moreover, a decrease in emission around the Fluorescein peak wavelength of 515 nm is observed and a shoulder starts to form in this wavelength region. This spectrum or color shift is the essence of the ratiometric fluorescence imaging. By measuring the fluorescence intensity at two wavelengths, as indicated in the figure with the two narrow bandpass filters, the spectrum shift can be quantified by the ratio between them. As the ratio changes with film height, it is a measure to determine the film height.

The measured spectra for fluorophore concentrations of $0.2\,\mathrm{mmol\,L^{-1}}$ and $0.3\,\mathrm{mmol\,L^{-1}}$ are shown in Figure 5.12c and Figure 5.12e. Due to the increase in fluorophore concentration, emitted Fluorescein photons have a higher probability of encountering another fluorophore before they leave the fluid film. Therefore, the effect of reabsorption and reduction in Fluorescein emission is higher. A larger shift in the measured spectra can be observed and the shoulders around the wavelength of 515 nm are located at lower magnitudes. The spectra peaks for the larger film heights in Figure 5.12e are even found at a larger wavelength than the Eosin Y emission peak wavelength of 537 nm. For these film heights, reabsorption and re-emission of both fluorophores becomes more dominant and can also occur multiple times, which results in a larger shift of the overall emission spectrum.

Figure 5.12b, Figure 5.12d, and Figure 5.12f show the results of the high reflection background. The behavior is very similar to the results of the low reflection background. The spectra shape changes and shifts with increasing film height and fluorophore concentration. However, when comparing the spectra with the results of the low reflection background for the same fluorophore concentrations, it can be observed that the spectra change is significantly larger. Due to the higher surface reflectivity of the background, the reabsorption effect is more dominant. The relative decrease of the Fluorescein emission spectrum and the relative increase of the Eosin Y emission spectrum results in a larger shift of the spectrum.

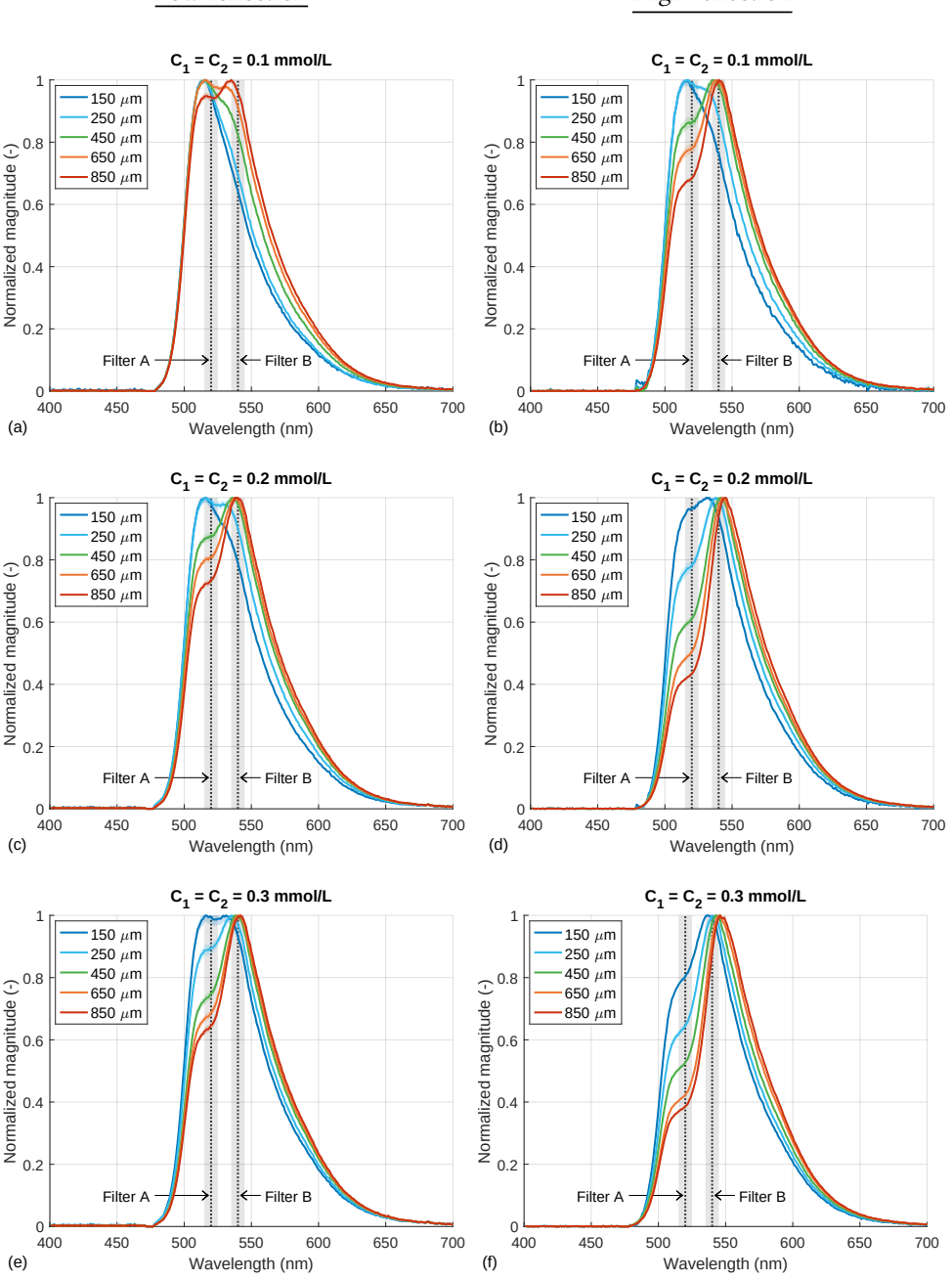

Figure 5.12: Measured average spectra ($\pm 1\sigma$) for varying film heights and for low reflection (left column) and high reflection (right column).

5.4.3 Experimental validation

The measured and modeled ratios for varying film heights and fluorophore concentrations are shown in Figure 5.13. The measured ratios are determined with the measured spectra in Figure 5.12. The modeled ratios are determined with the analytical model with surface reflection in Section 5.3.1. The results for the low reflection background $(\rho = 0.06)$ are shown in Figure 5.13a. The modeled and measured results agree well, especially for the fluorophore concentrations of 0.1 mmol L^{-1} and 0.2 mmol L^{-1}. For the fluorophore concentration of 0.3 mmol L^{-1}, the model slightly underestimates the ratio, in comparison to the experimental results.

Figure 5.13b shows the results for the high reflection background $(\rho = 0.92)$. The ratios are significantly higher compared to the results of the low reflection background. The modeled and measured ratios agree very well.

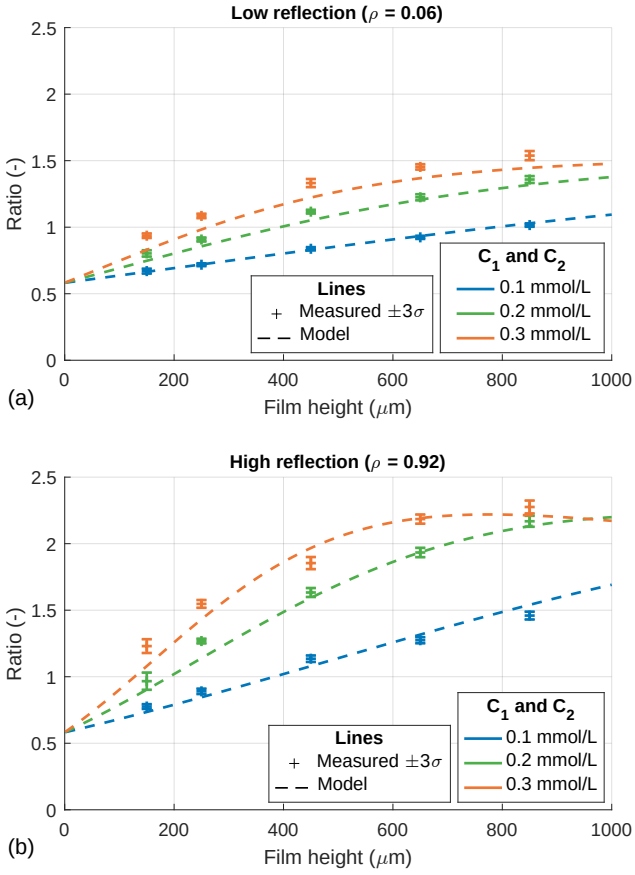

Figure 5.13: Modeled and measured ratio for varying film heights and fluorophore concentrations. (a) Low reflection background. (b) High reflection background.

5.5 Discussion

This section presents the discussion on the analytical model, the experimental method, and the experimental validation.

5.5.1 Analytical model

The analytical model describes the fluorescence of a thin fluid film in which two fluorophores are dissolved, including the effects of reabsorption and surface reflectivity. The analytical model needs the fluorophore spectral properties as input. These can be measured but can also be retrieved from online databases. Care must be taken when determining the absorption coefficient with the logarithm base in the Beer–Lambert law (decimal or natural). Only specular surface reflection is considered in the analytical model. In reality, diffuse reflection can also be present, depending on the optical properties of the background. Moreover, the reflection at the top interface is neglected. In practice, the measurements will be done through a transparent viewing window and part of the excitation light and fluorescence emission will reflect on the viewing window back into the fluid film. However, the amount of reflection will be small, because of the presumably small difference in refractive index between the transparent window material (e.g. glass or plastic) and the fluid.

One of the main assumptions in the analytical model is that the intensity of the fluorescence emission is low relative to the external excitation light intensity. Therefore, the increase in fluorescence due to the reabsorption has been neglected. When looking at the intensity plots in Figure 5.11, it can be seen that the fluorescence intensities can reach values of around 10–20% of the incident intensity, which was set to unity. Therefore, the assumption that the fluorescence intensity is negligible relative to the direct excitation light intensity does not hold. The contribution is relatively small, but the model description will be more accurate when the additional fluorescence emission is included.

The results from the analytical model clearly demonstrate the influence of the film height, the fluorophore concentration, and the surface reflectivity on the fluorescence intensities through the spectral bandpass filters and the corresponding ratio. The analysis of the ratiometric fluorescence measurement method has only been done with equal concentrations for both fluorophores. Of course, this is not required and one can change the ratio between the fluorophore concentrations to improve the measurement response. By changing these concentrations, the ratio between the fluorescence emissions through the spectral bandpass filters will change as well, as can be observed in the expressions for the ratio limits in Equation (5.13) and Equation (5.14).

The analytical model has proven to be an effective design tool to optimize the measurement response of ratiometric fluorescence imaging for a desired film height range. It can be tuned by the selection of the fluorophores and their spectral properties, the fluorophore concentrations, but also the surface reflectivity.

5.5.2 Measured spectra

The fluorescence spectra of thin fluid films have been experimentally determined for varying film heights, fluorophore concentrations and two different surface reflectivities. The measured fluorescence spectra give a more intuitive understanding of the change in the normalized spectra, and the working principle behind the measurement method. The ex-

perimental results clearly demonstrate the influence of the surface reflectivity. The variation in the normalized fluorescence spectra and the corresponding ratios is much more severe for backgrounds with a high surface reflectivity.

The excitation angle in the experiment and the model is different. The model assumes that the incident excitation light is perpendicular to the fluid film, while the excitation angle in the experiment was about 30°. However, the actual excitation angle inside the fluid film will be less because of the refraction when the excitation light enters the viewing window (the channel slide). Moreover, it has been shown numerically and experimentally that the excitation angle has a minor influence on the measurement response up to a few tens of degrees [120].

During the measurements with the high reflectivity backgrounds, small gas bubbles slowly appeared on the aluminum surface. As the aluminum was exposed to the alkaline fluid (pH of about 10), it is assumed that these gas bubbles were hydrogen gas, which forms due to alkaline corrosion of the aluminum. To minimize their influence, the measurements were performed directly after filling the channel slides. For future research, it is recommended to limit the pH or to use a different background material.

5.5.3 Experimental validation

The experimental validation in Section 5.4.3 shows the modeled and measured fluorescence ratio for a variation of the film height, fluorophore concentrations, and two different surface reflections. The modeled fluorescence ratios are directly computed with the analytical model with surface reflection in Section 5.3.1. The experimental fluorescence ratios are determined from the measured spectra in Section 5.4.2. The modeled and measured fluorescence ratios are in very good agreement. Any deviations between the results can be attributed to the assumptions in the analytical model and the deviation in excitation angle, as explained in Section 5.5.1 and Section 5.5.2, respectively.

The results from the analytical model and the experiment both demonstrate that the surface reflectivity has a significant impact on the fluorescence emissions and the corresponding ratio. Depending on the application and the possibility to adjust the background, the ratio range can be increased by increasing the surface reflectivity, hereby improving the measurement accuracy. Care must taken to have a uniform surface reflectivity to ensure a reliable measurement response over the entire measurement area.

5.6 Conclusion

The present work presents the development of a new analytical model and experimental study of the ratiometric fluorescence film height measurement method. This method uses two fluorophores, which are dissolved in the fluid, and relies on the fluorescence emission and reabsorption, due to the spectral overlap in the absorption and emission spectra of both fluorophores. The overall fluorescence emission is measured through two narrow bandpass filters, each with a central wavelength near the peak emission wavelength of one of the fluorophores. The ratio between the two fluorescence emission intensities varies with the film height.

The analytical model is based on the model description as presented by Hidrovo and Hart [1]. The model is extended to include the emission and reabsorption of both fluo-

rophores and the influence of background surface reflectivity. Two different analytical models are developed: one without surface reflection and one with surface reflection. The analytical models are used to study the fluorescence intensities and the corresponding ratio for varying fluorophore concentrations, film heights and surface reflectivities.

The fluorescence spectra of thin fluid films have also been experimentally determined. The results from the analytical model and the measurements combine into an improved understanding of the working principle behind the measurement method and the influence of the various parameters on the measurement response. The simulated and experimental fluorescence ratios agree very well and prove the effectiveness of the analytical model. This model is an efficient design tool which can be used to quickly optimize the measurement response. It can be tuned by the selection of the fluorophores and the corresponding spectral properties, the fluorophore concentrations, and the surface reflectivity.

III

Film height steering

6

A novel concept for film height steering

Part I of this thesis (chapter 2–4) presented various EHL models to describe and analyze the elastohydrodynamic lubrication in the roll-to-plate nanoimprint process. Here, the pressure distributions are determined for a given film height distribution, considering the elastic deformation of the elastomeric roller material and the tensioned web. Chapter 4 also showed that substrate waviness will result in undesired variations in both the film height and pressure distribution.

This chapter presents a new method to steer the film height in elastohydrodynamic lubrication. It is based on inverse lubrication theory, which assumes that the pressure distribution is known beforehand. If so, the problem statement can be inverted, and the film height distribution is determined for a given pressure distribution. If we can apply the desired pressure distribution onto a liquid film, the hypothesis is that we will necessarily end up with the film height distribution that corresponds to this pressure distribution. This concept is explored in a numerical model of a deformable tilting pad slider bearing.

Part of this chapter was presented as:
Snieder, J., & van Ostayen, R. A. J. (2023, September 5–7). *Film height control in hydrodynamic lubrication using inverse Lubrication theory* [conference presentation]. 48th Leeds-Lyon Symposium on Tribology, Leeds, UK.

6.1 Introduction

Various industrial processes, such as squeeze-roll coating, roller-based UV-cure nanoimprinting, or lithographic printing, apply thin liquid films on a solid substrate [41, 43, 77, 96]. In each of these processes, a fluid film is trapped between two sliding surfaces: the substrate and a roller or a tensioned web around a roller. The fluid film height is a key parameter and is typically determined by the interaction between the hydrodynamic forces of the fluid film and the elastic forces of the sliding surfaces. The strong coupling between them is described by elastohydrodynamic lubrication theory [95, 96, 106], which can be used to predict the film height and pressure distribution. Any variations in the surface topography, such as substrate waviness or variations in the substrate thickness or the roller diameter, will result in undesired variations in both the film height and pressure distribution.

A promising method to realize a constant and stable fluid film, irrelevant of variations in the surface topography, is inspired by inverse hydrodynamic lubrication. Inverse hydrodynamic lubrication theory was introduced by Mohrenstein-Ertel [145–147] and further developed by Blok [57]. In this specific mode of fluid film lubrication, the pressure distribution in the lubricated contact is known beforehand. This is typically the case in strongly elastically deformed contacts, such as rubber seals [148–150], or very flexible sliding surfaces, such as foil bearings [57, 59]. The pressure distribution is governed by the large elastic deformation. The fluid film height, which is negligibly small compared to the elastic deformation, does not influence the pressure distribution significantly. The problem definition can therefore be inverted, in comparison to classic hydrodynamic lubrication theory, which is involved with finding the pressure distribution for a given film height distribution. Inverse hydrodynamic lubrication instead is involved with finding the film height distribution that will be generated for a specific pressure distribution [59].

In this chapter, a novel concept is presented to steer the film height distribution in a lubricated contact by applying the corresponding pressure distribution. The working principle and feasibility of this concept are studied in a one-dimensional numerical model. A parameter study is performed to investigate the influence of the various parameters in the numerical model.

6.2 Concept of film height steering

Figure 6.1 explains the concept of film height steering for a tilting pad slider bearing:

1. The first step in Figure 6.1a shows a rigid tilting pad slider bearing. The starting point is the definition of the initially prescribed, desired film height $h_{\text{initial}}(x)$, which is formed between the rigid top and bottom surface. Due to hydrodynamic action, the pressure distribution $p_{\text{initial}}(x)$ is generated. The pressure distribution is balanced with the predefined load, which is applied on the rigid slider.

2. Next, in Figure 6.1b, the rigid slider is replaced with a deformable slider. Ideally, we would like to apply the generated, initial pressure distribution directly to the fluid film, to end up with the corresponding film height distribution. In this concept, we approach this effect by applying a finite number of loads on the deformable slider surface, hereby mimicking the pressure distribution. The applied loads are balanced

with the initial pressure distribution. Therefore, the resulting film height $h(x)$ will be close to the initially prescribed, desired film height $h_{\text{initial}}(x)$.

3. Figure 6.1c shows the last step, in which the rigid substrate surface is no longer flat. The deformable slider will deform conform the substrate non-flatness. As the applied loads are constant in magnitude (i.e., force-controlled), the film height $h(x)$ will again be close to the initially prescribed, desired film height $h_{\text{initial}}(x)$.

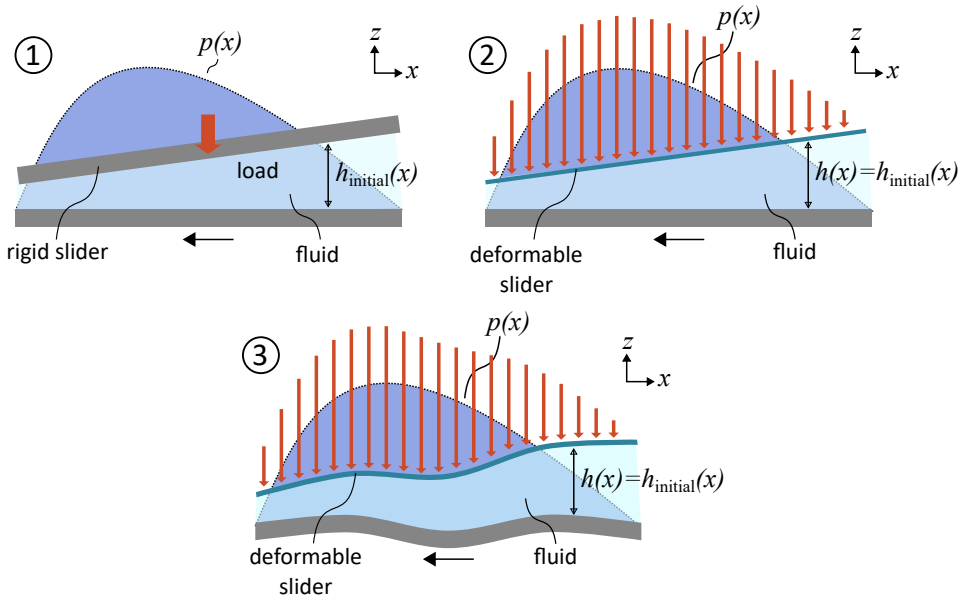

Figure 6.1: Schematic of the working principle behind the film height steering concept.

6.3 Model description

This section describes the setup of the numerical model, including the governing equations and the numerical implementation.

The modeled system geometry can be seen in Figure 6.2. A thin fluid film with a dynamic viscosity η is formed between a deformable slider of length L and a non-flat rigid substrate surface. The waviness of the substrate, which has a constant surface velocity u, is characterized by the wavelength λ_{sub} and the amplitude a_{sub}. The fluid film geometry, which is described by the film height $h(x)$, includes a boosting zone at the leading edge to facilitate the fluid inflow between the slider and the substrate. The final film height h_{f} is found at the trailing edge of the slider. The converging fluid film geometry results in a hydrodynamic pressure build-up $p(x)$ in the fluid film. The stationary, deformable slider elastically deforms because of the pressure build-up from below and the uniformly distributed loads per unit length q_i, which are applied on top of the slider. The sum of these loads per unit length is given by F_{L}. The elastic deformation will affect the film height, in return, and hereby the hydrodynamic pressure build-up.

The model is governed by two physics, which are coupled into an elastohydrodynamic lubrication (EHL) model, as shown in Figure 6.2. The flow modeling in the fluid film is described by lubrication theory and the elastic deformation of the deformable slider is determined by the pure bending of slender beams theory. These physics are solved together to determine the elastic deformation of the deformable slider and the pressure build-up in the fluid film.

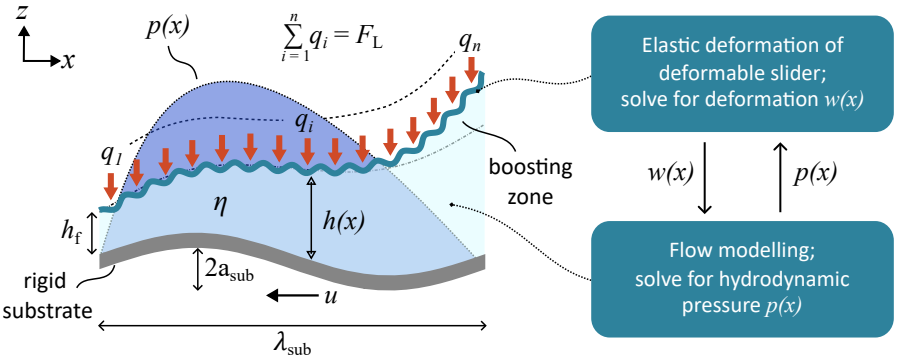

Figure 6.2: Schematic of the deformable slider. The amplitudes of the film height and elastic deformation are highly exaggerated for visualization purposes.

6.3.1 Governing equations

To reduce the number of inputs that determine the solution, the equations are scaled. Before the equations are presented, the definition of the dimensionless variables is discussed. The variables are scaled with the following reference parameters, which are identified by the subscript *r*:

$$\begin{aligned} X &= \frac{x}{x_r}, \quad \Lambda_{sub} = \frac{\lambda_{sub}}{x_r} \\ P &= \frac{p}{p_r}, \quad Q = \frac{q}{p_r x_r} \\ H &= \frac{h}{h_r}, \quad W = \frac{w}{h_r}, \quad A_{sub} = \frac{a_{sub}}{h_r}. \end{aligned} \tag{6.1}$$

The reference parameters are chosen in such a way to minimize the number of input parameters:

$$x_r = L, \quad h_r = \sqrt{\frac{\eta L^2 u}{F_L}}, \quad p_r = \frac{F_L}{L}. \tag{6.2}$$

The dimensionless scaling yields a computational domain with unit length. The dimensionless, steady-state, incompressible Reynolds equation determines the hydrodynamic pressure distribution P for a film height distribution H:

$$\frac{\partial}{\partial X}\left(-H^3 \frac{\partial P}{\partial X} - 6H\right) = 0. \tag{6.3}$$

The Reynolds equation assumes Newtonian fluid behavior and isothermal conditions. Zero pressure boundary conditions are applied on the edges of the domain:

$$P|_{X=0} = 0, \quad P|_{X=1} = 0. \tag{6.4}$$

The definition of the film height distribution differs in each solution step and will be presented in the following subsection. The elastic deformation of the slider is determined with the dimensionless Euler-Bernoulli equation for pure bending of infinitely wide beams:

$$\frac{\partial^2}{\partial X^2}\left(B\frac{\partial^2 W}{\partial X^2}\right) = P - \sum_{i=1}^{n} Q_i \delta(X - X_i). \tag{6.5}$$

The dimensionless bending stiffness number B is defined as:

$$B = \frac{D}{L^2}\sqrt{\frac{\eta u}{F_{\mathrm{L}}^3}}, \tag{6.6}$$

with bending stiffness D. It is a function of the elastic modulus E, Poisson ratio ν and slider thickness t:

$$D = \frac{Et^3}{12(1-\nu^2)}. \tag{6.7}$$

Equation (6.5) determines the elastic deformation of the slider W, which is subjected to the pressure distribution P and a number of n loads per unit length Q_i. The loads are uniformly distributed over the slider length on the locations X_i, which are defined by:

$$X_i = \frac{i - 0.5}{n}. \tag{6.8}$$

The boundary conditions of the slider are free at both ends:

$$\left.\frac{\partial^2 W}{\partial X^2}\right|_{X=0} = 0, \quad \left.\frac{\partial^2 W}{\partial X^2}\right|_{X=1} = 0, \quad \left.\frac{\partial^3 W}{\partial X^3}\right|_{X=0} = 0, \quad \left.\frac{\partial^3 W}{\partial X^3}\right|_{X=1} = 0. \tag{6.9}$$

6.3.2 Solution procedure

The equations are implemented in the finite element method (FEM) software COMSOL Multiphysics ® [151]. The final solution is found in several solution steps, which are executed sequentially. The solution steps are applied on the same computational domain.

1. A schematic of the model setup for the first solution step is shown in Figure 6.3. The goal of this step is to compute the required loads per unit length Q_i to apply to the slider. The pressure distribution P is determined for an initially prescribed, desired film height distribution H, as defined in Equation (6.10). The slider deformation is not yet included in this step. A virtual boosting zone with film height $H_{\mathrm{b,i}}$ is introduced at the leading edge of the slider to facilitate the fluid inflow between the slider and the substrate. Moreover, the pressure distribution is balanced by a given load per unit length F_{L}. The dimensionless load equilibrium in Equation (6.12) is

satisfied by adjusting the film height offset $H_{0,\mathrm{i}}$. In this step, a temporary boundary condition is used to determine the loads per unit length Q_i. The slider is pinned at the locations X_i, as defined by Equation (6.8). The loads per unit length Q_i are then given by the resulting reaction forces to keep the slider displacement in these locations at zero while being subjected to the pressure distribution.

2. Figure 6.4 shows the model setup for the second solution step. The slider deformation is added to the film height definition, see Equation (6.13). The flexibility of the slider allows it to deform towards the initially prescribed, desired film height distribution. It is important to understand that the film height offset H_0 and inclination parameter k_x effectively determine the position and orientation of the slider. The film height offset H_0 is found with the load equilibrium in Equation (6.14), by balancing the pressure distribution with the applied loads per unit length. The inclination parameter k_x is determined with Equation (6.15), by balancing the moments which are applied on the slider. The slider deformation on top of the rigid body motion is determined with the beam equation in Equation (6.5). As the beam is essentially floating in space, any rigid body motion of the beam itself is suppressed by the integrals in Equation (6.16).

3. In the last step, which is shown in Figure 6.5, the substrate waviness is added to the film height definition, see Equation (6.17). The substrate motion can be simulated in a quasi-static manner, by varying the position shift variable X_{shift}, hereby effectively moving the substrate waviness underneath the slider. Moreover, the load equilibrium and moment equilibrium from Equation (6.14) and Equation (6.15), respectively, are applied in this step as well.

Solution step 1

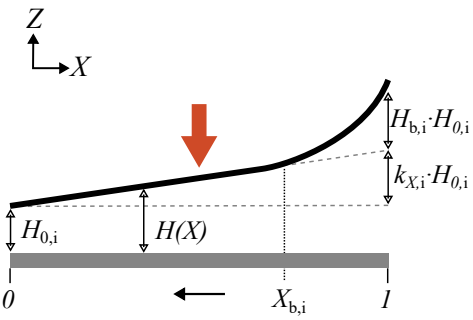

Figure 6.3: Model setup - solution step 1.

Film height:

$$H = H_{0,\mathrm{i}}\left(1 + k_{x,\mathrm{i}}X + H_{\mathrm{b,i}}\right), \tag{6.10}$$

$$H_{\mathrm{b,i}} = \begin{cases} 0 & \text{for } X < X_{\mathrm{b,i}}, \\ k_{\mathrm{b,i}}\left(\frac{X - X_{\mathrm{b,i}}}{X_{\mathrm{b,i}}}\right)^2 & \text{for } X \geq X_{\mathrm{b,i}}, \end{cases} \tag{6.11}$$

with the initially prescribed film height offset $H_{0,\mathrm{i}}$, inclination parameters $k_{x,\mathrm{i}}$ and $k_{\mathrm{b,i}}$, and boosting zone position $X_{\mathrm{b,i}}$.

Load equilibrium:

$$\int_0^1 P \,\mathrm{d}X = 1. \tag{6.12}$$

Solution step 2

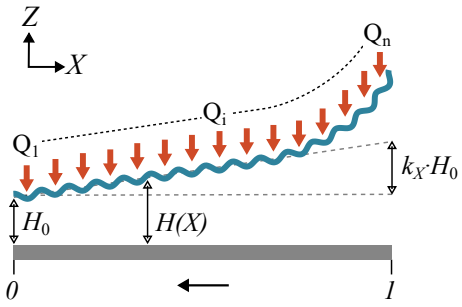

Figure 6.4: Model setup - solution step 2.

Film height:

$$H = H_0\,(1 + k_x X) + W. \tag{6.13}$$

Load and moment equilibrium:

$$\int_0^1 P\mathrm{d}X = \sum_{i=1}^{n} Q_i, \tag{6.14}$$

$$\int_0^1 PX\mathrm{d}X = \sum_{i=1}^{n} Q_i X_i. \tag{6.15}$$

Rigid body motion suppression:

$$\int_0^1 W\,\mathrm{d}X = 0, \quad \int_0^1 \frac{\partial W}{\partial X}\,\mathrm{d}X = 0. \tag{6.16}$$

Solution step 3

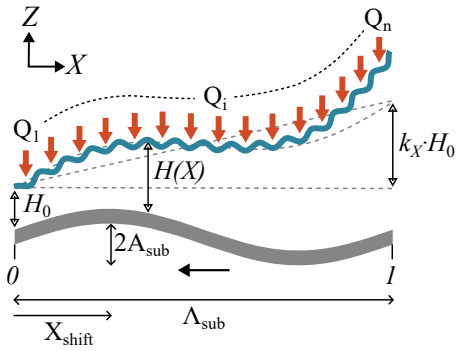

Figure 6.5: Model setup - solution step 3.

Film height:

$$H = H_0\,(1 + k_x X) + W - H_{\mathrm{sub}}, \tag{6.17}$$

The substrate waviness H_{sub} is defined as:

$$H_{\mathrm{sub}} = A_{\mathrm{sub}} \cos\left(\frac{2\pi}{\Lambda_{\mathrm{sub}}}\,(X - X_{\mathrm{shift}} - 0.5)\right). \tag{6.18}$$

The factor 0.5 positions the waviness, such that the peak is centered with respect to the slider.

6.4 Results and discussion

The numerical model is solved for the input parameters as listed in Table 6.1. The resulting scaling parameters, which are determined with Equation (6.1), are shown in Table 6.2. The dimensionless scaling of the governing equations yield a minimal set of parameters which fully describe the numerical problem. These parameters are divided in the bearing parameters and the substrate waviness parameters.

- Bearing parameters:
  - dimensionless bending stiffness number B,
  - number of applied loads n,
  - initially prescribed inclination parameter $k_{x,\mathrm{i}}$,
  - initially prescribed inclination parameter $k_{\mathrm{b,i}}$,
  - boosting zone location X_{b}.
- Substrate waviness parameters:
  - amplitude A_{sub},
  - wavelength Λ_{sub},
  - waviness position shift X_{shift}.

Two parameter studies are performed to show the influence of the bearing parameters and the substrate waviness parameters on the pressure and film height distribution, respectively. In the first parameter study, the bearing parameters are varied in the numerical model of a deformable slider on a flat substrate. In the second parameter study, the substrate waviness parameters are varied for a fixed set of bearing parameters to study the behavior of the deformable slider on a wavy substrate.

Table 6.1: Input parameters.

Parameter	Value	Unit
L	50	mm
F_{L}	200	$\mathrm{N\,m^{-1}}$
η	10	mPa s
u	0.5	$\mathrm{m\,s^{-1}}$
E	3	MPa
ν	0.4	-
t	0.15	mm

Table 6.2: Scaling parameters.

Parameter	Value	Unit
x_{r}	50	mm
h_{r}	250	µm
p_{r}	4000	Pa

6.4.1 Variation of the bearing parameters

In this parameter study, the numerical model is solved for a variation of the bearing parameters to illustrate the ability of the slider to deform towards the initially prescribed, desired film height profile. As substrate waviness is excluded, it is only required to solve the first two solution steps of the numerical solution procedure in Section 6.3.2.

The starting point of the parameter study is the set of nominal bearing parameters in Table 6.3. From here, the dimensionless bending stiffness number B, the number of applied loads n, and the initially prescribed inclination parameter $k_{x,\mathrm{i}}$ are varied around their nominal value one at a time, while the other parameters are fixed.

Table 6.3: Nominal bearing parameters.

Parameter	Value	Unit
B	1×10^{-5}	-
n	15	-
$k_{x,\mathrm{i}}$	1.2	-
$k_{\mathrm{b,i}}$	2	-
$X_{\mathrm{b,i}}$	2/3	-

The results of the parameter study can be seen in Figure 6.6. Each plot shows the dimensionless film height and pressure distributions for a variation of one of the bearing parameters, while the other bearing parameters are fixed. The initially prescribed, desired film height distribution and corresponding pressure distribution are indicated by the dashed lines. They are the resulting distributions of the first solution step in Section 6.3.2. Overall, it can be seen that the film height and pressure distributions closely resemble the initially prescribed, desired distributions.

Figure 6.6a shows the result for a variation of the dimensionless bending stiffness number B. The flexibility of the slider allows it to elastically deform towards the initially prescribed, desired film height distribution. As a result, a physical boosting zone is created near the leading edge, due to the global elastic deformation of the slider. The physical shape approaches the virtual boosting zone of the initially described, desired film height distribution for a decreasing dimensionless bending stiffness number. At the same time, the local elastic deformation of the slider increases as well. A wavy deformation pattern can be observed, due to the combination of the discrete loads on top of the slider and the hydrodynamic pressure distribution acting from below. The elastic deformation affects the film height and hereby the pressure distribution. However, the variation in the pressure distributions is relatively small and the final pressure distributions for a variation of the dimensionless bending stiffness number B are very close to the reference distribution.

The result for a variation of the number of applied loads n is shown in Figure 6.6b. When the number of applied loads is increased, the distance between the applied loads decreases and therefore the elastic deformation of the slider decreases as well. The film height and pressure distributions are close to the reference distributions.

Figure 6.6c shows the result for a variation of the initial inclination parameter $k_{x,\mathrm{i}}$. This parameter effectively changes the orientation of the slider. Because of this change, the pressure distribution shifts. For each value of the inclination parameter, the slider is well able to approach the initially prescribed, desired film height distribution and the corresponding pressure distribution.

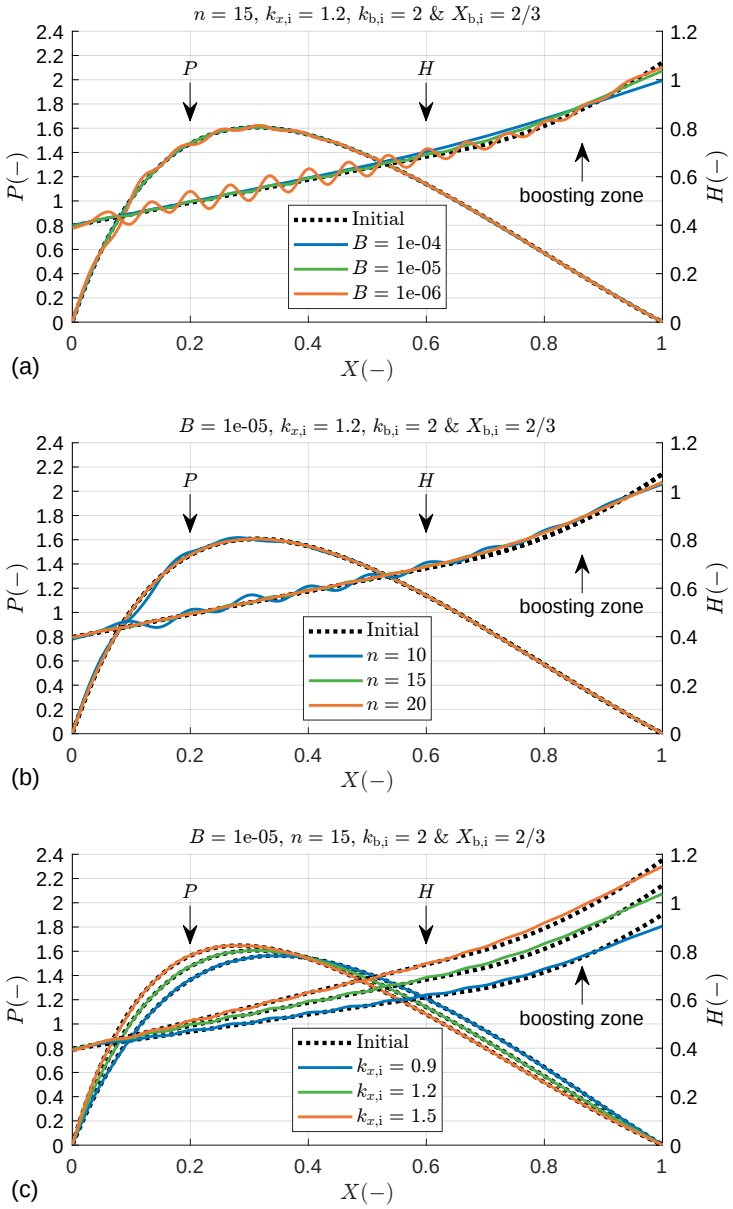

Figure 6.6: Film height and pressure distributions for a deformable slider on a flat substrate surface for a variation of the bearing parameters. The initially prescribed, desired film height and pressure distributions are indicated by the dashed lines. (a) Variation of the dimensionless bending stiffness number B. (b) Variation of the number of loads per unit length n. (c) Variation of the inclination parameter $k_{x,\mathrm{i}}$.

6.4.2 Variation of the substrate waviness parameters

In this parameter study, the substrate waviness parameters are varied to study their influence on the final film height H_f and the ability of the deformable slider to approach the initially prescribed, desired film height distribution on a wavy substrate. The final film height is found at the trailing edge of the slider at $X = 0$. The numerical model is solved for the nominal bearing parameters as listed in Table 6.3. All solution steps (1-3) of the solution procedure in Section 6.3.2 are computed.

Figure 6.7a shows the result of the slider on a substrate in three situations, which are indicated by (A), (B), and (C). The substrate is flat in situation (B). In situation (A) and situation (C), the substrate shows a waviness with an amplitude A_{sub} of 3 and a wavelength Λ_{sub} of 5. Due to the variation in the substrate waviness position shift X_{shift}, which is either 0 or 0.5, the slider is found above a peak in situation (A) and above a valley in situation (C), respectively. It can be observed that the flexibility of the slider allows it to deform conform the substrate waviness.

The corresponding film height and pressure distributions in Figure 6.7b show little variation. The largest differences are found near the boosting zone at the leading edge. Here, due to the combination of the finite stiffness of the slider and the presence of substrate waviness, the slider is not able to fully conform to the initially prescribed, desired film height distribution. However, all distributions are very close to the desired distributions.

The influence of substrate waviness is further analyzed in Figure 6.8. Here, the final film height H_f, which is found at the trailing edge (at $X = 0$), is shown for a variation of the substrate waviness parameters. The final film height of the initially prescribed, desired film height distribution is indicated by the dotted lines.

Figure 6.8a shows the final film height H_f for a variation of the substrate waviness position shift X_{shift} and the substrate waviness amplitude A_{sub}. By varying the substrate waviness position shift from 0 to 1, the substrate waviness is effectively moved underneath the slider by one substrate waviness wavelength Λ_{sub}. The substrate waviness wavelength itself is fixed at a value of 5, similar to the situation in Figure 6.7.

In the case of a flat substrate, when the substrate waviness amplitude is set to zero, the final film height is constant. It is slightly smaller than the desired value, as can also be observed in Figure 6.7. When substrate waviness is introduced, the final film heights start to oscillate around this constant, due to the slider deformation. The offset increases with an increasing substrate waviness amplitude.

The final film heights for a variation of the substrate waviness wavelength Λ_{sub}, the substrate waviness amplitude A_{sub}, and two different values of the substrate waviness position shift X_{shift} are shown in Figure 6.8b. The plots start at a substrate waviness wavelength of 1, for which it is equal to the length of the deformable slider. The results for each value of the waviness position shift X_{shift} will be discussed separately.

When taking a closer look at the final film heights for the substrate waviness position shift X_{shift} of 0, it is observed that the final film heights for short substrate waviness wavelengths are significantly smaller than the initially prescribed, desired value. The offset increases with an increasing substrate waviness amplitude. From there, the final film heights quickly approach the desired value for longer substrate waviness wavelengths, with a small overshoot around the substrate waviness wavelength of 3. This behavior is best explained by taking a closer look at the film height profiles in the points (A) and (B),

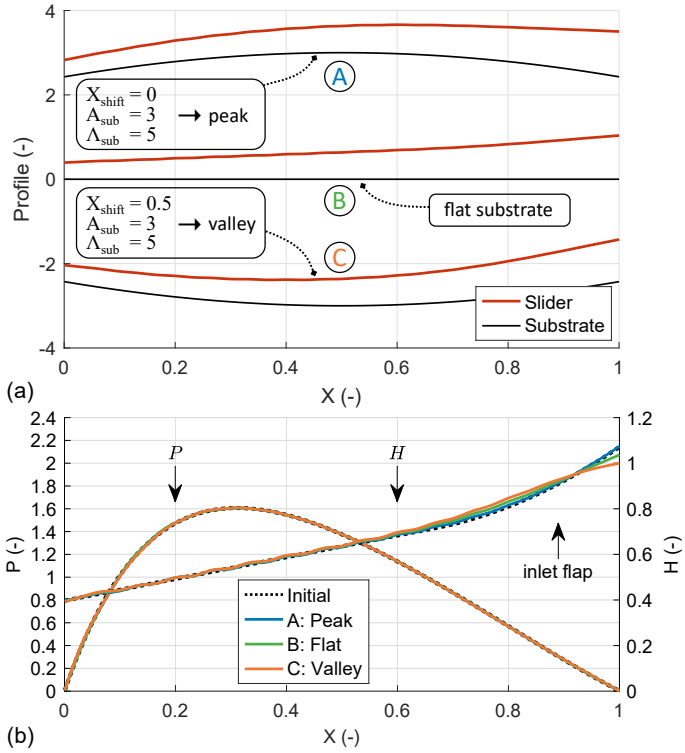

Figure 6.7: (a) Simulated height profiles of the slider on a substrate in three situations: peak (A), flat (B), and valley (C). (b) Corresponding film height and pressure distributions for the three situations.

as indicated in Figure 6.8b. Figure 6.9a shows the film height profile including substrate waviness in point (A), for which the slider is positioned above a peak. Due to the finite stiffness of the deformable slider and the short wavelength of the substrate waviness, the slider is not able to fully deform conform the substrate waviness. As a result, the final film height at (at $X = 0$) is considerably smaller than the initially prescribed, desired value. The film height profile in point (B) is shown in Figure 6.9b. Here, due to the longer substrate waviness wavelength, the slider is well able to deform conform the substrate waviness and the final film height is almost identical to the initially prescribed, desired value.

The final film heights in Figure 6.8b show a different trend for the substrate waviness position shift X_{shift} of 0.5. Here, the final film heights for short substrate waviness wavelengths are significantly larger than the initially prescribed, desired value. The difference with the desired value increases with an increasing substrate waviness amplitude. The film heights quickly approach the desired value for longer substrate waviness wavelengths, with a small undershoot around the substrate waviness wavelength of 3. The film height profiles in point (C) and (D) are shown in Figure 6.9c and Figure 6.9d, respectively. In both figures, the slider is positioned above a valley. The deformable slider is not able to deform towards the wavy substrate with the relatively short wavelength in Figure 6.9c. Therefore, the final film height (at $X = 0$) is considerably larger than the initially prescribed, desired

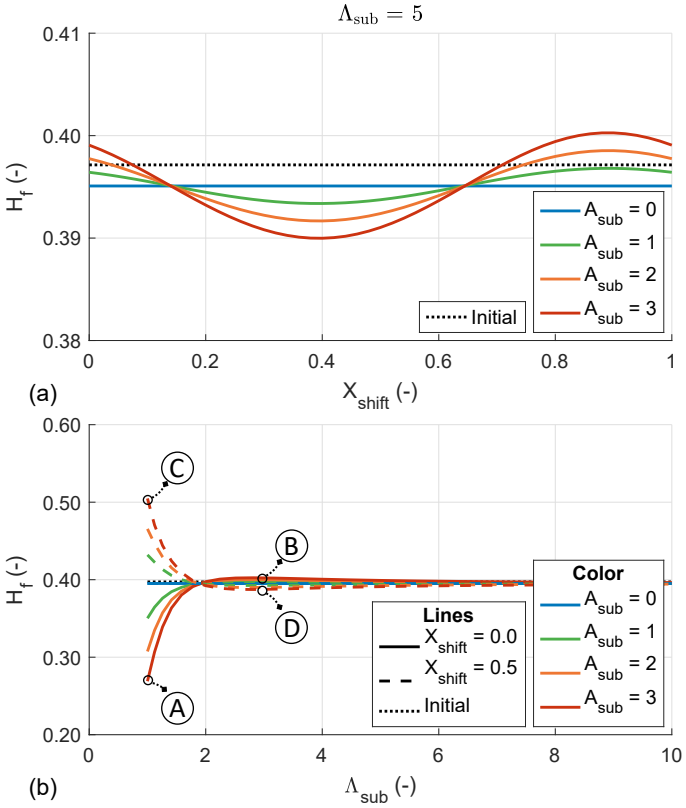

Figure 6.8: Final film height H_f for a variation of the substrate waviness parameters. The dotted lines refer to the final film height of the initially prescribed, desired film height distribution. a) Variation of the substrate waviness position shift X_{shift} and the substrate waviness amplitude A_{sub}. b) Variation of the substrate waviness wavelength Λ_{sub} and the substrate waviness amplitude A_{sub}.

value. The situation is different in Figure 6.9d, where the wavelength is longer. Here, the deformable slider deforms conform the substrate waviness and the final film height (at $X = 0$) is very close to the initially prescribed, desired value.

Overall, the difference between the final film height and the desired value increases for increasing substrate waviness amplitude and decreasing substrate waviness wavelength, as shown in Figure 6.8b. For this specific set of parameters, the final film heights are nearly identical to the desired value from a substrate waviness length of 2 onward. When the substrate waviness is moved underneath the slider, the final film heights will oscillate around the final film height value in the case of a flat substrate, as shown in Figure 6.8a.

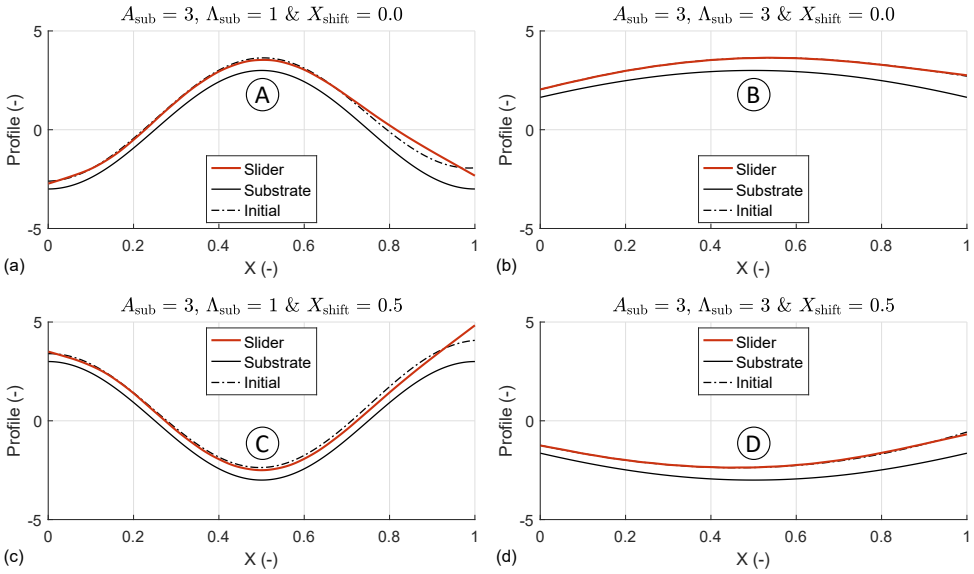

Figure 6.9: Height profiles of the slider including substrate waviness for a variation of the substrate waviness position shift X_{shift} and the substrate waviness wavelength Λ_{sub}. Each figure refers to a point as indicated in Figure 6.8b. The initially prescribed, desired film heights are indicated by the dashed lines.

6.5 Conclusion

This work presents a novel concept to steer the film height distribution in elastohydrodynamic lubrication by applying the corresponding pressure distribution. This concept is demonstrated in a one-dimensional numerical model of a deformable tilting pad slider bearing on a wavy substrate surface. The film height distribution can be steered by applying a number of discrete loads to the deformable slider surface, hereby approaching the pressure distribution of the initially prescribed, desired film height distribution.

The dimensionless setup of the elastohydrodynamic lubrication model yields a minimum set of dimensionless parameters, which are used in two parameter studies. In the first parameter study, the bearing parameters are varied to study the ability of the deformable slider to approach the desired film height distribution on a flat substrate. The results show that the deformable slider is well able to approach the initially prescribed, desired film height distribution for a range of bearing parameters. In the second parameter study, the substrate waviness parameters are varied to study their influence on the final film height near the trailing edge. The results show that the final film height H_F is very close to the desired value, even in the presence of substrate waviness. Differences start to occur when the substrate waviness wavelength is in the same range of the slider length.

In theory, any film height distribution can be realized. The ability of the deformable slider to conform to the desired film height distribution depends on the flexibility of the slider and the number of applied loads. The theoretical results prove the feasibility of the concept to steer the film height. The next step is experimental validation, to verify the performance in practice.

7

Steering and mapping the film height in a deformable slider bearing

The previous chapter presented a novel concept to steer the film height in elastohydrodynamic lubrication, inspired by inverse lubrication theory. This concept was explored in a numerical model of a deformable tilting pad slider bearing. It was shown that the film height distribution can be steered by applying a number of discrete loads to the deformable slider to approach the corresponding pressure distribution in the fluid film.

This chapter presents the experimental validation of the film height steering concept. The numerical model is extended for a two-dimensional deformable tilting pad slider bearing. It is directly used to determine the required loads to approach the pressure distribution. A novel load application with compliant compression springs applies these loads to the deformable slider. Moreover, the film height distribution is mapped with ratiometric fluorescence imaging. This measurement method was introduced and analyzed in Chapter 5.

This chapter, in combination with Chapter 6, is intended for publication in a tribology journal as:
Snieder, J., & van Ostayen, R. A. J. *A novel concept and experimental setup for steering and mapping the film height in a deformable slider bearing.* In preparation.

7.1 Introduction

The film height in elastohydrodynamic lubrication is determined by the interaction between the hydrodynamic forces within the fluid film and the elastic forces of the contacting surfaces. It has been shown that variations in the surface topography lead to undesired variations in both the fluid film geometry and the pressure distribution. In the previous chapter, a novel concept was introduced to steer the film height distribution in elastohydrodynamic lubrication. This concept is inspired by inverse hydrodynamic lubrication, in which the pressure distribution in the lubricated contact is known beforehand [57]. The feasibility was demonstrated through a parameter study using a one-dimensional numerical model of a deformable tilting pad slider.

The concept of film height steering is further explored and experimentally validated. A single slider pad of a tilting pad thrust bearing is used as a simplified test case. Tilting pad thrust bearings are typically used in applications such as turbines, compressors, and marine propulsion systems to manage high loads [56, 152, 153]. Here, the focus is not on their conventional function but on their use as a test platform to study and validate the film height steering concept.

This chapter presents the development of a numerical model and experimental test setup. The numerical model introduced earlier is extended to represent the single slider pad configuration. It is used to determine the required loads to approach the desired pressure distribution. In the experimental setup, the fluid film is formed between the deformable slider and a rotating, transparent surface. The experimental setup includes an innovative method for applying the loads to the deformable slider. It uses a support of compliant compression springs, which can be compressed individually. The film height distribution is mapped using ratiometric fluorescence imaging. This measurement method, which has been introduced earlier, provides a real-time, pixel-wise measurement of the fluid film thickness. Numerical and experimental results are presented for a variation of the viscosity and rotational velocity, offering insight into the system's behavior under different operating conditions. This serves as an initial step to demonstrate how the film height distribution can be manipulated by applying a prescribed load distribution.

7.2 Conceptual design

A high-level overview of the conceptual design of the experimental setup is shown in Figure 7.1. The setup consists of a rotating, transparent disk and a single, stationary, deformable tilting pad slider bearing. The rotating disk holds an amount of fluid (or lubricant), which is retained by an inner and outer border ring. The load that is applied on top of the slider, is discretized and concentrated in an array of point loads. Because of practical limitations, the number of applied loads is limited to 5×5. The loads are applied to load pads, which are bonded to the slider surface. The load pads will locally change the bending stiffness, which is taken into account when setting up the numerical model to determine the required loads. Due to hydrodynamic action, a fluid film is formed between the deformable slider and the transparent disk. The film height is mapped using the ratiometric fluorescence film height measurement. The transparent disk allows for a direct observation of the fluid film from below. The test conditions can easily be varied by changing the rotational speed of the disk or by replacing the fluid to adjust the viscosity.

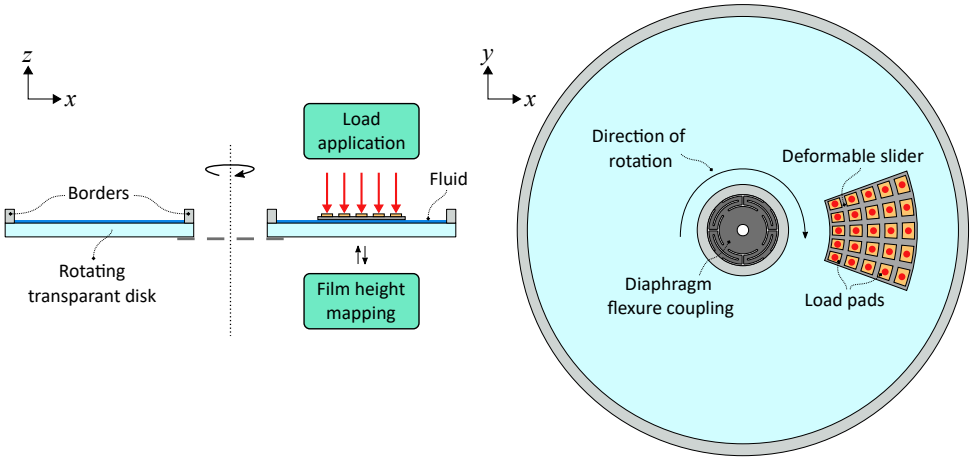

Figure 7.1: Conceptual design of the experimental setup. Left: cross-section side view. Right: top view.

7.3 Model description

This section describes the setup of the numerical model, including the governing equations and the numerical implementation. The approach is similar to the one-dimensional model setup in the previous chapter.

The modeled slider geometry is shown in Figure 7.2. It is defined by the inner radius R_i, outer radius R_o, and the slider angle θ_s. The mean radius R_m is shown for reference. The angle θ_b defines the location of the boosting zone, which will be explained in Section 7.3.2. The loads are applied to the yellow load pads, which are distributed over the slider surface. They are indicated by domain Ω_p, which is a subset of the full computational domain Ω with domain boundary $\partial\Omega$. The numbering of the load pads is shown as well. The rotating disk has a clock-wise rotational speed ω. The fluid enters the contact zone at the leading edge and leaves the contact zone at the trailing edge [154]. For clarity, the slider geometry along the mean radius R_m is shown to the right in Figure 7.2. The fluid film with film height distribution h and film height offset h_0 is defined between the deformable slider surface and the flat disk surface. The boosting zone with film height h_b is discussed in Section 7.3.2. The converging fluid film geometry results in a hydrodynamic pressure build-up p in the fluid film. The deformable slider will deform because of the pressure build-up from below and the uniformly distributed loads F_{ij} on top. The elastic deformation will affect the film height distribution in return, and hereby the hydrodynamic pressure build-up.

The model is governed by two physics, which are coupled into an elastohydrodynamic lubrication (EHL) model. The flow modeling in the fluid film is described by lubrication theory and the elastic deformation of the deformable slider is determined by Kirchhoff–Love theory for thin plates. These physics are solved together to determine the elastic deformation of the deformable slider and the pressure build-up in the fluid film.

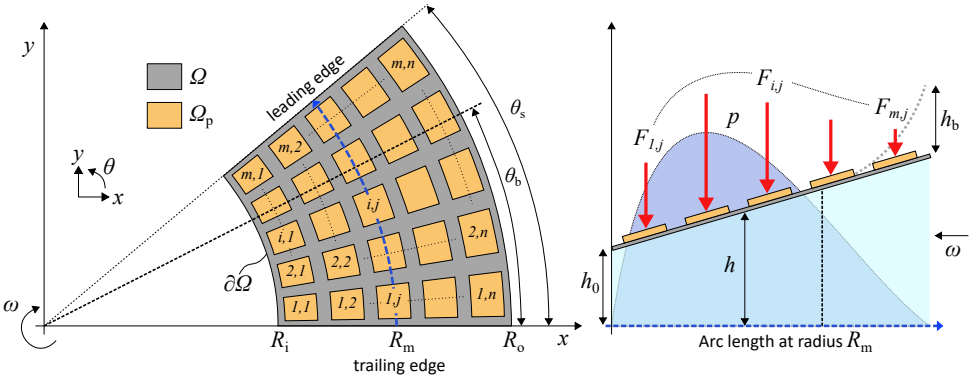

Figure 7.2: Left: the deformable slider geometry and computational domain. Right: slider geometry along the mean radius R_m.

7.3.1 Governing equations

The equations are applied on the computational domain Ω as shown in Figure 7.2. For readability and ease of comparing the numerical results with the experimental results, the equations are presented in dimensional format. The steady-state, incompressible Reynolds equation determines the hydrodynamic pressure distribution p for a film height distribution h:

$$\nabla\left(-\frac{h^3}{12\eta}\nabla p+\frac{h\omega}{2}\begin{bmatrix}+y\\-x\end{bmatrix}\right)=0,\quad\text{with}\quad\nabla=\begin{bmatrix}\frac{\partial}{\partial x}\\\frac{\partial}{\partial y}\end{bmatrix}. \tag{7.1}$$

Here, η is the dynamic viscosity of the resin, and ω is the rotational speed of the rotating disk. The Reynolds equation assumes Newtonian fluid behavior and isothermal conditions. Zero pressure boundary conditions are applied on domain boundary $\partial\Omega$. The definition of the film height distribution differs in specific solution steps and will be presented in the following subsection.

The elastic deformation of the slider is determined with Kirchhoff–Love thin plate theory for a transversely loaded, anisotropic, homogeneous plate [101]:

$$\nabla^2\left[D(x,y)\nabla^2 w\right]=-p+\sum_{i=1}^{m}\sum_{j=1}^{n}F_{ij}\delta\left(x-x_{ij},y-y_{ij}\right),\quad\text{with}\quad\nabla=\begin{bmatrix}\frac{\partial}{\partial x}\\\frac{\partial}{\partial y}\end{bmatrix}. \tag{7.2}$$

The bending stiffness $D(x,y)$ is not constant and varies over the surface, due to the presence of the load pads, which are indicated by domain Ω_p in Figure 7.2. The nominal bending stiffness of the slider surface is described by the elastic modulus E, Poisson ratio ν and slider thickness t:

$$D=\frac{Et^3}{12(1-\nu^2)}. \tag{7.3}$$

An effective bending stiffness is selected for the domain of the load pads. Here, the bending stiffness is five times the nominal bending stiffness of the slider. Equation (7.2) determines

the elastic deformation of the slider w, which is subjected to the pressure distribution p and a number of loads per unit length F_{ij}. The loads are concentrated on the centers of the load pads, which are distributed over the slider surface. Free boundary conditions are applied to the domain boundary $\partial\Omega$.

7.3.2 Solution procedure

The equations are implemented in the finite element method (FEM) software COMSOL Multiphysics ® [151]. The final solution is found in two steps, which are executed sequentially, using the same computational domain. This approach is similar to the first two solution steps in Chapter 6.

- Step 1

  The goal of this step is to compute the required loads F_{ij}, which are applied to the slider. The pressure distribution is determined for the initially prescribed, desired film height distribution. The slider deformation is not yet included in this step. A virtual boosting zone with film height $h_{\mathrm{b,initial}}$ is introduced at the leading edge of the slider to facilitate the fluid inflow between the slider and the disk. The film height in this step is then given by:

$$h = h_{0,\mathrm{initial}}\left(1 + k_{x,\mathrm{initial}}\left(\frac{x - R_\mathrm{i}}{R_\mathrm{o} - R_\mathrm{i}}\right) + k_{y,\mathrm{initial}}\left(\frac{y}{R_\mathrm{o} - R_\mathrm{i}}\right) + h_{\mathrm{b,initial}}\right),$$
$$h_{\mathrm{b,initial}} = \begin{cases} 0 & \text{for } \theta < \theta_\mathrm{b}, \\ k_{\mathrm{b,initial}}\left(\frac{\theta - \theta_\mathrm{b}}{\theta_\mathrm{s} - \theta_\mathrm{b}}\right)^2 & \text{for } \theta \geq \theta_\mathrm{b}, \end{cases} \quad \text{with } \theta = \operatorname{atan2}(y, x) \tag{7.4}$$

  With initial film height offset $h_{0,\mathrm{initial}}$, inclination parameters $k_{x,\mathrm{initial}}$, $k_{y,\mathrm{initial}}$ and $k_{\mathrm{b,initial}}$, and boosting zone angle θ_b. The pressure distribution is balanced by a given load F_tot:

$$\int_\Omega p \, \mathrm{d}A = F_\mathrm{tot}. \tag{7.5}$$

  The load equilibrium is satisfied by adjusting the film height offset $h_{0,\mathrm{initial}}$ in Equation (7.4). The slider is pinned at the locations (x_{ij}, y_{ij}), as indicated in Figure 7.2. The loads F_{ij} are then given by the resulting reaction forces to keep the slider displacement in these locations at zero while being subjected to the pressure distribution p from below.

- Step 2

  In this step, the slider deformation is added to the definition for the film height distribution:

$$h = h_0\left(1 + k_x\left(\frac{x - R_\mathrm{i}}{R_\mathrm{o} - R_\mathrm{i}}\right) + k_y\left(\frac{y}{R_\mathrm{o} - R_\mathrm{i}}\right)\right) + w, \tag{7.6}$$

  The boosting zone film height h_b from the first step is omitted. The slider will slightly deform to approach the initial film height distribution. It is important to understand that the film height offset h_0 and inclination parameters k_x and k_y now effectively

determine the position and orientation of the slider. The film height offset h_0 is found with the load equilibrium in Equation (7.7), by balancing the pressure distribution with the applied loads. The inclination parameters k_x and k_y are determined with Equation (7.8) and Equation (7.9), by balancing the moments which are applied on the slider. The load and moment balances are given by:

$$\int_\Omega p \, \mathrm{d}A = \sum_{i=1}^{m} \sum_{j=1}^{n} F_{ij}, \tag{7.7}$$

$$\int_\Omega px \, \mathrm{d}A = \sum_{i=1}^{m} \sum_{j=1}^{n} F_{ij} x_{ij}, \tag{7.8}$$

$$\int_\Omega py \, \mathrm{d}A = \sum_{i=1}^{m} \sum_{j=1}^{n} F_{ij} y_{ij}. \tag{7.9}$$

The slider deformation on top of the rigid body motion is determined with the beam equation in Equation (7.2). As the plate is essentially floating in space, any rigid body motion of the plate itself is suppressed by the following global boundary conditions:

$$\int_\Omega w \, \mathrm{d}A = 0, \tag{7.10}$$

$$\int_\Omega \frac{\partial w}{\partial x} \, \mathrm{d}A = 0, \tag{7.11}$$

$$\int_\Omega \frac{\partial w}{\partial y} \, \mathrm{d}A = 0. \tag{7.12}$$

The system of equations is iteratively solved.

7.3.3 Parameters

The geometry and material properties of the slider are listed in Table 7.1. They are based on the slider which is used in the experimental setup. Table 7.2 shows the input parameters for the first step of the numerical model.

Table 7.1: Slider parameters.

Parameter	Value	Unit
R_i	50	mm
R_m	75	mm
R_o	100	mm
θ_s	40	deg
E	2	MPa
ν	0.33	-
t	0.55	mm

Table 7.2: Model input parameters.

Parameter	Value	Unit
$k_{x,\mathrm{initial}}$	0	-
$k_{y,\mathrm{initial}}$	1.3	-
$k_{\mathrm{b,initial}}$	3	-
θ_b	$\frac{2}{3} \times \theta_\mathrm{s}$	deg
F_tot	10	N
η	0.9 / 8.6 / 16.3	mPa s
ω	40 / 60 / 80	RPM

7.4 Experimental setup

This section describes the experimental setup and the test conditions.

7.4.1 Hardware configuration

The experimental setup is shown in Figure 7.3 and Figure 7.4. In both figures, the disk is in motion and a fluid film is formed between the deformable slider and the rotating disk. The setup consists of a mechanical part and an imaging part.

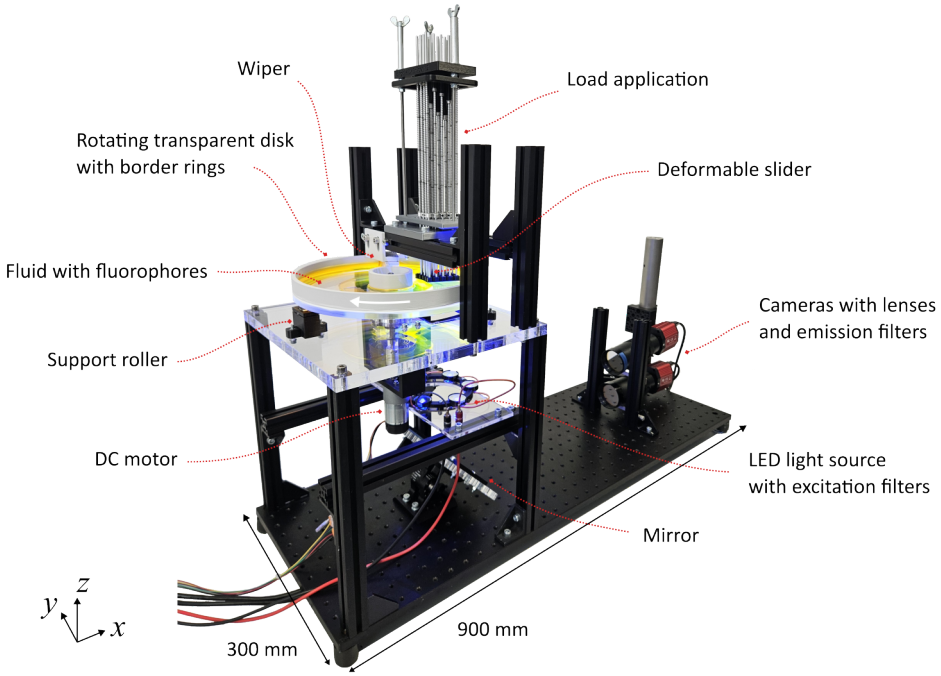

Figure 7.3: Experimental setup. The arrow indicates the direction of rotation.

The mechanical part contains the rotating disk, actuation, deformable slider, and the load application. The components are all mounted to a thick PMMA base plate. The rotating disk is made of highly transparent glass. It has a diameter of 250 mm and a thickness of 10 mm. The disk is rotated with a speed-controlled DC motor[1]. The output shaft of the motor is connected to the disk with a flexible diaphragm coupling for proper control of the degrees of freedom of the disk [155], see also Figure 7.1. The coupling is fabricated out of 0.2 mm thick laser-cut steel precision foil. It allows the disk to freely move in z, Rx, and Ry, while being constrained in x, y, and Rz (rotation of motor output shaft). Therefore, the disk is always in contact with the three crowned support rollers from below. An inner and outer border ring are bonded to the glass surface to retain the fluid, which is uniformly distributed before it reaches the deformable slider by the installed wiper. The

[1]DC motor: Pololu 4693 - 50:1 metal gear motor 24V with 64 CPR encoder.
Speed-control: Jrk G2 18v19 USB Motor Controller via the Jrk G2 software.

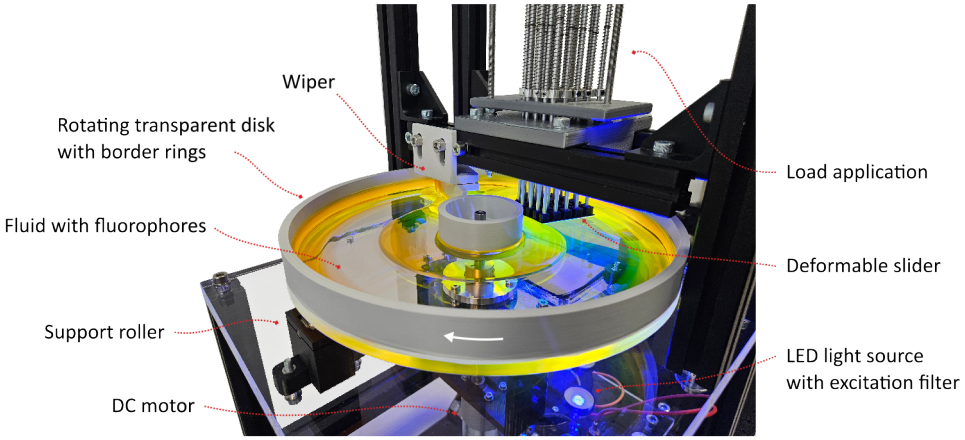

Figure 7.4: Close-up of the experimental setup. The arrow indicates the direction of rotation.

deformable slider is fabricated out of a flat polystyrene (PS) sheet of 0.55 mm thickness. The dimensions are listed in Table 7.1. It has an elastic modulus of 2.01 GPa, which has been determined in a 3-point bending test. The slider edges are finely sanded to ensure a well-defined contact between the slider surface and the rotating disk and to facilitate the fluid supply. The load pads are formed by a grid of 3D printed cells, which is bonded to the slider surface. The bonding layer[2] remains flexible and allows some motion between the 3D printed cells and the slider surface. This also justifies the use of an effective bending stiffness in the numerical model.

The load application is used to apply the loads to the deformable slider. It consists of a grid of 5 × 5 spring columns and the design shows some resemblance with a spring-bed support [156]. A schematic of the working principle of the load application can be seen in Figure 7.5. It shows a cross-section of five spring columns along the mean radius R_m, as indicated in Figure 7.2. Each spring column contains four compliant compression springs in series[3], which are placed around a lightweight, hollow aluminum tube. The effective spring stiffness of each spring column is equal to 0.025 N mm^{-1}. By compressing the stacked springs, a compression force is generated. The required forces and corresponding compression distances are determined in the numerical model. Here, the spring column weight is taken into account. The compression distances are then applied to the compression springs with a 3D printed profile comb, which is placed over the aluminum tubes. The aluminum tubes transfer the compression spring forces to the load pads on the deformable slider. Each load pad is equipped with a pocket to center the aluminum tube. Moreover, a small steel ball is glued to the aluminum tube ends, to approach a point contact. The load application has a few noteworthy advantages:

- In theory, any combination of loads can be applied to the deformable slider, by simply swapping the profile comb. Of course, the limits of the compression springs must be taken into account. These are usually provided by the manufacturer.

[2]Bonding layer: 3M 7955MP double sided transfer tape.
[3]Compression springs: Tevema D10855.

- The load application uses compliant compression springs, which are heavily compressed. Therefore, the applied loads are relatively constant. Any deformation of the deformable slider will not have a large impact on the magnitude of the applied loads.

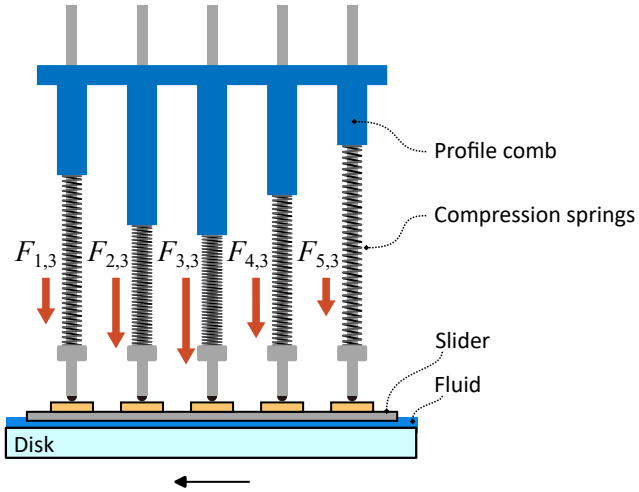

Figure 7.5: Cross-section of the load application along the mean radius R_m.

The imaging part contains the imaging components for the film height mapping. It uses high-power light-emitting diodes (LED) for illumination and various optical elements (lenses and excitation filters) to direct the LED light in the fluid film. The lubricant mixtures with dissolved fluorophores have a natural orange color. As the fluorophores are excited by the the blue LED light, they emit a green-yellow fluorescent light, as can be seen in Figure 7.3 and Figure 7.4. Other imaging components (mirror, emission filters, lenses, and cameras) are used to capture the fluorescence intensities, which are processed to obtain the film height map. More information about the imaging setup and the measurement method can be found in Section 7.4.2.

7.4.2 Ratiometric fluorescence imaging

The basic working principle of fluorescence and its use in film height mapping is explained. For a detailed explanation, the reader is referred to Chapter 5. Fluorescence is the process in which a fluorophore or fluorescent dye absorbs a photon at a specific wavelength and re-emits this photon at a higher, lower-energy wavelength [121, 122]. This phenomenon can be utilized to measure the fluid film height.

In laser-induced fluorescence (LIF), a fluorescent dye is dissolved in the lubricant and excited by a monochromatic light source (laser or LED). The emitted light intensity is a measure of the number of fluorophore molecules, which can be related to the film height [119, 130]. The emitted light intensity is directly proportional to the excitation light intensity, which is challenging to control accurately and can easily vary across the measurement surface and in time. To eliminate this dependency, ratiometric fluorescence

was introduced by Hidrovo and Hart [1]. This method was originally presented as emission reabsorption laser-induced fluorescence (ERLIF) and was used to measure the fluid film height between two stationary quartz plates. Ratiometric fluorescence imaging employs two fluorescent dyes, which are dissolved in the lubricant. The technique is best explained by the excitation and emission spectra, which characterize the fluorescent behavior of the fluorophores. The normalized spectra for Fluorescein and Eosin Y, which are used in this work, are shown in Figure 7.6. This figure also shows the spectrum of the LED light excitation source. The excitation spectrum describes the amount of photon absorption for each wavelength. After absorption, the photon is re-emitted at a higher wavelength. The probability of a photon emission at a specific wavelength is described by the emission spectrum. It is spectrally red-shifted relative to the excitation spectrum.

A large spectral overlap can be observed between the emission spectrum of Fluorescein and the excitation spectrum of Eosin Y. Photons emitted by Fluorescein can be absorbed by Eosin Y before they leave the fluid film, and re-emitted at higher wavelengths. As a result, the Fluorescein emission in the spectral overlap region is lowered and the overall fluorescence emission shows a red-shift. The probability of reabsorption depends on the fluid film height. Thicker films result in longer photon travel paths and a higher probability of reabsorption. The amount of reabsorption and corresponding red-shift is measured by capturing the overall fluorescence emission at two small wavelength bands, using spectral filters. These are typically chosen around the peak emission wavelengths for the highest measurement sensitivity [120]. The ratio between the two fluorescence emission intensities is a dimensionless measure of the film height, which is defined as:

$$\text{ratio} = \frac{\text{fluorescence emission through 540 nm filter}}{\text{fluorescence emission through 520 nm filter}} \tag{7.13}$$

By taking the ratio, measurement errors due to optical distortions and variations in excitation light are minimized. Calibration is required to find the relation between the fluorescence emission ratio and the film height [1, 135].

The optical setup and imaging components for ratiometric fluorescence imaging are shown in Figure 7.3 and Figure 7.4. The optical design is illustrated in Figure 7.7.

Excitation of the fluorophores is performed with six high-power, royal blue LED lights[4]. The LED light ring design is based on uniform illumination of distant targets with LED lights [157]. Each LED is equipped with a clip-on lens[5] to achieve the desired beam emission type for a uniform light distribution. Uniform illumination of the fluid film is not required for ratiometric fluorescence imaging, as the fluorescence emission ratio does not depend on the excitation light intensity. However, it is still beneficial for a uniform fluorescence emission intensity and high signal-to-noise ratio over the entire measurement area. The LED lights are covered with a 500 nm shortpass excitation filter to limit bleeding of the LED light into the camera filters, due to reflections of the LED light on the glass disk surface. The illumination is synchronized with the image acquisition to minimize light exposure outside of the imaging periods and reduce potential photobleaching of the fluorophores.

[4]LED light source: New Energy Cree Starboard XPE, 450-465 nm.
[5]Clip-on lens: LEDil FP11076 LISA2-W-CLIP.

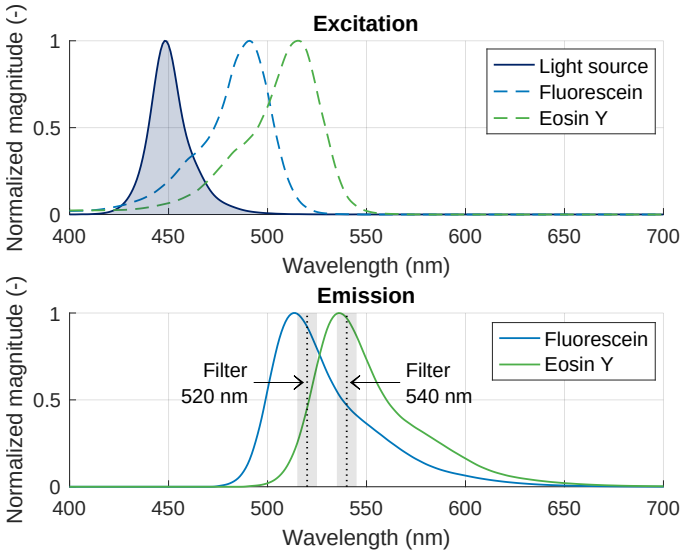

Figure 7.6: Measured excitation and emission spectra of Fluorescein and Eosin Y. The light source spectrum and spectral filters are shown as well.

Two scientific cameras[6] are used to capture the fluorescence emission at different wavelength bands. The upper camera is placed under a small angle (approximately 6°) to minimize disturbance of LED reflections. Each camera is equipped with a fixed focal length lens[7] and a large diameter spectral 10 nm bandpass filter. Camera A has a 520 nm center wavelength filter and camera B has a 540 nm center wavelength filter. A high-quality aluminum mirror (reflection over 95%) is used to view the fluid film from below. The mirror is deliberately installed to keep the entire setup low to ground, for increased stability. The camera images are acquired simultaneously and are post-processed in software. After subtracting the predetermined camera bias from each pixel gray value, the images are superimposed and aligned by using a predetermined projective transformation matrix. This is also referred to as image registration. The fluorescence emission ratios are computed by dividing the corresponding pixel intensities of both images. Finally, the pixel-wise film height map is found using the predetermined calibration curve, which correlates the ratio to the film height. The concentration of each fluorophore is equal to $0.4\,\mathrm{mmol\,L^{-1}}$, for which preliminary measurements have showed a high variation in ratio over the film heights of interest. Both fluorophores are dissolved in the fluid. The pH-value is increased to about 10 with sodium hydroxide (NaOH). An alkaline environment gives the highest quantum yields and ensures well-defined excitation and emission spectra [137, 139]. The ratiometric fluorescence imaging parameters are tuned for a good signal range and high signal-to-noise ratio. To achieve a high measurement signal-to-noise ratio, the measured signal intensities should be maximized within the desired film height range, while avoiding saturation of the camera pixels. Since the cameras are imaging a moving object, the

[6]Camera: Thorlabs CS126MU Kiralux 12.3 MP monochrome CMOS camera, 12-bit.
[7]Edmund Optics TECHSPEC® 75 mm DF Series.

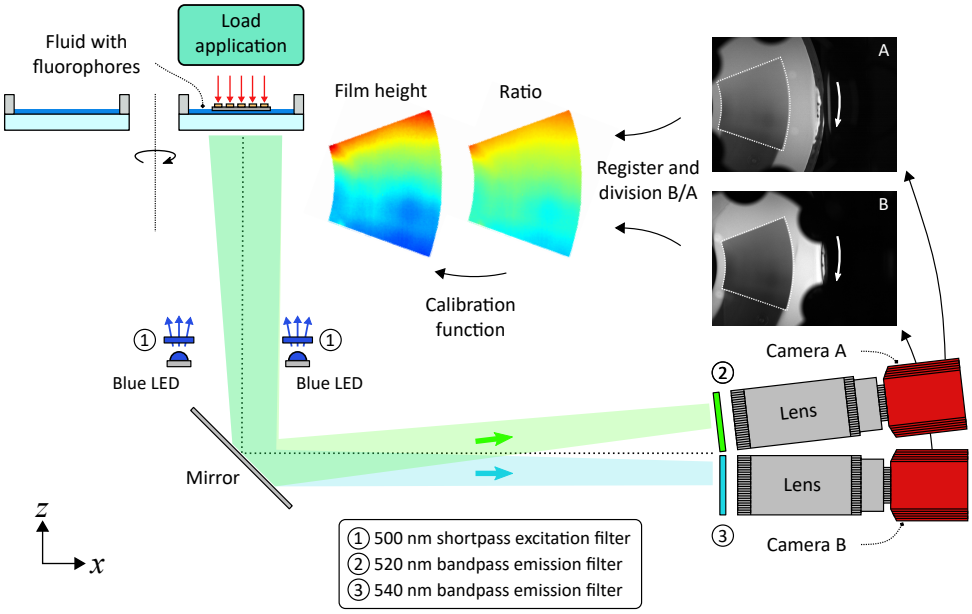

Figure 7.7: Schematic overview of the optical setup for ratiometric fluorescence imaging and data processing of the acquired images.

exposure time should be minimized to effectively capture a 'snapshot' of the fluid film. At a rotational speed of 60 RPM, the average contact transit time at the mean radius is about 111 ms. The exposure time must be considerably shorter to minimize blurring. Preliminary tests have been performed to tune the parameters: a LED light current of 0.2 A for each LED, pixel binning of 8×8, and a camera exposure time of 2 ms are selected. The pixel binning results in a decreased image resolution. However, the physical resolution is still 0.26 mm per binned pixel width and height, which is more than sufficient to accurately map the fluid film geometry. An additional advantage is that the pixel binning results in a reduced image file size (372 kb per image), which is beneficial for the data processing speed.

An illustrative example of the ratiometric fluorescence technique is shown in Figure 7.8. Here, a collectors coin of the SS Rotterdam is placed upside down in a thin fluid film with dissolved fluorophores, see Figure 7.8d. The fluid film height varies over the coin surface due to the coin surface topography. Ratiometric fluorescence imaging is used to reveal the surface topography. Thick fluid films are found on the receding areas, while thinner films are formed on the protrusions. The measured intensities through the spectral filters are shown in Figure 7.8a and Figure 7.8b, while the inverse ratio between them can be seen in Figure 7.8c. Here, the inverse ratio is deliberately shown, because the coin surface topography is the inverse of the film height. The fine details in both the ship figure and text are clearly distinguishable in the inverse ratio plot. Moreover, the magnitude of the inverse ratio differs over the coin surface, due to the variations in film height. This example nicely illustrates the ratiometric fluorescence technique and its ability to measure

the fluid film height. Of course, calibration of the method is still required to determine the relation between the ratio and the film height.

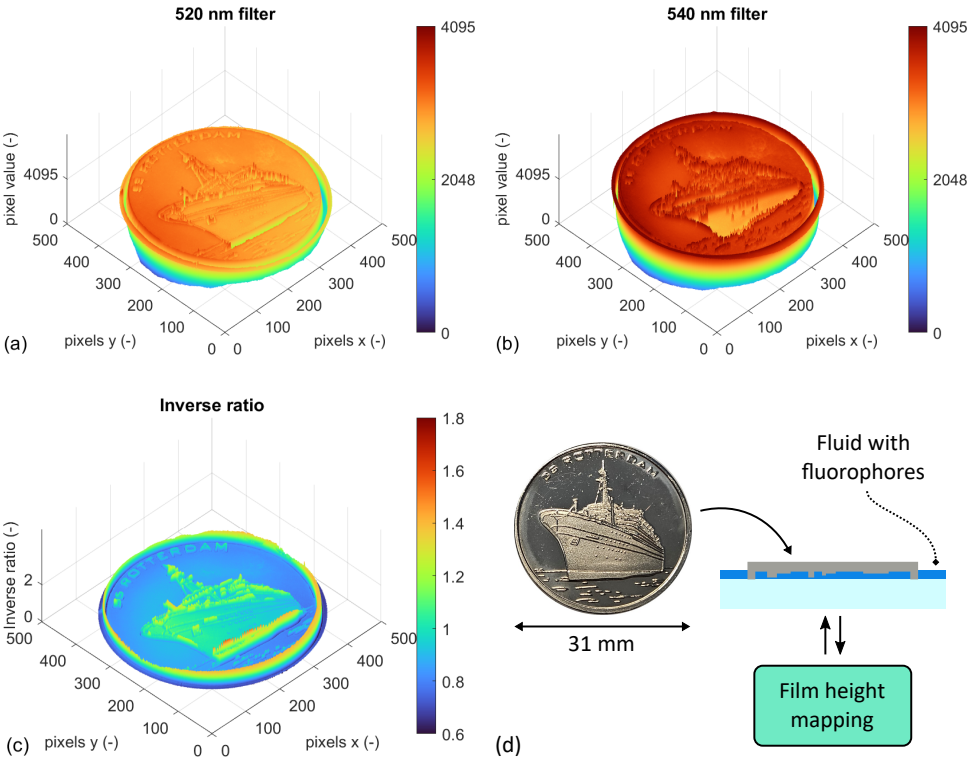

Figure 7.8: An illustrative example of ratiometric fluorescence imaging of the surface topography of a collectors coin. The measured intensities are the average of 50 measurements. (a) Pixel intensity for the 520 nm bandpass filter. (b) Pixel intensity for the 540 nm bandpass filter. (c) Ratio between the 520 nm image and 540 nm image. (d) Schematic of the measurement.

7.4.3 Calibration method

Calibration of the film height measurement method is required to relate the fluorescence emission ratio to the film height of the fluid film. Because the reflectivity of the surface background has a significant impact on the fluorescence emission intensities and the corresponding ratio, the conditions in the calibration must be identical to those in the actual experiment [119, 120, 133]. Therefore, the calibration measurements are performed with the same setup and deformable slider surface material.

The calibration method is schematically shown in Figure 7.9. A calibration plate is fabricated by bonding a polystyrene plate, identical to the slider material, to a stiff backing plate. The calibration plate is gently pressed on the fluid filled glass disk and a wedge shaped fluid film is formed by separating them with a 500 µm gauge block [158]. Two small weights are placed on the calibration plate ends for a well-defined contact with the glass disk. The local film height can be determined from the geometry of the fluid film.

The calibration tests are performed before and after the film height measurements, to validate the reliability of the measurement method. To be clear, this is a stationary measurement as the disk is not moving. The measured ratios are fitted with a calibration curve of the form: $R = c_1\left(1 - \exp\left(-c_2 h\right)\right) + c_3$, with ratio R, film height h and fitting constants c_1, c_2, and c_3. The resulting calibration curves are used in the film height measurements to determine the film height.

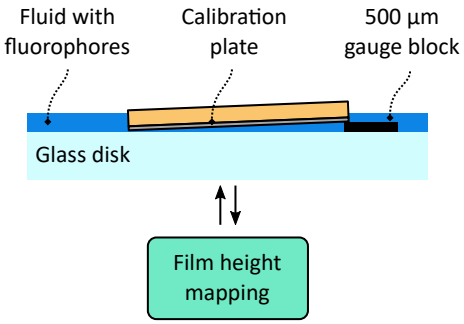

Figure 7.9: Schematic of the calibration measurement.

7.4.4 Test conditions

The numerical and experimental results are obtained for a variation of the rotational speed and the fluid viscosity. Three rotational speeds are used: 40 RPM, 60 RPM, and 80 RPM. Moreover, the setup is tested with three different lubricants. The lubricants are a mixture of deionized water and glycerol, in which the fluorophores are dissolved from 4 mmol L^{-1} stock solutions. By changing the ratio between the water and glycerol, the viscosity is adjusted. Glycerol is known to negatively affect the fluorescence emission, which is another reason to perform the calibration measurement [159].

The viscosities are determined with the empirical formula as presented by Cheng [160]. They are experimentally validated on an Anton Paar MCR 302 rheometer with the CP20-2/MRD/TI measuring cone. The results of the simulated and measured viscosities for a variation of the lubricant temperature are shown in Figure 7.10. They are in good agreement. To determine the effective viscosity during testing, the room temperature has been logged. The results are listed in Table 7.3.

The test procedure for each lubricant contains a number of tests. Before the setup is run, a calibration test with the specific lubricant is performed, as described in Section 7.4.3. In each calibration test, 50 images per camera are acquired and processed. Then for the actual measurements, after applying the loads to the deformable slider, the setup is run at a high rotational speed to ensure the formation of a stable fluid film. Film height measurements are then performed for the different rotational speeds. For each rotational speed, 100 images per camera are acquired and processed. The test procedure is concluded with a final calibration test.

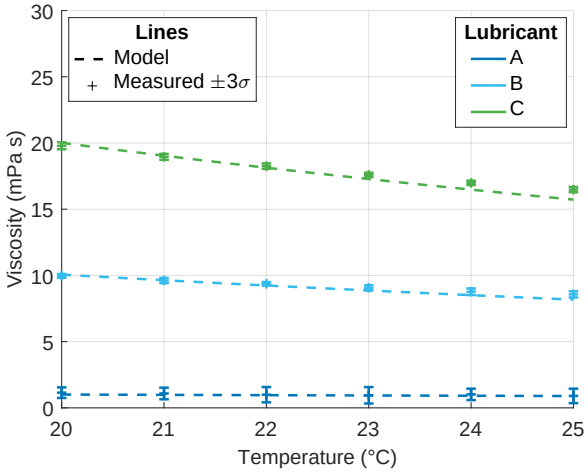

Figure 7.10: Simulated and measured viscosities for a varying lubricant temperature. The simulated viscosities are computed with the empirical formula as presented by Cheng [160].

Table 7.3: Effective lubricant viscosities as determined with the empirical formula from Cheng [160].

Lubricant	Volume fraction glycerol (-)	Temperature (°C)	Viscosity (mPa s)
A	0	23.5	0.9
B	0.53	23.7	8.6
C	0.63	24.3	16.3

7.5 Results

7.5.1 Numerical model

An example result of the numerical model can be seen in Figure 7.11. The figure shows 3D visualizations of the film height and pressure distributions which result from the two study steps in Section 7.3.2. The model input parameters are listed in Table 7.2. Additionally, the rotational speed and viscosity are equal to 60 RPM and 10 mPa s, respectively. The film height distribution from the first study step is shown in Figure 7.11a. The boosting zone at the leading edge is easily identified. The converging gap in the film height distribution leads to the pressure distribution in Figure 7.11b.

In the next study step, the elastic deformation of the deformable slider is taken into account. Figure 7.11c shows the film height distribution. The elastic deformation is varying over the slider surface, due to the varying bending stiffness. Moreover, it is observed that the deformable slider is not able to completely follow the initial film height distribution with the virtual boosting zone. The corresponding pressure distribution is shown in Figure 7.11d. The pressure distribution is very similar to the initial pressure distribution in Figure 7.11b, except for a small drop near the pressure peak, due to the elastic deformation of the slider surface.

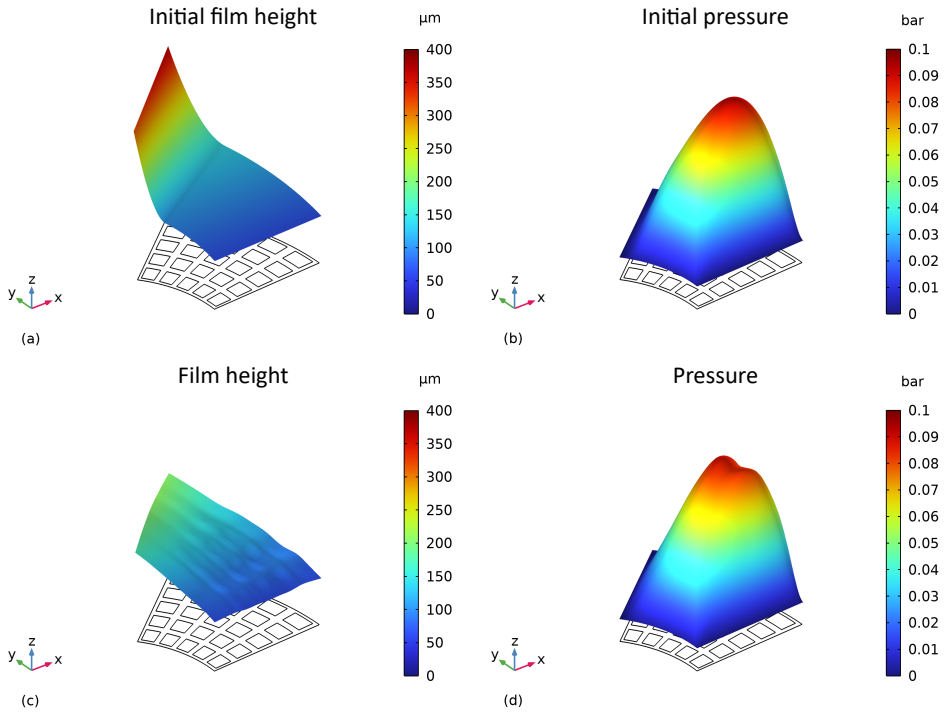

Figure 7.11: These figures show the modeled film height (left column) and pressure (right column). (a) Initial film height distribution including boosting zone with (b) corresponding pressure distribution. (c) Final film height distribution with (d) corresponding pressure distribution.

7

7.5.2 Fluorescence calibration

The results of the ratiometric fluorescence calibration tests are shown in Figure 7.12. The plots show the average fluorescence emission ratio and its standard deviation for the different lubricants. The calibration tests are performed before and after the film height measurements with the deformable slider, and the results are in good agreement. The ratio increases for increasing film height. Moreover, the standard deviation is significantly higher for low film heights, where the fluorescence emission intensities become lower and the signal-to-noise ratio decreases.

The formation of the wedge shaped fluid form turned out to be non-trivial. It appears that a thin fluid film remained present between the calibration plate and the glass disk surface. To compensate, the ratio plots are shifted with 25 µm, based on an analysis of the acquired images.

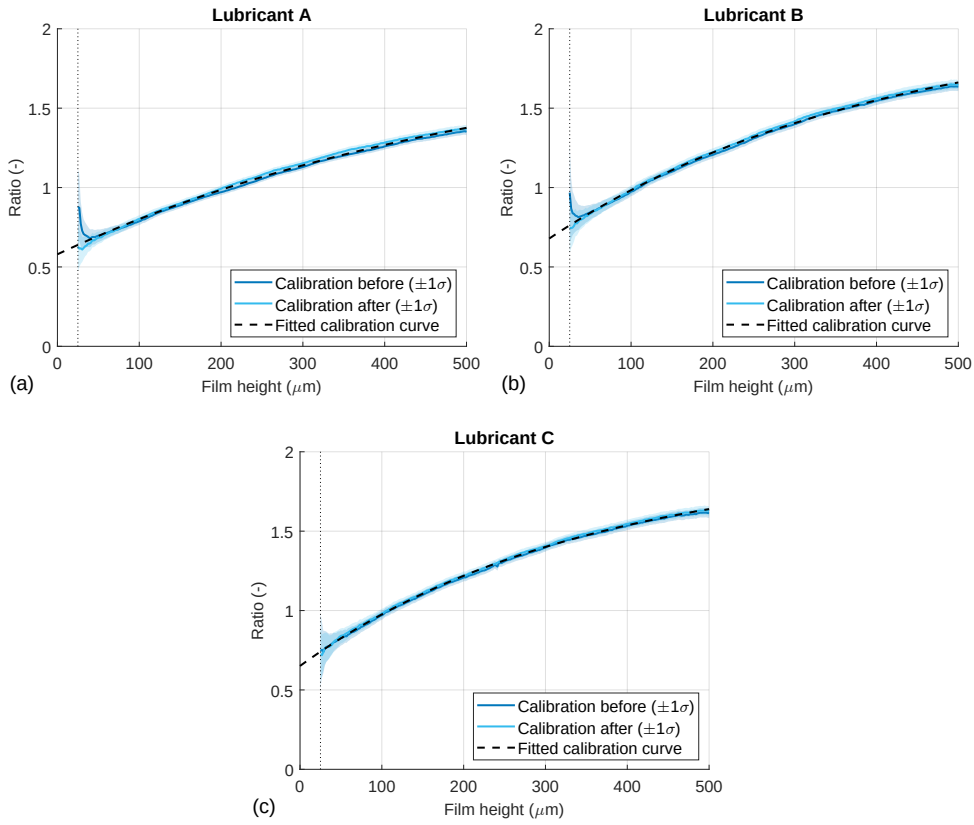

Figure 7.12: Calibration of the ratiometric fluorescence measurement for the three different lubricants. (a) Calibration curve for lubricant A. (b) Calibration curve for lubricant B. (c) Calibration curve for lubricant C.

7.5.3 Experimental validation

Figure 7.13–7.15 show the filled contour plots of the simulated and measured film heights for a variation of the rotational speed. In each figure, the simulated film heights are shown on the left and the measured film heights are shown on the right.

The numerical and experimental results for lubricant A are shown in Figure 7.13. The converging fluid film geometry can be clearly identified in both simulated and measured film height distributions. Moreover, it can be observed that the overall film height increases for an increasing rotational speed. All contour plots show distinct drops in the film height distribution. These are most clearly visible in the lower region of the slider surface, where dark blue regions can be observed. These regions are located on the load pads, on which the discrete loads are applied. The applied loads force the slider surface downwards, which results in a drop in film height. Increased film heights can be observed between the load pad regions, where the bending stiffness is relatively low. The result is a wavy deformation pattern, due to the combination of the discrete loads on top of the slider and the hydrodynamic pressure distribution acting from below. A few observations are

made for the measured film height distributions. A few contour plot contain some white areas in the lower right region of the slider. Here, the translation from the fluorescence ratio to the film height, via the calibration curve, is not properly functioning. Negative film heights are found, most likely due to a combination of very thin fluid films and a small measurement error in the calibration curve. For readability, the negative film heights are not included. Another noteworthy observation is made for the lower and upper left corners in the experimental results, which show a sharp increase in the film height magnitude. The film height increase is a result of reflections from the LED lights on the surface of the glass disk. Because of the high intensity of the LED light, part of the reflection bleeds through the spectral filters and is captured by the camera pixels, hereby distorting the measurement.

Figure 7.14 shows the simulated and measured film heights for lubricant B. An overall increase in film height magnitude can be observed compared to the results in Figure 7.13, due to the increase in viscosity. The LED light distortion in the lower and upper left corner of the slider surface is less pronounced, because of the increased fluorescence emission for thicker fluid films. Therefore, the magnitude of the LED light reflection is relatively lower and its influence on the fluorescence ratio and the corresponding film height is reduced. The simulated and measured film heights for lubricant C are shown in Figure 7.15. The film height magnitudes have further increased, due to the higher viscosity of lubricant C. The numerical and experimental results agree less in the upper region of the slider surface for all rotational speeds. The simulated contour plots show a clear increase in film height, which is not present in the measured film height contour plots. The LED light distortion in the lower and upper left corners is still slightly visible.

The contour plots of the simulated and measured film heights are an effective way to qualitatively compare the numerical and experimental results. Overall, good agreement is found between both. To be able to make a more quantitative comparison between the results from the numerical model and the experiment, Figure 7.16 shows the simulated and measured film heights along the arc length at the mean radius R_{m}. The figures show the average film height and standard deviation for each lubricant and for a variation of the rotational speed. In each graph, the magnitude of the film height are increasing for an increasing rotational speed. The wavy deformation pattern of the slider surface can be clearly identified in the simulated and measured film heights, which agree very well. The elastic deformation is most pronounced in the results for lubricant A, where it is relatively large compared to the film height magnitude. This graph also shows the highest standard deviation in measured film heights. The thin fluid films have a relatively low fluorescence emission and corresponding signal-to-noise ratio. The simulated and measured film heights for lubricant C (lower graph) show a clear difference for the larger film heights, which has also been observed in Figure 7.15.

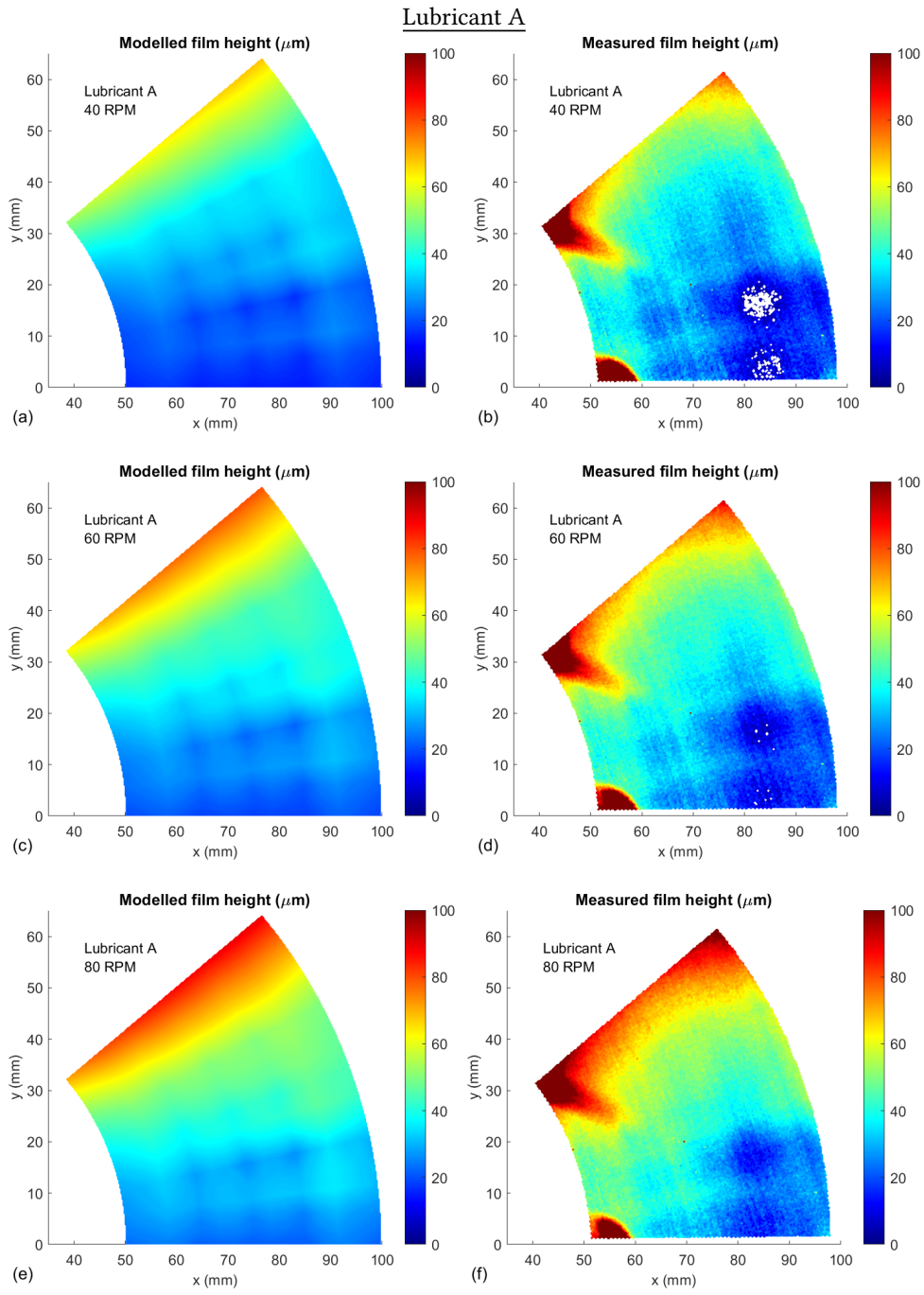

Figure 7.13: The simulated film height (left column) and measured film height (right column) for lubricant A and for a variation of the rotational speed.

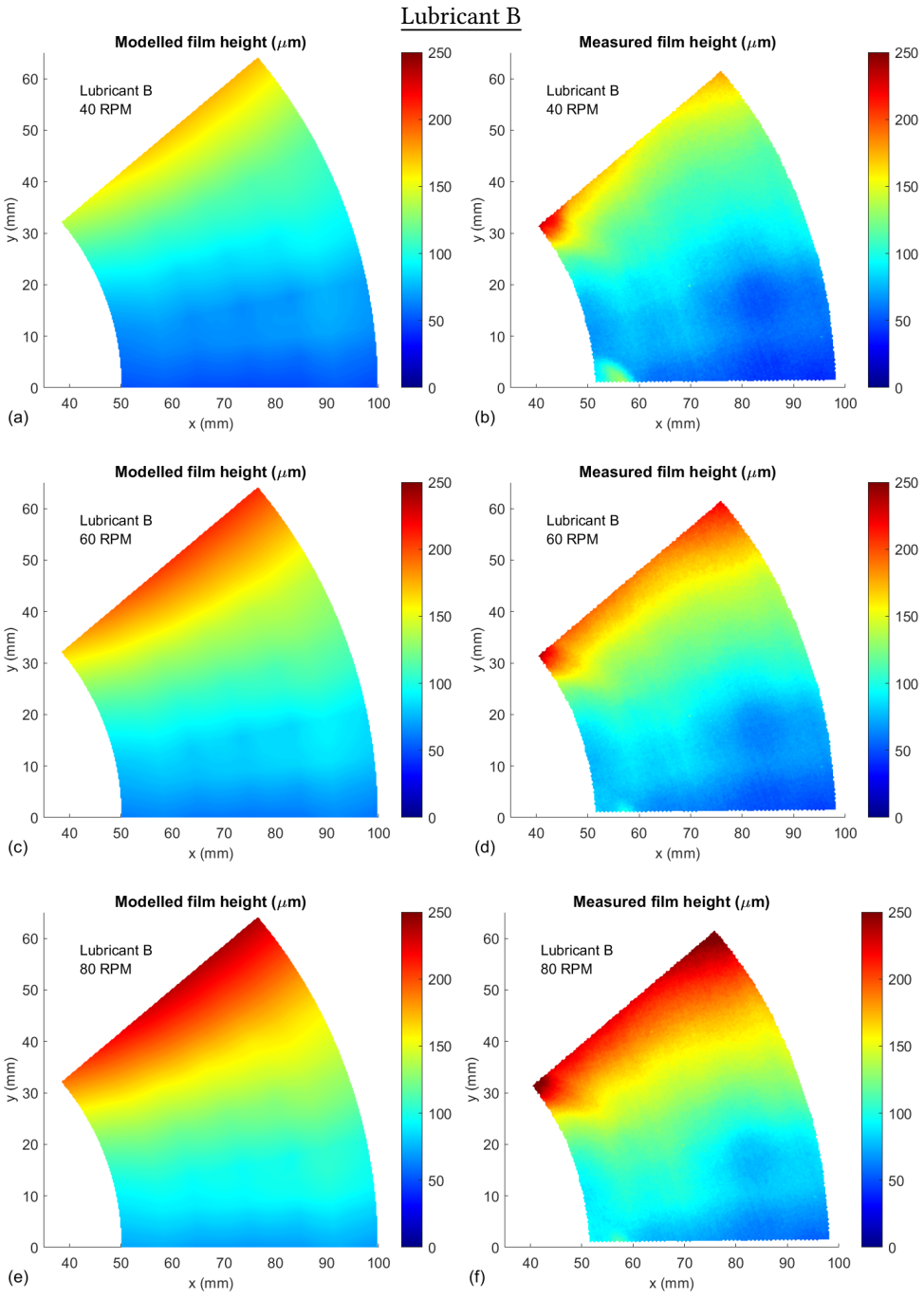

Figure 7.14: The simulated film height (left column) and measured film height (right column) for lubricant B and for a variation of the rotational speed.

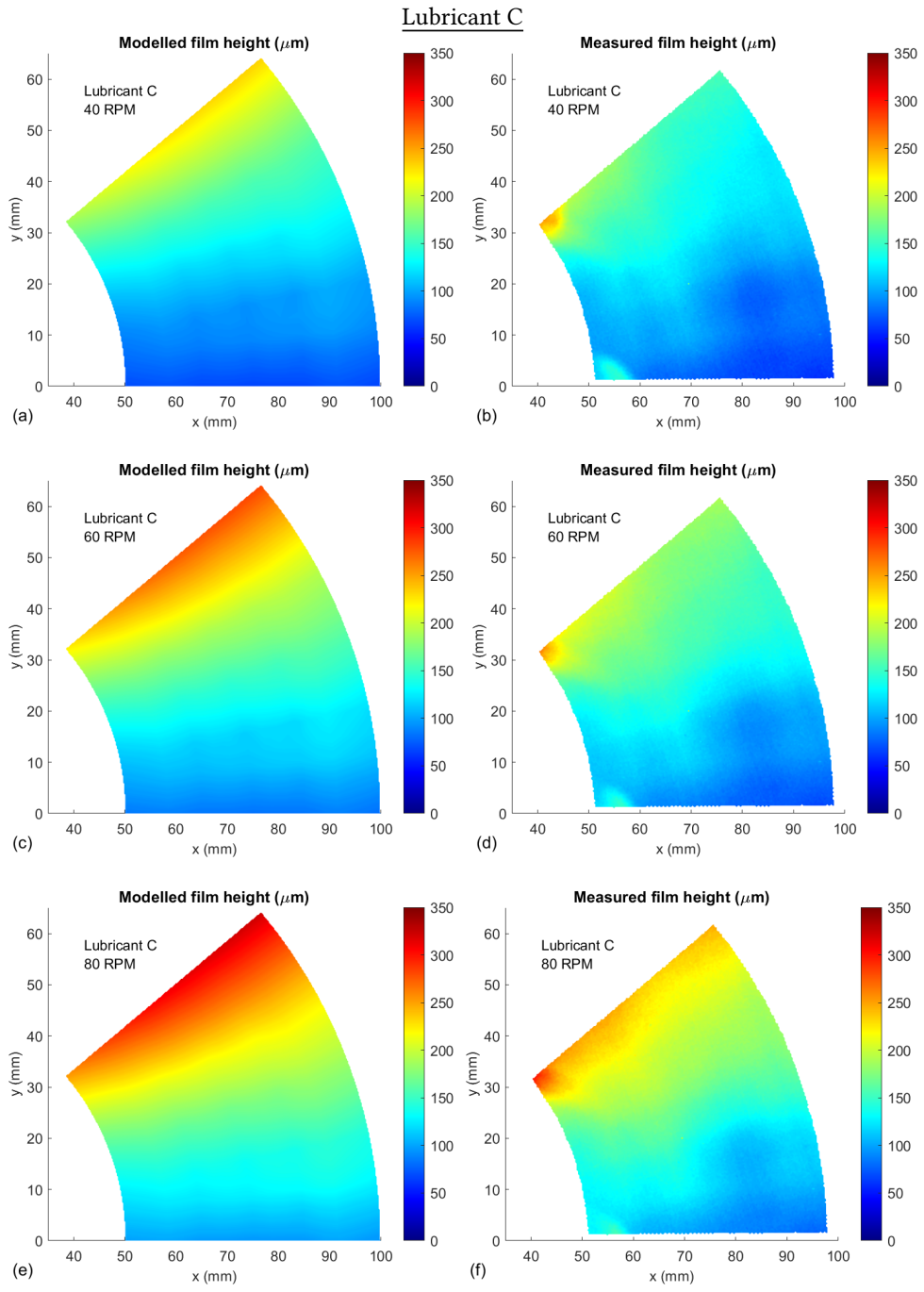

Figure 7.15: The simulated film height (left column) and measured film height (right column) for lubricant C and for a variation of the rotational speed.

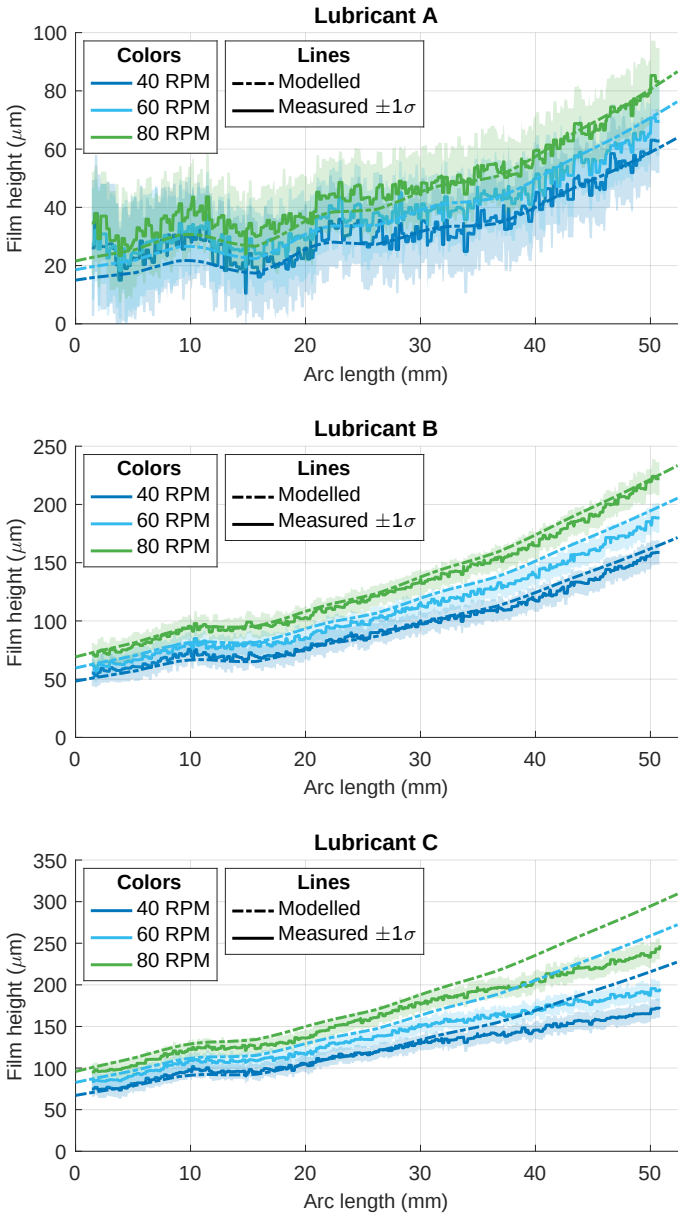

Figure 7.16: The simulated and measured film heights along the arc length at the mean radius R_m for lubricant A (top), B (middle), and C (bottom). To-do: add a small figure of the slider surface and indicate the arc length at radius Rm.

7.6 Discussion

In this section, the numerical model, experimental setup, and results are discussed.

7.6.1 Numerical model

The two-dimensional numerical model is an extension of the one-dimensional numerical model, which has been presented earlier. Lubrication theory for the pressure build-up in the fluid film and plate theory for the elastic deformation of the deformable slider are coupled in an elastohydrodynamic lubrication model, which is solved in two solution steps. In the first solution step, the model is directly used to find the required point loads applied to the top surface of the slider to approach the desired pressure distribution and corresponding film height distribution. In the second solution step, the two physics are coupled by including the elastic deformation of the slider in the film height definition.

The numerical model has proven to be a useful tool to quickly determine the loads to apply to the slider. The modular model setup allows for a relatively easy and straightforward variation of the slider geometry or the input parameters.

7.6.2 Experimental setup

An experimental setup is developed to experimentally validate the film height steering concept. A fluid film is generated between the deformable slider and a transparent, rotating disk. The setup uses a novel load application to apply the required loads to the deformable slider via a grid of compression springs. Due to spatial limitations, the number of applied loads is limited to 5×5. The fluid film geometry is mapped with ratiometric fluorescence imaging. In most fluorescence measurement setups, the excitation light and imaging components are placed orthogonal to the sample plane, hereby minimizing the excitation and viewing angles [161]. In this setup, due to the placement of the LED lights and cameras, the excitation and viewing angles are non-zero. However, when the excitation and viewing angles are limited to several tens of degrees, the impact on the fluorescence emission ratio is minor [120]. Unfortunately, the LED light ring with uniform illumination was not functioning as intended. LED light reflections on the glass surfaces distorted the measurement. The final film height measurements have been performed with two LED lights switched off, to minimize the overall LED light distortion.

For this specific application, the fluorophore concentrations, pixel binning, exposure time, and LED light intensity (drive current) have been tuned for a sufficient signal strength and signal-to-noise ratio over the film heights of interest. The parameters can be adjusted for other applications. Care must be taken to prevent photobleaching or saturation of the fluorophores by overexposure [120, 122, 161]. Therefore, calibration curves have been acquired before and after the actual film height measurements with the deformable slider. They closely agree, which increases the confidence in the proper functioning of the measurement technique. Additionally, lifetime tests have been performed to ensure the functioning of the method over an increased number of fluorophore excitations.

The pH of the tested lubricants has been increased to about 10 to ensure high quantum yields and well-defined excitation and emission spectra for both fluorophores. During testing, it has been observed that the pH value was slowly decreasing. This is most likely caused by dissolving carbon dioxide from the atmosphere. To improve the stability of the pH value, it is recommended to use a pH buffer instead of sodium hydroxide.

7.6.3 Results

The numerical results show that the final film height distribution does not fully agree with the desired, initially prescribed film height distribution. The bending stiffness of the slider does not allow it to fully deform towards the initially prescribed fluid film geometry. A relatively small boosting zone is created, which does help to facilitate the fluid supply in the lubricated contact. When the number of loads is increased, the bending stiffness of the slider can be decreased, as shown in Chapter 6. This will help to better approach the initially prescribed pressure distribution and corresponding film height distribution.

The simulated and measured film height distributions are presented for a range of viscosities and rotational speeds. The largest difference is found in the results for lubricant C. It is believed that this difference can be explained by the magnitude of the applied loads. The load application is designed to apply constant loads to the slider surface, independent of the film height. However, relatively large film heights will further compress the compression springs of the load application, hereby increasing the magnitude of the applied loads. This effect will be most pronounced near the leading edge of the slider surface, where the largest film heights are found. To reduce this effect, it is recommended to use compression springs with a lower spring stiffness or to stack even more compression in series to decrease the net spring stiffness.

Overall, it has been experimentally shown that the fluid film geometry between a deformable tilting pad slider bearing and a flat rotating disk can be steered by applying a prescribed load distribution. The next step will be to extend the numerical and experimental research to the situation of a non-flat substrate. The current numerical model and experimental setup can be expanded to study the ability of the deformable slider to maintain the fluid film geometry in the presence of substrate waviness. Care must be taken to apply loads with a constant magnitude and to use cameras with a sufficient depth of field, as the distance between the cameras and the fluid film is changing.

7.7 Conclusion

This present work presents the development of a numerical model and an experimental setup to validate the concept film height steering in elastohydrodynamic lubrication by applying a prescribed load distribution. This concept is inspired by inverse lubrication theory, in which the pressure distribution in the lubricated contact is known beforehand. It has been demonstrated for a single tilting pad deformable slider bearing and is considered as a first step for steering the film height in soft elastohydrodynamic lubrication.

A two-dimensional elastohydrodynamic lubrication model is developed to determine the required loads to apply to the deformable slider. The experimental validation is performed in a novel experimental setup for a range of viscosities and rotational speeds. The loads are applied to the slider with a grid of compliant compression springs and ratiometric fluorescence imaging is used to map the film height. The numerical and experimental results are in good agreement and show the ability of the concept to manipulate the fluid film between the deformable slider and the rotating disk. It is a promising method to also steer the film height distribution in the presence of substrate waviness. The foundations of the concept can be used in any soft elastohydrodynamic lubrication process which requires accurate control over the film height, such as squeeze-roll coating, roller-based UV-cure nanoimprinting, or lithographic printing.

8

Discussion

This chapter presents a discussion of the preceding chapters and the overall research objective. First, it reflects on the main implications of each part. Next, limitations and recommendations for future research and implementation are discussed.

8.1 Reflection

This study was divided into three parts, which directly relate to the threefold approach taken in this study: film height prediction, film height measurement, and film height steering. This section presents a brief summary of each part of the dissertation and reflects on their implications.

8.1.1 Film height prediction

In Part I, numerical models were developed to describe the elastohydrodynamic lubrication in roll-to-plate nanoimprinting. The model development was performed in several steps, in which the model complexity was increased to better capture the underlying physics of the roll-to-plate imprint process. The schematic of the roll-to-plate imprint process and the corresponding physics in Figure 8.1 illustrates the final model setup and the coupling between the various physics.

Chapter 2 presented the first development of the numerical model. A notable observation from the numerical results was that the web tension influences the pressure and film height distributions. By increasing the web tension, the effective stiffness of the elastomeric layer was slightly increased. This resulted in higher film pressures and lower film heights. Surprisingly, the results showed that the simulated minimum film heights agreed well with the measured layer heights from flat layer imprints. The simulated central (Couette) film height, which was assumed to be the correct estimator, was significantly higher than the measured layer height. This unexpected result encouraged a more accurate description of the physics of the roll-to-plate imprint process.

Therefore, the improved numerical model in Chapter 3 considered the bending stiffness of the tensioned web and the contact mechanics between the tensioned web and the roller. The dimensionless setup of the numerical model, described by five non-dimensionless numbers, resulted in an efficient simulation tool to accurately predict the film height in

roll-to-plate nanoimprinting. Due to the additions, good correspondence was found between the measured layer heights and the simulated final film heights, which are equal to the central (Couette) film heights. The chapter concluded with a technical note on survey diagrams for elastohydrodynamic lubrication, which showed that the results from the numerical model agree well with existing film height survey diagrams for soft-layered elastohydrodynamic lubrication. Moreover, it provided an explanation of how the non-dimensional similarity groups can be used to determine experimental curve fits to quickly predict the film height in roll-to-plate nanoimprinting.

The introduction of the contact mechanics and the tensioned web in the numerical model in Chapter 3 offers an additional advantage. As the fluid is trapped between the tensioned web and the substrate, the typical diverging geometry near the outlet of the contact, is missing. Therefore, it is no longer required to include a cavitation algorithm in the model, as has been done in the numerical model in Chapter 2. This concept could also be interesting to other elastohydrodynamic lubrication calculations, by introducing a virtual, flexible web with zero bending stiffness and a low web tension to the model setup.

Finally, in Chapter 4, substrate non-flatness was added to the numerical model, as shown in Figure 8.1. The results showed that substrate waviness caused deviations in the final film height. This effect was most pronounced for large amplitude, small wavelength substrate waviness, when the imprint roller was not able to conform to the substrate non-flatness. Only in the case of small amplitude, large wavelength substrate waviness, it could be sufficient to simply control the load on the imprint roller, as is common practice. This result motivated the development of a film height steering method to reduce or even eliminate the negative effect of the surface topography on the film height uniformity.

The numerical models clearly demonstrate how the various process parameters, machine parameters, and material properties influence the film height and pressure distributions in soft-layered elastohydrodynamic lubrication with tensioned webs. These insights can be used to determine the sensitivity of the film height and uniformity to the individual parameters. Moreover, the models serve as an efficient simulation tool to accurately predict the film height in roll-to-plate nanoimprinting. They can be used to tune the process parameters to achieve a desired film height.

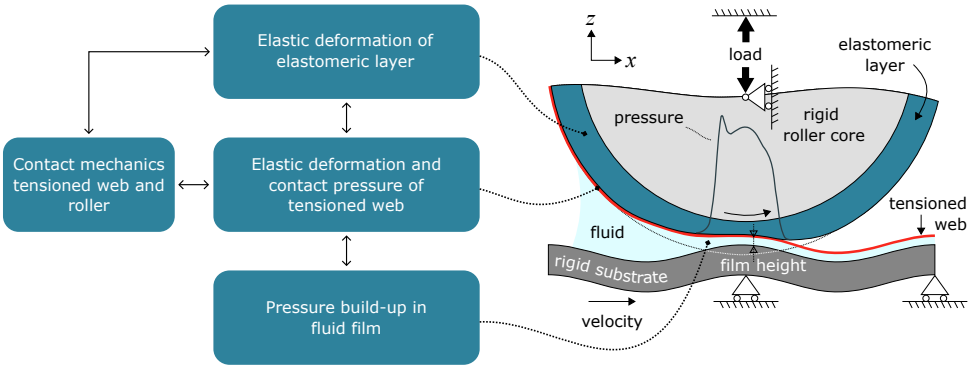

Figure 8.1: Schematic diagram of the imprint roller with tensioned web (i.e., flexible stamp) and the corresponding physics in the imprint process. Reproduced and adapted with permission from [60].

8.1.2 Film height measurement

Part II, which contains Chapter 5, presented the development of a novel analytical model and the experimental validation of the ratiometric fluorescence film height measurement method. The analytical model is an extension of the original model as provided by Hidrovo and Hart [1]. The new model includes the emission and reabsorption of both fluorophores and the influence of surface reflection of the background.

A key insight is the significant influence of the background surface reflectivity. A reflective background increases the fluorescence emissions and expands the fluorescence ratio range, thereby improving the measurement accuracy. Depending on the application and the ability to modify the background, a mechanical designer can adjust the surface reflectivity to increase the measurement accuracy.

These findings could be of interest to (mechanical) design engineers and anyone else who is interested in utilizing the phenomenon of fluorescence for film height mapping. The more accurate model description makes the analytical model an efficient design tool to predict the fluorescence ratio. Moreover, the analytical model can be used to study any combination of fluorophores, as long as the fluorophore spectral properties are available. This offers the possibility to tune and optimize the measurement response for a desired film height range, by adjusting the fluorophore concentrations and possibly the surface reflectivity.

8.1.3 Film height steering

The third part, which contains Chapter 6 and Chapter 7, presented a new concept to steer the film height in soft elastohydrodynamic lubrication. First, in Chapter 6, the feasibility of the concept to steer the film height was demonstrated in a one-dimensional elastohydrodynamic lubrication numerical model of a deformable tilting pad slider bearing. Next, in Chapter 7, the numerical model was extended for a two-dimensional deformable tilting pad slider bearing. The concept was experimentally validated using a novel experimental setup, in which a fluid film was formed between the deformable slider and a rotating disk.

The numerical and experimental results of these chapters demonstrated that the proposed concept is an effective method to steer the film height by applying a number of discrete loads to the deformable slider surface. The discrete loads approach the corresponding pressure distribution of the initially prescribed, desired film height distribution. These findings are also of interest to other soft elastohydrodynamic lubrication processes which require accurate control over the film height, such as liquid film coating, roller-based UV-cure nanoimprinting, or lithographic printing.

8.2 Limitations and recommendations

In this study, the roll-to-plate imprint process was considered as a form of fluid film lubrication. Following this vision, this study presented the development of theory and methods to predict, measure, and steer the film height in soft elastohydrodynamic lubrication. This development was specifically focused on the application of roll-to-plate nanoimprinting, but the methods and theory are not necessarily directly applicable to the roll-to-plate imprint process. This section presents a discussion upon the applicability of the developed methods and theory to roll-to-plate nanoimprinting. Furthermore, it discusses the limitations and recommendations for each part of this study.

8.2.1 Film height prediction

The numerical models in Part I (Chapter 2–4), which describe the elastohydrodynamic lubrication of soft-layered solids, were specifically developed for the roll-to-plate imprint process. As good agreement was found between the numerical and experimental results, confidence in approaching the roll-to-plate imprint process from a fluid film point of view was increased.

However, the model setup has its limitations. The presented models are restricted to a two-dimensional configuration, which is also referred to as a line contact. This setup implicitly assumes that all parameters remain constant along the imprint roller direction (i.e., y-direction). Moreover, due to this simplification, the substrate waviness in Chapter 4 is only defined along the imprint direction (i.e., x-direction), as shown in Figure 8.1. In reality, substrate waviness can extend over the surface (i.e., in both the x- and y-directions), as described in the introduction in Chapter 1. Additionally, deformation of the imprint roller (e.g., bending) may also occur. These variations in the substrate and roller topography will have an even larger negative influence on the film height and pressure distributions. Due to the limited bending compliance of the imprint roller, its conformity to the substrate non-flatness is further challenged. Although this phenomenon is not included in the numerical model, it is yet another confirmation of the need for a concept to steer the film height.

An important assumption in all numerical models, is the exclusion of imprint textures. These textures on the flexible stamp (or tensioned web) can show a wide variety in shape and dimensions, depending on the intended application. Typically, the texture dimensions will be in the same order of magnitude as the film height in the lubricated contact, and they can significantly influence the pressure distribution. In this study, it was decided to neglect the textures and to focus on the film height and pressure distributions for flat layers. For the most accurate description of the actual imprint process, it is recommended to include the textures in future work. In a first approximation, different textures can be modeled with flow factors, to investigate their significance and the need to include them in the numerical model [162].

As a result of this study, further research might also be conducted on other extensions and applications of the numerical model, to address the limitations listed above. Relevant extensions, besides the addition of the imprint textures, include the transition from two-dimensional to three-dimensional, and transient simulations to study the film height uniformity over time. Moreover, the numerical model can be used to tune or optimize the process parameters and machine parameters for the desired film height or ability to han-

dle variations in the substrate topography. The application of the numerical model is not limited to roll-to-plate nanoimprinting. Other coating technologies, such as liquid film coating and lithographic printing, may also benefit from the analyses, as their underlying physics is very similar. The model can be used to study the film height as a function of both the process and machine parameters.

8.2.2 Film height measurement

Part II (Chapter 5) presented the development of an extended analytical model to describe the ratiometric fluorescence film height measurement method. The application of this method in the roll-to-plate nanoimprint process is non-trivial, as has already been demonstrated in literature [163, 164]. First of all, optical access to the fluid film must be provided. Potential measurement locations could be downstream the roller contact, before curing, or after delamination of the flexible stamp. Secondly, the fluorophores must be dissolved in the UV-curable resins, preferably without altering its optical or mechanical performance. And lastly, if the measurement is performed after UV-curing, care must be taken not to destroy the fluorophores by the UV-light exposure. If applied correctly, ratiometric fluorescence imaging could provide a wealth of information on the film height magnitude and uniformity over the entire imprint area. This information can be used to adjust and improve the imprint process, for example.

A major limitation of the analytical model is the fact that it requires detailed information about the spectral material properties of the fluorophores. In the present study, this data is provided via extensive (and time consuming) fluorescence measurements. The model would benefit from access to a data bank to easily select and obtain the relevant information for each fluorophore. This offers the possibility to quickly compare and analyze the performance of different combinations of fluorophores and spectral bandpass filters. Moreover, future research can focus on extending the parameter studies with a variation of the ratio between the fluorophore concentrations. Other combinations of fluorophores, fluorophore concentrations, and spectral bandpass filters may be beneficial for increasing the ratio range for a specific film height range.

8.2.3 Film height steering

The results of the film height steering concept in Part III (Chapter 6–7) are promising, but the feasibility has only been demonstrated for a deformable tilting pad slider bearing, so far. Here, only the bottom surface (i.e., the rotating disk) is moving, while the deformable slider is stationary. Contrary, in roll-to-plate nanoimprinting, the top and bottom surface (i.e., roller and substrate) are moving with the same surface velocity. This challenges the application of the discrete loads to one of the moving surfaces. We recommend further research to focus on methods to facilitate the application of the film height steering concept in the roll-to-plate nanoimprint process.

Moreover, the numerical results in Chapter 6 clearly showed the feasibility and efficacy of the concept to steer the film height in the presence of varying substrate waviness. It must be noted that the analyzed waviness amplitudes were considerably smaller than the values that have been used in Chapter 4, which studied the influence of substrates waviness on the film height in roll-to-plate imprinting. In the latter, the waviness amplitudes were increased to about 180 times the final film height, while the maximum waviness am-

plitude in Chapter 6 was equal to about 8 times the final film height. It should be noted that both studies are different in nature, as the contact lengths and film heights in the lubricated contacts are completely different. Therefore, a direct comparison between the results would not be fair. Moreover, the results in Chapter 6 were mainly used to demonstrate the working principle behind the concept.

Lastly, in the current study, the film height steering concept has been tested on a flat substrate (i.e., the rotating disk). The feasibility of the film height steering concept on non-flat substrates has only been analyzed theoretically in Chapter 6. Further research might well be conducted on applying the film height steering concept to non-flat substrates. The experimental setup presented in Chapter 7 is well-suited for this purpose, as substrate waviness can be introduced by simply replacing the rotating transparent disk. Based on the theoretical results in Chapter 6 (i.e., Figure 6.8) it is believed that this concept is well able to steer the film height as long as the wavelength of the substrate waviness is about twice the length or width of the slider, depending on the direction of the waviness (i.e., radial or tangential). However, care must be taken to ensure that the distributed loads approach a zero-stiffness load application (i.e., constant force), regardless of the height variations in the surface topography of the disk. Moreover, due to these height variations, the optical distance between the fluid film and the cameras will continuously change. Different solutions are available to accurately measure the film height: by selecting cameras with a large depth of focus, by using cameras with auto-focus, or by moving the cameras back and forth during the measurement to keep the optical distance constant. For the last option, the cameras could be placed on a linear stage, of which the linear motion is synchronized with the disk's rotational speed and height variations in the surface topography.

9

Conclusion

This dissertation developed theory and methods to predict, measure, and steer the film height in soft elastohydrodynamic lubrication. It specifically focused on the application of roll-to-plate nanoimprinting, addressing the challenges of current roller-based imprint systems to achieve uniform film heights on large-area, non-flat substrates. The research was structured in three parts, which directly correspond to the goals of film height prediction, film height measurement, and film height steering. In this concluding chapter, each of these goals is addressed.

In the first part, numerical models were developed and experimentally validated to describe the soft elastohydrodynamic lubrication in roll-to-plate nanoimprinting. These models can be used to accurately predict the film height as a function of the process and machine parameters. The addition of the non-dimensional bending stiffness number, which describes the influence of the bending stiffness of the tensioned web, is considered to be one of the main contributions. The bending stiffness results in an additional hydrodynamic pressure peak and corresponding inlet film constriction near the inlet of the roller contact. It was shown that the bending stiffness and web tension have a significant influence on the film height and pressure distributions in the lubricated roller contact, and must be included for an accurate prediction of the film height. Based on the numerical results, it was observed that the introduction of bending stiffness and web tension causes a film height decrease of about 30%. Furthermore, the addition of substrate waviness to the numerical model clearly demonstrated its negative effect on the film height uniformity, which emphasized the need for a film height steering concept.

The second part presented a novel analytical model and the experimental validation of the ratiometric fluorescence film height measurement method. The original model, which was developed by Hidrovo and Hart [1], was extended with the emission and reabsorption of both fluorophores and the surface reflection of the background. The experimental and simulated results agreed very well for a wide range of film heights, fluorophore concentrations and two different background surface reflectivities. Therefore, the refined analytical model is considered to be a fast and accurate design tool to tune or optimize the measurement response for a desired film height range. Moreover, the measured fluorescence spectra in Section 5.4.2 clearly demonstrated how the shape of the spectra and the corre-

sponding fluorescence ratio changes for a variation of these parameters. This contributed to an intuitive understanding of the working principle behind the measurement method.

Lastly, the third part presented a novel concept to steer the film height in soft elastohydrodynamic lubrication, inspired by inverse lubrication theory. Unique contributions of this part are the development of an efficient one-dimensional and two-dimensional model to describe the elastohydrodynamic lubrication of the deformable slider, which is subjected to both hydrodynamic pressure (from below) and a number of discrete loads (on top). Moreover, the development of the novel experimental setup is considered to be a major contribution. The setup involved an innovative method to apply the discrete loads to the deformable slider surface, using a grid of compliant compression springs. Additionally, the fluid film height was mapped with ratiometric fluorescence imaging, which proved to be an efficient method to measure the film height over a large area at once. The numerical and experimental results were in good agreement for different velocities and viscosities, resulting in a film height range from about 15 µm to 250 µm. This confirmed the feasibility and efficacy of this innovative concept to steer the film height in soft elastohydrodynamic lubrication. Therefore, it can be concluded that this concept is a promising method to steer the film height in roll-to-plate nanoimprinting, to achieve uniform film heights on non-flat substrates.

To conclude, the three parts on film height prediction, film height measurement, and film height steering advance the understanding of film height behavior in soft elastohydrodynamic lubrication, with application to roll-to-plate nanoimprinting. The film height measurement method and the film height steering concept are not yet directly applicable to roll-to-plate nanoimprinting. Further work is recommended on methods to facilitate their application in the roll-to-plate nanoimprint process. Overall, the developed methods and theory provide a solid basis for future research and practical implementation to further improve the film height uniformity in soft elastohydrodynamic lubrication processes, such as liquid film coating, roller-based UV-cure nanoimprinting, or lithographic printing.

Bibliography

References

[1] C. H. Hidrovo and D. P. Hart, "Emission reabsorption laser induced fluorescence (ERLIF) film thickness measurement," *Measurement Science and Technology*, vol. 12, pp. 467–477, Apr. 2001.

[2] K. Liu, X. Yao, and L. Jiang, "Recent developments in bio-inspired special wettability," *Chemical Society Reviews*, vol. 39, pp. 3240–3255, July 2010.

[3] D. Quéré, "Non-sticking drops," *Reports on Progress in Physics*, vol. 68, p. 2495, Sept. 2005.

[4] D. Gropper, L. Wang, and T. J. Harvey, "Hydrodynamic lubrication of textured surfaces: A review of modeling techniques and key findings," *Tribology International*, vol. 94, pp. 509–529, Feb. 2016.

[5] P. B. Clapham and M. C. Hutley, "Reduction of lens reflexion by the "moth eye" principle," *Nature*, vol. 244, pp. 281–282, Aug. 1973.

[6] V. Kapsali, *Biomimetics for Designers: Applying Nature's Processes and Materials in the Real World*. New York: Thames & Hudson, Sept. 2016.

[7] S. Chang, D.-J. Kong, and Y. M. Song, "Advanced visual components inspired by animal eyes," *Nanophotonics*, vol. 13, pp. 859–879, Mar. 2024.

[8] D. Zhang, J. Ji, C. Yan, J. Zhang, Z. An, and Y. Shen, "Research advances in bio-inspired superhydrophobic surface: Bridging nature to practical applications," *Journal of Industrial and Engineering Chemistry*, vol. 140, pp. 20–46, Dec. 2024.

[9] T. B. H. Schroeder, J. Houghtaling, B. D. Wilts, and M. Mayer, "It's not a bug, it's a feature: Functional materials in insects," *Advanced Materials*, vol. 30, p. 1705322, May 2018.

[10] A. Blagodatski, A. Sergeev, M. Kryuchkov, Y. Lopatina, and V. L. Katanaev, "Diverse set of Turing nanopatterns coat corneae across insect lineages," *Proceedings of the National Academy of Sciences of the United States of America*, vol. 112, pp. 10750–10755, Aug. 2015.

[11] P. Vukusic, J. R. Sambles, C. R. Lawrence, and R. J. Wootton, "Quantified interference and diffraction in single Morpho butterfly scales," *Proceedings of the Royal Society of London. Series B: Biological Sciences*, vol. 266, pp. 1403–1411, July 1999.

[12] S. Kinoshita, S. Yoshioka, and K. Kawagoe, "Mechanisms of structural colour in the Morpho butterfly: Cooperation of regularity and irregularity in an iridescent scale," *Proceedings of the Royal Society of London. Series B: Biological Sciences*, vol. 269, pp. 1417–1421, July 2002.

[13] T. M. Fletcher, *The Evolution of Speed: An Empirical and Comparative Analysis of Drag-Reducing Scales in Early Fishes.* PhD thesis, University of Leeds, Sept. 2015.

[14] C. J. Lloyd, J. Peakall, A. D. Burns, G. M. Keevil, R. M. Dorrell, P. B. Wignall, and T. M. Fletcher, "Hydrodynamic efficiency in sharks: The combined role of riblets and denticles," *Bioinspiration & Biomimetics*, vol. 16, p. 046008, June 2021.

[15] T. Shahan, "Eyes of a holcocephala fusca robber fly." `https://commons.wikimedia.org/wiki/File:Eyes_of_a_Holcocephala_fusca_Robber_Fly.jpg`, July 2009.

[16] A. Honkanen and V. B. Meyer-Rochow, "The eye of the parthenogenetic and minute moth Ectoedemia argyropeza (Lepidoptera: Nepticulidae)," *European Journal of Entomology*, vol. 106, pp. 619–629, Jan. 2013.

[17] D. Tiller, "Glasswing butterfly." `https://commons.wikimedia.org/wiki/File:Greta_oto.jpg`, Aug. 2008.

[18] R. H. Siddique, G. Gomard, and H. Hölscher, "The role of random nanostructures for the omnidirectional anti-reflection properties of the glasswing butterfly," *Nature Communications*, vol. 6, p. 6909, Apr. 2015.

[19] D. Descouens, "Morpho Didius Male." `https://commons.wikimedia.org/wiki/File:Morpho_didius_Male_Dos_MHNT.jpg`, June 2011.

[20] R. A. Potyrailo, R. K. Bonam, J. G. Hartley, T. A. Starkey, P. Vukusic, M. Vasudev, T. Bunning, R. R. Naik, Z. Tang, M. A. Palacios, M. Larsen, L. A. Le Tarte, J. C. Grande, S. Zhong, and T. Deng, "Towards outperforming conventional sensor arrays with fabricated individual photonic vapour sensors inspired by Morpho butterflies," *Nature Communications*, vol. 6, p. 7959, Sept. 2015.

[21] "The Lotus effect - biomimetics at its best." `https://www.nanotech-solutions.com/en/nanotechnology/lotus-effect`.

[22] H. Ensikat, P. Ditsche, C. Neinhuis, and W. Barthlott, "Superhydrophobicity in perfection: The outstanding properties of the lotus leaf," *Beilstein Journal of Nanotechnology*, vol. 2, pp. 152–61, Mar. 2011.

[23] "Copper Shark (Carcharhinus Brachyurus)." `https://www.supercoloring.com/coloring-pages/copper-shark-carcharhinus-brachyurus`.

[24] H. Hauser, *Nanoimprint Lithography for Solar Cell Texturisation.* PhD thesis, University of Freiburg, Jan. 2013.

[25] S. Dottermusch, R. Schmager, E. Klampaftis, S. Paetel, O. Kiowski, K. Ding, B. S. Richards, and U. W. Paetzold, "Micro-cone textures for improved light in-coupling and retroreflection-inspired light trapping at the front surface of solar modules," *Progress in Photovoltaics: Research and Applications*, vol. 27, no. 7, pp. 593–602, 2019.

[26] L. Clasing, D. Werner-Meier, L. W. Veldhuizen, and U. Blieske, "Experimental assessment of nanoimprinted textured frontsheets for PV modules," Sept. 2022.

[27] C. Ji, G. Zhu, C. Zhang, S. Nam, Q. Li, L. Xia, W. Zhang, D. Banerjee, and L. Guo, "Lenticular-lens-based colored antiglare dashboard surfaces," *Advanced Materials Technologies*, vol. 2, pp. 1–7, Nov. 2016.

[28] D. van der Heijden, A. Casimiro, J. M. ter Meulen, K. Keskinbora, and E. Ercan, "Advancing towards higher contrast, energy-efficient screens with advanced anti-glare manufacturing technology," *Nanomanufacturing*, vol. 4, pp. 241–248, Dec. 2024.

[29] J. M. ter Meulen, L. Veldhuizen, A. Kommeren, A. G. Willems, M. Dielen, E. Driessen, R. A. Neelen, E. Ercan, K. K. G. Tam, and B. J. Titulaer, "33-6: Roll-to-plate nanoimprint lithography for high-volume production of AR glasses: Equipment, materials, and processes," *SID Symposium Digest of Technical Papers*, vol. 52, pp. 447–449, May 2021.

[30] J. M. ter Meulen, E. Ercan, D. van der Heijden, P. Veldhuizen, and M. Ballottin, "Large-area nanoimprinting as a viable solution for AR waveguide manufacturing," in *SPIE AR, VR, MR Industry Talks 2023*, vol. 12450, p. 1245011, SPIE, Mar. 2023.

[31] M. Ballottin, N. Jansen, A. Scheidegger, E. Ercan, and J. M. ter Meulen, "Practical considerations for large-area nanoimprinted augmented reality waveguides," in *Advances in Patterning Materials and Processes XLI*, vol. 12957, pp. 85–91, SPIE, Apr. 2024.

[32] F. Dundar Arisoy, K. W. Kolewe, B. Homyak, I. S. Kurtz, J. D. Schiffman, and J. J. Watkins, "Bioinspired photocatalytic shark-skin surfaces with antibacterial and antifouling activity via nanoimprint lithography," *ACS Applied Materials & Interfaces*, vol. 10, pp. 20055–20063, June 2018.

[33] N. Atthi, M. Dielen, W. Sripumkhai, P. Pattamang, R. Meananeatra, P. Saengdee, O. Thongsook, N. Ranron, K. Pankong, W. Uahchinkul, J. Supadech, N. Klunngien, W. Jeamsaksiri, P. Veldhuizen, and J. M. ter Meulen, "Fabrication of high aspect ratio micro-structures with superhydrophobic and oleophobic properties by using large-area roll-to-plate nanoimprint lithography," *Nanomaterials*, vol. 11, p. 339, Feb. 2021.

[34] H. Kordy, "Process abilities of the riblet-coating process with dual-cure lacquers," *CIRP Journal of Manufacturing Science and Technology*, vol. 11, pp. 1–9, Nov. 2015.

[35] H. O. G. Benschop, A. J. Guerin, A. Brinkmann, M. L. Dale, A. A. Finnie, W.-P. Breugem, A. S. Clare, D. Stübing, C. Price, and K. J. Reynolds, "Drag-reducing riblets with fouling-release properties: Development and testing," *Biofouling*, vol. 34, pp. 532–544, May 2018.

[36] S. Chou, P. Krauss, and P. Renstrom, "Imprint of sub-25 nm vias and trenches in polymers," *Applied Physics Letters*, vol. 67, pp. 3114–3116, Nov. 1995.

[37] H. Schift and A. Kristensen, "Nanoimprint lithography," in *Springer Handbook of Nanotechnology* (B. Bhushan, ed.), Springer Handbooks, pp. 239–278, Berlin, Heidelberg: Springer, 2007.

[38] "Morphotonics Nanoimprint Technologies." `https://www.morphotonics.com`.

[39] S. Chen, H. Chen, Y. F. Gao, X. F. Chen, Z. B. Hao, J. Zhang, Z. Chen, and H. X. Ge, "Fabrication of slanted gratings with high refractive index starting from master nanoimprint mold," *Optics Express*, vol. 32, pp. 40886–40897, Nov. 2024.

[40] H. Schift, P. Urwyler, P. M. Kristiansen, and J. Gobrecht, "Nanoimprint lithography process chains for the fabrication of micro- and nanodevices," *Journal of Micro/Nanolithography, MEMS, and MOEMS*, vol. 13, p. 031303, July 2014.

[41] N. Kooy, K. Mohamed, L. T. Pin, and O. S. Guan, "A review of roll-to-roll nanoimprint lithography," *Nanoscale Research Letters*, vol. 9, no. 1, pp. 1–13, 2014.

[42] J. Haisma, M. Verheijen, K. van den Heuvel, and J. van den Berg, "Mold-assisted nanolithography: A process for reliable pattern replication," *Journal of Vacuum Science & Technology B: Microelectronics and Nanometer Structures Processing, Measurement, and Phenomena*, vol. 14, pp. 4124–4128, Nov. 1996.

[43] S. H. Ahn and L. J. Guo, "Large-area roll-to-roll and roll-to-plate nanoimprinting lithography: A step toward high-throughput application of continuous nanoimprinting," *ACS Nano*, vol. 3, no. 8, pp. 2304–2310, 2009.

[44] H. Lan, "Large-area nanoimprint lithography and applications," in *Micro/Nanolithography - A Heuristic Aspect on the Enduring Technology*, pp. 43–68, London: IntechOpen, May 2018.

[45] J. Snieder, M. Dielen, and R. A. J. van Ostayen, "Simulating the residual layer thickness in roll-to-plate nanoimprinting with tensioned webs," *Micromachines*, vol. 13, p. 461, Mar. 2022.

[46] P. Yi, H. Wu, C. Zhang, L. Peng, and X. Lai, "Roll-to-roll UV imprinting lithography for micro/nanostructures," *Journal of Vacuum Science & Technology B*, vol. 33, p. 060801, Oct. 2015.

[47] M. Colburn, A. Grot, B. J. Choi, M. Amistoso, T. Bailey, S. V. Sreenivasan, J. G. Ekerdt, and C. Grant Willson, "Patterning nonflat substrates with a low pressure, room temperature, imprint lithography process," *Journal of Vacuum Science & Technology B: Microelectronics and Nanometer Structures Processing, Measurement, and Phenomena*, vol. 19, pp. 2162–2172, Nov. 2001.

[48] D. J. Resnick and H. Schift, "Imprint lithography," in *Microlithography: Science and Technology* (B. W. Smith and K. Suzuki, eds.), pp. 595–677, Boca Raton: CRC Press, 3 ed., 2020.

[49] T. Köpplmayr, L. Häusler, I. Bergmair, and M. Mühlberger, "Nanoimprint lithography on curved surfaces prepared by fused deposition modelling," *Surface Topography: Metrology and Properties*, vol. 3, no. 2, 2015.

[50] M. J. Haslinger, A. R. Moharana, and M. Mühlberger, "Antireflective moth-eye structures on curved surfaces fabricated by nanoimprint lithography," in *35th European Mask and Lithography Conference (EMLC 2019)*, vol. 11177, p. 111770K, International Society for Optics and Photonics, Aug. 2019.

[51] R. Ji, M. Hornung, M. A. Verschuuren, R. van de Laar, J. van Eekelen, U. Plachetka, M. Moeller, and C. Moormann, "UV enhanced substrate conformal imprint lithography (UV-SCIL) technique for photonic crystals patterning in LED manufacturing," *Microelectronic Engineering*, vol. 87, no. 5-8, pp. 963–967, 2010.

[52] M. A. Verschuuren, M. Megens, Y. Ni, H. Van Sprang, and A. Polman, "Large area nanoimprint by substrate conformal imprint lithography (SCIL)," *Advanced Optical Technologies*, vol. 6, no. 3-4, pp. 243–264, 2017.

[53] H. Lan and H. Liu, "UV-Nanoimprint Lithography: Structure, Materials and Fabrication of Flexible Molds," *Journal of Nanoscience and Nanotechnology*, vol. 13, pp. 3145–3172, May 2013.

[54] ASTM C1048-04, "Standard specification for heat-treated flat glass - kind HS, kind FT coated and uncoated glass," May 2012.

[55] ASTM C1172-19, "Standard specification for laminated architectural flat glass," Feb. 2019.

[56] B. J. Hamrock, S. R. Schmid, and B. O. Jacobson, *Fundamentals of Fluid Film Lubrication.* No. 169 in Mechanical Engineering, New York: Marcel Dekker, 2nd ed., 2004.

[57] H. Blok, "Inverse problems in hydrodynamic lubrication and design directives for lubricated flexible surfaces," tech. rep., Delft University of Technology, 1965.

[58] D. Zhu, "Elastohydrodynamic lubrication (EHL)," in *Encyclopedia of Tribology* (Q. J. Wang and Y.-W. Chung, eds.), pp. 874–889, Boston, MA: Springer US, 2013.

[59] H. Moes, "Lubrication and beyond (lecture notes code 115531)," tech. rep., University of Twente, Enschede, The Netherlands, 2000.

[60] J. Snieder and R. A. J. van Ostayen, "Elastohydrodynamics of roll-to-plate nanoimprinting on non-flat substrates," in *Papers and Presentations from the COMSOL Conference 2023*, (Munich), 2023.

[61] A. van Erven, M. Steltenpool, M. Bos, J. Rutten, G. van der Hofstad, J. Muller, H. de Groot, J. de Ruijter, A. Tavakoliyaraki, B. Titulaer, and G. Rajeswaran, "Gen5 production tool for light management textures," in *2012 38th IEEE Photovoltaic Specialists Conference*, pp. 000690–000693, June 2012.

[62] H. Tan, A. Gilbertson, and S. Y. Chou, "Roller nanoimprint lithography," *Journal of Vacuum Science & Technology B: Microelectronics and Nanometer Structures*, vol. 16, pp. 3926–3928, Nov. 1998.

[63] S. Ahn, J. Cha, H. Myung, S. M. Kim, and S. Kang, "Continuous ultraviolet roll nanoimprinting process for replicating large-scale nano- and micropatterns," *Applied Physics Letters*, vol. 89, p. 213101, Nov. 2006.

[64] J. J. Dumond and H. Yee Low, "Recent developments and design challenges in continuous roller micro- and nanoimprinting," *Journal of Vacuum Science & Technology B*, vol. 30, no. 1, p. 010801, 2012.

[65] B. W. Smith and K. Suzuki, eds., *Microlithography: Science and Technology*. Boca Raton: CRC Press, third edition ed., 2020.

[66] J. P. Gomez-Constante, P. R. Pagilla, and K. R. Rajagopal, "A thermomechanical description of the mold filling process in roll-to-roll nanoimprinting lithography," *Applications in Engineering Science*, vol. 1, p. 100001, Mar. 2020.

[67] Y. Cui, X. Wang, C. Zhang, J. Wang, and Z. Shi, "Numerical investigation for the resin filling behavior during ultraviolet nanoimprint lithography of subwavelength moth-eye nanostructure," *Coatings*, vol. 11, p. 799, July 2021.

[68] J. Götz, A. Alvarez Rueda, S. Ruttloff, L. Kuna, M. Belegratis, U. Palfinger, D. Nees, P. Hartmann, and B. Stadlober, "Finite element simulations of filling and demolding in roll-to-roll UV nanoimprinting of micro- and nanopatterns," *ACS Applied Nano Materials*, p. acsanm.1c04059, Feb. 2022.

[69] U. Tahir, J. I. Kim, S. Javeed, A. Khaliq, J.-H. Kim, D.-I. Kim, and M. Y. Jeong, "Process optimization for manufacturing functional nanosurfaces by roll-to-roll nanoimprint lithography," *Nanomaterials*, vol. 12, p. 480, Jan. 2022.

[70] A. Jain and R. T. Bonnecaze, "Fluid management in roll-to-roll nanoimprint lithography," *Journal of Applied Physics*, vol. 113, p. 234511, June 2013.

[71] J. P. Gomez-Constante, P. R. Pagilla, and K. R. Rajagopal, "A thermomechanical and photochemical description of the phase change process in roll-to-roll nanoimprinting lithography," *International Journal of Engineering Science*, vol. 169, p. 103564, Dec. 2021.

[72] M. Colburn, B. J. Choi, S. V. Sreenivasan, R. T. Bonnecaze, and C. G. Willson, "Ramifications of lubrication theory on imprint lithography," *Microelectronic Engineering*, vol. 75, pp. 321–329, 2004.

[73] N. Kehagias, V. Reboud, C. M. Sotomayor Torres, V. Sirotkin, A. Svintsov, and S. Zaitsev, "Residual layer thickness in nanoimprint: Experiments and coarse-grain simulation," *Microelectronic Engineering*, vol. 85, no. 5-6, pp. 846–849, 2008.

[74] H. K. Taylor, "Defectivity prediction for droplet-dispensed UV nanoimprint lithography, enabled by fast simulation of resin flow at feature, droplet, and template scales," in *Alternative Lithographic Technologies VIII*, vol. 9777, (San Jose, California, United States), International Society for Optics and Photonics, Mar. 2016.

[75] J. Seki, Y. Oguchi, N. Kiyohara, K. Suzuki, K. Nagane, S. Narioka, T. Nakayama, Y. Shiode, S. Aihara, and T. Asano, "Enabling nanoimprint simulator for quality verification: Process-design co-optimization toward high volume manufacturing," in *Design-Process-Technology Co-optimization for Manufacturability XIV*, vol. 11328, p. 113280N, International Society for Optics and Photonics, Mar. 2020.

[76] H. Taylor, "Fast simulation of pattern formation and process dependencies in roller nanoimprint lithography," *MRS Proceedings*, vol. 1529, p. 205, Jan. 2013.

[77] J. MacPhee, J.-A. Shieh, and B. J. Hamrock, "The application of elastohydrodynamic lubrication theory to the prediction of conditions existing in lithographic printing press roller nips," *Proceedings of the Twenty-first Research Conference of the IARIGAI*, pp. 242–276, 1991.

[78] Y.-K. Xue, D. T. Gethin, and C. H. Lim, "Numerical modelling of the contact between lithographic printing press rollers by soft EHL theory," *Proceedings of the Institution of Mechanical Engineers, Part J: Journal of Engineering Tribology*, vol. 208, pp. 257–268, Dec. 1994.

[79] S. J. Abbott, N. Kapur, P. A. Sleigh, J. L. Summers, and H. M. Thompson, "A review of deformable roll coating systems," *Convertech & e-Print*, vol. 1, pp. 89–93, May 2011.

[80] B. Grashof and A. Delgado, "Analysis of influencing parameters in deformable roll coating of counter-rotating rolls," *Journal of Coatings Technology and Research*, vol. 12, pp. 63–73, Jan. 2015.

[81] P. K. Gupta, "On the heavily loaded elastohydrodynamic contacts of layered solids," *Journal of Lubrication Technology*, vol. 98, pp. 367–372, July 1976.

[82] C. Hooke, "The elastohydrodynamic lubrication of a cylinder on an elastomeric layer," *Wear*, vol. 111, pp. 83–99, Aug. 1986.

[83] A. A. Elsharkawy and B. J. Hamrock, "Elastohydrodynamic lubrication of elastomeric-coated surfaces in line contact," *Proceedings of the Institution of Mechanical Engineers, Part J: Journal of Engineering Tribology*, vol. 209, pp. 119–130, June 1995.

[84] A. Cochrane, K. Tjiptowidjojo, R. T. Bonnecaze, and P. R. Schunk, "Elastohydrodynamics of roll-to-roll UV-cure imprint lithography," *Industrial and Engineering Chemistry Research*, vol. 58, no. 37, pp. 17424–17432, 2019.

[85] W. Habchi, *Finite Element Modeling of Elastohydrodynamic Lubrication Problems*. Hoboken, NJ: John Wiley & Sons, 2018.

[86] J. A. Greenwood, "Elastohydrodynamic lubrication," *Lubricants*, vol. 8, p. 51, May 2020.

[87] W. Habchi, D. Eyheramendy, P. Vergne, and G. Morales-Espejel, "A full-system approach of the elastohydrodynamic line/point contact problem," *Journal of Tribology*, vol. 130, no. 2, pp. 1–10, 2008.

[88] S. Alakhramsing, R. van Ostayen, and R. Eling, "Thermo-hydrodynamic analysis of a plain journal bearing on the basis of a new mass conserving cavitation algorithm," *Lubricants*, vol. 3, no. 2, pp. 256–280, 2015.

[89] A. Fischer, "A special newton-type optimization method," *Optimization*, vol. 24, pp. 269–284, Jan. 1992.

[90] M. S. Carvalho, "Elastohydrodynamics of tensioned web roll coating process," *International Journal for Numerical Methods in Fluids*, vol. 41, pp. 561–576, Feb. 2003.

[91] "COMSOL Multiphysics® v. 6.0. COMSOL AB, Stockholm, Sweden.." `www.comsol.com/release/6.0`.

[92] C. J. Hooke, "Elastohydrodynamic lubrication of soft solids," *Tribology Series*, vol. 32, pp. 185–197, Jan. 1997.

[93] U. Tahir, Y. Shim, M. Kamran, D.-I. Kim, and M. Jeong, "Nanofabrication techniques: Challenges and future prospects," *Journal of Nanoscience and Nanotechnology*, vol. 21, pp. 4981–5013, May 2021.

[94] D. Dowson and Z. Jin, "The influence of elastic deformation upon film thickness in lubricated bearings with low elastic modulus coatings," *Tribology Series*, vol. 17, pp. 263–269, Jan. 1990.

[95] D. J. Coyle, "Forward roll coating with deformable rolls: A simple one-dimensional elastohydrodynamic model," *Chemical Engineering Science*, vol. 43, pp. 2673–2684, Jan. 1988.

[96] S. F. Kistler and P. M. Schweizer, eds., *Liquid Film Coating*. Dordrecht: Springer Netherlands, 1997.

[97] W. Habchi, "A numerical model for the solution of thermal elastohydrodynamic lubrication in coated circular contacts," *Tribology International*, vol. 73, pp. 57–68, May 2014.

[98] W. Habchi, D. Eyheramendy, P. Vergne, and G. Morales-Espejel, "Stabilized fully-coupled finite elements for elastohydrodynamic lubrication problems," *Advances in Engineering Software*, vol. 46, pp. 4–18, Apr. 2012.

[99] D. Dowson and C. M. Taylor, "Cavitation in bearings," *Annual Review of Fluid Mechanics*, vol. 11, pp. 35–65, Jan. 1979.

[100] T. V. Kármán, *Festigkeitsprobleme im maschinenbau*. Encyklopädie der mathematischen wissenschaften, Teubner, 1910.

[101] S. P. Timoshenko and S. Woinowsky-Kreiger, *Theory of Plates and Shells*. New York: McGraw-Hill Book Company, 2 ed., Dec. 1959.

[102] D. Bulut, N. Bader, and G. Poll, "Cavitation and film formation in hydrodynamically lubricated parallel sliders," *Tribology International*, vol. 162, p. 107113, Oct. 2021.

[103] Y. Zhao, H. C. Liu, G. E. Morales-Espejel, and C. H. Venner, "Effects of solid viscoelasticity on elastohydrodynamic lubrication of point contacts," *Tribology International*, vol. 171, p. 107562, July 2022.

[104] M. Marian, M. Bartz, S. Wartzack, and A. Rosenkranz, "Non-dimensional groups, film thickness equations and correction factors for elastohydrodynamic lubrication: A review," *Lubricants*, vol. 8, p. 95, Oct. 2020.

[105] H. G. Elrod, "A cavitation algorithm," *Journal of Lubrication Technology*, vol. 103, pp. 350–354, July 1981.

[106] J. Snieder, M. Dielen, and R. A. J. van Ostayen, "Elastohydrodynamic lubrication of soft-layered rollers and tensioned webs in roll-to-plate nanoimprinting," *Proceedings of the Institution of Mechanical Engineers, Part J: Journal of Engineering Tribology*, vol. 237, pp. 1871–1884, Oct. 2023.

[107] D. Dowson and G. R. Higginson, "A numerical solution to the elasto-hydrodynamic problem," *Journal of Mechanical Engineering Science*, vol. 1, pp. 6–15, June 1959.

[108] D. Dowson, E. S. Song, and C. M. Taylor, "Non-dimensional groups in elastohydrodynamic lubrication," in *Tribology Series* (D. Dowson, C. M. Taylor, T. H. C. Childs, M. Godet, and G. Dalmaz, eds.), vol. 25 of *Thin Films in Tribology*, pp. 237–242, Elsevier, Jan. 1993.

[109] H. van Leeuwen, "Nondimensional groups - The most important legacy of Harmen Blok," in *GfT Tagungsband 2019: Tagungsband Der 60. Tribologie-Fachtagung, 23. September Bis 25. September 2019 in Göttingen, Reibung, Schmierung Und Verschleiß*, (Göttingen, Germany), pp. 442–451, Gesellschaft für Tribologie e.V., Sept. 2019.

[110] K. L. Johnson, "Regimes of elastohydrodynamic lubrication," *Journal of Mechanical Engineering Science*, vol. 12, pp. 9–16, Feb. 1970.

[111] C. Liu, "Implementing the weak form in COMSOL Multiphysics," Jan. 2015.

[112] M. Quinten, *A Practical Guide to Optical Metrology for Thin Films*. Weinheim, Germany: Wiley-VCH Verlag GmbH & Co. KGaA, Oct. 2012.

[113] P. Dou, Y. Jia, P. Zheng, T. Wu, M. Yu, T. Reddyhoff, and Z. Peng, "Review of ultrasonic-based technology for oil film thickness measurement in lubrication," *Tribology International*, vol. 165, p. 107290, Jan. 2022.

[114] M. Schirru and M. Varga, "A Review of ultrasonic reflectometry for the physical characterization of lubricated tribological contacts: History, methods, devices, and technological trends," *Tribology Letters*, vol. 70, p. 129, Dec. 2022.

[115] M. Visscher, *The Measurement of the Film Thickness and the Roughness Deformation of Lubricated Elastomers*. PhD thesis, Technische Universiteit Eindhoven, Eindhoven, 1992.

[116] H. A. Spikes, "Thin films in elastohydrodynamic lubrication: The contribution of experiment," *Proceedings of the Institution of Mechanical Engineers, Part J: Journal of Engineering Tribology*, vol. 213, pp. 335–352, May 1999.

[117] H. A. Spikes, "Sixty years of EHL," *Lubrication Science*, vol. 18, no. 4, pp. 265–291, 2006.

[118] S. Albahrani, D. Philippon, P. Vergne, and J.-M. Bluet, "A review of in situ methodologies for investigating EHD contacts," *Proceedings of the Institution of Mechanical Engineers, Part J: Journal of Engineering Tribology*, vol. 230, no. 1, pp. 86–110, 2015.

[119] G. Poll, A. Gabelli, P. G. Binnington, and J. Qu, "Dynamic mapping of rotary lip seal lubricant films by fluorescent image processing," in *Fluid Sealing* (B. S. Nau, ed.), pp. 55–77, Dordrecht: Springer Netherlands, 1992.

[120] P. Lok, "Lubrication-film height imaging for hydrostatic bearings with fluorescence," Master's thesis, Delft University of Technology, Delft, Aug. 2022.

[121] J. R. Lakowicz, ed., *Principles of Fluorescence Spectroscopy*. Boston, MA: Springer US, 2006.

[122] M. Sauer, J. Hofkens, and J. Enderlein, "Basic principles of fluorescence spectroscopy," in *Handbook of Fluorescence Spectroscopy and Imaging*, ch. 1, pp. 1–30, John Wiley & Sons, Ltd, 2011.

[123] J. F. W. Herschel, "On a case of superficial colour presented by a homogeneous liquid internally colourless," *Philosophical Transactions of the Royal Society of London*, vol. 135, pp. 143–145, 1845.

[124] adm_venator, "The fluorescent glow of gin and tonic in the sun." `www.reddit.com/r/chemistry/comments/bwf0uq/the_fluorescent_glow_of_gin_and_tonic_in_the_sun/`, June 2019.

[125] J. Blosser, "Bottle of UV illuminated tonic water (pouring)." `https://commons.wikimedia.org/wiki/File:Bottle_of_UV_Illuminated_Tonic_Water_(Pouring).jpg`, Oct. 2019.

[126] R. P. Haugland, *Handbook of Fluorescent Probes and Research Products*. Eugene, Or.: Molecular Probes, Inc, 9th edition ed., Jan. 2002.

[127] G. G. Stokes, "On the change of refrangibility of light," *Philosophical Transactions of the Royal Society of London*, vol. 142, pp. 463–562, 1852.

[128] A. E. Smart and R. A. J. Ford, "Measurement of thin liquid films by a fluorescence technique," *Wear*, vol. 29, pp. 41–47, July 1974.

[129] R. A. J. Ford and C. A. Foord, "Laser-based fluorescence techniques for measuring thin liquid films," *Wear*, vol. 51, pp. 289–297, Dec. 1978.

[130] C. Myant, T. Reddyhoff, and H. Spikes, "Laser-induced fluorescence for film thickness mapping in pure sliding lubricated, compliant, contacts," *Tribology International*, vol. 43, pp. 1960–1969, Nov. 2010.

[131] T. Reddyhoff, J. H. Choo, H. A. Spikes, and R. P. Glovnea, "Lubricant flow in an elastohydrodynamic contact using fluorescence," *Tribology Letters*, vol. 38, pp. 207–215, June 2010.

[132] T. Hagemeier, M. Hartmann, M. Kühle, D. Thévenin, and K. Zähringer, "Experimental characterization of thin films, droplets and rivulets using LED fluorescence," *Experiments in Fluids*, vol. 52, pp. 361–374, Feb. 2012.

[133] T. Wittek, "Optische Untersuchungen zum Schmierungszustand im Reibkontakt von Synchronisierungen," Master's thesis, Leibniz Universität Hannover, Mar. 2018.

[134] N. M. Husen, T. Liu, and J. P. Sullivan, "The ratioed image film thickness meter," *Measurement Science and Technology*, vol. 29, p. 065301, June 2018.

[135] M. Chennaoui, M. Fowell, H. Liang, and A. Kadiric, "A novel set-up for in situ measurement and mapping of lubricant film thickness in a model rolling bearing using interferometry and ratiometric fluorescence imaging," *Tribology Letters*, vol. 70, p. 85, Sept. 2022.

[136] M. C. Mota, P. Carvalho, J. Ramalho, and E. Leite, "Spectrophotometric analysis of sodium fluorescein aqueous solutions. Determination of molar absorption coefficient," *International Ophthalmology*, vol. 15, pp. 321–326, Sept. 1991.

[137] E. A. Slyusareva and M. A. Gerasimova, "pH-Dependence of the absorption and fluorescent properties of fluorone dyes in aqueous solutions," *Russian Physics Journal*, vol. 56, pp. 1370–1377, Apr. 2014.

[138] M. Enoki and R. Katoh, "Estimation of quantum yields of weak fluorescence from eosin Y dimers formed in aqueous solutions," *Photochemical & Photobiological Sciences*, vol. 17, pp. 793–799, June 2018.

[139] M. M. Martin and L. Lindqvist, "The pH dependence of fluorescein fluorescence," *Journal of Luminescence*, vol. 10, pp. 381–390, July 1975.

[140] J. H. Lambert, *Photometria sive de mensura et gradibus luminis, colorum, et umbrae [Photometry, or, on the measure and gradations of light intensity, colors, and shade]*. Augsburg, Germany: Eberhardt Klett, 1760.

[141] Beer, "Bestimmung der Absorption des rothen Lichts in farbigen Flüssigkeiten [Determination of the absorption of red light in colored liquids]," *Annalen der Physik*, vol. 162, no. 5, pp. 78–88, 1852.

[142] L. S. Herculano, L. C. Malacarne, V. S. Zanuto, G. V. B. Lukasievicz, O. A. Capeloto, and N. G. C. Astrath, "Investigation of the photobleaching process of Eosin Y in aqueous solution by thermal lens spectroscopy," *The Journal of Physical Chemistry B*, vol. 117, pp. 1932–1937, Feb. 2013.

[143] R. McCluney, *Introduction to Radiometry and Photometry*. Boston: Artech House, second edition ed., 2014.

[144] J. L. Marshall, P. Williams, J.-P. Rheault, T. Prochaska, R. D. Allen, and D. L. DePoy, "Characterization of the reflectivity of various black materials," in *SPIE Astronomical Telescopes + Instrumentation* (S. K. Ramsay, I. S. McLean, and H. Takami, eds.), (Montréal, Quebec, Canada), p. 91474F, July 2014.

[145] A. M. Ertel, "Hydrodynamic theory of lubrication, based on new principles," *Applied Mathematics and Mechanics*, vol. 3, no. 2, pp. 1–14, 1939.

[146] A. Von Mohrenstein, "Hydrodynamic bearing," Mar. 1956.

[147] E. Popova and V. L. Popov, "On the history of elastohydrodynamics: The dramatic destiny of Alexander Mohrenstein-Ertel and his contribution to the theory and practice of lubrication," *ZAMM - Journal of Applied Mathematics and Mechanics / Zeitschrift für Angewandte Mathematik und Mechanik*, vol. 95, no. 7, pp. 652–663, 2015.

[148] A. F. C. Kanters, J. F. M. Verest, and M. Visscher, "On reciprocating elastomeric seals: Calculation of film thicknesses using the inverse hydrodynamic lubrication theory," *Tribology Transactions*, vol. 33, pp. 301–306, Jan. 1990.

[149] B. S. Nau, "An historical review of studies of polymeric seals in reciprocating hydraulic systems," *Proceedings of the Institution of Mechanical Engineers, Part J: Journal of Engineering Tribology*, vol. 213, pp. 215–226, Mar. 1999.

[150] G. K. Nikas, "Eighty years of research on hydraulic reciprocating seals: Review of tribological studies and related topics since the 1930s," *Proceedings of the Institution of Mechanical Engineers, Part J: Journal of Engineering Tribology*, vol. 224, pp. 1–23, Jan. 2010.

[151] "COMSOL Multiphysics® v. 6.2. COMSOL AB, Stockholm, Sweden.." `www.comsol.com/release/6.2`.

[152] N. Heinrichson, *On the Design of Tilting-Pad Thrust Bearings*. PhD thesis, Technical University of Denmark, 2007.

[153] M. He and J. M. Byrne, "Fundamentals of fluid film thrust bearing operation and modeling," in *Asia Turbomachinery & Pump Proceedings*, 2018.

[154] A. Almqvist and F. P. Ràfols, "Scientific computing with applications in tribology: A course compendium," tech. rep., Luleå University of Technology, 2019.

[155] S. Awtar and A. Slocum, "Flexure systems based on a symmetric diaphragm flexure," in *Proceedings of the ASPE 2005 Annual Meeting*, 2005.

[156] S. Yang, W. Zheng, M. Jiang, S. Pei, and H. Xu, "A comparative experimental study on large size center and bi-directional offset spring-bed thrust bearing," *Proceedings of the Institution of Mechanical Engineers, Part J: Journal of Engineering Tribology*, vol. 234, pp. 134–144, Jan. 2020.

[157] I. Moreno, J. Muñoz, and R. Ivanov, "Uniform illumination of distant targets using a spherical light-emitting diode array," *Optical Engineering*, vol. 46, p. 033001, Mar. 2007.

[158] A. Hunter, R. Dwyer-Joyce, and P. Harper, "Calibration and validation of ultrasonic reflection methods for thin-film measurement in tribology," *Measurement Science and Technology*, vol. 23, p. 105605, Sept. 2012.

[159] H. Feldman, M. A. Iron, D. Fixler, S. Moshkov, N. Zurgil, E. Afrimzon, and M. Deutsch, "Fluorophore spectroscopy in aqueous glycerol solution: The interactions of glycerol with the fluorophore," *Photochemical & Photobiological Sciences*, vol. 20, pp. 1397–1418, Nov. 2021.

[160] N.-S. Cheng, "Formula for the viscosity of a glycerol-water mixture," *Industrial & Engineering Chemistry Research*, vol. 47, pp. 3285–3288, May 2008.

[161] C. A. Combs, "Fluorescence microscopy: A concise guide to current imaging methods," *Current Protocols in Neuroscience*, Jan. 2010.

[162] N. Patir and H. S. Cheng, "An average flow model for determining effects of three-dimensional roughness on partial hydrodynamic lubrication," *Journal of Lubrication Technology*, vol. 100, pp. 12–17, Jan. 1978.

[163] K. Kobayashi, N. Sakai, S. Matsui, and M. Nakagawa, "Fluorescent UV-curable resists for UV nanoimprint lithography," *Japanese Journal of Applied Physics*, vol. 49, p. 06GL07, June 2010.

[164] S. Kubo, T. Tomioka, and M. Nakagawa, "Resolution limits of nanoimprinted patterns by fluorescence microscopy," *Japanese Journal of Applied Physics*, vol. 52, p. 06GJ01, June 2013.

Acknowledgments

This dissertation is the final result of my PhD research, which has been a rewarding yet challenging experience. Many people supported me along the way and I would like to thank and acknowledge them here.

First of all, I would like to thank my promotors Ron and Just, for the support over all these years. You both helped me grow in my research skills and my writing, for which I am thankful. Thank you, Ron, for your guidance and enthusiasm. I am always impressed by your expertise in tribology and your ability to come up with elegant solutions for various challenges. I remember meeting you by chance, while walking from the train station to the university. We discussed the possibility of doing a PhD, something I had always kept in mind, and here we are. It is remarkable how such a small moment can have such a big impact. Thank you Just, for your insights and help in steering the research direction and structure. It is much appreciated.

I would also like to thank my colleagues at Morphotonics, for always making me feel welcome during my weekly visits. The collaboration with industry was a great motivation for doing this research and I enjoyed working together. Thank you Bram and Jan Matthijs, for your support, insights, and our monthly discussions. Special thanks also go to Marc, for working together on the publications within this dissertation.

My gratitude goes out to all my colleagues in the department of Precision and Microsystems Engineering. It was great to work in a department with so many talented researchers and great support staff. The department has an excellent lab support team. I would like to thank Alex, Bradley, Gideon, Rob, and Spiridon, for assisting me with the experiments. A special thanks goes out to Patrick, for all the support and encouragement with the experimental set-ups.

I am thankful for the support from the colleagues in my office in the early phase of my PhD. Thank you, Abdullah, Ali A. D., Freek, Jelle R., Joep, Niranjan, Reinier, Thijs, Werner, for making me feel welcome and for helping me settle in my new job. I would also like to thank my direct colleagues, Ad, Ali A. N., Ali H., Dave, Dilek, Francesco, Gerben, Malte, Marcin, Nima, Pedro, Sifeng, Xinxin, and many more, for all the chats, discussions, laughs, support, and fun activities. And not to forget the trips to the conferences and the summer school. I really enjoyed the travels with some of you to Lyon, Leeds, Munich, and Visp. Special thanks go to a few colleagues in particular. Dave and Malte, I am very happy with you as my paranymphs and I am sure that I feel much more confident with you at my side. Thanks for your support. Ali, our office manager, thank you for always smiling (Life's Good!) and listening. And last but not least, Ad, my PhD buddy from almost day one. We followed the same trajectory, starting and defending within a month from each other. Thank you for sharing all memorable moments in the PhD trajectory.

Part of this research focused on fluorescence, imaging, and optics, which were not directly in my field of expertise. I owe my gratitude to Pieter, for explaining me all the ins and outs of the ratiometric fluorescence technique, to Nandini for answering all my optics

questions, and to Astrid for supporting me with the spectral measurements at TNW. During the research, I also worked together with several master students. Thank you Daniel, Julian, Kees, Rob, and Tobias, for your enthusiasm and the many inspiring discussions about your graduation projects.

Finally, I would like to thank my friends and family. I am extremely grateful for the unconditional support and love of my parents, Frank and Marinka, my sister, Anne, and all the other members of my family. It means a lot to me. But most of all, I want to thank my partner, Alexandra, for standing by my side. Thank you for being there when I most needed it, for putting things in perspective. This thesis would not be there if it was not for you. I look forward to the years to come.

Jelle
Rotterdam, December 2025

Curriculum Vitæ

Jelle Snieder

07-02-1992 Born in Amsterdam, The Netherlands

Education

2020–2025 PhD in Mechanical Engineering
Delft University of Technology

Dissertation:	Film height in soft elastohydrodynamic lubrication
Promotor:	Dr. ir. Ron A.J. van Ostayen
Promotor:	Prof. dr. ir. Just L. Herder

2014–2017 MSc in Mechanical Engineering
Delft University of Technology

Thesis:	Development of an air-based contactless transport demonstrator
Supervisor:	Dr. ir. Ron A.J. van Ostayen

2010–2014 BSc in Mechanical Engineering
Delft University of Technology

Experience

2025–present Mechanical Design Engineer
ASML

2020–2024 Mechanical Engineer (part-time)
Morphotonics

2018–2020 Mechatronic System Engineer
Demcon

List of publications

Journal publications

4. **Snieder, J.**, & van Ostayen, R. A. J. *A novel concept and experimental setup for steering and mapping the film height in a deformable slider bearing.* In preparation.

3. **Snieder, J.**, & van Ostayen, R. A. J. *Extended analytical model and experimental validation of the ratiometric fluorescence film height measurement method.* To be submitted.

2. **Snieder, J.**, Dielen, M., & van Ostayen, R. A. J. (2023). *Elastohydrodynamic lubrication of soft-layered rollers and tensioned webs in roll-to-plate nanoimprinting.* Proceedings of the Institution of Mechanical Engineers, Part J: Journal of Engineering Tribology, 237(10), 1871–1884. https://doi.org/10.1177/13506501231183860.

1. **Snieder, J.**, Dielen, M., & van Ostayen, R. A. J. (2022). *Simulating the residual layer thickness in roll-to-plate nanoimprinting with tensioned webs.* Micromachines, 13(3), 461. https://doi.org/10.3390/mi13030461.

Conference publications

1. **Snieder, J.**, & van Ostayen, R. A. J. (2023). *Elastohydrodynamics of roll-to-plate nanoimprinting on non-flat substrates.* Papers and Presentations from the COMSOL Conference 2023. Comsol Conference 2023, Munich.

Included in this thesis.

Conference presentations

5. **Snieder, J.**, & van Ostayen, R. A. J. (2023, October 25–27). *Elastohydrodynamics of roll-to-plate nanoimprinting on non-flat substrates* [conference presentation and poster presentation]. Comsol Conference 2023, Munich, Germany. 🗎

4. **Snieder, J.**, & van Ostayen, R. A. J. (2023, September 5–7). *Film height control in hydrodynamic lubrication using inverse lubrication theory* [conference presentation]. 48th Leeds-Lyon Symposium on Tribology, Leeds, UK. 🗎

3. **Snieder, J.**, & van Ostayen, R. A. J. (2022, July 10–15). *Elastohydrodynamics of roll-to-plate nanoimprinting with tensioned webs* [conference presentation]. 7th World Tribology Congress, Lyon, France. 🗎

2. **Snieder, J.**, & van Ostayen, R. A. J. (2021, November 16–17). *Simulating the layer thickness in roller-based imprinting with pre-tensioned flexible stamps* [conference presentation]. 20th International Conference on Nanoimprint and Nanoprint Technologies (virtual), Espoo, Finland. 🗎

1. **Snieder, J.**, & van Ostayen, R. A. J. (2021, May 27–28). *Simulating the layer thickness in roll-to-plate nanoimprint lithography* [conference presentation]. 7th International Conference on Polymer Replication on Nanoscale (virtual), Windisch, Switzerland. 🗎

MSc thesis projects supervised

- Rob Neelen, *Large scale overlay: a study into accuracies in roll-to-plate nanoimprint lithography*, 2021.

- Kees Pijnenburg, *Development of novel manufacturing method for a contactless handling system using a variable outlet restriction*, 2022.

- Tobias Neeft, *Development and prototype of a textured nanoimprinted air bearing system*, 2023.

- Julian Bleeker, *Multilayer thin film thickness measurement method*, 2023.

- Daniel Blommestein, *Passive film thickness control in hydrodynamic lubrication on non-flat surfaces*, 2023.

🗎 Included in this thesis.

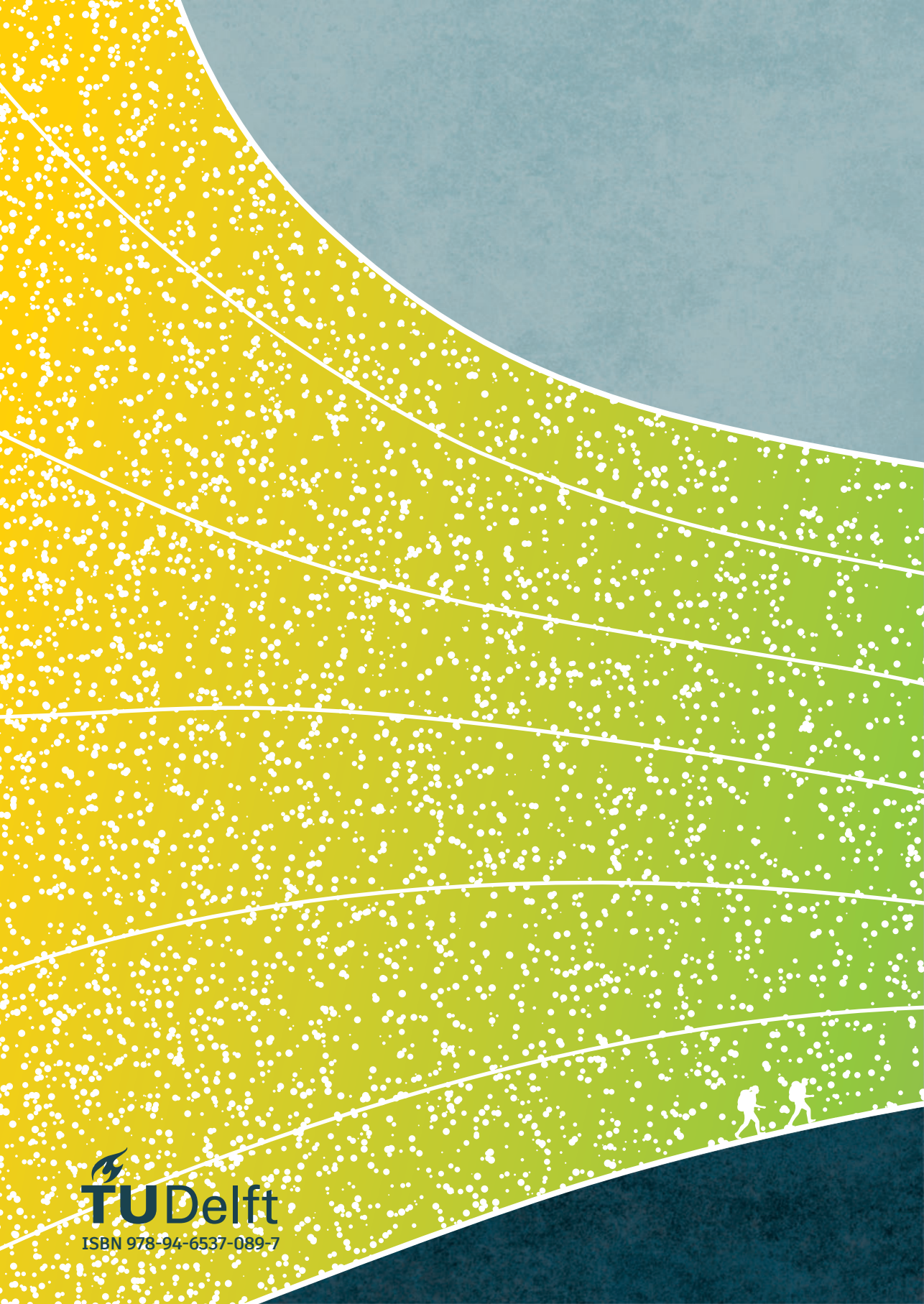

ISBN 978-94-6537-089-7